

Giant magnetoresistance in spin valves

Citation for published version (APA):

Willekens, M. M. H. (1997). *Giant magnetoresistance in spin valves*. [Phd Thesis 1 (Research TU/e / Graduation TU/e), Applied Physics and Science Education]. Technische Universiteit Eindhoven.
<https://doi.org/10.6100/IR497819>

DOI:

[10.6100/IR497819](https://doi.org/10.6100/IR497819)

Document status and date:

Published: 01/01/1997

Document Version:

Publisher's PDF, also known as Version of Record (includes final page, issue and volume numbers)

Please check the document version of this publication:

- A submitted manuscript is the version of the article upon submission and before peer-review. There can be important differences between the submitted version and the official published version of record. People interested in the research are advised to contact the author for the final version of the publication, or visit the DOI to the publisher's website.
- The final author version and the galley proof are versions of the publication after peer review.
- The final published version features the final layout of the paper including the volume, issue and page numbers.

[Link to publication](#)

General rights

Copyright and moral rights for the publications made accessible in the public portal are retained by the authors and/or other copyright owners and it is a condition of accessing publications that users recognise and abide by the legal requirements associated with these rights.

- Users may download and print one copy of any publication from the public portal for the purpose of private study or research.
- You may not further distribute the material or use it for any profit-making activity or commercial gain
- You may freely distribute the URL identifying the publication in the public portal.

If the publication is distributed under the terms of Article 25fa of the Dutch Copyright Act, indicated by the "Taverne" license above, please follow below link for the End User Agreement:

www.tue.nl/taverne

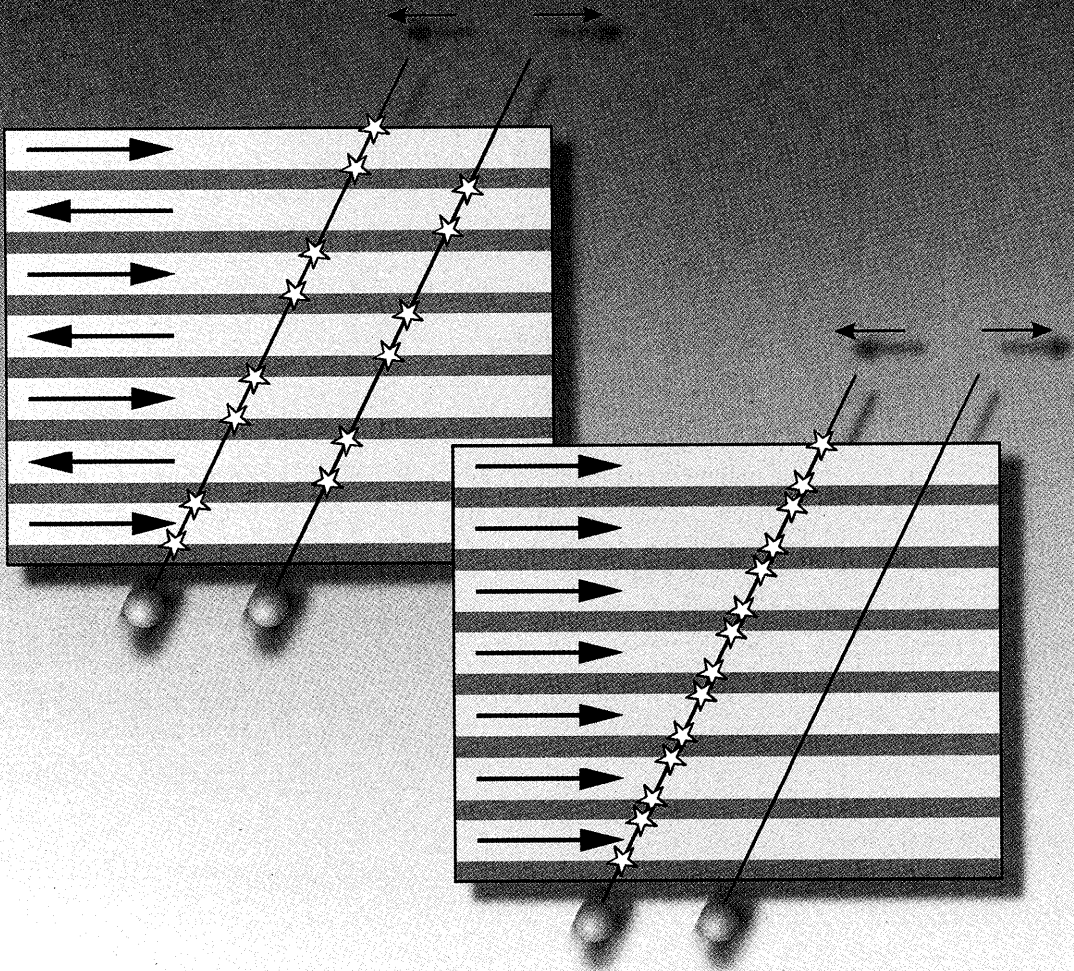
Take down policy

If you believe that this document breaches copyright please contact us at:

openaccess@tue.nl

providing details and we will investigate your claim.

Giant Magneto Resistance in Spin Valves



M.M.H. Willekens

**Giant Magnetoresistance
in
Spin Valves**

PROEFSCHRIFT

ter verkrijging van de graad van doctor aan de
Technische Universiteit Eindhoven, op gezag van de
Rector Magnificus, prof.dr. M. Rem, voor een
commissie aangewezen door het College voor
Promoties in het openbaar te verdedigen op
woensdag 15 oktober 1997 om 16.00 uur

door

Marcus Marinus Henricus Willekens

geboren te Tilburg

Dit proefschrift is goedgekeurd door de promotoren:

prof.dr.ir. W.J.M. de Jonge
en
prof.dr. R. Coehoorn

Copromotor:
dr.ir. H.J.M. Swagten

CIP-DATA LIBRARY TECHNISCHE UNIVERSITEIT EINDHOVEN

Willekens, Marcus Marinus Henricus

Giant Magnetoresistance in Spin Valves / by
Marcus Marinus Henricus Willekens. -
Eindhoven : Technische Universiteit Eindhoven, 1997. - Proefschrift. -
ISBN 90-386-0567-6

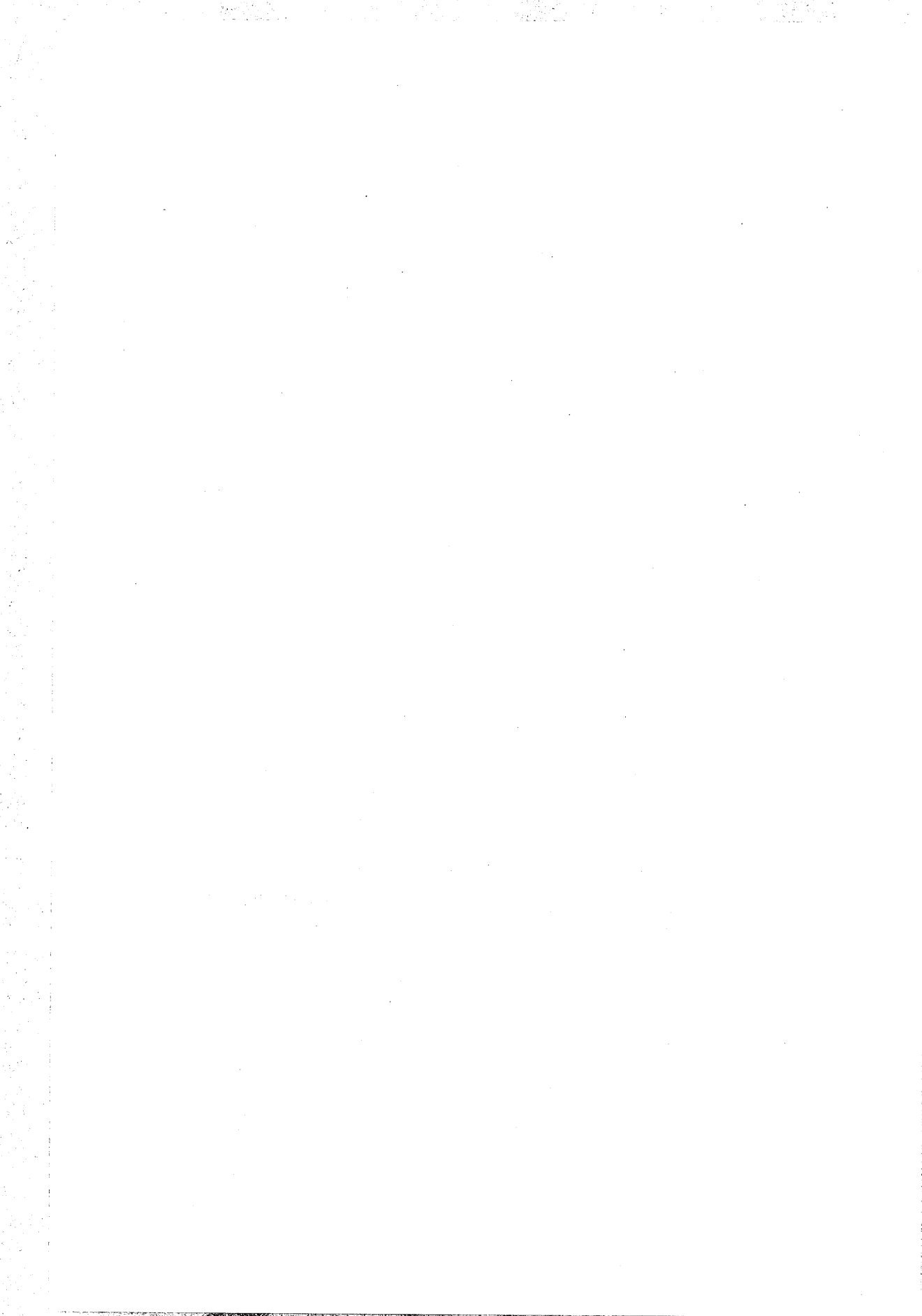
NUGI 812

Trefw.: magnetoweerstand / magnetische dunne lagen / metallische multilagen.
Subject headings: giant magnetoresistance / spin valves / magnetism.

Druk: Universiteitsdrukkerij TU Eindhoven

The work described in this thesis has been performed at the Eindhoven University of Technology within the framework of a collaboration between the Solid State Division (group Cooperative Phenomena) of the Physics Department of the Eindhoven University of Technology and the Magnetism group at the Philips Research Laboratories Eindhoven (PRLE), both situated in Eindhoven, the Netherlands.

aan mijn moeder



Contents

1	General introduction	1
1.1	A bit of history	1
1.2	Magnetoresistance	4
1.3	This thesis	10
2	Experimental	13
2.1	Sample preparation.....	13
2.2	Sample characterization	15
2.2.1	Magnetometry.....	15
2.2.2	The Fluxgate Magnetometer.....	16
2.2.3	The SQUID Magnetometer	19
2.2.4	The Magneto Optical Kerr Effect.....	23
2.3	Magnetoresistance	27
2.4	X-ray analysis.....	29
3	Modelling of the GMR effect	33
3.1	Introduction.....	33
3.2	Semiclassical treatment of resistance in thin layers	36
3.2.1	The Boltzmann transport equation	36
3.2.2	Boltzmann transport equation for a thin film.....	37
3.2.3	Influence of the boundaries.....	41
3.2.4	Boltzmann transport equation for a magnetic multilayer.....	43
3.2.5	Approximations in the semiclassical models.....	49
3.3	Analytical approach to the CB-model.....	50
3.3.1	Derivation of analytical expressions for the GMR effect	50
3.3.2	Validity of the analytical expressions.....	52
3.3.3	A study of the local conductance, $G(z)$	56
3.4	Quantum mechanical models	63
3.5	CPP geometry.....	66
4	Magnetic and transport behavior of AF-coupled layers with a limited number of repetitions	71
4.1	Introduction.....	71
4.2	The samples.....	73
4.3	Results	74
4.4	Discussion.....	77
4.5	Conclusions.....	84
5	Spin valves for the investigation of spin dependent scattering: interface versus bulk	87
5.1	Introduction.....	87
5.2	Co/Ru/Co/Cu/Co spin valves.....	90
5.2.1	Magnetization of AF-biased spin valves.....	90

5.2.2	Magnetoresistance of AF-biased spin valves.....	93
5.3	Exchange-biased spin valves.....	95
5.3.1	Magnetization of exchange-biased spin valves.....	96
5.3.2	Magnetoresistance of exchange biased spin valves.....	97
5.4	Conclusions.....	98
6	interface intermixing and magnetoresistance in Co/Cu/Co spin valves	99
6.1	Introduction.....	99
6.2	Samples with intermixed interface(s).....	100
6.3	Results.....	103
6.4	Discussion.....	106
6.4.1	No interface spin-dependent scattering.....	108
6.4.2	No bulk spin-dependent scattering.....	110
6.5	Conclusions.....	113
7	Analysis of scattering lengths in Co/Cu/Co and Co/Cu/Co/Cu spin valves	115
7.1	Introduction.....	115
7.2	Experimental.....	117
7.3	Results.....	117
7.4	Model calculations.....	122
7.5	Discussion.....	128
7.6	Conclusions.....	132
8	Interface-selective determination of spin-dependent scattering	133
8.1	Introduction.....	133
8.2	Model calculations.....	134
8.3	Experimental.....	137
8.4	Results and discussion.....	138
8.5	Conclusions.....	150
9	Enhanced giant magnetoresistance in spin valves sandwiched between insulating NiO	151
9.1	Introduction.....	151
9.2	Experimental.....	152
9.3	Interpretation.....	157
9.4	Discussion.....	160
9.5	Conclusions.....	165
	References	167
	Samenvatting	177
	List of publications	181

Dankwoord

183

Curriculum Vitae

184



1. *General introduction*

1.1 A bit of history

As nature has provided us with permanent magnets in the form of magnetized rocks (consisting mainly of magnetite, Fe_3O_4) many millions of years ago, prehistoric men already may have wondered about the attracting and repelling forces between magnets. We do not know that for a fact, however, since prehistoric men did not write down all their observations quite as accurately as we do today. One of the first researchers on the area of magnetism that we do know of (Hec80) was the Greek natural philosopher Thales from Miletus in the sixth century B.C. By that time the knowledge of smelting iron was already developed and in fact iron and steel were in fairly common use. Thales was the first to teach about the attractive forces between a lodestone (Fe_3O_4) and iron.

Although today those magnetized rocks of magnetite are called "lodestones", a name originating from "leading stone" (lode being old English for "leading" or "guiding") and referring to the use in magnetic compasses, Thales from Miletus will probably not have used this word. This is because until nearly 1200 A.D., there is no reference in Western literature to the north-south orienting property of magnets, and the term lodestone did not appear until about 1500. In addition we mention here that according to a Chinese legend the Chinese Emperor Hwang-ti (ca. 2600 B.C.) already used a lodestone to guide his war chariot through a dense fog, which probably led him to victory. Anyhow, although the attracting forces must have been known for ages, not much progress was made on the area of magnetism in the Middle Ages and around 1200 A.D., the only (Hec80) practical application for a magnet was a magnetic compass. Several hundreds of years later this application was still not very reliable, as we can learn from the journey of Christopher Columbus in 1492.

Now, jumping to our contemporary society, the applications of magnets are numerous, much more than most people might realize. Magnets are literally all around us, sometimes clearly visible, but many times hidden inside all sorts of apparatus such as a refrigerator door, a TV, or a car. In his book "Driving Force, the natural magic of magnets" J.D. Livingston (Liv96) presents a comprehensive overview of the use of all kinds of magnets. One important current application of magnetism, that has grown enormously in interest over the past decades because of the introduction of computers, is that of magnetic data storage and retrieving, and in fact it is today's largest and fastest growing use of magnets (Liv96). Also the investigations described in this thesis are meant to form a contribution to this particular field of interest.

The history of magnetic recording started (Pou1899) almost one century ago, in Denmark. In 1898 Valdemar Poulsen was the first to demonstrate in his

laboratory the principle of magnetic recording. As a recording medium he used a steel piano wire. Magnetic domains were "written" in the wire by means of an electromagnet (the "magnetic head") moving along it, making use of magnetic induction: An electrical current through the electromagnet produces a magnetic field that aligns the local magnetization direction in the wire. With the same induction principle the recorded information can be read: the magnetic head moves, preferably at the same speed, along the wire again and the stored magnetic pattern in the wire induces a varying current, thereby reproducing the originally stored information.

Via Poulsen magnetic recording found its first application in a telegraphone that could record messages while the owner of the telegraphone was not at home. Figure 1.1 is a detailed drawing taken from the 1905 patent of the telegraphone by Poulsen. Clearly visible are two reels (e and e') with the magnetic wire wound around it and in the middle three electromagnets (m , m' , and m''). The middle magnet, m , is the recording and reproducing magnet whereas m' or m'' is for obliterating the existing record before recording a new message, depending on the direction in which the wire moves.

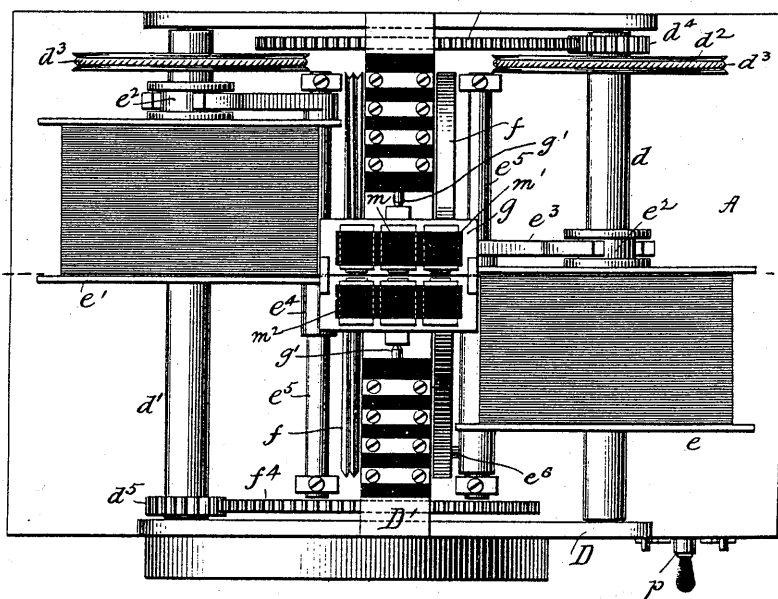


Figure 1.1: Detailed drawing representing a part of the telegraphone. Clearly visible are two reels (e and e') containing the magnetized wire and three magnets (m , m' , and m'') in the middle. This drawing is taken from the 1905 patent of the telegraphone by Poulsen.

Around World War II, the magnetic wire was replaced by a nonmagnetic substrate coated with fine magnetic particles. These so called magnetic tapes are still in use today, although the fabrication process and composition have changed. For instance, the magnetic material on a video tape or floppy disk consists of particles CrO_2 or $\gamma\text{-Fe}_2\text{O}_3$ with a size of ca. $0.2 \mu\text{m}$ (Lui93).

Read and write heads are nowadays often of the yoke type. A schematic picture of such a head in combination with a magnetic tape is shown in figure 1.2. To write information in the film one has to pass a current through the coil. This current defines the magnetization direction of the yoke. The magnetic field across the gap of the yoke in turn will magnetize the tape immediately below it, thus creating a domain pattern in the film. To read the stored information the tape is led along the same head again. Now the magnetization direction in the magnetic yoke will follow the domain pattern of the tape and thus induce an induction voltage in the coil.

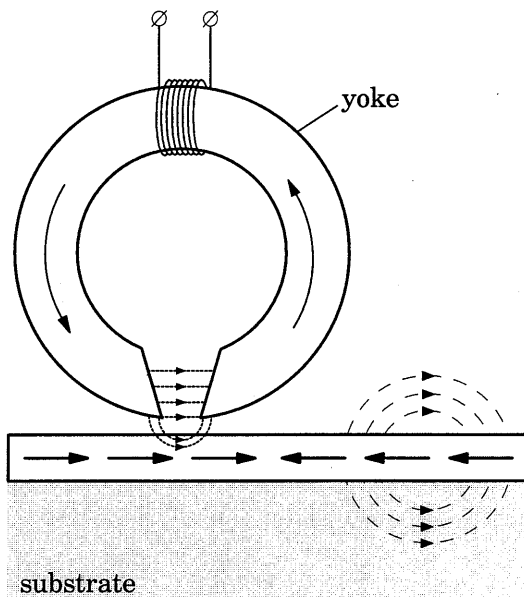


Figure 1.2: Schematic representation of a yoke-type magnetic read/write head. Writing: the magnetic field across the gap in the yoke, induced by a current through the coil around the yoke, magnetizes the tape. Reading: the domain pattern of the tape causes a varying magnetic induction in the yoke and thus a current through the coil around the yoke. The figure is based on a figure by J. Smits (Smi92).

In state-of-the-art read heads the induction coil is often replaced by a magnetoresistive element (MRE), as is shown schematically in figure 1.3. This is an element whose resistance depends on the direction of its magnetization, and thus on the direction and strength of the applied magnetic field. Therefore the stored information in the tape will determine the resistance of the MRE and, when a current is passed through the MRE, changes of resistance can be measured from which the stored information can be reproduced. An advantage of such an MRE above the induction coil is that now the measured signal does not depend on the speed of the tape.

The spin valves described in this thesis do demonstrate this property: The resistance of the spin valve depends on the strength of an external applied magnetic field. Although we are not directly concerned with optimizing the effect for the above described application, part of the enormous interest in the phenomenon of magnetoresistance of course does originate from this important application. Although we will not explain them in this introduction, we would like to mention that there are more applications for magnetoresistive elements, for instance in position, speed, and proximity sensors, or in magnetoresistive random access memories (MRAM).

1.2 Magnetoresistance

There are several different causes of magnetoresistance. First of all, we should note that it is not necessary to study a magnetic material to obtain a magnetoresistance effect. All (non)magnetic metals exhibit the ordinary magnetoresistance effect, which means an increase in electrical resistance as a function of the internal magnetic induction \vec{B} (Jan57). This effect is induced by the Lorentz force $e\vec{v} \times \vec{B}$, that causes the electrons to move along helical trajectories, instead of traveling along straight lines when $\vec{B} = 0$. This will only result in a significant effect when the Lorentz force is strong enough to curve the electron trajectories appreciably within the electron mean free path, an effect that can be expected to be strongest in pure samples at low temperatures that are subject to a strong magnetic field (Pip89). For instance, a polycrystalline Cu sample at $T = 4$ K in a field of 10 T was found to increase its resistance by a factor of 14 (Lau59).

The structures that are investigated in this thesis however, are not pure bulk materials, but consist of a stack of very thin metallic layers that are alternately magnetic and nonmagnetic. The thickness of these layers is typically 2-200 Å, which reduces the mean free path of the electrons in comparison with the bulk value because of boundary scattering. Another important contribution to the scattering in thin films is grain-boundary scattering. For instance, Rijks *et al.* (Rij95) have shown that in thin films of Cu and $\text{Ni}_{80}\text{Fe}_{20}$ grown on a Ta buffer

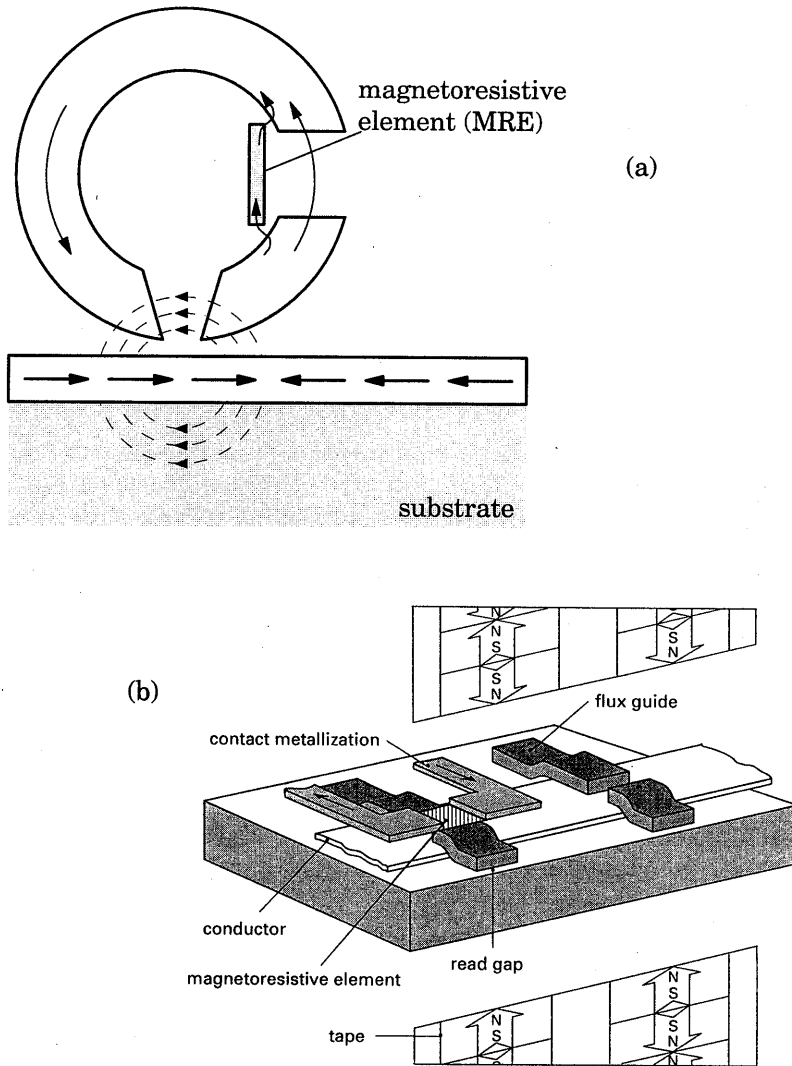


Figure 1.3: (a) Schematic representation of a magnetic read head with a MRE element. The resistance of the MRE depends on the magnetic induction through the yoke, which is induced by the domain pattern of the tape moving along it. The figure is based on a figure by J. Smits (Smi92). (b) Actual design of a multiple track yoke-type magnetic read head. For the purpose of clarity the bit length in (b) is not on scale, and the MRE and contact metallization have not been drawn for one of the heads in (b). (figure taken from Coe97)

layer, the average grain size is significantly smaller than the intrinsic electron mean free path. The reduction of the mean free path is probably the most

important reason why we do not observe the ordinary magnetoresistance effect mentioned above in our samples. In fact, in our samples we observe a decrease of resistance when the magnetic field is increased.

A second magnetoresistance effect occurs in ferromagnetic materials. In these materials the resistance depends on the angle between the magnetization and the current direction. In general the resistance is minimal when the magnetization points perpendicular to the current direction and maximal when magnetization and current are parallel. Because of this anisotropy in the scattering of the electrons, this effect is referred to as anisotropic magnetoresistance (AMR). It is believed (Smi51) that AMR is caused by the interaction between the electron spin and the lattice via the spin-orbit coupling. The AMR ratio, which is defined as $\Delta\rho \equiv (\rho_{\parallel} - \rho_{\perp})/\rho_{\parallel}$, amounts typically to a few % at room temperature. For instance, in bulk alloys of NiFe and NiCo the AMR effect can be greater than 5% (McG75). In thin films of $\text{Ni}_{80}\text{Fe}_{20}$ the observed AMR effect is smaller than in the bulk due to additional scattering (grain boundaries, film boundaries,...) and amounts to about 2% (Rij96), which still enables the use as a MRE in a magnetic read head. It is, however, also not the AMR effect that is the subject of this thesis.

The magnetoresistance effect that is studied in this thesis occurs in samples which are composed of a stack of alternately magnetic and nonmagnetic layers of well chosen layer composition and layer thicknesses. The so-called giant magnetoresistance (GMR) effect observed in such systems occurs upon a transition from a state where all magnetization directions of the layers are aligned parallel to a state where they are aligned antiparallel. The phenomenon that gives rise to this magnetoresistance effect is spin-dependent scattering (SDS). In materials like Co or permalloy ($\text{Ni}_{80}\text{Fe}_{20}$), e.g., conduction electrons with their spin parallel to the (local) magnetization direction experience less resistance than electrons with their spin antiparallel to the magnetization direction. Also scattering at the interfaces between the magnetic and nonmagnetic layers can be strongly spin-dependent. The reason for SDS and the modelling of this type of magnetoresistance will be explained in detail in chapter 3. Assuming for a moment that there is SDS, we will now explain how SDS affects the resistance of the total multilayer stack and can result in magnetoresistance, using the analogon of a simple resistor model.

In figure 1.4 the electron trajectories are drawn for two conduction electrons with opposite spin direction. In figure 1.4a the electron with its spin parallel to the magnetization direction of all magnetic layers, this is a spin-up electron, experiences less scattering than the electron with its spin antiparallel to the magnetization, i.e., spin-down. The conductivity of the multilayer structure in the parallel state will therefore be determined mainly by the spin-up electrons. In figure 1.4b the magnetization directions of neighboring magnetic layers are antiparallel such that a spin-up electron in one layer will be a spin-down electron

in an adjacent layer and vice versa. On the average both electrons will now experience the same amount of scattering or, equivalently, the same resistance. Note that in the example of figure 1.4 spin-up electrons experience less resistance than spin-down electrons, which is in fact the case for Co/Cu or $\text{Ni}_{80}\text{Fe}_{20}/\text{Cu}$ multilayers, but that for a well chosen layer composition this situation can be reversed (Geo94), such that the spin-down electrons experience less resistance than the spin-up electrons.

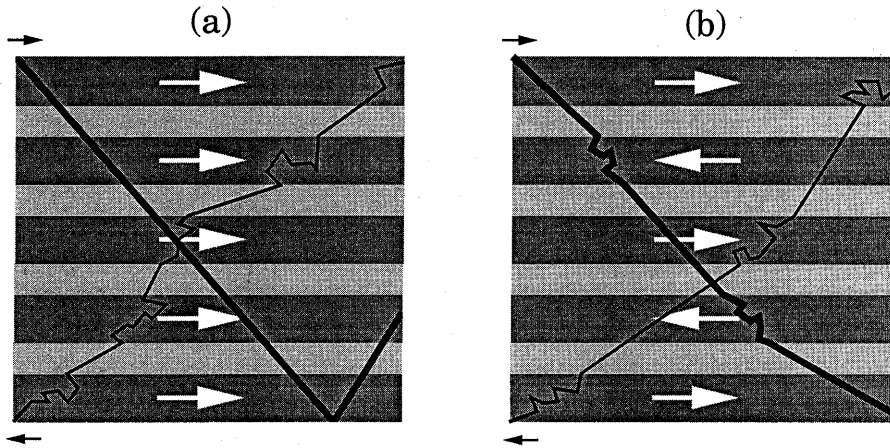


Figure 1.4: Schematic representation of the conductance in a magnetic multilayer. White arrows indicate the magnetization direction in the magnetic layers. Black arrows indicate the electron spin. Electrons with their spin parallel to the local magnetization experience less resistivity. In (a) all magnetization directions are aligned parallel, in (b) the magnetization directions of neighboring magnetic layers are aligned antiparallel

In figure 1.5 we have translated this physical picture into a resistor model for the case of a trilayer. Here the resistance of the up-electrons is modelled by a small spin-up resistor R_u , and the resistance of the down-electrons by a large spin-down resistor R_d . For simplicity we have neglected a resistor representing the spacer. A more detailed description of a resistor model including also the spacer resistivity was given by Edwards *et al.* (Edw91) who introduced the resistor model to explain GMR in magnetic superlattices. From figure 1.5 it can now easily be calculated that the total resistance in the parallel state $R_p = 2R_u R_d / (R_u + R_d)$ is smaller than the total resistance in the antiparallel state $R_{ap} = (R_u + R_d) / 2$ because of the "short circuiting" of the up-electrons in the former case. This leads to a magnetoresistance ratio of:

$$\text{MR ratio} \equiv \frac{R_{ap} - R_p}{R_p} = \frac{(R_u - R_d)^2}{4R_u R_d} \quad (1.1)$$

In view of this physical mechanism the GMR effect is sometimes alternatively referred to as the magnetic valve effect, a term introduced by Slonczewski (Slo89), or the spin valve effect, a term introduced by Dieny *et al.* (Die91a).

The GMR ratio can be appreciably larger than the AMR ratio. For instance, the maximum GMR ratio up till now is measured in an Fe/Cr superlattice, where the Fe layers are coupled antiferromagnetically over the Cr layers, and amounts to 220% at $T = 1.5$ K (Sch94), whereas the room-temperature record value is 65% obtained in Co/Cu multilayers (Par91). This difference in magnitude compared to the AMR ratio, explains why this magnetoresistance effect is referred to as *giant* magnetoresistance, GMR, and it explains the enormous interest from industrial companies and scientists all over the world. It should be noted, however, that not each combination of magnetic and nonmagnetic materials demonstrates a (large) GMR ratio such that the prefix "giant" sometimes is somewhat misleading.

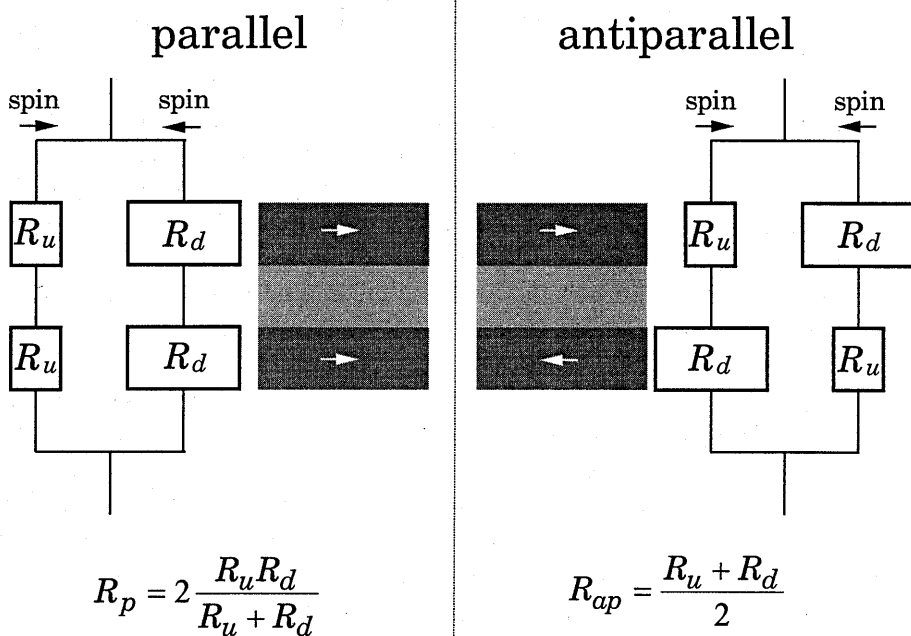


Figure 1.5: Resistor model from which it can be calculated that the resistance in the parallel state, R_p , is smaller than the resistance in the antiparallel state, R_{ap} , assuming $R_u < R_d$. Again, white arrows indicate the magnetization directions in the magnetic layers and black arrows indicate the electron spin.

Finally we would like to remark that the GMR effect can be measured in two main geometries, *viz.* with the current in the plane of the layers (the CIP-geometry) or with the current perpendicular to the plane of the layers (the CPP-geometry). Figure 1.4 represents the CIP-geometry where the current flows in the plane of the layers. Note that, although in this case there is on the average no charge transport in the direction perpendicular to the layers (the drift velocity in this direction is zero), electrons can still cross the nonmagnetic layers from one magnetic layer to another magnetic layer (a necessary condition to obtain the GMR effect) because of the z-component of the Fermi velocity. When the individual layer thicknesses, however, become much larger than the electron mean free path, electrons will be scattered in the nonmagnetic spacer layer, and the GMR effect will disappear as we will explain in chapter 3.

When realizing that the GMR effect basically originates from electrons that travel from one magnetic layer to another magnetic layer, where their scattering rate depends on the direction of the magnetization, one can imagine that the GMR effect is larger in the CPP-geometry. In this case the multilayer structure is better exploited, since the electrons are forced to travel through *all* magnetic layers and interfaces. Moreover, it can be shown that, due to spin accumulation at the interfaces that only occurs in the CPP-geometry, no longer the mean free path λ of the electrons compared to the individual layer thickness is decisive for the magnitude of the GMR effect, but the spin-flip diffusion length, l_{sf} . This length is equal to the average distance between two successive scattering processes upon which the spin of an electron flips from spin-up to spin-down or vice versa. Spin flip can occur upon scattering at impurities, due to the spin-orbit interaction, or upon electron-magnon scattering. Since in real multilayer systems l_{sf} may be an order of magnitude larger than λ , the GMR effect in the CPP-geometry can be expected to persist to a much larger layer thickness. Indeed, an enhancement of CPP-magnetoresistance compared to CIP-magnetoresistance has been observed (Pra91, Gij93, Oep96). Experimentally, however, the measurement of CPP-magnetoresistance is much more difficult than the measurement of CIP-magnetoresistance. This is mainly caused by the very small resistance of the multilayer stack in the perpendicular direction. In principle this problem can be solved by reducing the lateral dimensions of the films which, of course, increases the resistance of the stack. In practice, however, this size reduction should be so drastic (a typical length scale is 3-10 μm) that rather advanced microfabrication techniques are required, combined with a more complicated measuring structure. Recent CPP-measurements are also performed on so-called nanowires that are fabricated by means of electrodeposition in the pores of nanoporous membranes (Voe95, Blo97, Dub97), which is a relatively easy way to realize a CPP-measurement. All experiments described in this thesis are performed in the current *in plane* geometry, CIP.

1.3 This thesis

In 1986 for the first time antiferromagnetic exchange coupling between thin ferromagnetic layers was observed (Grü86). Antiferromagnetic coupling was found between two thin metallic 100 Å Fe layers across a thin nonmagnetic 8 Å Cr layer. Due to this antiferromagnetic coupling the magnetization directions of the magnetic layers can switch between parallel and antiparallel upon the application of an external magnetic field, which is a necessary requirement to obtain the GMR effect. Two years later the GMR effect was first measured, again first in Fe/Cr multilayer systems (Bai88) and in a Fe/Cr/Fe sandwich (Bin89). It was immediately recognized that this effect was caused by the phenomenon of spin-dependent scattering. Since that time the GMR effect is extensively investigated.

A number of studies has since then been concerned with maximizing the GMR effect by finding a suitable combination of magnetic and nonmagnetic materials, in combination with the optimum layer thickness. Other studies have been carried out with the objective to obtain a structure that displays a large change of resistance within an applied field of only several Oersted. This is one of the requirements for the use as MRE in a magnetic read head. A third group of investigations has been aimed at finding the spatial origin of the spin-dependent scattering. This could be in the bulk of the layers, e.g., due to scattering at bulk defects such as dislocations, stacking faults, vacancies, impurities, or grain boundaries, or at the interfaces with the nonmagnetic layers due to, for instance, geometrical or compositional roughness or spin-dependent potential steps at the interfaces. The majority of the experiments described in this thesis belongs to this third group.

Disentanglement of bulk and interface contributions is not a trivial task. This can already be understood when realizing that it is impossible to eliminate the interfaces. Irrespective of the thickness of the magnetic layers, an electron always has to cross two interfaces to reach a second magnetic layer. On the other hand, annealing experiments (just to give an example), that aim to increase the intermixing in the direct neighborhood of the interfaces can also affect the scattering in the bulk of the layers.

Magnetic multilayers in which the antiparallel state arises from the antiferromagnetic coupling, such as the Fe/Cr system quoted above, have a great disadvantage in studies of the spatial origin of the GMR effect. Each modification of the interfaces, to study the effect of the modification on the spin-dependent interface scattering, can also alter the magnitude of the coupling strength. This in turn can result in changes in the degree of antiparallel alignment and thus indirectly disturb the GMR effect, which is an extra complicating factor in the interpretation of the measurements. Moreover, the coupling strength in a multilayer need not be the same between each pair of layers, as we will show in

chapter 4. In that chapter we demonstrate this for a multilayer with a large perpendicular anisotropy, such that each layer reverses its magnetization direction at a well defined magnetic field, resulting in sharp transitions (steps) in the $M(H)$ -curve. This enables us to determine the coupling strength between each pair of layers and it appears that the strength of this coupling gradually increases when going from the substrate to the top of the stack.

Therefore we prefer to study spin valves with only two magnetic layers separated by a nonmagnetic layer thick enough to assure that the magnetic layers are *not* coupled to each other. One of the magnetic layers is free to follow the direction of an external applied field, while the magnetization direction of the other layer is biased in a certain direction to obtain the necessary antiparallel state. In such a structure we can safely modify the interfaces without changing the degree of antiparallel alignment. The design and behavior of these "biased spin valves" is discussed in chapter 5.

In chapter 6 we discuss the effect of intermixing at the interfaces of sputtered Cu/Cu spin valves. The Co/Cu interfaces in these spin valves are intentionally intermixed by codeposition or alternately depositing Co and Cu. Due to the sputter fabrication process an intrinsic interface zone of a few Å intermixed Co and Cu is always present at the interfaces in these spin valves. Upon increasing the thickness of this interface zone up to a nominal value of 36 Å, we observe a gradual decrease of the GMR ratio.

In chapter 7 we concentrate on bulk properties instead of the interface. By shifting a thin Ru barrier layer, that scatters all incident electrons diffusely, through a Co/Cu spin valve, we analyze the scattering lengths of Co and Cu. From our measurements we could not find a large difference between the mean free paths for the spin-up and spin-down electrons, $\lambda_{\text{Co}}^{\uparrow}$ and $\lambda_{\text{Co}}^{\downarrow}$ respectively.

Therefore we have investigated the interface scattering in more detail, as discussed in chapter 8. By choosing a suitable structure we have eliminated the bulk contribution to the spin-dependent scattering. Interface SDS was clearly established in both Co/Cu/Co and NiFe/Cu/NiFe spin valves.

Finally in chapter 9 we discuss the possible electron reflection effect at the outer boundaries of Co/Cu spin valves, since this may enhance the GMR effect of a spin valve essentially to the value of an infinite superlattice. More specifically we investigated whether there is an enhanced reflectivity when the spin valve is terminated with isolating NiO instead of a conducting material. Although we did measure an enhanced GMR ratio and although it was impossible to fit our data without assuming reflection at the outer boundaries, we were not able to prove this reflectivity effect in a (more) straightforward way.

2. Experimental

In this chapter the fabrication of the samples and the various measurement techniques are explained briefly.

2.1 Sample preparation

All the samples described in this thesis were grown at Philips research laboratories by means of high vacuum magnetron sputter deposition. Sputter deposition is a process where a target material is bombarded with highly energetic particles in a high-vacuum chamber. In our case the bombarding particles are Ar-ions, an inert gas that does not react with the target material. As a result of the collisions of the Ar-ions with the target, target atoms leave the target surface and condense on a substrate that is facing the target, to form a thin film. Before the sputtering process is started, the vacuum chamber is evacuated to a background pressure of typically 5×10^{-7} Torr (7×10^{-5} Pa), whereas the actual sputtering occurs at an Ar-pressure of $\approx 7 \times 10^{-3}$ Torr (0.9 Pa). With these values and a typical deposition rate of 1-3 Å/s, the impurity concentration of, for example, oxygen in the grown films proved to be below 0.5 at. % (Blo93).

Figure 2.1 shows the sputter process schematically. Here the target serves as a cathode and the Ar-ion bombardment is started with an electrical discharge between anode and cathode. Apart from target atoms also a number of secondary electrons is emitted from the target surface due to the ion bombardment. These electrons are accelerated in the electric field between anode and cathode and their collisions with the Ar-gas produce the ionization required to sustain the discharge. Underneath the target a permanent magnet assembly is present that provides a magnetic field which prevents these secondary electrons to go to the anode or even to the substrate where it could cause unwanted heating. Thus a combination of an electric and a magnetic field confines the electrons (and thus the Ar-plasma) to a region just above the target surface, ensuring an effective sputtering process.

The specific sputter deposition apparatus used, can contain three different targets (for instance Co, Cu and Ru). The sample holder can accommodate ten substrates that in our case always have the dimensions $4 \times 12 \text{ mm}^2$. When it is necessary to apply a magnetic field during growth, the substrates are placed between permanent magnets which reduces the maximum number of substrates to six. Thus, within one deposition run only ten (six) samples can be grown. Thereafter the substrates have to be replaced by new (empty) substrates, and the vacuum chamber has to be re-evacuated. Multilayers consisting of various layers of different materials can be grown by repeatedly rotating the sample holder

such that the substrate faces the correct target, and then starting the Ar-ion bombardment by removing the shutter.

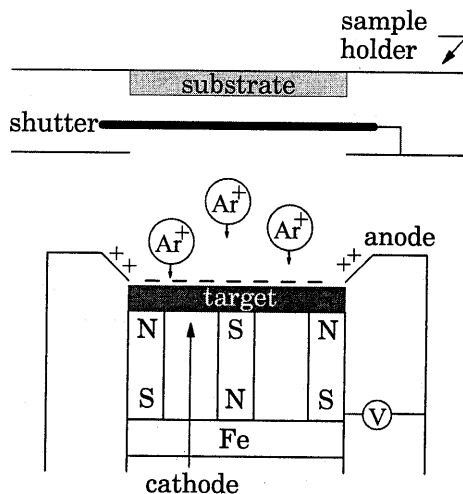


Figure 2.1: Schematic representation of the sputter process. Drawing is not on scale, especially the Ar-ions are too large.

To determine the sputter deposition rate versus applied power, a so-called satellite run is performed before each deposition run. In the satellite run a film is grown from each target material, with a thickness of approximately 500 Å. Afterwards the thickness of these three films is ex-situ determined from glancing angle X-ray diffraction experiments, yielding an accuracy of better than 5%. It should be noted however that in order to complete a deposition run and a satellite run within one day, the satellite run is performed at a slightly higher background pressure of $\approx 2 \times 10^{-6}$ Torr (3×10^{-4} Pa).

When we compare the sputter deposition method with the vapor deposition method (Molecular Beam Epitaxy, MBE), there are some advantages and some disadvantages. One of the major advantages of sputter deposition is that it enables the growth of films of almost any material. In vapor deposition the high melting temperature of some materials can cause practical problems which are absent in the sputter deposition because here the target atoms are removed from the target by a mechanical process. Another advantage is that targets can be interchanged faster (every day) than in an MBE-apparatus, mainly because the vacuum required for MBE operation is higher (10^{-8} - 10^{-9} Pa). In addition, variation of the Ar-sputter pressure enables one to control the kinetic energy of the atoms that arrive at the substrate. When the Ar-pressure increases, the number of energetic atoms decreases due to inelastic collisions with the Ar-atoms. This leads to less intermixing at the interfaces, but, at the same time the

grain diameters become smaller, and the interface roughness increases. A disadvantage of sputter deposition is that the Ar-ions that bombard the target can reflect back from the target as neutral Ar-atoms, and reach the substrate where they bombard the growing film. In general this results in an enhanced interdiffusion and/or surface roughness of the interfaces between subsequent layers compared to vapor deposition. From a viewpoint of industrial applications, sputter deposition is most important mainly because it is faster and enables bulk production.

2.2 Sample characterization

2.2.1 Magnetometry

A magnetometer measures the magnetic moment of a sample as a function of the applied magnetic field. The value of this moment provides information on the thickness of the layers, or, when the thickness is already known from other experiments, determination of the magnetic moment can result in the observation of reduced or enhanced magnetic moments with respect to the bulk value. When a magnetic field is applied in different directions, comparison of the magnetization curves shows whether magnetic anisotropy, a preferential direction for the magnetization, is present in the sample. Also quantities like coercive field, saturation magnetization, and exchange biasing field can be determined from a magnetization curve. Note that in the research field of magnetic multilayers, quantities such as layer thickness and saturation field can be used to calculate the strength of the antiferromagnetic coupling between the layers, when present.

All magnetization curves in this thesis were determined by means of a VSM (Vibrating Sample Magnetometer), a fluxgate, a SQUID (Superconducting Quantum Interference Device) or a MOKE (Magneto Optical Kerr Effect) magnetometer. Fluxgate and SQUID magnetometry are suitable for a quantitative determination of the magnetic moment of a specimen. Both these methods are based on the detection of flux originating from a sample. For carrying out these two methods, the sample is placed in a superconducting pick-up coil that is connected to the actual fluxgate or SQUID. Since the magnetic flux through a superconducting ring is quantized to $\Phi = n\Phi_0$ with $\Phi_0 = h/(2e)$ and n an integer ≥ 0 (h is planck's constant, e is electron charge), the sample will induce a supercurrent in the pick-up coils that will keep the flux at a constant value. Via this supercurrent the flux originating from the sample is transported from the pick-up coil to the fluxgate or SQUID. In this respect the fluxgate and the SQUID are different from a VSM (which is also suitable for a quantitative measurement of a magnetic moment), where the sample is vibrating in a (normal) pick-up coil to cause an induction voltage. The main differences between

fluxgate and SQUID are contained in the conversion process from supercurrent to magnetic moment.

MOKE magnetometry measures changes in the polarization state of light caused by reflection on a magnetic surface. These changes yield a qualitative measure for the magnetic moment. Although no quantitative values for the moment are obtained, MOKE has a number of advantages compared to fluxgate and SQUID magnetometry, especially for the research of thin films. For instance, MOKE is a local probe measuring over an area of typically $100\ \mu\text{m}$ diameter, whereas a fluxgate and a SQUID magnetometer measure the overall magnetic moment of a sample. This local sensitivity enables the use of wedge-shaped samples, where quantities depending on the layer thickness can be measured in one sample where only one layer thickness is varied. In that case, the effects of variations of other growth parameters are eliminated. A second advantage of MOKE is that the time needed to measure a magnetization curve at room temperature is typically two orders of magnitude smaller than for a fluxgate or SQUID magnetometer.

In the next three paragraphs we will briefly discuss the principle of operation of the fluxgate, the SQUID, and the MOKE magnetometer, respectively.

2.2.2 The Fluxgate Magnetometer

Our home-made fluxgate is a ring core magnetometer. The ring-shaped core is made of a magnetic material with high permeability and is driven cyclically to saturation by means of a magnetic field $H_d = \hat{H} \sin(2\pi ft)$ originating from an alternating current I_d in the drive coil, as is indicated in figures 2.2 and 2.3.

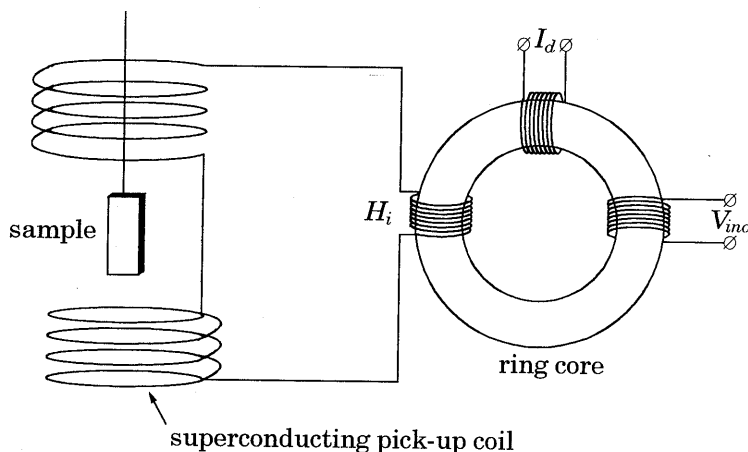


Figure 2.2: Schematic representation of the fluxgate magnetometer.

To understand the principle of fluxgate operation, we will make some simplifying assumptions. Firstly it is assumed that the magnetic induction B inside the ring core as a function of the magnetic field strength H shows no hysteresis, as is indicated in figure 2.3a. A second assumption is that H_d varies linearly with time, as is shown in figure 2.3b, instead of the actual sinusoidal behavior. Note that the amplitude \hat{H} of H_d is larger than H_{sat} , the saturation field of the magnetic ring.

When the magnetic flux remains entirely within the ring core, the induction voltage V_{ind} across the sensing coil will be given by:

$$V_{ind} = -NA \frac{dB}{dt} \quad (2.1)$$

where N is the number of turns of the sensing coil and A is the cross-sectional area of the ring core. The time variation of V_{ind} resulting from H_d is shown by the solid line in figure 2.3d. V_{ind} is symmetrical, i.e. V_{ind} only contains odd harmonics of the frequency f of the driving current. To be more specific, it can be shown from a Fourier analysis that:

$$V_{ind} = \sum_n -\frac{16}{\pi n} NA \mu_0 \mu_r \hat{H} f \sin\left(\frac{n \pi H_{sat}}{2 \hat{H}}\right) \cos(2\pi n f t) \quad (2.2)$$

where $n = 1, 3, 5, \dots$, μ_0 is the permeability of vacuum, and μ_r is the relative permeability of the ring core.

Now suppose that besides H_d there is another, constant, field $H_i \ll \hat{H}$ present. In our case this extra field is caused by the supercurrent through the superconducting input coil induced by the flux of a magnetic sample, but in principle also the earth's magnetic field would do. This extra field will change the time variation of the magnetic field H acting on the ring core, and thus also the time variation of the magnetic induction B inside the ring and, via equation (2.1), the induction voltage V_{ind} across the sensing coil, in the way shown by the dashed lines in figures 2.3b, c, and d. The induction voltage now has become asymmetrical and from a Fourier analysis it follows that:

$$V_{ind} = \sum_{n,m} -\frac{16}{n\pi} NA \mu_0 \mu_r f \hat{H} \cos\left[\frac{n \pi H_i}{2 \hat{H}}\right] \sin\left[\frac{n \pi H_{sat}}{2 \hat{H}}\right] \cos(2\pi n f t) + \frac{16}{m\pi} NA \mu_0 \mu_r f \hat{H} \sin\left[\frac{m \pi H_i}{2 \hat{H}}\right] \sin\left[\frac{m \pi H_{sat}}{2 \hat{H}}\right] \sin(2\pi m f t) \quad (2.3)$$

where $n = 1, 3, 5, \dots$ and $m = 2, 4, 6, \dots$

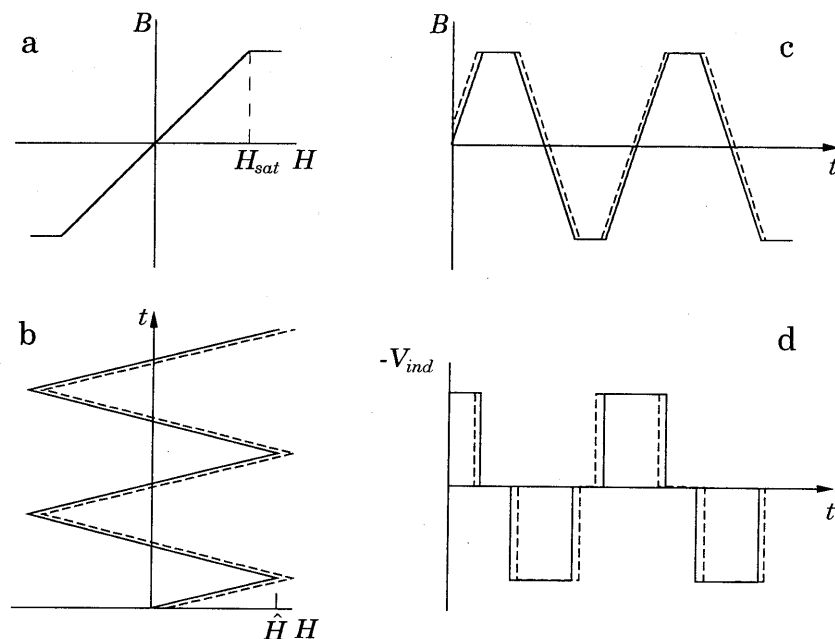


Figure 2.3: a) Idealized B - H curve for the ring core of the fluxgate magnetometer, b) Variation of the magnetic field strength H in the ring core as a function of time, c) Variation of the magnetic induction B in the ring core as a function of time, d) Variation of the induction voltage V_{ind} across the sensing coil as a function of time. In b), c) and d) the solid line reflects the situation without a sample, whereas the dashed line is valid when the sample induces an extra field H_i in the ring core.

Since $H_i \ll \hat{H}$, the contribution of the odd harmonics to V_{ind} is larger than the contribution of the even harmonics. However, the even harmonics contain the desired information on the input field, as they are proportional to H_i for $H_i \ll \hat{H}$. Thus, when one is able to filter one of the even harmonics out of the induction voltage, this will be a measure for the input field, from which the supercurrent can be calculated that was caused by the flux originating from the magnetic sample. Via a simple calibration the magnetic moment of the sample can be determined.

The above example only served to explain the principle of operation. In reality things are more complicated. For example: our fluxgate contains two ring cores with common input and sense coils. When the drive current for both cores is equal in magnitude but opposite in sign, the contribution of the odd harmonics

to V_{ind} is strongly reduced. It can be shown that for a more realistic $B-H$ curve of the ring, showing a little hysteresis, the second harmonic becomes dominant. Note also that the actual time dependence of the drive current is not linear, but varies like a sine, which changes the equation for V_{ind} , without further changing the principle of operation. This enables the use of lock-in technique. The internal oscillator of a lock-in amplifier is used to generate the drive current with a frequency of $f = 50$ kHz and the same amplifier (in the $2f$ -detection mode) is used to measure the second harmonic in the induction voltage.

To make sure that the measured signal indeed originates from the sample, the ring cores in our fluxgate are contained in a superconducting box to shield external fields such as, for instance, the field that is applied in the fluxgate to be able to measure the magnetic moment of the sample as a function of the magnetic field. Moreover, to increase the signal to noise ratio, the position of the sample within the pick-up coils is modulated with a frequency of 5 Hz. This frequency is very low with respect to the drive current ($f = 50$ kHz), so it does not affect the operation of the fluxgate, but enables again a phase sensitive detection with a lock-in technique.

For our fluxgate the sensitivity amounts to $6.6 \times 10^{-9} \text{ Am}^2$ ($= 6.6 \times 10^{-6} \text{ emu}$). The maximum attainable field amounts to $H_{\max} = 6.4 \times 10^6 \text{ A/m}$ ($B_{\max} = 8 \text{ T}$), and the temperature of the measurement can be varied between $T = 1.5 \text{ K}$ and $T \approx 220 \text{ K}$.

For more details about fluxgate magnetometry in general the reader is referred to a review article by F. Primdahl (Pri79) and references therein, whereas the specific design of our fluxgate is described in (Bra91).

2.2.3 The SQUID Magnetometer

The SQUID magnetometer in our laboratory, a r.f.-type SQUID, is bought from Quantum-Design (model MPMS-5S). Similar to the fluxgate magnetometer the sample is positioned in the middle of a superconducting pick-up coil. This section is only meant to clarify the principles of how the supercurrent induced by the sample in the pick-up coil is converted to an output reading. Needless to say that this section is a simplification of reality, because only those ingredients necessary to understand the principle of operation are shown.

Besides the superconducting pick-up coil through which the flux has to be constant, the SQUID magnetometer uses a superconducting ring that contains a Josephson junction, as is shown in figure 2.4. This ring is actually called the SQUID.

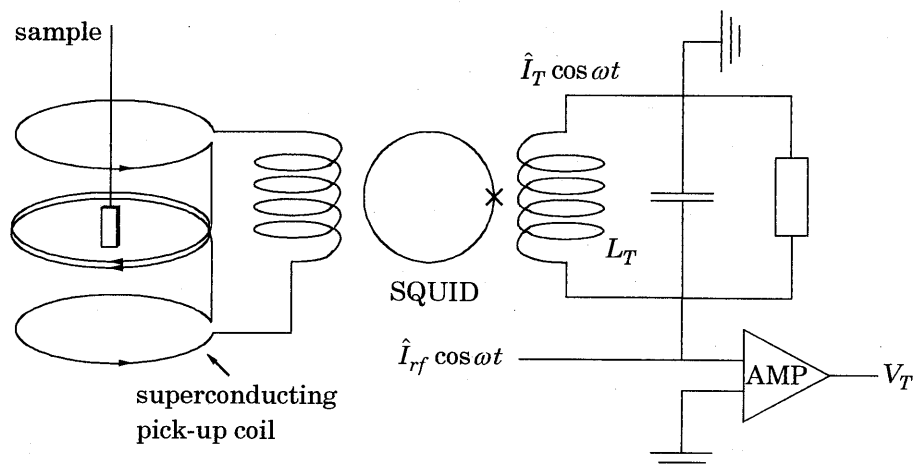


Figure 2.4: Schematic representation of the SQUID magnetometer.

To understand the SQUID method we have to recall the direct current (d.c.) and alternating current (a.c.) Josephson effect: When there is a phase difference θ between the wavefunctions in the superconductors on both sides of a Josephson junction, a d.c. supercurrent I_s will flow through the junction (without generating a voltage across it) that depends on θ :

$$I_s = I_c \sin \theta \quad (2.4)$$

This is called the d.c. Josephson effect. I_c , the critical current, is the maximum d.c. current that can flow through the junction without generating a voltage. When a current larger than I_c is passed through the junction, a voltage V appears across it and the supercurrent oscillates at a frequency $\omega = V / \Phi_0$, the a.c. Josephson effect.

For a superconducting ring containing a Josephson junction, such as the SQUID, the phase difference over the junction θ and the flux Φ through the ring are related according to:

$$\theta = \frac{-2\pi\Phi}{\Phi_0} \quad (2.5)$$

Due to the Josephson junction, the flux through the SQUID is not strictly quantized anymore, although the supercurrent I_s will still partly shield the external flux. When an external flux Φ_e is applied, the flux Φ through the SQUID is given by:

$$\Phi = \Phi_e + LI_s = \Phi_e + LI_c \sin \theta = \Phi_e - LI_c \sin\left(\frac{2\pi\Phi}{\Phi_0}\right) \quad (2.6)$$

where L is the self-inductance of the SQUID. Figure 2.5 shows Φ as a function of Φ_e for $LI_c = 1.25\Phi_0$. Only those parts with a positive slope indexed with quantum number n are stable, those with negative slope are not. The dashed lines represent transitions between the stable quantum states with $\Delta n = \pm 1$.

Because the supercurrent I_s partly shields the external flux, Φ_e , the flux through the SQUID, Φ , will increase less rapidly than Φ_e . When I_s reaches its maximum value I_c at $\Phi_e = \Phi_{ec}$ and $\Phi = \Phi_c$, the junction switches momentarily into a non-zero voltage state, and the SQUID makes a transition to the next quantum state ($n = 1$). Similar transitions follow when $\Phi_e = \Phi_{ec} + n\Phi_0$ or, when the external flux decreases, at $\Phi_e = -(\Phi_{ec} + n\Phi_0)$. When the SQUID describes a hysteresis loop from the state $n = 0$ to $n = 1$ and back to $n = 0$, the energy dissipated, ΔE , is determined from the area of the loop divided by L .

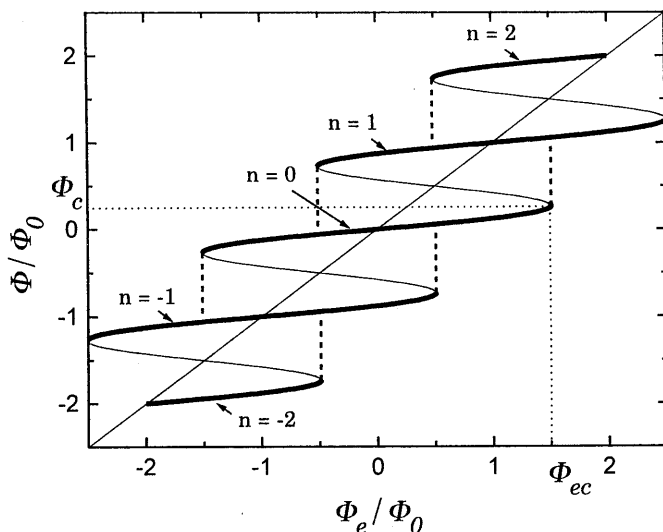


Figure 2.5: The flux Φ through the SQUID as a function of the external applied flux Φ_e for $LI_c = 1.25\Phi_0$.

A tank circuit with inductance L_T is coupled to the SQUID by a mutual inductance M , and is driven by a radiofrequency (r.f.) current: $I_{rf} = \hat{I}_{rf} \cos \omega t$ (see figure 2.4). When the current in the coil of the tank circuit is given by: $I_T = \hat{I}_T \cos \omega t$, the r.f. flux sensed by the SQUID is:

$$\Phi_{rf} = M\hat{I}_T \cos \omega t = MQ\hat{I}_{rf} \cos \omega t \quad (2.7)$$

where Q is the quality factor of the tank circuit. As long as $\hat{I}_T < \Phi_{ec}/M$, the SQUID will make no transitions. In this case the voltage V_T across the tank circuit is a linear function of the r.f. current \hat{I}_{rf} , as is shown in figure 2.6 by the solid line. As soon as $\hat{I}_T = \Phi_{ec}/M$, at point A in figure 2.6, the SQUID will make a transition to the $n = +1$ or $n = -1$ state depending on the direction of the current and later in the same rf-cycle the SQUID will return to the $n = 0$ state. The energy ΔE that is dissipated in making these transitions is extracted from the tank circuit. This energy loss will decrease \hat{I}_{rf} and thus \hat{I}_T a little and in principle many cycles in the tank circuit are needed to regain sufficient energy to enable a new transition to $n = \pm 1$. When \hat{I}_{rf} is further increased, progressively less cycles are needed for the tank circuit to recover from the energy losses, which causes the SQUID to make transitions more frequently until, finally, the SQUID makes a transition at each peak value (positive and negative) of I_{rf} , represented by point B in figure 2.6. Between A and B, the mean peak value of the voltage V_T is constant. In practice the variations in this region in the peak value of V_T due to the variations in \hat{I}_{rf} are too small to be observed. A further increase of \hat{I}_{rf} beyond point B will again result in a linear increase of V_T , until at point C in figure 2.6 a transition to the state with $n = \pm 2$ occurs, etc.

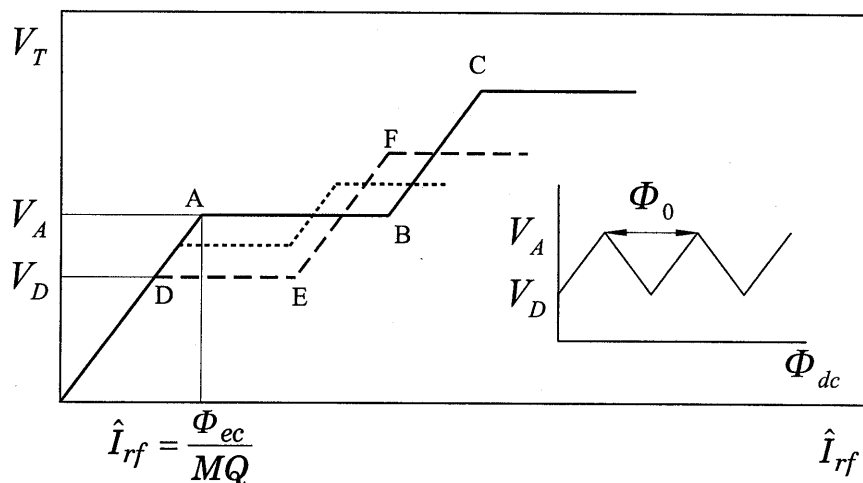


Figure 2.6: The voltage V_T as a function of the amplitude of the rf current, \hat{I}_{rf} . The solid line represents the situation where $\Phi_{dc} = n\Phi_0$ and the dashed line represents the situation where $\Phi_{dc} = (n + \frac{1}{2})\Phi_0$. For all other values of Φ_{dc} , the first plateau is contained within the solid line and the dashed line as indicated by the dotted line valid for $\Phi_{dc} = (n \pm \frac{1}{4})\Phi_0$.

Now suppose that besides the flux originating from the tank circuit, there is an extra constant (d.c.) contribution to the flux of $\frac{1}{2}\Phi_0$ (the d.c. flux originates from the current in the pick-up coil induced by the sample). This will shift the hysteresis curve plotted in figure 2.5 $\frac{1}{2}\Phi_0$ to the left. As a result the first transition from $n=0$ to $n=1$ will already take place at $\Phi_e = \Phi_{ec} - \frac{1}{2}\Phi_0$, corresponding to a smaller r.f. current, as indicated by point D in figure 2.6. For the transition from $n=0$ to $n=-1$ at $\Phi_e = -(\Phi_{ec} + \frac{1}{2}\Phi_0)$ however, a larger current is needed and these transitions start only at point F in figure 2.6. The variation of V_T as a function of I_{rf} in the presence of an extra d.c. flux contribution of $\frac{1}{2}\Phi_0$ is shown by the dashed line in figure 2.6.

When the extra d.c. flux contribution increases to Φ_0 , which means a shift of the curve in figure 2.5 over a distance Φ_0 to the left, the relation between V_T and \hat{I}_{rf} is given again by the solid line in figure 2.6. In fact the solid line in figure 2.6 is valid for $\Phi_{dc} = n\Phi_0$, and the dashed line is valid whenever $\Phi_{dc} = (n + \frac{1}{2})\Phi_0$. For all other values of Φ_{dc} , the first plateau of the $V_T(\hat{I}_{rf})$ -curve is contained between the solid and dashed line in figure 2.6. As an example we have shown the dotted line that is valid for $\Phi_{dc} = (n \pm \frac{1}{4})\Phi_0$.

The amplitude of the r.f. current is tuned to a value between A and E in figure 2.6 where V_T is always on the first plateau for each value of Φ_{dc} . For that case the variation of V_T as a function of Φ_{dc} is shown in the inset in figure 2.6. Since V_T is a periodic function of Φ_{dc} , it is not suitable to determine the value of Φ_{dc} . Therefore a feedback current is also applied to the SQUID. When Φ_{dc} increases with $\delta\Phi_{dc}$ a current is fed back to the SQUID that produces an opposing flux of $-\delta\Phi_{dc}$. The feedback current maintains the SQUID locked at a constant flux (near an integral number of Φ_0), such that it serves as a null detector in a feedback circuit. The final output signal of the SQUID magnetometer is the voltage over a resistor in the feedback circuit, that is proportional to $\delta\Phi_{dc}$. Via a simple calibration the magnetic moment of the sample in the pick-up coil can be determined. More detailed information on SQUID operation can be found in (Sch77, Bar82, Gal76, and Bon95).

For the SQUID-magnetometer a sensitivity of 10^{-7} emu ($=10^{-10}$ Am²) is claimed by the manufacturer. The temperature can be varied between 1.7 K and 400 K. The maximum attainable magnetic field amounts to 5 T.

2.2.4 The Magneto Optical Kerr Effect

The Magneto Optical Kerr Effect (MOKE) originates from a difference in the complex Fresnel reflection coefficients

$$\tilde{r}_{\pm} = r_{\pm} \exp(i\varphi_{\pm}) \quad (2.8)$$

between right-handed circularly polarized light (+) and left-handed circularly polarized light (-), that exists for the reflection at magnetic samples. One can discern two distinct Kerr effects: Kerr rotation θ_K , when the phases of the reflection coefficients are different ($\varphi_+ \neq \varphi_-$), and Kerr ellipticity ε_K , when their amplitudes are different ($r_+ \neq r_-$). The exact definitions of θ_K and ε_K are given by:

$$\theta_K = \frac{1}{2}(\varphi_+ - \varphi_-) = \frac{1}{2} \Delta\varphi \quad \text{and} \quad \varepsilon_K = \frac{r_+ - r_-}{r_+ + r_-} \quad (2.9)$$

In figure 2.7 both Kerr effects are illustrated. Now we will explain how these two effects are measured in our home-made MOKE-magnetometer.

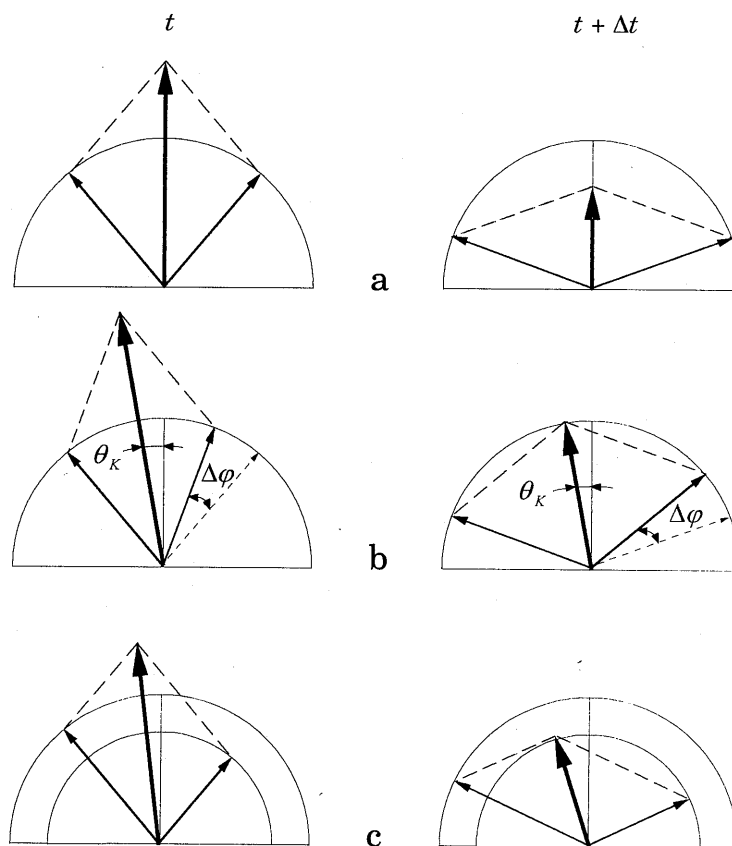


Figure 2.7: a) linearly polarized light can be described as a superposition of RCPL and LCPL, b) Kerr rotation results from a phase difference between RCPL and LCPL, c) Kerr ellipticity results from a difference in amplitude between RCPL and LCPL.

As a light source a HeNe-laser is used which provides a linearly polarized laser beam. This linearly polarized light can be described by the superposition of two orthonormal components, x and y , running in phase. A photoelastic modulator (PEM) will advance or retard the phase of one of the components, say the y -component, according to $\delta = \delta_0 \sin(2\pi ft)$. In our case the modulation frequency $f = 50$ kHz. As a result, the polarization state of the light emerging from the PEM will be modulated. For instance, when $\delta_0 = 90^\circ$, the polarization state of the light after the PEM will oscillate between right-handed circularly polarized light (RCPL) and left-handed circularly polarized light (LCPL), as is shown in figure 2.8c for one period of the PEM. Figure 2.8e shows the polarization states of the light after reflection from a sample demonstrating the Kerr ellipticity effect. In this particular case the amplitude of LCPL is reduced by 50%. Similarly figure 2.8g shows the polarization states after reflection from a sample introducing the Kerr rotation effect. In general the effects are quite small, typically a few mdeg. The light after reflection is passed through an analyser such that only the x -component of the reflected light will reach the detector. As shown in figure 2.8f and h, Kerr ellipticity will induce an f -modulation in the intensity of the x -component of the reflected light while Kerr rotation induces a $2f$ -modulation in the intensity of the x -component. This again enables the use of a lock-in technique. The internal oscillator of the PEM provides a reference signal f ($= 50$ kHz) or $2f$ for the lock-in amplifier that measures the ellipticity or rotation signal respectively.

Unlike fluxgate and SQUID magnetometry, that measure the overall magnetic moment of a sample, MOKE is a local probe of the magnetization, defined by the laser spot. Moreover, the MOKE signal contains only information on a layer of thickness about twice the penetration depth of the light (Zep91). This penetration depth is typically 10-100 nm for metals in the visible wavelength range (Vor93). The region closest to the surface will obviously contribute most to the MOKE signal. This fact will be used in chapter 4.

Up to now our MOKE apparatus is only suitable for measurements at room temperature. An extension with a flow cryostat to enable measurements at low temperatures is currently in progress. The maximum attainable field amounts to approximately $H_{\max} \approx 800$ kA/m ($B_{\max} \approx 1$ T) when the field is aligned perpendicular to the sample surface (polar geometry), and approximately 400 kA/m ($B = 0.5$ T) when the field is parallel to the sample plane (longitudinal geometry), depending on the distance between the poles of our electromagnet.

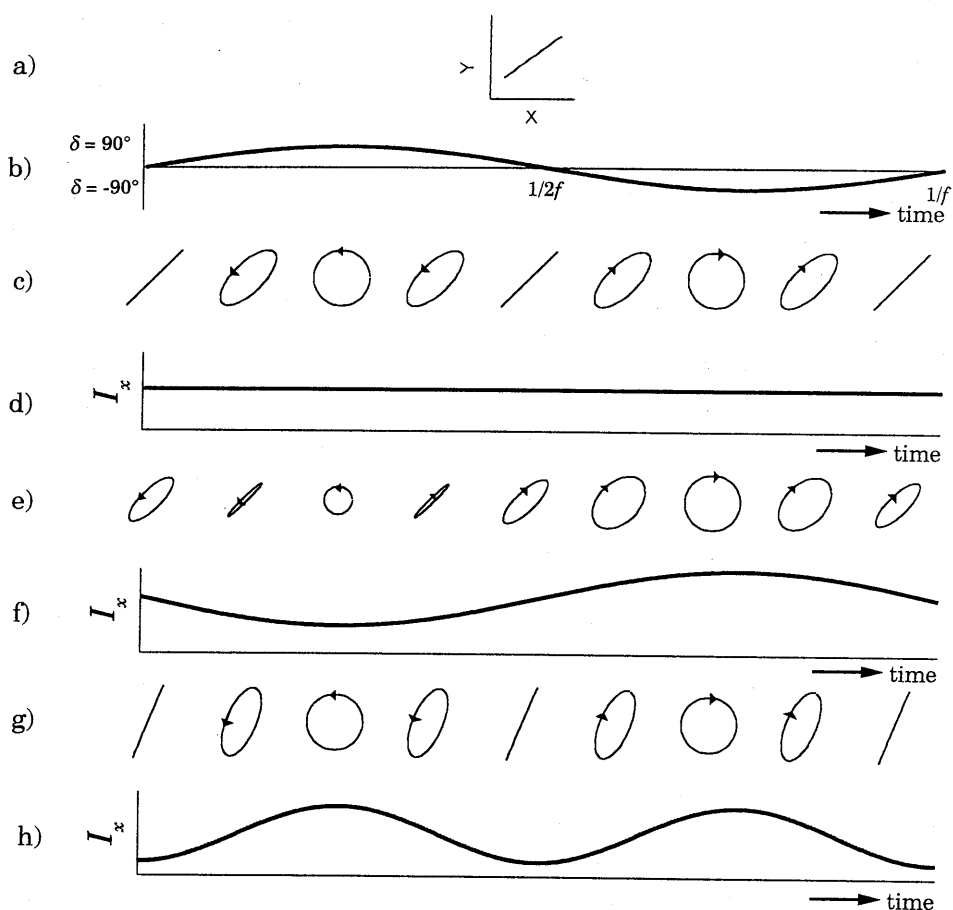


Figure 2.8: Explanation of the MOKE measurement technique: a) linearly polarized laser light enters the PEM, b) retardation of the y-component of the light induced by the PEM as a function of time for one period of the PEM, c) polarization states of the light emerging from the PEM as a function of time, d) x-component of the intensity of the light emerging from the PEM, e) and f) polarization states and x-component of the intensity, respectively, as a function of time for light reflected from a sample showing Kerr ellipticity. The Kerr ellipticity has induced an f -dependence in the x-component of the reflected light. g) and h) polarization states and x-component of the intensity, respectively, as a function of time for light reflected from a sample showing Kerr rotation. The Kerr rotation has induced a $2f$ -dependence in the x-component of the reflected light. The arrows in the figure indicate the polarization state of the light, for instance, LCPL and RCPL.

2.3 Magnetoresistance

The resistance of the samples is measured in a standard four probe setup. A requirement for this setup to be used is that the diameter of the contact between each probe and the sample surface is small with respect to the spacing s between the probes, a condition that is fulfilled in our apparatus. In this home-made apparatus four collinear pressure contacts are pressed on the sample to make electrical contact, as is shown in figure 2.9.

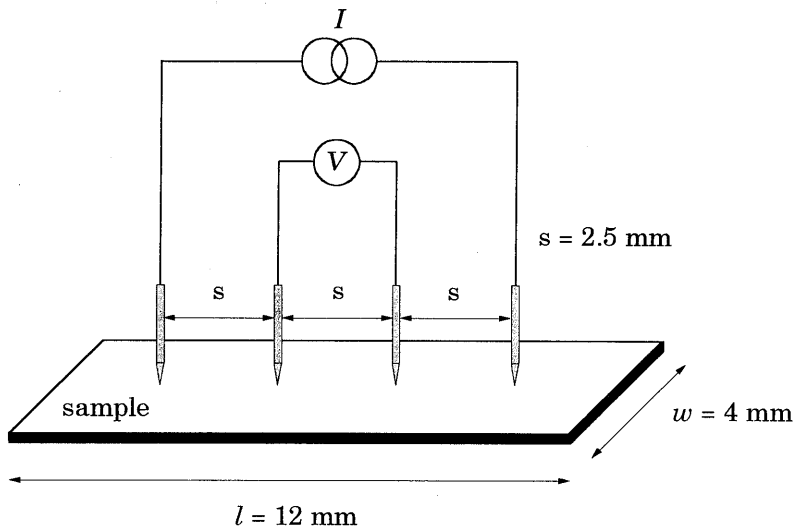


Figure 2.9: Schematic representation of the measurement setup of the magnetoresistance equipment.

A current source applies an alternating current of approximately $I = 1$ mA and a frequency of $f = 80$ Hz to the outer two contacts. The voltage V is measured across the inner contacts. The resistance R is then simply determined by:

$$R = \frac{V}{I} \quad (2.10)$$

In case of an infinite sheet with an infinitesimal thickness, d , much smaller than the spacing between the contacts, the sample can be considered as essentially two-dimensional, and it can be shown (Wie79) that the resistivity of the sample is given by:

$$\rho = \frac{V}{I} \frac{\pi d}{\ln 2} \approx 4.5324 d R \quad (2.11)$$

For a finite rectangular sample of dimensions $l \times w$ however, equation (2.11) is not correct anymore. In general the resistivity of such a sample can be written as:

$$\rho = \frac{V}{I} dC = RdC \quad (2.12)$$

where C depends on both l/w and w/s and is tabulated by F.M. Smits (Smi57). In figure 2.10 we have reproduced the results of Smits for our sample geometry, i.e., a rectangular sample with $l/w = 3$. It follows that for $w/s \approx 1$ the factor $C \approx w/s$. In our case, with sample dimensions usually 4×12 mm and $w/s = 4/2.5 = 1.6$, the resistivity is given by: $\rho \approx 1.58Rd$.

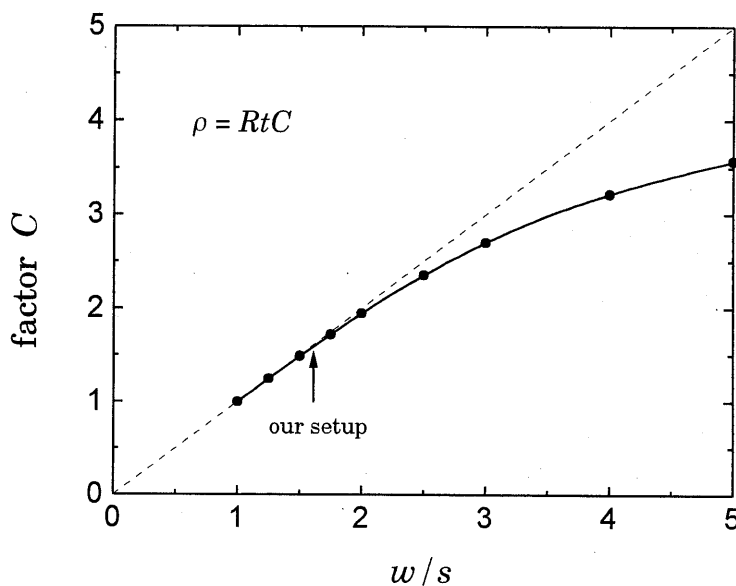


Figure 2.10: The factor C in equation 2.12 as a function of w/s for the case $l/w = 3$, according to F.M. Smits (Smi57).

For a finite thickness, d , another correction factor is needed whenever $d/s > 0.4$. In our specific setup this means that an extra correction factor would be necessary for samples thicker than 1 mm, at least 10^4 times the thickness of our samples.

To facilitate comparison with samples of other dimensions, a common way to present the resistivity of multilayered thin films, is the sheet resistance, R_s , or the sheet conductance, G_s . The sheet resistance is the resistance that would be

obtained for a square sample with a homogeneous current distribution, and is defined as:

$$R_S = \frac{1}{G_S} \equiv \frac{\rho}{d} = \frac{w}{s} R \quad (2.13)$$

As we will show in chapter 3, the absolute change in sheet conductance (ΔG) between parallel and antiparallel alignment of the magnetization directions of the various layers in a magnetic multilayer or spin-valve, is the most relevant macroscopic quantity to represent the magnetoresistance .

In our equipment, the reference signal of a lock-in amplifier is used as a reference for the current source that generates the alternating current ($I \approx 1$ mA, $f = 80$ Hz). The measured alternating voltage is amplified (100 or 1000 times). A compensation voltage with the same phase and frequency as the alternating current is subtracted from this amplified voltage. The amplitude of the compensation voltage is adjusted to the same amplitude as the measured voltage in zero magnetic field. Then, changes in the resistance resulting from the application of a magnetic field can be measured as a deviation from zero voltage, which allows the lock-in amplifier to operate at the most sensitive scale.

Whence the resistance is measured as a function of magnetic field, the magnetoresistance can be calculated from:

$$MR = \frac{R_{ap} - R_p}{R_p} = \frac{G_p - G_{ap}}{G_{ap}} \quad (2.14)$$

where R_{ap} (G_{ap}) denotes the sheet resistance (conductance) for antiparallel magnetization directions and R_p (G_p) the sheet resistance (conductance) for parallel alignment of the magnetization directions.

In our apparatus the sample is positioned in a flow cryostat bought from Oxford (type: CF1200) in which the temperature can be varied between $T = 1.5$ K and $T = 350$ K. The cryostat is located between the poles of an electromagnet with a maximum magnetic field of $H_{\max} = 1075$ kA/m ($B_{\max} = 1.35$ T).

2.4 X-ray analysis

Information on the layer thickness or, in case of a multilayer, the multilayer period can be obtained from X-ray diffraction measurements. In addition, these measurements provide information on the crystal structure and interface quality.

In these experiments X-rays, emitted from a Cu-source ($\lambda = 1.54050$ Å and $\lambda = 1.54434$ Å), impinge on the sample surface and the intensity of the reflected beam is measured. In most experiments the angle of incidence is θ and the

reflected X-rays are detected at an angle 2θ with respect to the incoming beam, as is shown in figure 2.10. This is called a θ - 2θ measurement. When θ is typically below 50 mrad (2.85°), the technique is sometimes denoted as GIXA (Glancing-Incidence X-Ray Analysis, Boe95). The angles at which constructive interference occurs are determined by the Bragg-condition (Kit86):

$$2d \sin \theta = n\lambda \quad (n = 1, 2, 3, \dots) \quad (2.15)$$

When, for a single layer, a diffraction peak is observed at an angle $2\theta \geq 40^\circ$, d is of the order of 2 \AA or smaller (with $n = 1$). In this case, the calculated d can be related to the distance between the lattice planes parallel to the surface. For instance, the distance between the (111)-Co planes in a fcc-structure amounts to 2.0467 \AA , such that a diffraction peak can be expected at $2\theta = 44.2^\circ$. However, when Co is grown in a (100)-orientation, the distance between the lattice planes is only 1.7723 \AA , and a diffraction peak is expected at $2\theta = 51.5^\circ$. In this way one can, in principle, determine the element at which the diffraction occurs as well as the growth direction. When two materials of lattice parameter d_1 and d_2 are grown on top of each other to form a multilayer with periodicity D , it can be shown (Seg73) that higher order multilayer peaks ($2D \sin \theta = n\lambda$) occur around the diffraction peaks at the positions $2d_1 \sin \theta_1 = \lambda$ and $2d_2 \sin \theta_2 = \lambda$. When peaks in the diffraction spectrum occur at small angles ($2\theta < 10^\circ$), $d \geq 8.5 \text{ \AA}$ and represents the film thickness or, in a multilayer sample, the multilayer period.

Interface roughness at the interfaces between various layers reduces the specular reflection and gives rise to diffuse scattering in all directions. Thus, when the height of the peaks is analyzed, information can be obtained about the interface quality.

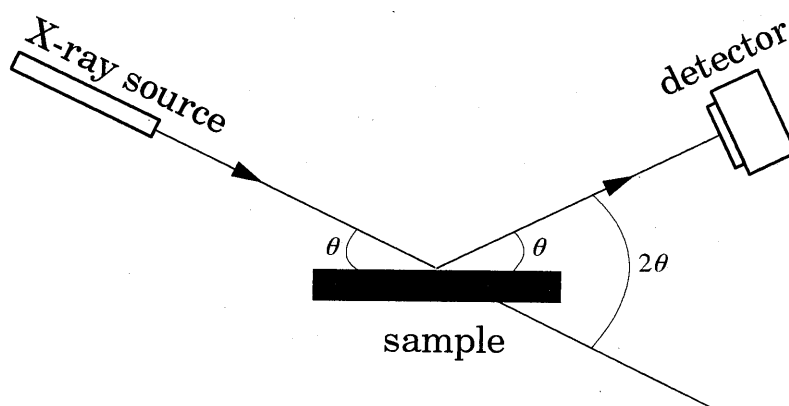


Figure 2.11: Schematic setup of the X-ray diffraction apparatus.

Information on the quality of the texture can be obtained by measuring a rocking-curve. In this geometry the angles of the sample and detector are first tuned to a Bragg-reflection angle. Next, the sample is rotated over an angle α while the detector remains at a fixed position, and the intensity is measured as a function of the angle α . For a single crystal the intensity of the reflected beam is zero when θ does not satisfy the Bragg-condition ($\alpha \neq 0$), but when the sample is composed of different crystallites with various orientations, a finite intensity is measured for $\alpha \neq 0$. Thus the width of the rocking-curve (usually expressed as the full width at half maximum FWHM) provides a measure of the spread in the orientation of the crystallites in the sample.

3. Modelling of the GMR effect

3.1 Introduction

In the general introduction of chapter 1, the GMR effect was explained using the analogy of an extremely simple resistor model built up of different resistors representing the different, spin-dependent, scattering of spin-up and spin-down electrons. Let us now consider the possible origins of this spin dependence.

First of all, we should realize that in ferromagnetic metals at low temperatures scattering is caused mostly by impurities, defects, and grain boundaries (in the case of a thin film), and there is no magnon scattering that results in a spin-flip or phonon scattering. This means that the spin direction of an electron does not change when the electron scatters. In that case, the conduction is the sum of independent contributions from spin-up and spin-down electrons ($\sigma = \sigma^\uparrow + \sigma^\downarrow$), which is often referred to as the two-current model as introduced by Mott (Mot36).

In Fe, Co, Ni and their alloys, the magnetism is caused by the d-electrons. In the band structure of these materials the d-electron band is exchange split. This results in a different density of electron states (DOS) for spin-up¹ and spin-down electrons at the Fermi level, as is shown in figure 3.1 (Coe97). The scattering probability is proportional to the DOS at the Fermi level (see, e.g., Tsy96) but, by definition, inversely proportional to the relaxation time τ (the mean time between two scatter events). Thus, in general, a difference in this DOS between spin-up and spin-down electrons will result in different contributions to the conductivity ($\propto \tau$) from spin-up and spin-down electrons. Tacitly we have assumed here that the s- and p-electrons, that give the largest contribution to the conduction, may scatter to the available d-band electron states. Campbell and Fert (Woh82) provide a table of a parameter α_b (b denoting bulk), defined as $\alpha_b = \rho^\downarrow / \rho^\uparrow$, for dilute impurities in bulk Ni, Co, and Fe. As this type of scattering occurs in the bulk of the ferromagnetic materials we refer to it as bulk spin-dependent scattering.

In our layered structures where different materials are grown on top of each other, there will always be some intermixing at the interfaces especially in sputtered samples. One could therefore imagine that the (spin-dependent) scattering from a zone near the interfaces is often larger than the scattering probability in the bulk.

¹ It is common practice to denote the majority electrons (upper band in fig. 3.1) as spin-up electrons, although in fact the projection of the spin along the magnetization direction (z-axis) for these electrons has the quantum number $s_z = -\frac{1}{2}$.

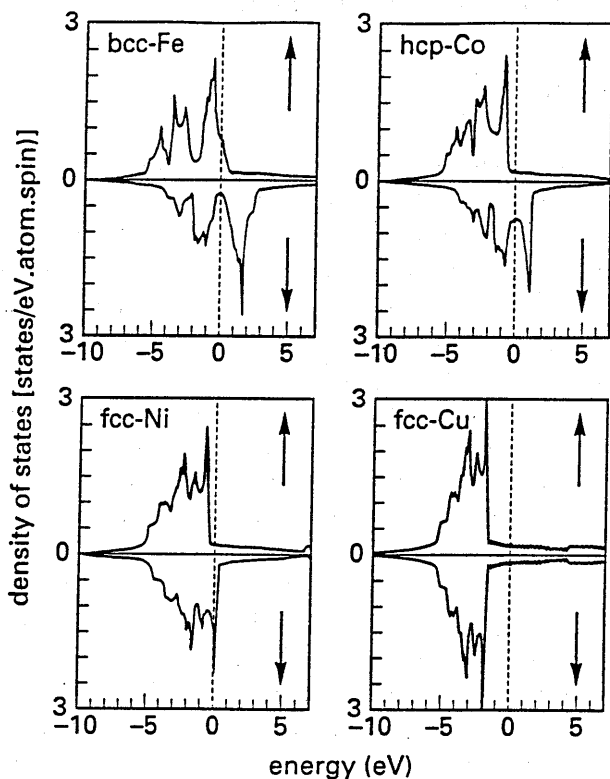


Figure 3.1: Densities of states for the elemental metals Fe, Co, Ni, and Cu, as obtained from selfconsistent ab initio band structure calculations using the Augmented Spherical Wave (ASW) method. Arrows indicate the spin-direction. This figure is taken from Coehoorn (Coe97).

Another effect, that occurs at the interfaces, is that electrons that cross the interface between two different materials will experience a potential difference. As a result some of these electrons will be specularly reflected, indicated by a reflection coefficient R , some electrons will be transmitted, indicated by a transmission coefficient T , and the remainder of the electrons will be diffusely scattered (due to roughness and impurities at the interface), indicated by a coefficient D ($D = 1 - T - R$) (see also figure 3.5). Because of the exchange splitting of the d-band in the magnetic layers, the potential difference at the interfaces is spin-dependent and therefore also the coefficients R , T , and D , describing the interface scattering, will be spin-dependent which can thus result in magnetoresistance. It is generally believed that this potential scattering at the interfaces is not very important when the conduction is primarily determined by the s- and

p-electrons, but it can be important when also the d-electrons contribute substantially to the conduction (Ste92).

Finally geometrical roughness (deviations from a flat interface between two homogeneous materials), can contribute to the magnetoresistance when the potentials in the magnetic layers are spin-dependent. This is because whether or not an electron experiences an interface to be flat, depends on the characteristic scale of the roughness compared to the Fermi wavelength of the electron, λ_F (Zim67, Sof67). Thus different values of λ_F for spin-up and spin-down electrons affects the spin-dependent parameters R , T , and D .

Above we have given a number of possible origins of the observed spin-dependent scattering. Of course, not each combination of materials will necessarily behave in the same way and sometimes bulk spin-dependent scattering will dominate whereas in other systems some form of interface spin-dependent scattering may dominate. In addition the relative weight of interface versus bulk spin-dependent scattering depends on the layer thickness. The question which effect is actually responsible for the GMR effect is still a matter of debate in literature and is discussed also in several chapters of this thesis. Below we will treat some theoretical models and explain how bulk and interface spin-dependent scattering are described in these models. We will limit ourselves here mainly to the current-in-plane (CIP) geometry in accordance with the experiments described in this thesis. At the end of this chapter, in section 3.5, we will briefly indicate the differences with the current-perpendicular-to-plane (CPP) geometry.

Up to now we have only discussed spin-dependent scattering. However, spin-dependent scattering in the bulk of the layers or at the interfaces is not the only condition necessary to obtain a GMR effect. Another condition is that the multilayer or spin valve must have the possibility to switch between a state where the magnetization directions of the various layers are aligned antiparallel and a state where they are aligned parallel. Equally important, at least in current-in-plane systems, is that the electrons can travel from one magnetic layer to another magnetic layer without diffuse scattering in between. Only in this case the electrons experience a difference between a parallel and an antiparallel configuration of the magnetizations. Thus, when the mean free path of the conduction electrons is much smaller than the spacer layer thickness, there will be no GMR. In that case the layers can be represented by resistors in parallel. On the other hand, the resistor model used in chapter 1, where the resistors are in series both in the spin-up channel and in the spin-down channel, is only appropriate for a mean free path of the spin-up and spin-down electrons that is much larger than the multilayer period.

Although resistor models are very suitable to introduce the GMR effect, they present a too simple picture of reality. More realistic models to describe GMR are based on two different approaches. One approach is a semiclassical description,

the other a quantum mechanical. Since the semiclassical models generally provide more insight, are simple to apply to trilayers as well as to superlattices, and seem to describe the experimental data just as well as the quantum mechanical models, we have chosen to analyse our measurements with the semiclassical Camley-Barnas model. This model, based on the Boltzmann transport equation, will therefore be described in detail in the next sections. In section 3.4 we will briefly review some aspects of quantum mechanical models.

3.2 Semiclassical treatment of resistance in thin layers

3.2.1 The Boltzmann transport equation

The Boltzmann transport equation can be used to evaluate the electron distribution function of a system of electrons which is not in equilibrium. To derive this equation (see for instance Cou74, Dug77, Ros77), first an electron distribution function $f(\vec{k}, \vec{r}, t)$ in the six-dimensional phase space is defined, such that $f dk_x dk_y dk_z dx dy dz$ represents the probability of finding an electron with a wavevector within a volume $dk_x dk_y dk_z$ about \vec{k} and a position in real space within $dx dy dz$ about \vec{r} at a time t . When the electron system is subject to an applied electric field \vec{E} , the distribution function f will change with time due to changes in momentum $\hbar \vec{k}$ and position \vec{r} . Following the volume element $d\vec{k} d\vec{r}$ as a function of time and using a Taylor series expansion we obtain:

$$\left(\frac{\partial f}{\partial t}\right)_{\text{Field}} = -\frac{dk_x}{dt} \frac{\partial f}{\partial k_x} - \frac{dk_y}{dt} \frac{\partial f}{\partial k_y} - \frac{dk_z}{dt} \frac{\partial f}{\partial k_z} - \frac{dx}{dt} \frac{\partial f}{\partial x} - \frac{dy}{dt} \frac{\partial f}{\partial y} - \frac{dz}{dt} \frac{\partial f}{\partial z} \quad (3.1)$$

where $\frac{d\vec{k}}{dt}$ simply follows from the semiclassical equation of motion: $\frac{d\vec{k}}{dt} = \frac{1}{\hbar} e\vec{E}$ with e the electron charge. This however would mean that \vec{k} increases uniformly with time leading to an ever increasing current. In practice the electrons will be slowed down by collisions and a steady state will occur. In this state the rate of change of the distribution function due to the field is exactly balanced by the scattering such that:

$$\frac{df}{dt} = \left(\frac{\partial f}{\partial t}\right)_{\text{Field}} + \left(\frac{\partial f}{\partial t}\right)_{\text{scat}} = 0$$

which is equivalent to

$$\frac{df}{dt} = -\frac{d\vec{k}}{dt} \cdot \vec{\nabla}_k f - \frac{d\vec{r}}{dt} \cdot \vec{\nabla}_r f + \left(\frac{\partial f}{\partial t} \right)_{\text{scat}} = 0 \quad (3.2)$$

Equation (3.2) is called the Boltzmann transport (BT)-equation.

In the literature usually an approximation is made to solve this Boltzmann equation. It states that when the field is removed, any distribution function f will exponentially return to its equilibrium distribution f_0 with a characteristic relaxation time τ , due to the scattering of the conduction electrons. Hence:

$$\left(\frac{\partial f}{\partial t} \right)_{\text{scat}} = -\frac{f - f_0}{\tau} \equiv -\frac{g}{\tau} \quad (3.3)$$

where $f = f_0 + g$ with perturbation $g \ll f_0$.

For an electron gas at thermal equilibrium the function f_0 is the Fermi-Dirac distribution function that in terms of energy can be written as

$$f_0(\varepsilon) = \frac{1}{\exp[(\varepsilon - \varepsilon_F) / k_B T] + 1} \quad (3.4)$$

where ε is the kinetic energy $\frac{1}{2}mv^2$ when the approximation is made that one is dealing with a free electron gas.

3.2.2 Boltzmann transport equation for a thin film

Fuchs (Fuc38) and later Sondheimer (Son52) were the first to apply the BT-equation to calculate the conductivity of a thin film. The calculation proceeds as follows. Consider a homogeneous thin film of dimensions $l \times w \times d$ (with thickness $d \ll l, w$), parallel to the x-y-plane, as is shown in figure 3.2. In that case from the three spatial partial derivatives only $\partial f / \partial z$ will be nonzero, because only in this direction the outer surfaces of the film can influence f . Suppose further that the electric field is applied in the x-direction: $E = (E_x, 0, 0)$. In that case equation (3.2) reduces to:

$$\frac{1}{\hbar} eE_x \frac{\partial f}{\partial k_x} + v_z \frac{\partial f}{\partial z} = -\frac{g}{\tau} \quad (3.5)$$

Remembering that $\frac{\partial f}{\partial k_x} = \frac{\partial f}{\partial v_x} \frac{dv_x}{dk_x} = \frac{\partial f}{\partial v_x} \frac{\hbar}{m}$, this is equivalent to

$$\frac{\partial g}{\partial z} + \frac{g}{\tau v_z} = -\frac{eE_x}{m v_z} \frac{\partial f_0}{\partial v_x} \quad (3.6)$$

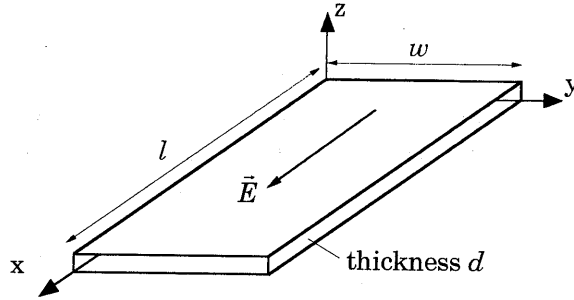


Figure 3.2: Schematic representation of a thin film parallel to the x-y-plane. The film dimensions are $l \times w \times d$, with $d \ll l, w$. An electric field \vec{E} is applied in the x-direction.

where only linear terms are taken into account and the second-order term $E_x(\partial g / \partial v_x)$, which leads to deviations from Ohm's law, has thus been omitted. The general solution to equation (3.6) takes the form:

$$g(\vec{v}, z) = -\frac{eE_x\tau}{m} \frac{\partial f_0}{\partial v_x} \left\{ 1 + F(\vec{v}) \exp\left(\frac{-z}{\tau v_z}\right) \right\} \quad (3.7)$$

where F is a function of the velocity only, that has to be determined from boundary conditions. The most simple assumption for the boundary conditions is to assume that the scattering at the outer boundaries of the film is completely diffuse. In this case the distribution function of the electrons leaving the surface must be independent of the direction of \vec{v} . Since electrons leaving the surface at $z = 0$ move in the opposite direction from electrons leaving the surface at $z = d$, it is convenient to discriminate between electrons moving in the positive z-direction and electrons moving in the negative z-direction. The solution of equation (3.6) under the assumption of completely diffuse scattering at the outer boundaries is therefore given by:

$$\begin{aligned} g^+(\vec{v}, z) &= -\frac{eE_x\tau}{m} \frac{\partial f_0}{\partial v_x} \left[1 - \exp\left(\frac{-z}{\tau v_z}\right) \right] \\ g^-(\vec{v}, z) &= -\frac{eE_x\tau}{m} \frac{\partial f_0}{\partial v_x} \left[1 - \exp\left(\frac{d-z}{\tau v_z}\right) \right] \end{aligned} \quad (3.8)$$

where the superscript '+' denotes electrons with $v_z > 0$ and the superscript '-' electrons with $v_z < 0$.

The current density J is given by the total charge density multiplied by the average velocity. In the case of a thin film parallel to the x-y-plane, the current density depends on z due to the diffuse scattering at the outer surfaces. Hence:

$$J(z) = \frac{e}{4\pi^3} \int f(\vec{k}, z) v_x d^3k \quad (3.9)$$

Since in the equilibrium state with distribution function f_0 there will be no net current, this is equivalent to:

$$J(z) = \frac{e}{4\pi^3} \left(\frac{m}{\hbar}\right)^3 \int v_x [g^+(\vec{v}, z) + g^-(\vec{v}, z)] d^3v \quad (3.10)$$

Note that when there would be no z -dependence equation (3.9) would have the form:

$$J = \frac{e}{4\pi^3} \int -eE_x \tau v_x \frac{df_0}{d\varepsilon} v_x dk_x dk_y dk_z \quad (3.11)$$

in which the volume element can be transformed according to $dk_x dk_y dk_z = (1/\hbar v) dS d\varepsilon$, where S denotes a surface of constant energy. Thus:

$$J = \frac{e^2 E_x \tau}{4\pi^3 \hbar} \int \int_{S_\varepsilon} \frac{v_x^2}{v} \left(-\frac{df_0}{d\varepsilon}\right) dS d\varepsilon \quad (3.12)$$

Now, at $T = 0K$, $-\frac{df_0}{d\varepsilon}$ essentially behaves as a δ -function so that only electrons at the Fermi surface can contribute to the conductivity. Therefore equation (3.12) reduces to:

$$J = \frac{e^2 E_x \tau}{4\pi^3 \hbar} \int_{S_F} \frac{v_x^2}{v} dS_F \quad (3.13)$$

where S_F denotes the Fermi surface. Assuming now a free electron gas with an isotropic velocity distribution, it follows from symmetry arguments that:

$$J = \frac{e^2 E_x \tau}{12\pi^3 \hbar} \int_{S_F} v_F dS_F \quad (3.14)$$

Now inserting $mv_F = \hbar k_F$ and $\int_{S_F} dS_F = 4\pi k_F^2$ one obtains:

$$J = \frac{e^2 \tau}{12\pi^3 \hbar} \frac{\hbar k_F}{m} 4\pi k_F^2 E_x = \sigma E_x \quad (3.15)$$

and remembering that the density of electron states, n , within the Fermi sphere is just $\frac{4}{3} \pi k_F^3 / 4\pi^3$, one finally finds:

$$\sigma = \frac{ne^2 \tau}{m} \quad (3.16)$$

which is the well-known Drude expression for the bulk conductivity σ .

Returning to equation (3.8) it is clear now that far from the surfaces the bulk conductivity is obtained. In a region within the characteristic length $\tau \langle v_z \rangle$, which is smaller than τv_F , from the surface, however, the exponent in this equation decreases the conductivity. As we will find later (in section 3.3 and chapter 7), this characteristic length is to a good approximation given by $\tau \langle v_z \rangle = \frac{1}{2} \lambda$, with $\lambda \equiv \tau v_F$ the electron mean free path. This is schematically indicated in figure 3.3. The figure shows the contributions to the current density $J = \sigma E$ from electrons with $v_z < 0$ and $v_z > 0$ separately as well as the total current density as a function of position in the film. When the film is thick compared to the mean free path λ , the current density in the middle of the film (which is far away from the outer boundaries where the electrons are scattered in a diffuse way) reaches the bulk value.

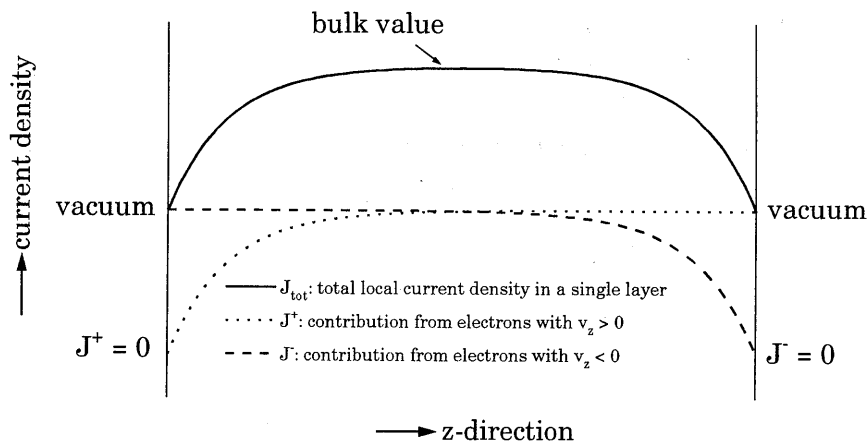


Figure 3.3: Schematic representation of the local current density $J(z)$ in a homogeneous thin film. At the boundaries where the electrons are scattered diffusely, the current density is reduced. Apart from the total current density, also the local current density for the + ($v_z > 0$) and - ($v_z < 0$) electrons separately is shown.

3.2.3 Influence of the boundaries

The decrease of the conductivity in a region with a thickness of the order of λ from the surface is exponential, as stated above; The contribution of this term (in Eqs. 3.7 and 3.8) is determined by boundary conditions. These conditions determine $F(\vec{v})$ in equation (3.7). In the above example it was assumed that the scattering at the outer boundaries is completely diffuse. However, more generally, in the theory of Fuchs and Sondheimer a specular reflection coefficient p is defined. Here p represents the probability that an electron is specularly reflected. Thus p varies between $p = 0$ for completely diffuse scattering, in which case equation (3.7) takes the form of equation (3.8), and $p = 1$ for completely specular reflection. Note that in the latter case the velocity in the field direction is not altered by the boundary scattering and the conductivity will therefore be equal to the bulk conductivity.

This description of the boundary scattering by one single parameter p in the range between 0 and 1 is perhaps the most simple description of the presence of the outer boundaries. In fact, the specularity parameter should depend on the angle of incidence. This was for instance recognized by Parrot (Par65) who, by analogy with light reflecting from a surface, introduced a step function for the specular reflectivity coefficient:

$$p(\theta) = \begin{cases} 1 & \theta_C \leq \theta \leq 90^\circ, \\ 0 & 0 \leq \theta < \theta_C \end{cases} \quad (3.17)$$

where $\theta = 0$ corresponds to normal incidence. Below a critical angle θ_C , all electrons are scattered diffusely and above θ_C all electrons are scattered specularly.

Ziman (Zim67) has calculated reflections of plane waves from a rough surface. The introduction of geometrical roughness was shown also to result in an angle dependence of p . In general the precise behavior of the function $\zeta(x,y)$, where ζ denotes the deviation in the z-direction from the ideal surface, is not known. A common approach is therefore to assume some statistical properties that characterize the roughness. In this approach ζ is considered as a random variable with a Gaussian distribution. In that case the two important parameters that describe the geometrical roughness are the root mean square of the height deviations of the ideal flat surface, $\eta = \sqrt{\langle \zeta(x,y)^2 \rangle}$, and the in-plane lateral correlation length L . In a simple picture L can be viewed as a measure of the flat parts of the surface. According to Ziman, the probability of specular reflection for electrons incident normal to the surface depends for the case $L^2 < 16\pi^2\eta^2$ on the ratio of the electron wavelength $\lambda_F (= h/mv)$ and η as

$$p(\lambda) = \exp\left(-\frac{16\pi^3\eta^2}{\lambda_F^2}\right) \quad (3.18)$$

which is a very crude approximation neglecting for instance the angle dependence. Finally, Ziman discussed the effects of glancing incidence and postulated that the exponent in equation (3.18) should be reduced by a factor of $\cos^2 \theta$.

Soffer (Sof67) pointed out that in the result of Ziman the requirement of electron flux conservation was not satisfied for the outgoing flux density distribution. He extended the method to include oblique incidence and modified it to satisfy the flux conservation requirement. For the case of zero correlation length ($L = 0$), this results in a specularly parameter with an angle dependence given by:

$$p(\cos \theta) = \exp\left[-(4\pi\eta / \lambda_F)^2 \cos^2 \theta\right] \quad (3.19)$$

In figure 3.4 the specular reflection coefficient p is shown as a function of θ for $\lambda_F = 5 \text{ \AA}$ and different values of η .

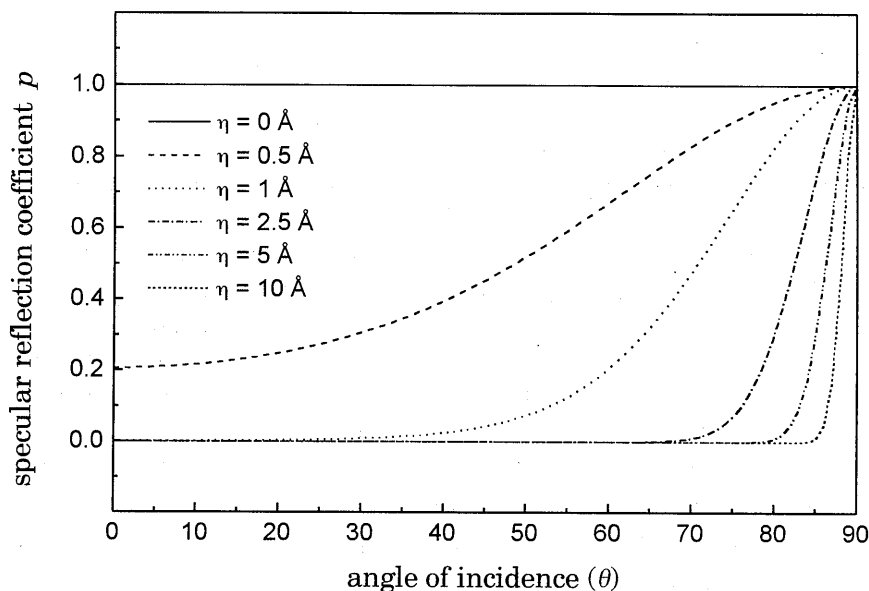


Figure 3.4: The specular reflection coefficient according to Soffer (Eq. 3.19) as a function of the angle of incidence, for different values of η (in \AA) and $\lambda_F = 5 \text{ \AA}$.

Theoretically we have learned now that the specularity parameter p does depend on the angle of incidence, although from an experimental point of view this is difficult to verify in layered structures exhibiting GMR. In fact, it is not even clear whether or not specular reflections do occur in magnetic multilayers. Only recently the first indications on specular reflectivity have been reported (Ege97, Swa97, chapter 9). Moreover, most GMR experiments are not specifically designed, and therefore not particularly suitable to investigate the angle dependence in detail. Therefore this angle dependence is often neglected when fitting experimental data of the GMR effect.

3.2.4 Boltzmann transport equation for a magnetic multilayer

A) The Camley-Barnas (CB) model

Carcia and Suna (Car83) were the first to use a solution of the BT-equation to calculate the resistance of a nonmagnetic metallic multilayer. Next, in 1989 Camley and Barnas (Cam89, Bar90) used an extension of the Fuchs-Sondheimer theory, where the BT-equation is solved to calculate the conductivity of a magnetic multilayer. In this model solutions like equation (3.8) now have to be found for each layer separately. An extra complication for the description of magnetic layers is that, as mentioned before, the scattering in these layers will be spin-dependent. This means that spin-up and spin-down electrons possess a different relaxation time τ and/or mean free path $\lambda = \tau v_F$. This results in four ' g -functions': g_{\uparrow}^+ , g_{\downarrow}^+ , g_{\uparrow}^- and g_{\downarrow}^- (where \uparrow denotes spin-up and \downarrow spin-down) instead of two. Such a separation between spin-up and spin-down electrons is only allowed in the absence of magnon scattering that would cause spin-flips from spin-up to spin-down and vice versa. Generally this is correct at low temperatures although, for instance, for Co/Cu multilayers it has been reported (Gij94, Oep96) that spin-flip scattering is still relatively weak at room temperature.

At the interfaces between the various layers the g -functions are coupled to each other by spin-dependent reflection (R) and transmission (T) coefficients (see figure 3.5a). For instance at the interface between layer A and B:

$$g_{\sigma}^+(\text{B}) = T^{\sigma} g_{\sigma}^+(\text{A}) + R^{\sigma} g_{\sigma}^-(\text{B}) \quad (3.20)$$

with σ the spin direction (\uparrow or \downarrow), T^{σ} the probability of coherent transmission, and R^{σ} the probability of specular reflection. The remainder, $D^{\sigma} = 1 - T^{\sigma} - R^{\sigma}$, gives the probability of diffuse scattering. Within the Camley-Barnas model T , R , and D are purely phenomenological fitting parameters, independent of the angle of incidence. Besides the spin directions, the coefficients T , R and D , will be different for different interfaces. These coefficients actually determine $F(\bar{v})$ from equation (3.7). Assumptions that are frequently made within the (CB) model are

completely diffuse scattering at the outer boundaries of the multilayer and $R^\sigma = 0$ at the inner interfaces.

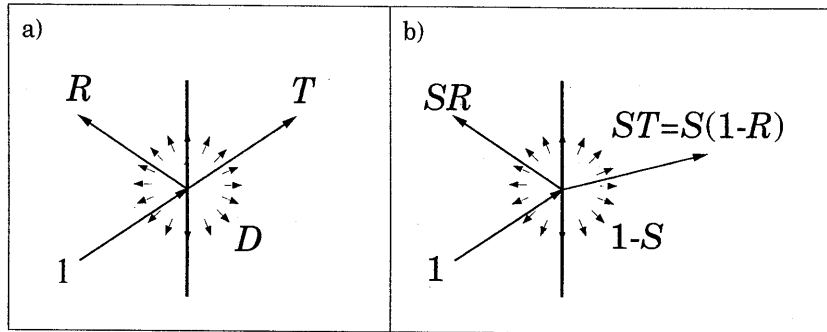


Figure 3.5: a) Schematic representation of the spin-dependent interface parameters T , R , and D according to the CB-model. b) Schematic representation of the spin-dependent interface parameters T , R , and D according to the FH-model. S ($0 \leq S \leq 1$) accounts for the effects of roughness (see text). Note that different inner potentials on each side of the interface result in refraction of the incoming electrons.

For each individual layer i between z_{i-1} and z_i the conductance can now be calculated from:

$$G_i = \frac{1}{E_x} \int_{z_{i-1}}^{z_i} J_i(z) dz \quad (3.21)$$

where

$$J_i(z) = \frac{e}{4\pi^3} \left(\frac{m}{\hbar}\right)^3 \int \sum_{\sigma=\uparrow,\downarrow} \sum_{+,-} v_x g_{i\sigma}^\pm(\vec{v}, z) d^3v \quad (3.22)$$

and the conductance of the whole multilayer stack is given by:

$$G_{\text{tot}} = \sum_i G_i \quad (3.23)$$

To calculate the Giant MagnetoResistance (GMR) ratio, this calculation must be performed in case of antiparallel magnetization directions between adjacent magnetic layers, G_{ap} , and in case of parallel alignment, G_p .

What is necessary to obtain a GMR ratio is spin-dependent scattering (SDS), which means that one kind of electrons (\uparrow or \downarrow) experiences considerably more resistance than electrons of opposite spin direction. As mentioned in the introduction, the question whether the SDS occurs mainly in the interior (bulk) of the ferromagnetic layers or at the interfaces between the magnetic layers and the nonmagnetic spacer is still a matter of debate in literature as we will show in chapters 6, 7 and 8. In the CB-model SDS in the bulk of the magnetic layers can be modelled by spin-dependent mean free paths ($\lambda^\uparrow \neq \lambda^\downarrow$). These mean free paths enter the g -functions (see Eq. 3.8) via $\tau^{\uparrow(\downarrow)} v_z = \lambda^{\uparrow(\downarrow)}$, where θ is the angle between the electrons velocity and the z -axis, and can therefore influence the conductivity. SDS at the interfaces between the various layers can be modelled by choosing the coefficients R , T , and D spin-dependent (see Eq. 3.20). In section 3.3 we will investigate the CB-model in more detail.

B) The Hood-Falicov (HF) model

As mentioned before, in the CB-model the interface parameters R , T , and D are purely phenomenological fitting parameters. Based on a number of experimental results (Ful92a, Bau91, Bai88) and from comparison of experimental data with model calculations (Lev90, Bar90a, Bar90), Hood and Falicov (Hoo92) in 1992 argued that spin-dependent interface scattering could play an important role and that the CB-model makes some unsuitable approximations in particular with respect to interfacial scattering. In the CB-model the difference between the inner potential on either side of an interface is neglected. Therefore the CB-model does not take into account differences between the Fermi velocities on both sides of an interface, nor any angular dependence of the scattering. Hood and Falicov (HF) introduced a constant inner potential, $V_{i\sigma}$, within each layer, that is spin-dependent in the magnetic layers. In this case, assuming that the scattering is completely elastic and completely coherent, the reflection and transmission coefficients (see figure 3.5b) can easily be calculated (Gas74) by quantum mechanically matching free-electron-like plane-wave functions and their derivatives at each interface. As an example figure 3.6 shows calculated reflection coefficients for spin-up and spin-down electrons that move in the magnetic layer towards the spacer layer. The transmission coefficients T simply follow from $T = 1 - R$. Clearly the reflection and transmission coefficients depend now on the angle of incidence, θ , which is the angle between the electron velocity and the normal to the interface.

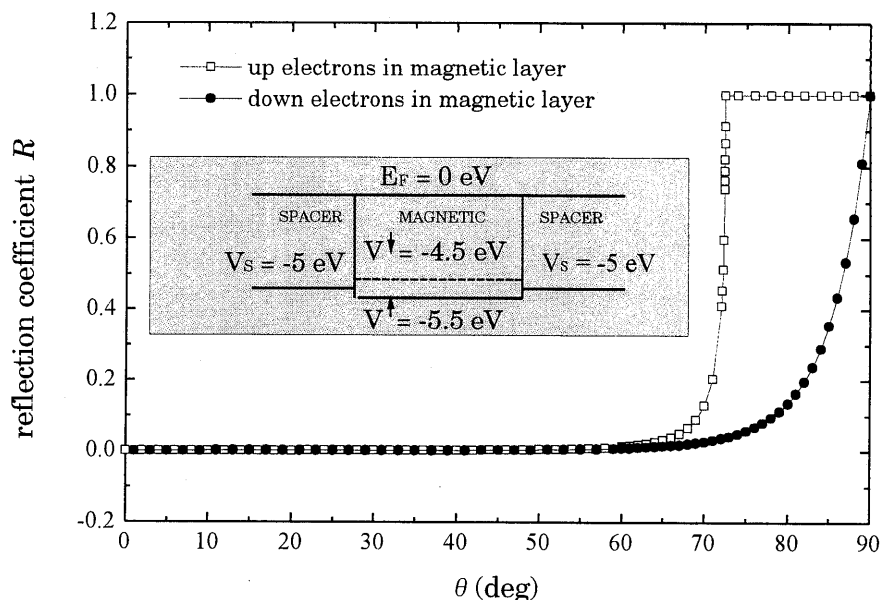


Figure 3.6: Reflection coefficient R as a function of angle of incidence θ for spin-up and spin-down electrons at the Fermi level, moving in the magnetic layer and impinging on the interface with the spacer. R is calculated by quantum mechanical matching the wave functions at the interfaces.

One of the consequences of the introduction of material-dependent potentials is that electrons incident at grazing angles can be totally internally reflected, as can be seen in figure 3.6. When all magnetization directions are aligned parallel, the electrons that are totally reflected are confined within one layer and experience only bulk scattering in this layer. The effect is called electron channelling and can strongly influence the current distribution in the multilayer. This is illustrated in figure 3.7.

In figure 3.7 the in-plane current density is shown for spin-up electrons, $J^\uparrow(z)$, and spin-down electrons, $J^\downarrow(z)$, separately, for the case of an infinite multilayer composed of $25 \text{ \AA} \text{ M}/25 \text{ \AA} \text{ NM}/25 \text{ \AA} \text{ M}$ (M denotes a magnetic layer, and NM the nonmagnetic spacer). In figure 3.7 only one period of the multilayer ($1/2\text{M}/\text{NM}/1/2\text{M}$) is shown. In figure 3.7a and b, the calculation is performed for parallel alignment of the magnetization directions, and in figure 3.7c and d for antiparallel alignment.

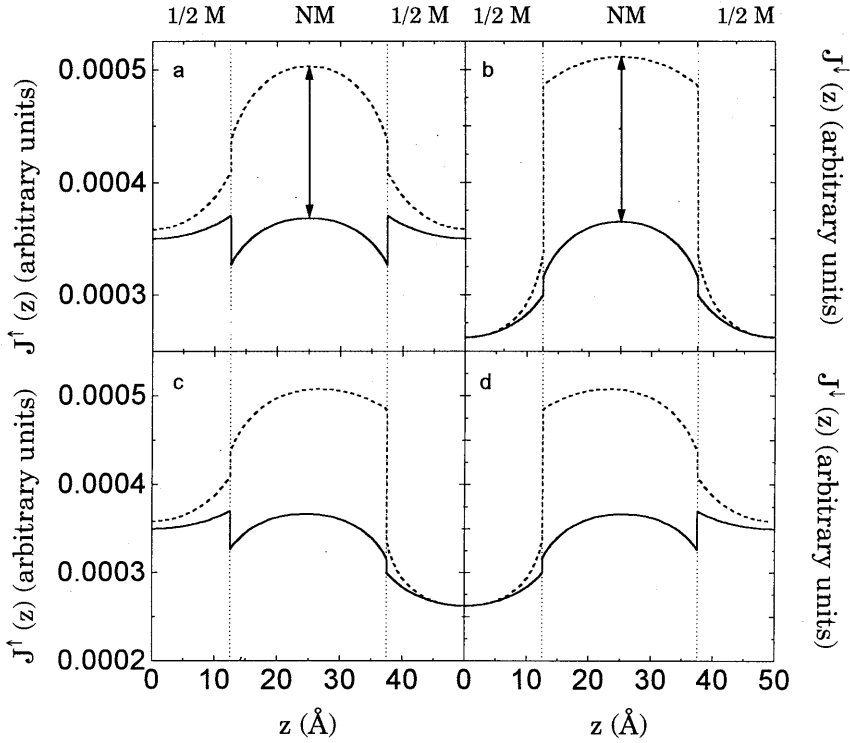


Figure 3.7: Local current density as a function of position in the layers of a superlattice. Only one unit cell ($\frac{1}{2}M/NM/\frac{1}{2}M$) is shown. In a) and b) the magnetization directions are aligned parallel, in c) and d) antiparallel. The local current density is calculated for two different spacer potentials: solid line $V_S = -4\text{eV}$, dashed line $V_S = -5\text{eV}$. The arrows indicate the increase in local current density which is for spin-down electrons in the parallel alignment larger than for spin-up electrons due to channelling. For further explanation see text.

As input parameters we have chosen $V^\uparrow = -5.5\text{ eV}$ and $V^\downarrow = -4.5\text{ eV}$. To investigate only the effect of channelling, we have chosen spin-independent relaxation times: $\tau^\uparrow = \tau^\downarrow = 0.02 \times 10^{-13}\text{ s}$ in the magnetic layers, and $\tau_S = 0.04 \times 10^{-13}\text{ s}$ in the spacer. The solid lines in figure 3.7 represent the situation where $V_S = -4\text{ eV}$, and the dashed lines represent the situation where $V_S = -5\text{ eV}$. A change in spacer potential from -4 eV to -5 eV increases the Fermi velocity v_F , so, for a given relaxation time τ it will result in a larger current density both for spin-up and spin-down electrons. When the spacer potential is $V_S = -4\text{ eV}$ none of the electrons in the spacer layer can reflect totally. A spacer potential of -5 eV

however allows only the spin-down electrons, incident at grazing angles, to be totally internally reflected in the spacer, which results in a larger increase in current density for the down electrons with respect to the up electrons, as indicated with the arrows in figure 3.7a and b. This asymmetry in spin-up and spin-down electrons due to channelling results in only a small magnetoresistance effect. For the particular case of figure 3.7 the magnetoresistance ratio amounts to $9.8 \times 10^{-3} \%$ when $V_S = -5$ eV compared to $1 \times 10^{-3} \%$ when $V_S = -4$ eV. Even when the relaxation times are $\tau^\uparrow = \tau^\downarrow = 2 \times 10^{-13}$ s and $\tau_S = 4 \times 10^{-13}$ s, close to the values of Hood and Falicov, the GMR ratio will not be larger than 0.67 % when the spacer potential $V_S = -5$ eV. Channelling in combination with other sources of spin-dependent scattering, however, can help to obtain a large magnetoresistance ratio, as pointed out by Hood and Falicov (Hoo92).

Recently Butler *et al.* (But96) showed from more sophisticated calculations based on a realistic band structure that indeed majority (spin-up) electrons in Co/Cu multilayers may undergo total internal reflection within the copper layers if the component of their Fermi momentum parallel to the layers exceeds the Fermi momentum of Co. They concluded that channelling may significantly contribute to the GMR effect. However, although the concept of different potentials in different layers thus seems realistic, the incorporation of a realistic band structure in the GMR calculations is nontrivial. In the HF-model constant potentials within each layer are determined by assuming that all valence electrons form a single free-electron-like band with an isotropic effective mass. This effective mass is taken larger than the free electron mass ($m = 4m_0$) to account for the narrow bands of the d-electrons. The difference in potential for spin-up and spin-down electrons must yield the correct bulk magnetic moment of the ferromagnetic material. The assumption of all s and d electrons in one single free-electron-like conduction band results in a much too high conductivity and therefore some believe that it is more realistic to neglect the potential differences (Zha95).

Moreover, the HF-model still contains one phenomenological spin-dependent parameter, S ($0 \leq S \leq 1$), that averages the effects of defects and impurities at the interfaces and the effects of geometrical roughness. In fact S denotes the degree of specular scattering ($S = 1 - D$) (see figure 3.5b). When $S = 1$, the reflection and transmission are determined completely by the potential difference between the various layers. It appears that the value of the GMR crucially depends on the value of S and moreover its spin-dependence. Thus the number of fitting parameters is larger than in the CB-model. Furthermore, as far as roughness is concerned, Hood, Falicov and Penn (Hoo94) just included the result found by Soffer (Eq. 3.19) in their S -parameter which is only correct for the limiting case of zero in-plane correlation length ($L = 0$). Physically of course it is difficult to imagine this limit as one would expect that the minimum value of L should be of the order of an atomic diameter ($\approx 2 \text{ \AA}$).

3.2.5 Approximations in the semiclassical models

In this section we will summarize the approximations made in the semiclassical model descriptions presented above. The first approximation is of course that we use a semiclassical theory which is not always allowed, but we will come back to this in section 3.3. At this point we will confine ourselves to remark that classical means that we think of electrons as pointlike particles and semi comes from the fact that we take into account Fermi-Dirac statistics and, in some models, quantum mechanical matching of wave functions at the interfaces and quantum mechanically evaluated scattering rates.

Semiclassical models are based on the BT-equation which is usually written in the form of equation (3.5). To obtain this equation we have only used the first term of a Taylor series to arrive at equation (3.1). Furthermore we have neglected the term in the BT-equation arising from the magnetic field ($\vec{v} \times \vec{B}$) since this results in effects much smaller than discussed here (Cam89, Bar90). Next, the BT-equation is solved in the relaxation time approximation. This approximation assumes that the distribution function f does not influence the rate at which an electron experiences collisions or the distribution function emerging from collisions, which is actually not true. However, it can be shown (Ash76) that the relaxation time approximation provides the same description as the full BT-equation when applied to an isotropic metal with isotropic elastic impurity scattering when the impurities are distributed homogeneously in the metal. This seems to be the assumption generally made to solve the BT-equation in literature.

The semiclassical theory treats the conduction electrons as a free electron gas. Often the Fermi-velocity is taken constant throughout the whole multilayer, thereby neglecting potential differences between different materials. When, like in the HF-model potential differences are taken into account, other assumptions are made to calculate these potentials that are at least also questionable.

Reflection and transmission at the interfaces are described in many different ways, depending for instance on the fact if one takes into account potential differences. The CB-model, in its most simple form, applied to a spin valve structure, assumes completely diffuse scattering at the outer boundaries, introduces an angle (of incidence) independent, purely phenomenological transmission parameter T at the interfaces, and neglects specular reflection at the interfaces or outer boundaries. In more sophisticated versions the interfaces are described for instance by thin layers in which the mean free path is strongly reduced. (Joh91).

The semiclassical models discussed in this thesis adopt an isotropic mean free path independent of the film thickness within the bulk of the layers. To quantitatively fit experimental data however also grain boundary scattering should be taken into account. Within the semiclassical approach Dieny (Die91)

introduces therefore an anisotropic mean free path where λ_{\perp} is different from λ_{\parallel} (\perp and \parallel here refer to perpendicular and parallel to the film plane). In addition grain boundary scattering may give rise to a mean free path that depends on the film thickness, see for instance Rijks *et al.* (Rij95).

Finally we have made a clear distinction between spin-up and spin-down electrons and we assumed that this spin-direction is not changed by the scattering process. This is only allowed at low temperatures where electron-magnon scattering resulting in spin-flips is absent. However, even at these low temperatures a residual spin-flip scattering will exist due to spin-orbit coupling.

In view of all this it won't be surprising that we can not interpret fits with the CB-model in a fully quantitative manner. A well known fact is for instance that when the parameters are adjusted to fit the MR-ratio $\Delta R/R_p$, the conductivity found is often too high (Bar91, Die93a, Lev90). In spite of all these approximations and neglects, however, the most simple form of the CB-model appears already to be suitable to, at least qualitatively, describe experimental data very well as long as we are not dealing with extremely thin layers where we certainly have to use a fully quantum mechanical model. This seems to justify all of the approximations and explains why the model is used so often. In the next section we will simplify the CB-model equations to obtain analytic expressions that do provide insight in the influence of the various parameters and still preserve the correct qualitative behavior.

3.3 Analytical approach to the CB-model

In this section we will derive simple (approximate) analytical expressions for the layer thickness dependence of the current density J , the conductance G , and the difference $\Delta G = G_p - G_{ap}$. These expressions are then used to obtain some qualitative feeling of the influence of, for instance, the outer boundaries, or the difference between bulk and interface spin-dependent scattering on the local current density. We will qualitatively show how input parameters like transmission T or diffusive scattering D act different on different electrons (spin-up, spin-down, +, and -), and what parts of a specific multilayer structure contribute to the GMR effect.

3.3.1 Derivation of analytical expressions for the GMR effect

As a starting point we use equation (3.22). In this equation we insert the general solution for the g -function that is now split up for \uparrow and \downarrow electrons which results in an extra factor $\frac{1}{2}$ compared to equation (3.7):

$$g_{\pm}^{\uparrow\downarrow} = -\frac{1}{2} e E_x \tau v_x \frac{\partial f_0}{\partial \varepsilon} \times \left[1 + F_{\pm}^{\uparrow\downarrow} \exp\left(\frac{\mp z}{\tau |v_z|}\right) \right] \quad (3.24)$$

To solve equation 3.22 we make use of spherical coordinates with $v_x = v \sin \beta \cos \phi$ and $v_z = v \cos \beta$. Furthermore we make a transition from an integral over velocity to an integral over energy inserting:

$$d^3 v = v^2 \sin \beta dv d\beta d\phi \text{ where } dv = d\varepsilon / mv$$

Inserting all this in equation (3.22) results in:

$$J_x(z) = -\frac{e^2 \tau E_x m^2}{8\pi^3 \hbar^3} \iiint \sum_{+,-,\uparrow,\downarrow} v^3 \sin^3 \beta \cos^2 \phi \frac{\partial f_0}{\partial \varepsilon} \left[1 + F_{\pm}^{\uparrow\downarrow} \exp\left(\frac{\mp z}{\tau v \cos \beta}\right) \right] d\varepsilon d\beta d\phi \quad (3.25)$$

First we will integrate over the energy ε . To perform this integration we use:

$$-\int_0^{\infty} \Psi(\varepsilon) \frac{\partial f_0}{\partial \varepsilon} d\varepsilon = \Psi(\varepsilon_F) \quad (3.26)$$

which is a $T = 0$ K approximation. Hence equation (3.25) takes the form:

$$J_x(z) = \frac{e^2 E_x m^2 v_F^2}{8\pi^3 \hbar^3} \int_{\varphi=0}^{2\pi} \int_{\beta=0}^{\pi/2} \sum_{+,-,\uparrow,\downarrow} \lambda^{\uparrow\downarrow} \left[1 + F_{\pm}^{\uparrow\downarrow} \exp\left(\frac{\mp z}{\lambda^{\uparrow\downarrow} \cos \beta}\right) \right] \sin^3 \beta \cos^2 \phi d\beta d\phi =$$

$$J_x(z) = \frac{e^2 E_x m^2 v_F^2}{8\pi^2 \hbar^3} \int_{\beta=0}^{\pi/2} \sum_{+,-,\uparrow,\downarrow} \lambda^{\uparrow\downarrow} \left[1 + F_{\pm}^{\uparrow\downarrow} \exp\left(\frac{\mp z}{\lambda^{\uparrow\downarrow} \cos \beta}\right) \right] \sin^3 \beta d\beta \quad (3.27)$$

where we also used the definition of the mean free path $\lambda^{\uparrow\downarrow} \equiv v_F \tau^{\uparrow\downarrow}$. Equation (3.27) is the final equation that has to be solved in the CB-model after $F_{\pm}^{\uparrow\downarrow}$ is calculated from the boundary conditions.

To obtain analytical expressions we have to make an additional approximation to dispose of the $\cos \beta$ term in the exponent and its pre-factor $F_{\pm}^{\uparrow\downarrow}$. At this moment we simply replace $\cos \beta$ by a fixed averaged value γ ($0 < \gamma \leq 1$), and later we will try to determine an appropriate value for this γ . In fact, $\lambda \cos \beta$ (or $\gamma \lambda$) denotes the distance from an interface in which the current density deviates from the bulk value. Since electrons move in various directions due to their Fermi velocity, the averaged value of this distance will be smaller

than λ . When we have inserted $\cos \beta = \gamma$, we can perform the integration² over β yielding $2/3$. This results in the following approximate analytical expression for the z -dependent current density :

$$J_x(z) = \frac{e^2 E_x m^2 v_F^2}{12\pi^2 \hbar^3} \sum_{+, -} \sum_{\uparrow, \downarrow} \lambda^{\uparrow, \downarrow} \left[1 + F_{\pm}^{\uparrow, \downarrow} \exp\left(\frac{\mp z}{\gamma \lambda^{\uparrow, \downarrow}}\right) \right] \quad (3.28)$$

Next we will define a "local conductance" as a function of z position for up and down, + and - electrons separately, yielding:

$$G_{\pm}^{\uparrow, \downarrow}(z) = \frac{e^2 m^2 v_F^2}{12\pi^2 \hbar^3} \lambda^{\uparrow, \downarrow} \left[1 + F_{\pm}^{\uparrow, \downarrow} \exp\left(\frac{\mp z}{\gamma \lambda^{\uparrow, \downarrow}}\right) \right] = \quad (3.29)$$

$$C_0 \lambda^{\uparrow, \downarrow} \left[1 + F_{\pm}^{\uparrow, \downarrow} \exp\left(\frac{\mp z}{\gamma \lambda^{\uparrow, \downarrow}}\right) \right]$$

3.3.2 Validity of the analytical expressions

First of all we note that the exponent in equation (3.28) comes from boundary conditions. This exponent disappears for the case of bulk materials where there are no boundaries and the current density does not depend on z , or, in a thin film, for the case of complete specular reflection which means that $F_{\pm}^{\uparrow, \downarrow} = 0$. For these cases we obtain:

$$\frac{J_x}{E_x} = \frac{e^2 m^2 v_F^2}{6\pi^2 \hbar^3} (\lambda^{\uparrow} + \lambda^{\downarrow}) \quad (3.30)$$

which is the correct Drude expression for the bulk conductivity (see Eqs. 3.15 and 3.16).

Next, we will calculate the conductivity for a single nonmagnetic layer with thickness d , electron mean free path λ , and diffuse scattering at the outer boundaries. According to our analytical model the conductivity is given by:

$$\frac{\sigma}{\sigma_0} = 1 + \frac{\gamma}{k} \left[\exp\left(-\frac{k}{\gamma}\right) - 1 \right] \quad (3.31)$$

² When we take $\cos \beta = \gamma$, $\sin^3 \beta$ is in principle also a constant. We prefer, however, to make only the approximation $\cos \beta = \gamma$ in the exponent, and perform the integration, yielding $\int \sin^3 \beta d\beta = 2/3$, because this results in the correct bulk conductivity.

where $k = d/\lambda$. In figure 3.8 we have compared the conductivity, calculated with our analytical expression, to the conductivity calculated with the CB-model. In this calculation we assumed $\gamma = 3/8$, since for this value our analytical expression reduces to the well known Fuchs-Sondheimer expression for large k : $\sigma/\sigma_0 = 1 - 3/8k$. Indeed we conclude that for this value for γ , the conductivity according to our analytical expression agrees very well with the results of the CB-model.

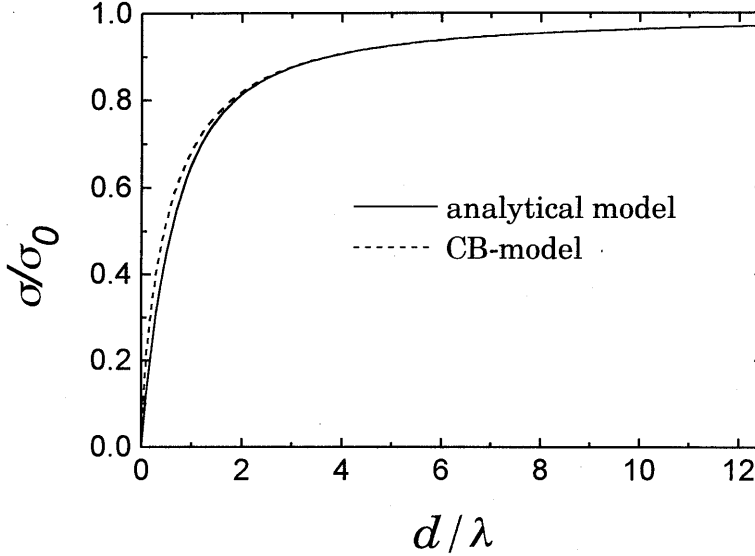


Figure 3.8: Conductivity of one single magnetic layer calculated with our analytical expression (Eq. 3.31) with $\gamma = 3/8$, compared to the conductivity calculated with the CB-model.

Finally we will investigate the quantity $\Delta G = G_p - G_{ap}$ as a function of spacer layer thickness and magnetic layer thickness. Of course, we can also write down an analytical expression for the conductivity and GMR ratio ($\Delta G/G_{ap}$). For the case of a trilayer system the conductivity is, however, already a sum of twelve terms that does not provide much information. Therefore we will confine ourselves here to derive an analytical expression for ΔG only, that *does* provide insight in the role of the various parameters. When we compare the results of our analytical approach with the CB-model, however, we will consider both ΔG and the GMR ratio. Although we used $\gamma = 3/8$ to calculate the conductivity of a single film, we will learn in chapter 7 that for an analytical approach of the quantity ΔG , a somewhat larger value of γ , $\gamma = 1/2$, yields a better description. Therefore we have taken $\gamma = 1/2$ in the following calculations. We will perform the calculation for a trilayer $d_{m1} \text{ \AA} M/d_{nm} \text{ \AA} NM/d_{m2} \text{ \AA} M$ where M is a magnetic layer and NM

is a nonmagnetic layer. At the outer boundaries of the trilayer completely diffusive scattering is assumed ($D^\sigma = 1$). We neglect specular reflections at the interfaces such that the only interface parameters are T^σ and D^σ with $D^\sigma = 1 - T^\sigma$. First we will assume that there is interface spin-dependent scattering ($T^\uparrow \neq T^\downarrow$), but *no* bulk spin-dependent scattering ($\lambda^\uparrow = \lambda^\downarrow = \lambda_m$). In that case the analytical approach with $\gamma = 1/2$ yields:

$$\Delta G_{\text{int}} = C_0 \lambda_m^2 \exp\left(-\frac{2d_{nm}}{\lambda_{nm}}\right) (T^\uparrow - T^\downarrow)^2 \prod_{i=1,2} \left[1 - \exp\left(-\frac{2d_{mi}}{\lambda_m}\right)\right] \quad (3.32)$$

Next, we will assume that there is *only* bulk spin-dependent scattering ($\lambda^\uparrow \neq \lambda^\downarrow$) and *no* interface (spin-dependent) scattering ($T^\uparrow = T^\downarrow = 1$). This yields:

$$\Delta G_{\text{bulk}} = C_0 \exp\left(-\frac{2d_{nm}}{\lambda_{nm}}\right) \prod_{i=1,2} \left\{ \lambda^\uparrow \left[1 - \exp\left(-\frac{2d_{mi}}{\lambda^\uparrow}\right)\right] - \lambda^\downarrow \left[1 - \exp\left(-\frac{2d_{mi}}{\lambda^\downarrow}\right)\right] \right\} \quad (3.33)$$

For the case of interface spin-dependent scattering (Eq. 3.32), we have shown ΔG and the GMR ratio as a function of spacer layer thickness (d_{nm}) in figures 3.9a and 3.9c, and as a function of magnetic layer thickness (d_m), in figures 3.9b and 3.9d, respectively. For comparison we have also calculated ΔG and the GMR ratio using the CB-model (dashed lines in figure 3.9). Although the absolute value of $\Delta G_{\text{analytical}}$ is, in general, different from ΔG_{CB} , figure 3.9 shows again that their qualitative behavior is the same. Also the GMR ratio shows qualitatively the same behavior as within the CB-model. Since variations in ΔG according to the analytical approach occur on the same scale as according to the CB-model, the choice of $1/2\lambda$ in the exponent of equation (3.27) seems reasonable. Although not explicitly shown, there is also good agreement between the qualitative behavior of our analytical approach and the CB-model when assuming bulk spin-dependent scattering.

The advantage of the analytical expressions, (3.32) and (3.33), is that one can immediately recognize how the various parameters will influence ΔG . For instance, it is clear that ΔG decreases in an exponential-like way as a function of spacer layer thickness, d_{nm} . This is true when interface spin-dependent scattering is assumed as well as when bulk spin-dependent scattering is assumed. For this same reason Barthél my and Fert (Bar91) and Dieny *et al.* (Die94) have derived analytical expressions for the GMR ratio. To compare their results with our expressions, equations (3.32) and (3.33) should be divided by the conductance in the antiparallel (or parallel) situation, that is proportional to λd , when $d \gg \lambda$.

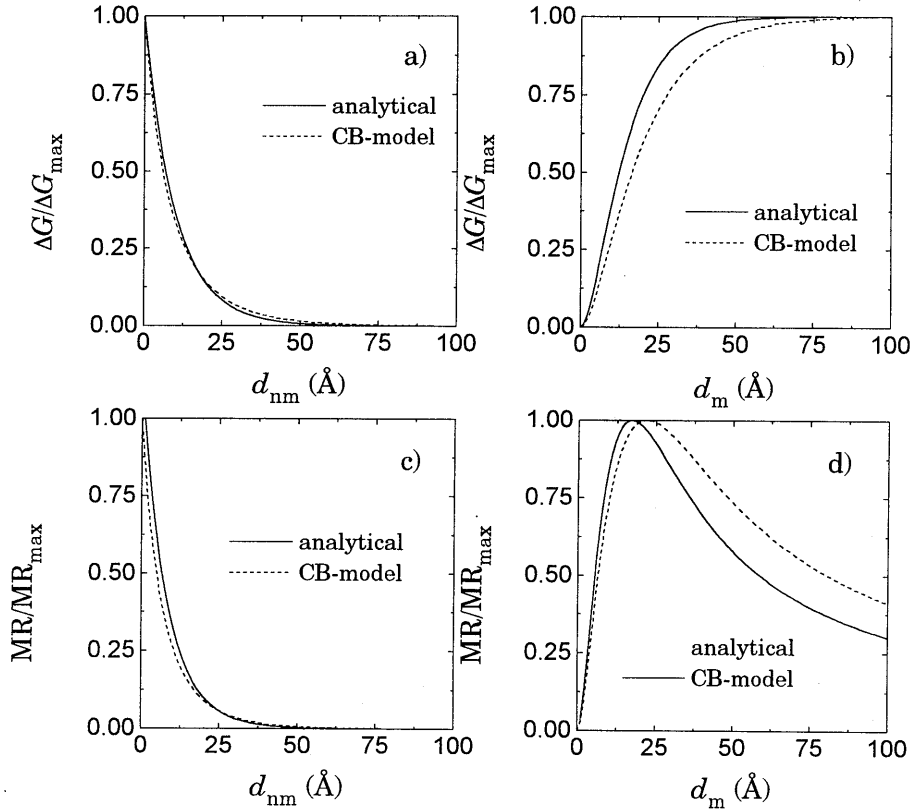


Figure 3.9: ΔG and GMR ratio for the case of only interface spin-dependent scattering, as a function of spacer layer thickness for $d_m = 25$ Å (a and c) and as a function of magnetic layer thickness for $d_{nm} = 25$ Å (b and d) calculated with equation (3.32) (solid lines) and with the CB-model (dashed lines).

Barthélemy and Fert calculated the ratio $\Delta R/R_{ap}$ for M/NM multilayers for the case of only spin-dependent interface scattering ($\lambda^\uparrow = \lambda^\downarrow = \lambda_m \equiv \lambda$). In agreement with our equation (3.32), they find that the GMR ratio is proportional to $(T^\uparrow - T^\downarrow)^2$. An analytical expression for the limiting case that $d_{nm} \gg \lambda$, yields an exponential decrease of the GMR ratio with d_{nm} as $\exp(-d_{nm}/\lambda)$. An analytical expression for the limiting case that $d_m \gg \lambda$, yields a decrease with d_m as λ/d_m . Both these results are consistent with our expressions apart from the factor $\frac{1}{2}\lambda$ instead of λ in the exponent.

Dieny presents two phenomenological expressions for the dependence of the GMR ratio of a trilayer on the magnetic layer thickness and nonmagnetic layer thickness, respectively:

$$\frac{\Delta R}{R}(d_m) = \left(\frac{\Delta R}{R}\right)_0 \left[1 - \exp\left(\frac{-d_m}{l_m}\right) \right] / \left(1 + \frac{d_m}{d_0} \right) \quad (3.34)$$

and

$$\frac{\Delta R}{R}(d_{nm}) = \left(\frac{\Delta R}{R}\right)_1 \left[\exp\left(\frac{-d_{nm}}{l_{nm}}\right) / \left(1 + \frac{d_{nm}}{d_0} \right) \right] \quad (3.35)$$

Here $(\Delta R/R)_{0,1}$ are constants that depend on the specific combination of magnetic and nonmagnetic layers and on the thicknesses of the layers that are not varied in thickness. d_0 is an effective thickness that represents the shunting of the current in all layers except the layer whose thickness is varied. In accordance with our expressions, Dieny (Die94) has proposed that for systems of practical interest $l_m \approx \frac{1}{2}\lambda_{\uparrow}$ (λ_{\uparrow} represents the longer of the two mean free paths λ^{\uparrow} or λ^{\downarrow}) and $l_{nm} \approx \frac{1}{2}\lambda_{nm}$, because an electron only "sees" an effective layer thickness $d/\cos\theta$ (θ is the angle between the electron velocity and the normal to the plane of the layers). Without going into further detail, we note that, for $l = \frac{1}{2}\lambda$, equations (3.34) and (3.35) contain similar terms like $\exp(-2d_{nm}/\lambda_{nm})$ and $[1 - \exp(-2d_m/\lambda^{\uparrow(\downarrow)})]$ as in our analytical expressions, and contain more or less the same physical information. This will be the central item in chapter 7.

It is important to realize that equations (3.32) and (3.33), and also the analytical expressions derived by Barthél my and Dieny, only provide a model behavior, but that in a real system other aspects play an important role. For instance, equations (3.32) and (3.33) imply that ΔG is maximal for zero spacer thickness, $d_{nm} = 0$. In reality, of course, a restriction on the allowed thickness d_{nm} , is the condition of antiparallel alignment in the absence of a magnetic field. Note also that ΔG is saturated for magnetic layers as thick as possible. However, since the conductance itself increases with the layer thickness, it is easy to imagine that there will be an optimum thickness to maximize the GMR ratio ($\equiv \Delta G/G_{ap}$), as is shown in figure 3.9d.

3.3.3 A study of the local conductance, $G(z)$

The analytical expressions of the local conductance, $G(z)$, for spin-up, spin-down, +, and - electrons separately (Eq. 3.29) enables us to investigate how an interface or boundary acts on the various electrons, and how these electrons

contribute to the conductance in the various layers. In this section it will become clear which parts of a trilayer structure contribute (most) to the GMR effect. In other words, we will show the *local* difference $G_p(z) - G_{ap}(z) \equiv \Delta G(z)$, which is the *local* contribution to the GMR effect. The total GMR effect can be calculated by integrating $\Delta G(z)$ over z , yielding equations like (3.32) and (3.33).

We will calculate the local conductance for a trilayer system $25 \text{ \AA} \text{ M} / 25 \text{ \AA} \text{ NM} / 25 \text{ \AA} \text{ M}$, for the two extreme cases of interface spin-dependent scattering or bulk spin-dependent scattering. As in the previous section we assume complete diffusive scattering at the outer boundaries. At the interfaces the transmission coefficients are given by T^\uparrow and T^\downarrow . As is common in the CB-model the reflection coefficient R is neglected such that the diffuse interface scattering is given by: $D^{\uparrow(\downarrow)} = 1 - T^{\uparrow(\downarrow)}$.

1) interface spin-dependent scattering:

In this specific example, where all three layers have identical thickness ($d_{m1} = d_{nm} = d_{m2} = 25 \text{ \AA}$) we assumed no bulk spin-dependent scattering ($\lambda^\uparrow = \lambda^\downarrow \equiv \lambda_m = 20 \text{ \AA}$). The mean free path in the spacer was chosen identical to λ_m , thus $\lambda_{nm} = 20 \text{ \AA}$. At the magnetic/nonmagnetic interfaces we assumed a maximum scattering asymmetry between spin-up and spin-down electrons defined by $T^\uparrow = 1$ and $T^\downarrow = 0$. In figure 3.10 we show the *local* conductance split up for \uparrow and \downarrow , + and - electrons for both cases where the magnetization directions are aligned parallel (a, b, c, and d) and antiparallel (e, f, g, and h). In these figures the \uparrow electrons have their spin parallel to the magnetization direction in the first magnetic layer, $0 \leq z \leq 25 \text{ \AA}$.

What is observed in these figures is that each time when electrons are scattered diffusely, at the outer boundaries or at the interfaces, the *local* conductance for these electrons drops to zero. Thereafter it increases exponentially with a characteristic length of the order of half the mean free path, $\frac{1}{2}\lambda = 10 \text{ \AA}$, in each layer for all electrons. In figure 3.10 (i) and (j) we carried out the summation over + and - electrons yielding the total *local* conductance for \uparrow and \downarrow electrons for the parallel and antiparallel alignment respectively. Finally in figure 3.10 (k) the contributions from the \uparrow and \downarrow electrons were added up to obtain the total *local* conductance in parallel and antiparallel alignment. The black area in the lower half of this plot indicates the local difference $\Delta G(z) = G_p(z) - G_{ap}(z)$. Clearly for this case the spin-dependent scattering results only in a difference in local conductance (current density) within the magnetic layers. When the quantities in figure 3.10 (k) are integrated over the thickness of the trilayer, we obtain the macroscopical conductance for parallel (G_p) and antiparallel (G_{ap}) alignment as well as (black area) their difference $\Delta G \equiv G_p - G_{ap}$.

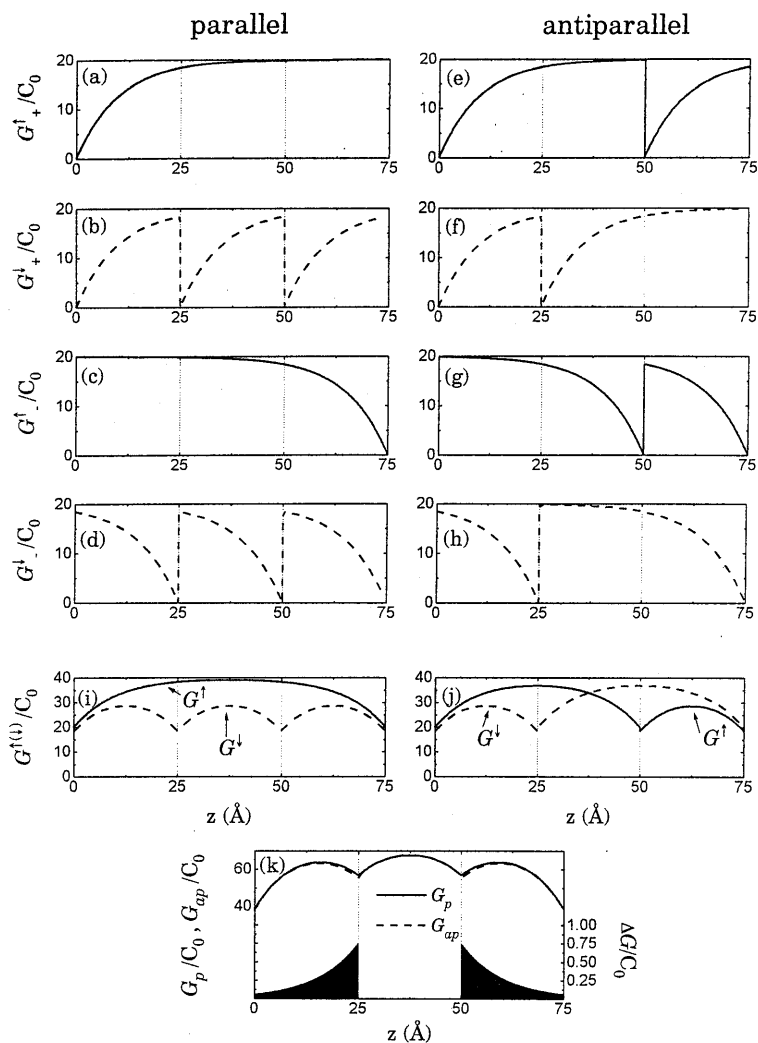


Figure 3.10: Local conductivities as a function of position in the trilayer $25 \text{ \AA} M_1/25 \text{ \AA} NM/25 \text{ \AA} M_2$ where at the interfaces maximum spin-dependent scattering is assumed ($T^\uparrow = 1$, $T^\downarrow = 0$) and in the bulk no spin-dependent scattering ($\lambda = 20 \text{ \AA}$ throughout the whole trilayer). First the contributions from $(+\uparrow)$, $(+\downarrow)$, $(-\uparrow)$, and $(-\downarrow)$ electrons are calculated separately for parallel (a, b, c, and d) and antiparallel (e, f, g, and h) magnetization directions. Then in i) and j) the summation over $+$ and $-$ is performed, and finally in k) the summation over \uparrow and \downarrow is performed, yielding the total local conductivity. The black area in k) denotes the local difference between the parallel and antiparallel magnetization configuration.

At this point we would like to remark that to obtain a large GMR ratio, spin-dependent scattering alone is not enough. For instance imagine the example of figure 3.6 (k) with extremely thin magnetic layers. Although this does not affect the spin-dependent scattering at the interfaces, the diffuse scattering at the outer boundaries restricts the region where $\Delta G(z) \neq 0$ to a very small area. In fact the boundaries cut off the black area representing the total change of sheet conductance ΔG . Thus, to optimize ΔG it is necessary not only to have spin-dependent scattering, but also to have a region where the local conductance may be different between parallel and antiparallel magnetization directions. Later, in figure 3.12 we will demonstrate that this region not necessarily has to be a magnetic layer.

2) bulk spin-dependent scattering:

In figure 3.11 we show the *local* conductance split up for \uparrow and \downarrow , + and - electrons for both cases where the magnetization directions are aligned parallel (a, b, c, and d) and antiparallel (e, f, g, and h). In these figures the \uparrow electrons have their spin parallel to the magnetization direction in the first magnetic layer, $0 \leq z \leq 25 \text{ \AA}$. In this specific example, where all three layers have identical thickness ($d_{m1} = d_{nm} = d_{m2} = 25 \text{ \AA}$) we assumed no interface scattering ($T^\uparrow = T^\downarrow = 1$). In the magnetic layers the mean free path was chosen spin-dependent now ($\lambda^\uparrow = 20 \text{ \AA}$ and $\lambda^\downarrow = 2 \text{ \AA}$). The mean free path of the electrons in the spacer layer was chosen equal to λ^\uparrow , thus $\lambda_{nm} = 20 \text{ \AA}$.

What is observed in these figures is that whenever the electrons are diffusely scattered at the outer boundaries, their *local* conductance drops to zero as in the previous case. Inside the magnetic layers in this case, the *local* conductance of the \downarrow electrons is, of course, smaller than for the \uparrow electrons. At the interfaces, where an electron enters an other layer, the conductivity changes to the value belonging to that layer via an exponential growth or decay with a characteristic length of the order of half the mean free path in the layer ($\frac{1}{2}\lambda = 1 \text{ \AA}$ for \downarrow electrons and $\frac{1}{2}\lambda = 10 \text{ \AA}$ for \uparrow electrons). Again in figure 3.11 (i) and (j), the contributions of + and - electrons are added, and in figure 3.11 (k) the total *local* conductance is shown for parallel and antiparallel alignment and the black area represents $\Delta G(z)$. As in the previous case there is only a contribution to the GMR effect in the magnetic layers because only there $\Delta G(z) \neq 0$. This is caused by the fact that we have neglected specular reflections ($R = 0$). In our next and final example we will show that also in a nonmagnetic layer it is possible that $\Delta G(z) \neq 0$.

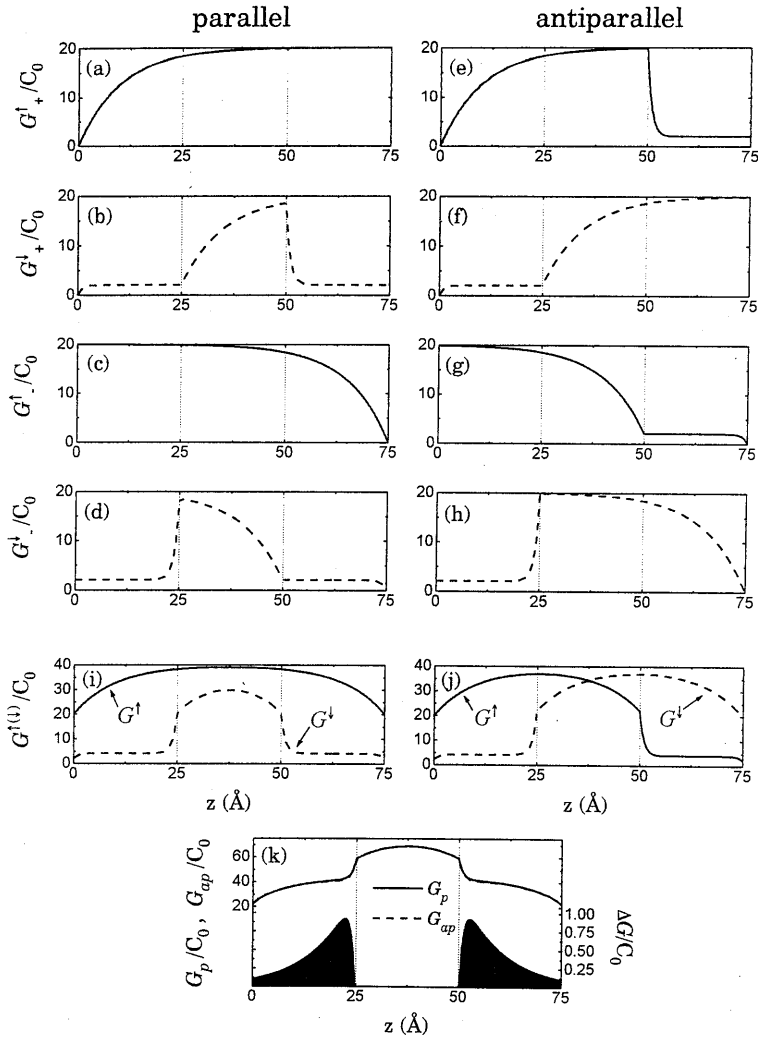


Figure 3.11: Local conductivities as a function of position in the trilayer $25 \text{ \AA} M_1/25 \text{ \AA} \text{ NM}/25 \text{ \AA} M_2$ where in the bulk large spin-dependent scattering is assumed ($\lambda^\uparrow = 20 \text{ \AA}$, $\lambda^\downarrow = 2 \text{ \AA}$ and in the spacer $\lambda = 20 \text{ \AA}$) and at the interfaces no spin-dependent scattering ($T^\uparrow = T^\downarrow = 1$). First the contributions from $(+\uparrow)$, $(+\downarrow)$, $(-\uparrow)$, and $(-\downarrow)$ electrons are calculated separately for parallel (a, b, c, and d) and antiparallel (e, f, g, and h) magnetization directions. Then in i) and j) the summation over $+$ and $-$ is performed, and finally in k) the summation over \uparrow and \downarrow is performed, yielding the total local conductivity. The black area in k) denotes the local difference between the parallel and antiparallel magnetization configuration.

3) with a nonmagnetic "back layer"

As a final case we will calculate the local conductance for the system: $25 \text{ \AA} \text{ M}/25 \text{ \AA} \text{ NM}_1/25 \text{ \AA} \text{ M}/25 \text{ \AA} \text{ NM}_2$, where M represents a magnetic layer and $\text{NM}_{1,2}$ nonmagnetic layers. Again we will assume perfectly diffuse scattering at the outer boundaries. We will refer to NM_1 as the spacer layer and to NM_2 as the back layer. Again we will assume a maximum interface asymmetry $T^\uparrow = 1$ and $T^\downarrow = 0$. The mean free paths are taken equal in each layer for each spin-direction ($\lambda^\uparrow = \lambda^\downarrow = \lambda = 50 \text{ \AA}$), thus there is no bulk spin-dependent scattering.

Again figures 3.12 (a)-(d), (e)-(h) show the local conductance for \uparrow , \downarrow , $+$, and $-$ electrons for the parallel and antiparallel configuration respectively. Whenever the electrons are scattered diffusely, at the outer boundaries or at the interfaces, their local conductance drops to zero, and then increases exponential to the bulk value, with a characteristic length of 25 \AA , defined by half the mean free path.

In figure 3.12 (k) the total local conductance in the parallel, $G_p(z)$, and antiparallel, $G_{ap}(z)$, configuration is shown as well as their local difference (black area), $\Delta G(z)$. This specific structure is chosen to demonstrate that even in a nonmagnetic layer there may be a difference in the *local* conductance between parallel or antiparallel alignment of the magnetic layers, as is shown in the back layer. We will utilize this feature in chapter 8. A necessary condition to achieve this is that these layers can be reached by electrons that have travelled through at least two magnetic layers without being diffusely scattered. Since the outer boundaries in our calculations scatter all electrons diffuse this condition is not satisfied for the spacer layer. However, when we would allow specular reflections ($R \neq 0$), which means that electrons that have crossed the spacer once can reach the spacer again without being diffusely scattered, there would be a $\Delta G(z) \neq 0$ also in the spacer.

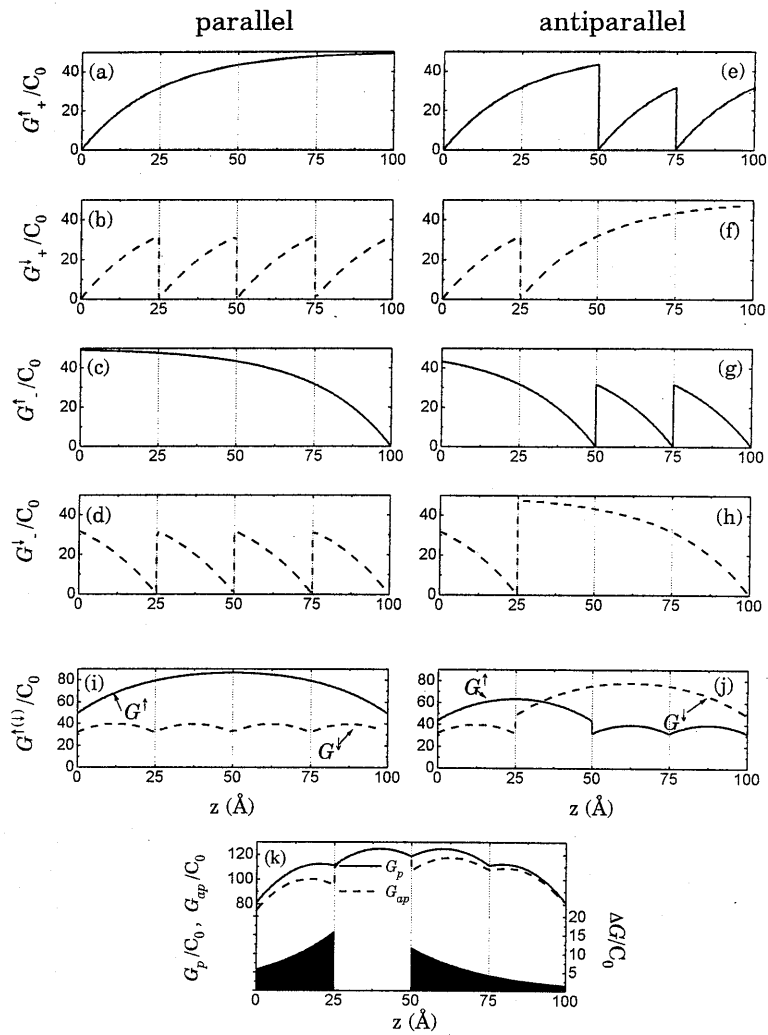


Figure 3.12: Local conductivities as a function of position in the structure $25 \text{ \AA} \text{ M}/25 \text{ \AA} \text{ NM}_1/25 \text{ \AA} \text{ M}/25 \text{ \AA} \text{ NM}_2$ where at the interfaces maximum spin-dependent scattering is assumed ($T^\uparrow = 1$, $T^\downarrow = 0$) and in the bulk no spin-dependent scattering ($\lambda = 50 \text{ \AA}$ throughout the whole trilayer). First the contributions from $(+\uparrow)$, $(+\downarrow)$, $(-\uparrow)$, and $(-\downarrow)$ electrons are calculated separately for parallel (a, b, c, and d) and antiparallel (e, f, g, and h) magnetization directions. Then in i) and j) the summation over $+$ and $-$ is performed, and finally in k) the summation over \uparrow and \downarrow is performed, yielding the total local conductivity. The black area in k) denotes the local difference between the parallel and antiparallel magnetization configuration.

3.4 Quantum mechanical models

When the layer thicknesses decrease, at some point a semiclassical description is no longer allowed and we should invoke the help of quantum mechanics. In general a quantum mechanical model is necessary

1. when it is no longer allowed to neglect quantization of electron momentum in the z-direction, k_z , due to the finite size of the samples in the z-direction. Quantization of k_z becomes important when A) $k_F d \leq 1$ where k_F is the Fermi wavevector³ and d is the layer thickness or B) when the mean free path λ is much larger than the layer thickness d .
2. in case of strong scattering. These effects become important when $k_F \lambda \leq 1$ where λ is the electron mean free path. This means that the description of an electron as a point particle is no longer valid.

For example, consider a thin film with thickness d and diffusely reflecting boundaries. For a very pure sample, in the limit that the (impurity) mean free path λ goes to infinity, semiclassical theory predicts that the conductivity also goes to infinity as $\sigma \propto d \ln(\lambda/d)$. This implies that in the absence of bulk scattering, the scattering due to boundary roughness does not result in any resistance, which is a non-physical result. Tesanovic *et al.* (Tes86) showed from a quantum mechanical approach that interface roughness in this case induces resistance even for electrons that travel almost parallel to the boundaries. This is caused by the quantization of k_z . Zhang and Butler (Zha95) recently showed that also a semiclassical model can be used to describe a thin layer in a correct way when an angle dependent specular parameter p is assumed at the boundaries and a cut-off angle of the incidence of electrons on the boundaries is introduced. Rijks (Rij96) has shown that the cut-off angle θ_C necessary to take the quantum-size effect into account is given by $\theta_C = \arccos(\pi/2dk_F)$, which effectively means that states with $|k_z| \leq \pi/2d$ are forbidden. This seems to be the most important effect of the k_z -quantization.

We will now briefly review some quantum mechanical models for the description of electrical transport phenomena in magnetic multilayers and spin valves. Quantum mechanical models, based on the Kubo-formalism, are given by Vedyayev (Ved92, Ved93), Camblong and Levy (CL) (Cam92, Cam95), and Levy, Zhang, and Fert (LZF) (Lev90, Zha92).

The quantum model of Vedyayev takes into account bulk spin-dependent scattering and spin-dependent potential barriers between successive layers. It also includes quantization of k_z . This model is used to fit experimental data on NiFe/Cu/NiFe/FeMn exchange-biased spin valves (Ved92). These spin valves

³ Since for the metallic structures that we consider in this thesis λ_F is only a few Å, we do not expect to be in the quantum mechanical limit where the layer thickness or electron mean free path is smaller than λ_F .

were chosen since a fit on the same data according to the Camley-Barnas model (Die93) had revealed earlier that in NiFe/Cu spin valves the spin-dependent scattering occurs only in the NiFe-bulk with $\lambda_{\text{NiFe}}^{\uparrow} = 110 \text{ \AA}$, $\lambda_{\text{NiFe}}^{\downarrow} = 10 \text{ \AA}$, and $\lambda_{\text{Cu}} = 215 \text{ \AA}$. The Vedyayev model, when potential steps at the interfaces are neglected, results in only slightly higher mean free paths with $\lambda_{\text{NiFe}}^{\uparrow} = 120 \text{ \AA}$, $\lambda_{\text{NiFe}}^{\downarrow} = 13 \text{ \AA}$, and $\lambda_{\text{Cu}} = 215 \text{ \AA}$. This is a direct consequence of the k_z -quantization that forbids electrons to travel (almost) parallel to the interfaces ($|k_z| \leq \pi/2d$). This of course reduces the conductivity and has in a model description to be compensated by the increase in mean free path. In view of the parameters found here, there seems to be no need to prefer the quantum model above the Camley-Barnas model.

The quantum model of Camblong and Levy incorporates also interface spin-dependent scattering. Bulk and interface spin-dependent scattering are accounted for in a unified way by treating the interfaces as additional thin layers, representing regions of interdiffusion, with a small mean free path, similar to Johnson and Camley (Joh91). In this approach transmission coefficients at the interface become angle dependent in a natural way. Although the model of Camblong and Levy is a quantum model, based on the Kubo formula in real space, approximations are made that are only allowed in the quasiclassical limit, i.e. when $L \gg \lambda^{\uparrow(\downarrow)} \gg \lambda_F$ where L is the total thickness of the structure, $\lambda^{\uparrow(\downarrow)}$ the mean free path of the conduction electrons and λ_F their Fermi wavelength. Thus the final result is quasiclassical again and agrees with results derived from the Boltzmann approach.

A third quantum model, which uses the Kubo formula in reciprocal space, is from Levy, Zhang and Fert (LZF). This model has only been applied to the case of an infinite multilayer. Also in this model approximations are made to obtain a simple expression for the conductivity, which limits the validity of the model as we will see in the next paragraph.

Zhang and Butler (Zha95) have solved the Kubo formula exactly (numerically) for a free electron model with random point scatterers for the cases of a homogeneous system, a thin film, and a multilayer. They calculated for instance the conductivity of a multilayer as a function of total thickness of the multilayer period. The multilayer in their calculations has a period of two layers where the mean free path in the first layer is 36.0555 a.u. and in the second layer 360.555 a.u. (with 1 a.u. = 0.529 \AA), and the thickness of the first layer is twice that of the second. They also calculated the conductivity of the same multilayer according to Fuchs/Sondheimer, Camblong/Levy and LZF. In figure 3.13 this comparison between the exact calculation and the other models is reproduced. The Camblong/Levy model results in exactly the same conductivity as the Fuchs/Sondheimer model, and deviates from the exact solution only for thin layers where the quasiclassical approach is not allowed. The LZF model however, only gives correct results for very thin and very thick periods and is

never better than the quasiclassical approach. In fact, for intermediate thickness there is quite a large deviation between the exact solution and LZF. Therefore it seems unrealistic to apply this model for experimental sandwiches or spin valves.

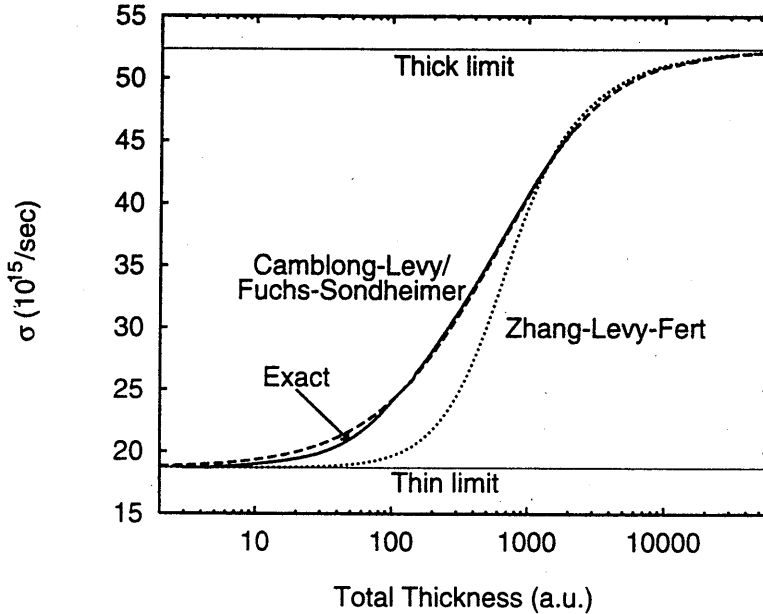


Figure 3.13: Conductivity as a function of the total thickness of a period for a periodic multilayer with a period of two layers and with mean free paths in each layer 36.0555 a.u. and 360.555 a.u., respectively. (1 a.u. = 0.529 Å.) The thickness of the first layer is twice that of the second. This figure has been reproduced from Zhang and Butler, (Zha95).

Finally we would like to mention here the quantum mechanical model of Barnas and Bruynseraede (Bar95, Bar96). This model investigates explicitly the influence of geometrical interface roughness that is described in terms of parameters η and L defined above. According to this model the GMR decreases as a function of L , but increases when η increases. The latter result seems to be in contradiction to the semiclassical model of Litvinov *et al.* (Lit97), who report a decrease of the GMR with increasing η . Experimental verification of these models however is extremely difficult since, although growth techniques have improved considerably over the past decades, it is still not possible to manipulate the interfaces in a controllable and reproducible way on the scale of a few Å.

In conclusion there seems to be no compelling reason at present to prefer a quantum mechanical model above a semiclassical model to describe the metallic

spin valves and multilayers of this thesis. However, also in any semiclassical model many approximations are made. In addition interface and boundary scattering are treated in various ways in the different semiclassical models, not all of which are realistic. Therefore the analysis of our experimental data within the Camley-Barnas semiclassical model is not meant to be fully quantitative. Qualitatively, however, this model is capable to describe our data very well.

3.5 CPP geometry

In this section we will briefly indicate the differences between the Current-In-Plane (CIP) geometry and the Current-Perpendicular-to-Plane (CPP) geometry. For a detailed overview of CPP magnetoresistance, theoretical as well as experimental, the reader is referred to (Gij97). The most essential difference is, of course, that in the CPP geometry the electrons have to travel through all the layers and all the interfaces, while in the CIP geometry there is no net electrical current in the z -direction. As a consequence spin accumulation effects will occur at the interfaces, that do not occur in the CIP geometry. This can best be explained in the following way. Imagine an interface between two ferromagnetic layers with opposite magnetization directions as is shown in figure 3.14. We assume that electrons with their spin parallel to the local magnetization direction experience less resistance than electrons with their spin antiparallel to the local magnetization direction. Furthermore, we define electrons with their spin parallel to the magnetization direction in the left magnetic layer as (+) electrons and electrons with their spin parallel to the magnetization direction in the right magnetic layer as (-) electrons. Far away from the interface, the current will then be carried mainly by (+) electrons in the left magnetic layers and by (-) electrons in the right magnetic layer. This means that the electron flux for electrons approaching the interface from the left is larger for the (+) electrons while the electron flux for electrons leaving the interface from the right is larger for (-) electrons. As a result there will be a spin accumulation of (+) electrons at the interface, as is shown in figure 3.14. This spin accumulation results in a spin-dependent contribution to the electrochemical potential.

The length to which the spin accumulation extends is determined by the spin diffusion length l_{sf} . This spin diffusion length is defined as:

$$l_{sf}^{-2} = (l^{\uparrow})^{-2} + (l^{\downarrow})^{-2} \quad (3.36)$$

with

$$l^{\uparrow(\downarrow)} = v_F \sqrt{\frac{\tau_{sf}}{3} \left(\frac{1}{\tau_{sf}} + \frac{1}{\tau^{\uparrow(\downarrow)}} \right)^{-1}} \approx v_F \sqrt{\tau_{sf} \tau^{\uparrow(\downarrow)} / 3} \quad (3.37)$$

where $\tau^{\uparrow(\downarrow)}$ is the relaxation time pertaining to scattering where the electron spin is conserved (impurities, defects), and τ_{sf} is the relaxation time pertaining to spin-flip scattering (magnons, spin-orbit). The total relaxation time τ for electrons with spin $\uparrow(\downarrow)$ is given by $1/\tau = 1/\tau_{sf} + 1/\tau^{\uparrow(\downarrow)}$. For nonmagnetic materials l_{sf} is given by: $l_{sf} = v_F(\tau_{sf}\tau^{\uparrow(\downarrow)}/6)^{1/2}$. At low temperatures, where electron magnon scattering is absent and the only spin-flip scattering is due to the spin-orbit coupling, l_{sf} can be a few 1000 Å for pure-metal systems (Gij97). Voegeli (Voe95) reported a l_{sf} of $l_{sf} > 600$ Å for Cu and $l_{sf} > 200$ Å for Co, measured in multilayered Co/Cu nanowires at $T = 4.2$ K, and Piraux (Pir96) reported a l_{sf} of $l_{sf} = 1400 \pm 150$ Å for Cu and $l_{sf} \approx 440$ Å for Co, measured in multilayered Co/Cu nanowires at $T = 77$ K. It appears that when $l_{sf} \gg d_m$ and d_{nm} , one can derive simple equations to calculate the GMR (Val93).

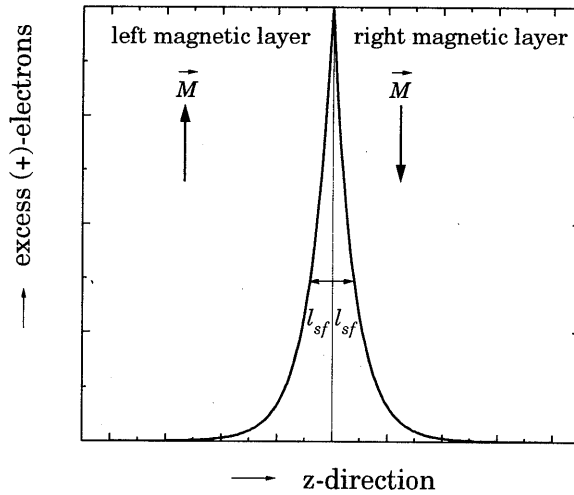


Figure 3.14: When a current is passed through the interface between two magnetic layers, there will be an accumulation of electrons at the interface. The accumulation decreases exponentially with the distance from the interface with a characteristic length l_{sf} the spin diffusion length.

We will now provide these simple equations that are usually used to describe the CPP magnetoresistance. First we will define two spin-asymmetry parameters, β and γ . β denotes the difference in resistivity between spin-up (ρ^{\uparrow}) and spin-down (ρ^{\downarrow}) electrons inside the magnetic layers and is given by:

$$\rho^{\uparrow(\downarrow)} = 2\rho_m^*[1-(+)\beta] \quad \text{or} \quad \frac{\rho^{\downarrow}}{\rho^{\uparrow}} = \frac{\lambda_m^{\uparrow}}{\lambda_m^{\downarrow}} = \frac{1+\beta}{1-\beta} \quad (3.38)$$

Here $\rho_m^* = \rho_m / (1 - \beta^2)$ with ρ_m the experimentally measurable resistivity of the magnetic layers. In nonmagnetic layers $\beta = 0$ and thus $\rho_{nm}^* = \rho_{nm}$. Analogous, γ denotes the difference for spin-up and spin-down electrons in the interface resistance $R_{m/nm}$ between the magnetic and nonmagnetic layers and is given by:

$$R_{m/nm}^{\uparrow(\downarrow)} = 2R_{m/nm}^* [1 - (+)\gamma] \quad \text{or} \quad \frac{R_{m/nm}^{\downarrow}}{R_{m/nm}^{\uparrow}} = \frac{1 + \gamma}{1 - \gamma} \quad (3.39)$$

where $R_{m/nm}^* = R_{m/nm} / (1 - \gamma^2)$.

The difference with CIP magnetoresistance is that in the limit where the individual layer thickness, d , is much smaller than l_{sf} , the two-current model of two independent spin-channels in parallel is applicable to the CPP geometry (Lee92, Val93). In that case, the resistances for parallel and antiparallel magnetization directions are given by:

$$R_{p(ap)} = \left(\frac{1}{R_{p(ap)}^{\uparrow}} + \frac{1}{R_{p(ap)}^{\downarrow}} \right)^{-1} \quad (3.40)$$

with

$$AR_p^{\uparrow(\downarrow)} = M \left\{ 2\rho_m^* [1 - (+)\beta] d_m + 2\rho_{nm}^* d_{nm} + 4AR_{m/nm}^* [1 - (+)\gamma] \right\} \quad (3.41)$$

$$R_{ap}^{\uparrow(\downarrow)} = \frac{R_p^{\uparrow} + R_p^{\downarrow}}{2} \quad (3.42)$$

where A (m^2) is the surface of the layers and M the number of bilayers M/NM .

As a final point we remark that in CPP geometry it is relatively easy, compared to CIP geometry, to separate bulk and interface contributions to the spin-dependent scattering. For this purpose equations (3.41) and (3.42) are combined to obtain:

$$A \sqrt{(R_{ap} - R_p) R_{ap}} = \beta \frac{d_m}{d_m + d_{nm}} \rho_m^* L + 2\gamma AR_{m/nm}^* M \quad (3.43)$$

where L is the total sample thickness, $L = M(d_m + d_{nm})$. When $\sqrt{(R_{ap} - R_p) R_{ap}}$ is measured as a function of the number of bilayers M (for constant L), there will be a linear dependence. β can be determined from the intercept with the vertical axis and γ follows from the slope, as is indicated in figure 3.15.

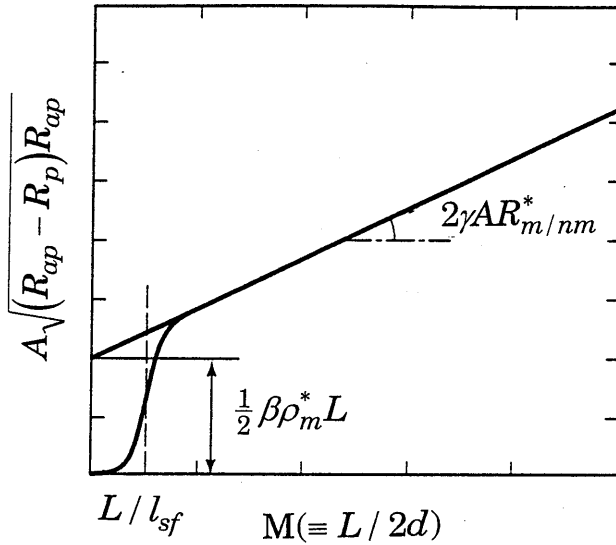


Figure 3.15: $\sqrt{(R_{ap} - R_p)R_{ap}}$ as a function of M , for constant L .

The thickness of the magnetic and nonmagnetic layer are chosen equal, $d_m = d_{nm} = d$, such that $M \equiv L/2d$. The parameters β and γ , that denote the spinasymmetry in the bulk and at the interfaces respectively, can be easily determined from the figure as is shown. Equations (3.41) and (3.42) are only valid in the limit where $l_{sf} \gg d$. When d increases, deviations from the linear dependence will occur when $M < L/l_{sf}$. Figure taken from Valet and Fert (Val93).

4. Magnetic and transport behavior of AF-coupled layers with a limited number of repetitions

The contents of this chapter is, in compressed form, published in the Symposium Proceedings of the Materials Research Society, Volume 313, p129 (1993).

4.1 Introduction

From around 1980 up to now, magnetic multilayers have been the subject of intensive investigation. Especially the (large) perpendicular anisotropy, oscillatory interlayer exchange coupling, and giant magnetoresistance, observed for some systems, have attracted much attention (Grü86, Bai88, Par90). Values for anisotropy constants (K) and the exchange coupling parameter (J) are often determined from transition and/or saturation fields of magnetization curves. However, this determination is not always a trivial calculation.

In general the quantities K and J can best be determined in systems with perpendicular (uniaxial) anisotropy. When a magnetic field is applied along the easy axis (perpendicular to the film plane), the layers will reverse their magnetization directions at well-defined fields due to the anisotropy. Such a sharp transition of the magnetization from one direction to the opposite direction is called a spin-flip transition. Thus the magnetization curves will show discrete steps at the fields where the magnetization direction of a magnetic layer reverses, contrary to the gradual rotation processes often observed in other systems. This simplifies the magnetization curves and in most cases their interpretation (Blo94).

Calculations of the magnetization (Die90, Fol91) and magnetoresistance (Fol91) for a sandwich containing two antiferromagnetic (AF) coupled magnetic layers with perpendicular anisotropy have been performed in two limiting cases. In one case the system is always in a state of absolute minimum energy. In this case the magnetization reversal will take place via domain wall motion and there are no energy barriers involved in the nucleation of domains or movement of domain walls. In the other case the system finds itself in a local energy minimum due to anisotropy and coupling induced energy barriers. In this case it is assumed in the calculation that each magnetic layer is *always* in a single domain state, and the magnetization reversal takes place by coherent rotation. Magnetization curves for both limiting cases are shown in figure 4.1 for different values of the anisotropy constant K . The solid line represents the single domain limit and the dashed line represents the case of absolute minimum energy and shows thus no hysteresis.

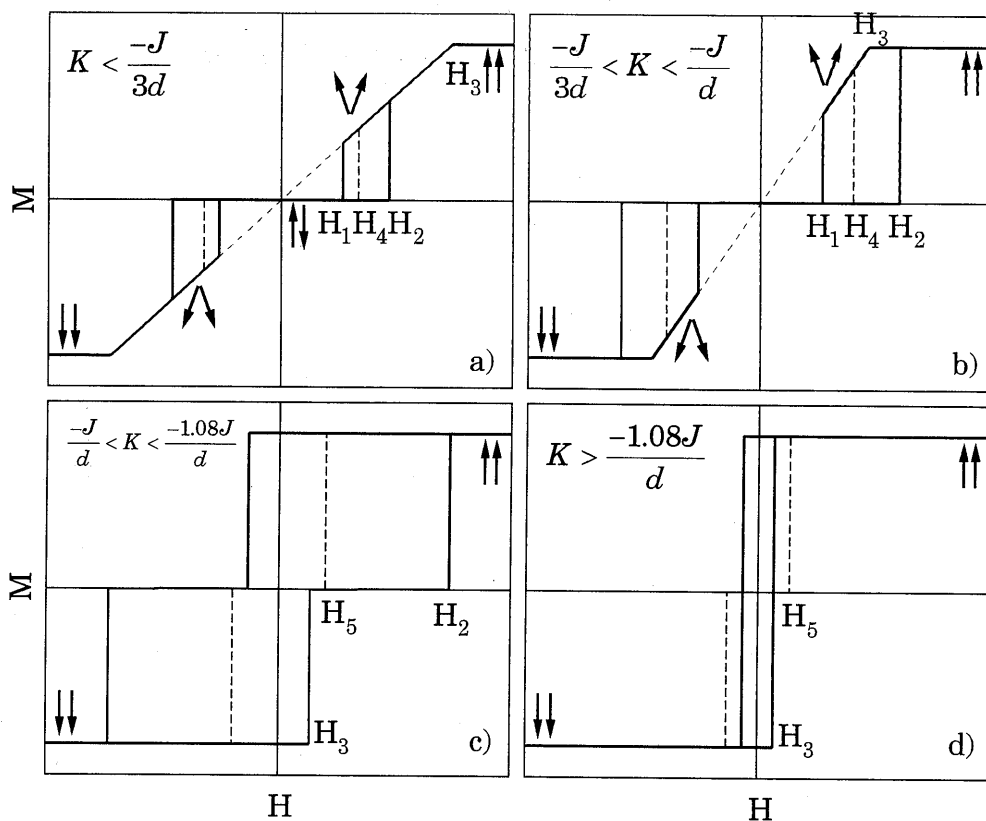


Figure 4.1: Schematic representation of two AF-coupled magnetic layers, each with thickness d , for different values of the anisotropy constant K compared to J/d . The solid lines represent the situation where the layers are always in a single domain state. The dashed lines represent the situation where the system is always in a state of absolute minimum energy. The arrows indicate the magnetization directions of the layers. The characteristic fields are given by ($J < 0$ for AF coupling):

$$(\mu_0 M_S H_1)^2 = 4K(K + J/d)^2 / (K - J/d);$$

$$H_2 = 2\sqrt{K(K - J/d)} / \mu_0 M_S; \quad H_3 = -2(K + J/d) / \mu_0 M_S;$$

$$H_4 = 2\sqrt{-K(K + J/d)} / \mu_0 M_S \quad \text{and} \quad H_5 = -J / \mu_0 M_S d$$

Measurements on AF coupled sandwiches with perpendicular anisotropy, however, show a wide variety of magnetization curves lying between the limiting curves of absolute minimum energy and coherent rotation (Blo92, Ben90). It is believed that the actual shape of the magnetization curve is also determined by lateral variations on a microscopic scale of the anisotropy and exchange inter-

actions, e.g. due to pinholes. Therefore the equations derived for the limiting cases are not applicable. In the case of a multilayer the finite number of repetitions can also play an important role in modifying the predictions given for the limiting cases.

To gain more insight in the magnetic behavior of such systems we have grown a series of multilayers with perpendicular anisotropy and AF-coupling. The number of layers was varied between 1 and 22. Magnetization loops have been measured with the Magneto Optical Kerr Effect (MOKE) as well as a Vibrating Sample Magnetometer (VSM). A capacitive torque magnetometer has been used to determine the magnetic anisotropy K . Magnetoresistance measurements have been performed at room temperature and at low temperature. A detailed investigation of the magnetization and magnetoresistance effect leads to an analysis within which it is possible to distinguish between the magnetization reversal and hysteresis of the individual layers. In the next sections we will show that K increases with the number of repetitions, that J increases when going from the bottom layer to the top layer, and that there is a clear distinction in the magnetoresistance between the magnetization reversal of an outer layer and that of an inner layer. The results of the measurements will be compared with theory.

4.2 The samples

The multilayers studied in this chapter were composed of $200 \text{ \AA Ru} + N \cdot (M + 8 \text{ \AA Ru}) + 22 \text{ \AA Ru}$. Here M is a magnetic layer composed of $M = 2 \text{ \AA Co} + 4 \cdot (3 \text{ \AA Co} + 6 \text{ \AA Pd}) + 5 \text{ \AA Co}$. The number of repetitions, N , varied from 1 to 22. All the samples were prepared at Philips Research Laboratories by means of HV-magnetron sputtering (see chapter 2). The multilayers were deposited at room temperature on oxidized silicon substrates. Prior to the 200 \AA Ru baselayer growth the substrates were given 30 min. glow-discharge treatment. The sputtering occurred at a background pressure of $7 \times 10^{-3} \text{ Torr}$ ($\approx 0.9 \text{ Pa}$). Before sputtering the sputtering chamber was evacuated to $4 \times 10^{-7} \text{ Torr}$ ($\approx 5 \times 10^{-5} \text{ Pa}$). The sputtering rates for Ru, Co, and Pd were 1, 2, and 3 \AA/s respectively.

Each magnetic layer M is composed of strongly ferromagnetically coupled Co layers using $(3 \text{ \AA Co} + 6 \text{ \AA Pd})$ as magnetic building blocks. Because of the well-known induced ferromagnetism in the Pd (near the Co) these building blocks act as single magnetic entities. It was shown earlier that Co/Pd multilayers show an easy axis perpendicular to the film plane for a Co thickness smaller than $\approx 8 \text{ \AA}$ (Car85, Bro87). Also Co/Ru multilayers exhibit a perpendicular easy axis for a Co-thickness smaller than $13\text{-}15 \text{ \AA}$ (Kes91, Oun92). The combination of Co/Pd multilayers and Ru spacer layers assures a large perpendicular anisotropy combined with a large magnetic moment. A comparable system has been used successfully before by Bloemen et al. (Blo92).

To assure large antiferromagnetic coupling between the magnetic layers we chose a spacer layer of 8 Å Ru. For this Ru thickness the coupling between two Co layers displays a maximum (Blo94).

4.3 Results

Figure 4.2 shows magnetoresistance measurements as well as magnetization loops obtained with VSM and MOKE as a function of applied field for $N = 2, 4,$ and 7 . In all the measurements the field was applied normal to the film plane, along the easy axis. Each transition shown in figure 4.2 corresponds to the magnetization reversal of an individual layer. For a given N all the measurements show the same transitions.

The bilayer ($N=2$) clearly shows a spin-flip transition. This behavior indicates that there is indeed antiferromagnetic (AF) coupling between the magnetic layers. This results in a region with zero magnetic moment for small magnetic fields when the layers are aligned antiparallel. The presence of a spin-flip transition also indicates that the magnetic anisotropy K (J/m^3) is larger than the exchange coupling divided by the film thickness, $-J/d$ (AF-coupling corresponds to $J < 0$). If this were not the case one would rather expect a spin-flop transition than a spin-flip transition (Die90). In a spin-flop transition the magnetization directions of the two layers, starting in zero field, remain antiparallel until, suddenly, they make a transition to a canted state at the spin-flop field $H_{sf} = H_2$, as is shown in figure 4.1a. In the canted state both magnetization directions are under an angle θ with the magnetic field where $\theta_1 = -\theta_2$. Upon a further increase of magnetic field, both magnetization directions gradually rotate to the field direction, until saturation is reached (at $H = H_3$ in figure 4.1a).

Note that the Kerr rotation is more sensitive to layers closer to the surface due to the finite penetration depth of the light. As a result the Kerr signal at low fields (state with AF-alignment) is non zero. This enables us in some cases to determine the magnetization direction of a particular layer of the stack. For instance, if we consider the bilayer we can see that the magnetization direction of the lower layer always reverses first, as the Kerr rotation does not change in sign when going from saturation to AF-alignment. This is indicated by the arrows in figure 4.2, where the left arrow represents the bottom layer and the right arrow the top layer.

From the magnetoresistance curve of for instance the bilayer it can be seen that the GMR ratio, defined as $(R(B) - R_p) / R_p$ with $R(B)$ the resistance at field B and R_p the resistance when all layers are aligned parallel, shows a maximum when all layers are aligned antiparallel. This is because the resistance is larger in case of antiparallel magnetizations (see e.g. chapter 1).

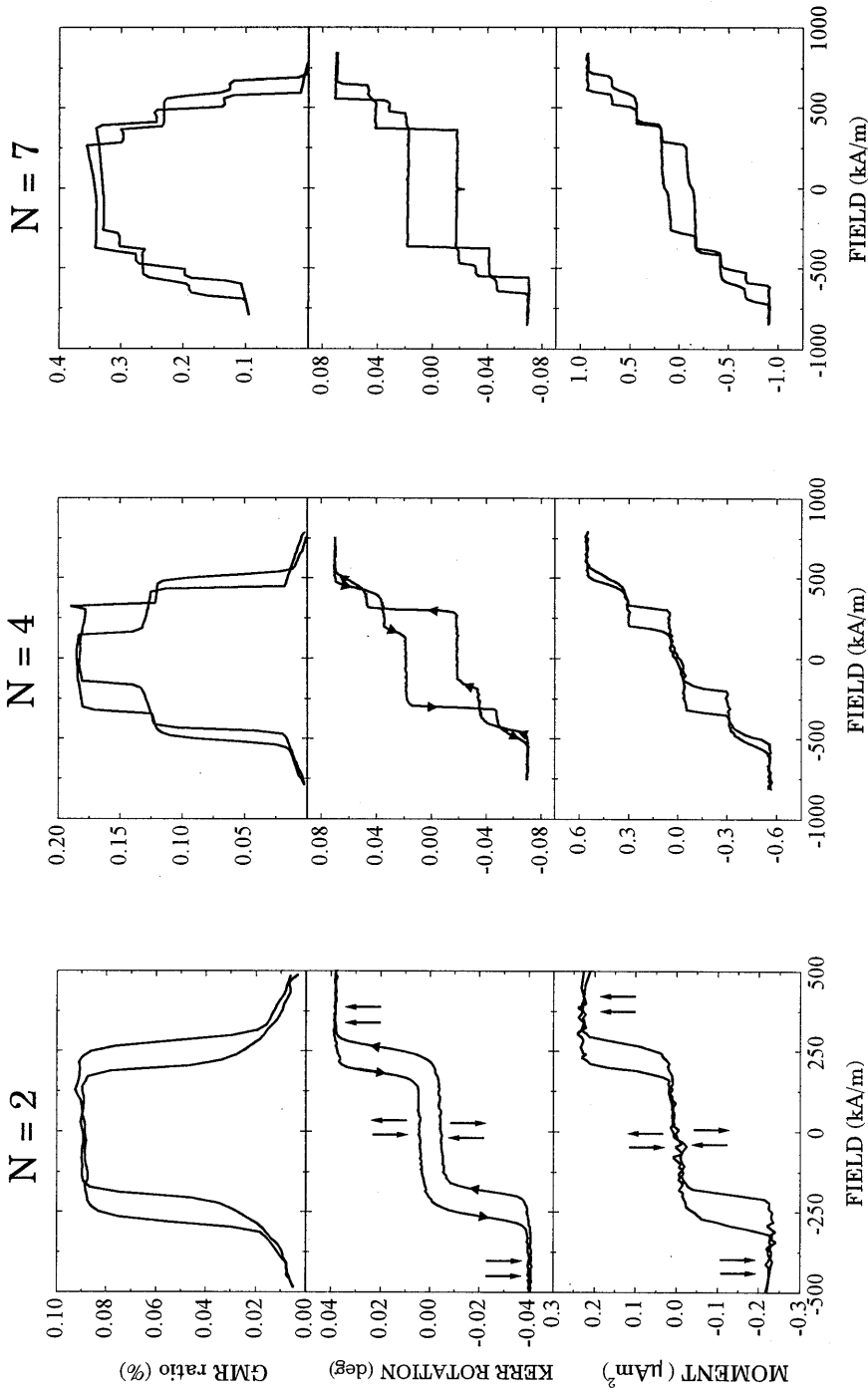


Figure 4.2: From top to bottom room temperature magnetoresistance, Kerr rotation and magnetization as a function of applied field for $\text{SiO}_2 + 200 \text{ \AA Ru} + N^*(M+8 \text{ \AA Ru})+22 \text{ \AA Ru}$ with $M = 2 \text{ \AA Co}+4^*(3 \text{ \AA Co}+4^*(3 \text{ \AA Co}+6 \text{ \AA Pd}))+5 \text{ \AA Co}$. The field was applied perpendicular to the film plane in all the measurements.

In the case of four magnetic layers the magnetization loops display four transitions between negative and positive saturation. For the Kerr loop the change in Kerr rotation is different for each transition, where the layer closest to the surface causes the largest change in Kerr rotation. This difference enables us again to determine which magnetic layer reverses the direction of its magnetization at that transition. If we number the layers in the sequence as they are grown (first grown layer = layer 1), the first transition when the field is decreased from saturation is a magnetization reversal of layer 3 (from $\uparrow\uparrow\uparrow$ to $\uparrow\uparrow\downarrow$). Equivalently the second transition corresponds to a reversal of layer 1 ($\uparrow\uparrow\downarrow$ to $\downarrow\uparrow\downarrow$), the third transition, which presents the largest step, corresponds with layer four ($\downarrow\uparrow\downarrow$ to $\downarrow\uparrow\downarrow$) and the fourth transition with layer 2 ($\downarrow\uparrow\downarrow$ to $\downarrow\downarrow\downarrow$).

When the number of layers increases, the MOKE loops, which are insensitive to the lower layers, display less transitions than the VSM and magnetoresistance measurements. From our measurements we can conclude that, for this specific set of samples, the information depth from the MOKE measurements is restricted to approximately 280 Å. Therefore it is no longer possible to establish the exact order in which the layers reverse their magnetization direction. However, from VSM and MR measurements it is clear that the layers still reverse one by one. As far as we can see from the MOKE loops the sequence in which the layers reverse their magnetization direction is always the same. Using the same numbering as above, the sequence in which the layers reverse their magnetization direction is: N-1, N-3, ..., 3, 1, N, 2, 4, ..., N-2 for N is even and N-1, N-3, ..., 2, 1, N, 3, 5, ..., N-2 for N is odd. This is consistent with the MR curves since the smallest changes in MR (around the origin) then correspond to the reversal of the outer layers. We will return to this in the discussion.

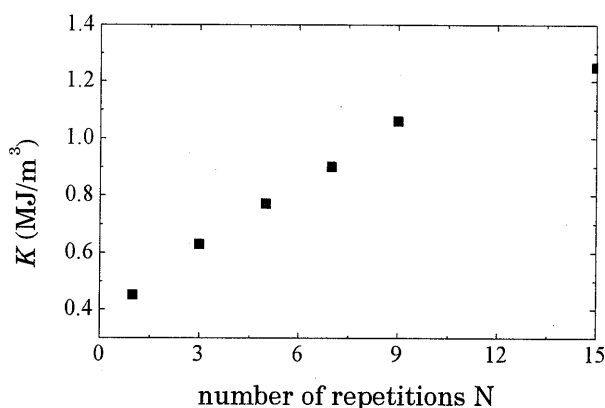


Figure 4.3: Magnetic anisotropy K as a function of the number of repetitions.

The magnetic anisotropy, K , is measured by means of a capacitive torque magnetometer (Rop93). Figure 4.3 shows K as a function of the number of repetitions N . Clearly K increases with the number of repetitions. In fact the measured value of the anisotropy is an averaged value over all the magnetic layers in the sample. When it is assumed that the magnetic anisotropy of a specific layer (i) is the same in all samples, the anisotropy of layer 2 can be calculated by subtraction of the anisotropy of layer 1 (measured from the sample with $N = 1$), the anisotropy of layer 3 can be calculated by subtraction of the anisotropies of layers 1 and 2, etc. Such a calculation indicates that the anisotropy of the various layers in our multilayers increases when going from the bottom layer to the top layer up to approximately a factor of 3 for $N \geq 10$.

4.4 Discussion

From the fact that within one sample each individual layer reverses its magnetization direction at a different field we can deduce that the layers are not all identical. For all the samples the sequence in which the layers reverse their magnetization direction is always the same. Starting from saturation and decreasing the field, the first layer to reverse its magnetization direction will be the layer which is AF coupled most strongly to its neighbors. For $N \geq 3$ this will always be an inner layer since such a layer is coupled with two neighbors whereas an outer layer has only one magnetic neighbor.

Since the layers always start to reverse from the top, apparently the AF coupling between two successive Co/Pd layers at the top of the multilayer is larger than the coupling between two layers at the bottom. The fact that the layers at the bottom are coupled less strongly than the top layers has also been observed in Fe/Si multilayers (Ful92, Koh97).

The difference in anisotropy between the top and bottom layer amounts to approximately a factor of 3. Two effects can account for an increase in anisotropy. Bruno (Bru88) has shown that interface roughness always reduces the anisotropy. When, according to Bruno, the interfaces are modelled as if they consist of terraces and craters of mean lateral size L , and σ denotes the modulus of the mean deviation from the flat interface (at $z = 0$) in the z -direction, a decrease of $2\sigma/L$ with a factor of 2 will result in an increase in anisotropy with a factor of 3. Another possible effect is an improvement in texture. In Co/Pd (Bro89) as well as in Co/Pt multilayers (Lin91) it was found that the perpendicular anisotropy displays a maximum in (111) textured samples. For Co/Pt multilayers also an increase in anisotropy was observed when the number of repetitions increased (Lin91). This was ascribed to the improvement in (111) texture.

Both effects can also contribute to an increase in AF coupling strength. It is well-known that the coupling strength depends on the crystalline orientation and

will thus be influenced by a change in texture. Interface roughness can result in variations in the spacer layer thickness. Variations around the optimum spacer will always reduce the coupling strength.

Determination of a value for the exchange coupling is not trivial. As mentioned above we are not in one of the two limiting cases of absolute minimum energy or local energy minimum due to anisotropy induced energy barriers. Thus the formulas for these cases derived by Dieny et al. and Folkerts (Die90, Fol91), shown in the caption of figure 4.1, are not valid in this case. Therefore we write the energy of the multilayers as:

$$E = -\mu_0 H M_S \sum_{i=1}^N d_i \cos \theta_i - \sum_{i=1}^{N-1} J_i \cos (\theta_i - \theta_{i+1}) \quad (4.1)$$

Here d_i is the thickness of layer i , M_S is the saturation magnetization of the magnetic layers, and θ_i is the angle between the magnetization direction of layer i and the easy axis (normal to the film plane). We now assume that a layer will reverse its magnetization direction whenever the energy difference between initial and final state is large enough to surmount a coercive force H_C : $E_i - E_F = 2\mu_0 M_S d_i H_{C,i}$. Thus, equation 4.1 is only calculated for angles $\theta_i = 0^\circ$ or $\theta_i = 180^\circ$. Note that equation (4.1) does not contain an anisotropy energy term $-K_i \cos^2 \theta_i$ since this term is the same for $\theta = 0^\circ$ and $\theta = 180^\circ$. According to this model the transition field H_F for an inner layer i , when the field is decreased from saturation, is given by

$$H_F = \frac{-J_{i-1} - J_i}{\mu_0 M_S d_i} - H_{C,i} \quad (4.2)$$

where J_i is the exchange coupling between layer i and layer $i+1$. For an outer layer this field is

$$H_F = \frac{-J}{\mu_0 M_S d} - H_C \quad (4.3)$$

Starting from the antiferromagnetic situation the coercive field should be added instead of subtracted.

Values for the exchange coupling can now be found by averaging two magnetization reversal transition fields of the same magnetic layer. This can be accomplished measuring an inner loop, i.e., by reversing the field course after a magnetization reversal of a magnetic layer until the magnetization direction of that layer reverses back to its original direction. This procedure is shown in figure 4.4a. The sequence of the successive transitions is indicated by numbers in the figure. For this particular sample ($N=4$) the coupling strength J , following

from the averaging, is shown in figure 4.4b and increases from $J = -0.7 \text{ mJ/m}^2$ for J_1 to $J = -0.89 \text{ mJ/m}^2$ for J_3 . These values for the coupling strength are comparable to those reported by Bloemen (Blo94) for the Co/Ru system with the same Ru-thickness.

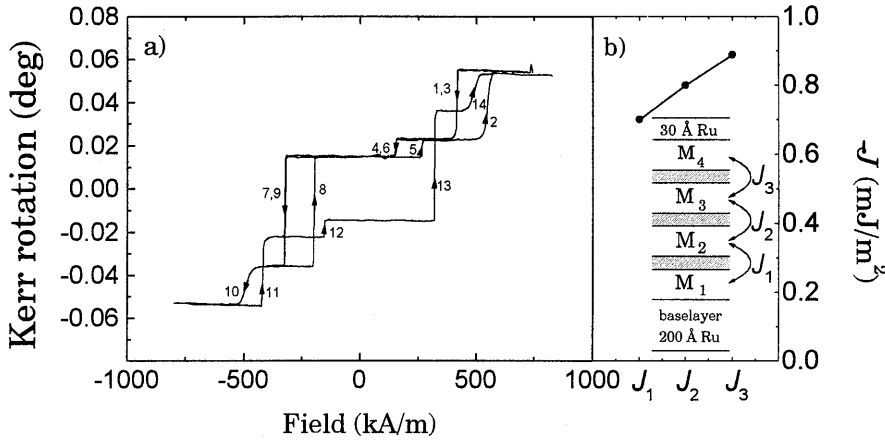


Figure 4.4: a) Kerr rotation as a function of applied field for the sample with 4 magnetic layers. The field course was reversed after each transition. The sequence of the successive transitions is indicated with numbers. b) calculated coupling strength.

We will now examine the magnetoresistance data in more detail. For $N = 7$ in figure 4.2 and $N = 6$ in figure 4.6, it appears that the GMR ratio at positive and negative saturation is not the same. This is however not quite true since in these figures it is actually not just the GMR ratio that is shown. At the time these samples were measured, the four pressure contacts in the magnetoresistance apparatus, described in chapter 2, were not yet put into use. The magnetoresistance curves in this chapter are obtained with contacts composed of gold wires that are attached to the sample with silver-paste. When the two voltage contacts are not positioned exactly on one line along the current direction, the measured resistance will additionally be influenced by the extraordinary Hall effect that is proportional to the magnetization (Dah88). It is this effect that is observed in the GMR ratio and causes the apparent difference in the positive and negative saturation value. We will not investigate this effect in further detail and return to the magnetoresistance.

The magnetoresistance displays a similar sequence of transitions as observed by VSM and MOKE. It appears that all transitions give rise to an equal change in MR, except for the change in MR due to the reversal of an outer layer which is systematically smaller (roughly a factor 2) than all the others. As we are dealing

with transitions between well-defined configurations as pointed out before, we are tempted to explain this interesting phenomenon first by a very simple resistor network.

With such a network, introduced by Edwards et al. (Edw91), it was possible to predict the giant MR as well as the damping of the effect with increasing spacer thickness. However, the model was designed essentially for a mean free path much longer than the layer thicknesses which justifies an averaging of resistivities in the up and down electron channels. This means implicitly that one can never discern between the magnetization reversal of an inner layer or one of the outer layers.

For this reason we have developed an alternative resistor model, in which the multilayer is represented by $N-1$ resistors in parallel, each resistor representing a bilayer of two half magnetic layers M separated by a Ru spacer layer. In figure 4.5 a schematic representation of our resistor model is shown.

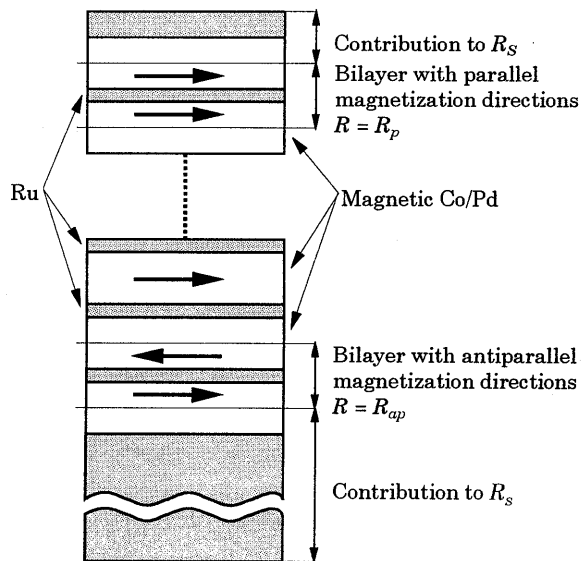


Figure 4.5: Schematic representation of our resistor model. Indicated are two different bilayers consisting of two half magnetic layers with parallel and antiparallel magnetization and resistance R_p and R_{ap} resp. Also indicated is the shunt resistance R_s .

The parallel and antiparallel configuration of the bilayer's magnetization directions relates to a difference in resistance due to the spin-dependent scattering mechanism. In the parallel configuration the resistance of the bilayer is denoted with R_p , and in the antiparallel configuration with R_{ap} . The Ru base and cap layers as well as the upper half of the top magnetic layer and the lower half of the bottom magnetic layer give rise to a shunt resistance, R_s . A similar procedure has been used by Dieny et al. to account for the shunting of the 'nonactive' part of a magnetic layer in a magnetically soft sandwich (Die92a).

It should be emphasized that in our model an outer layer is a part of only one sandwich resistor, whereas an inner layer is incorporated into two resistors. In other words, due to a reversal of an outer layer magnetization a mobile electron experiences only once a change in M , whereas a double change is seen when an inner layer changes its magnetization. This leads to different contributions to the MR effect of the reversal of an inner or outer magnetic layer. The total magneto-resistance between completely parallel and completely antiparallel configurations is according to our resistor model given by:

$$MR = \frac{\alpha + (N-1)\beta}{\alpha + (N-1)} - 1 \quad (4.4)$$

where $\alpha = R_{ap}/R_s$ and $\beta = R_{ap}/R_p$. Thus our model is also capable of introducing a N -dependence in the magnetoresistance. This N -dependence here originates solely from the presence of the shunt resistance, R_s , that becomes relatively less important when N increases.

In figure 4.6a and 4.6b the data for $N = 6$ are shown together with results of the parallel-resistor model. The relative changes in MR, and in particular the exclusive role of the outer layer, is very well recovered with a set of parameters (α, β) applicable for all N , which is shown in the fit of the total MR in figure 4.6c.

To substantiate the parallel-resistor model introduced above, we have also calculated the magnetoresistance as a function of the number of magnetic layers with the help of the Camley-Barnas model (see Camley et al. (Cam89) and chapter 3). It should be noted that within the CB-model two effects can contribute to the N -dependence of the GMR ratio. The first effect is the presence of the base- and caplayer of which the relative importance, similar to our resistance model, decreases when N increases. However, even without base and caplayer there can be a N -dependence within the CB-model, depending on the mean free paths of the conduction electrons in the magnetic layers. A N -dependence will appear when this mean free path is of the order of or larger than the total multilayer period. This effect is shown in figure 4.7 where we have calculated $\Delta G (=G_p - G_{ap})$ with the CB-model for the system $N^*(22 \text{ \AA} M + 8 \text{ \AA} NM + 22 \text{ \AA} M)$ where M represents a magnetic layer and NM a non magnetic spacer layer. In this particular example we assumed interface spin-dependent

scattering to be the cause of the MR-effect. To be specific we assumed that at the M/NM interfaces the up electrons are all coherently transmitted and the down electrons are completely diffusely scattered. Further we assumed completely diffusive scattering at the outer boundaries of the sample and varied the (spin-independent) mean free paths of the conduction electrons in the magnetic layer (λ_M) as indicated in the figure.

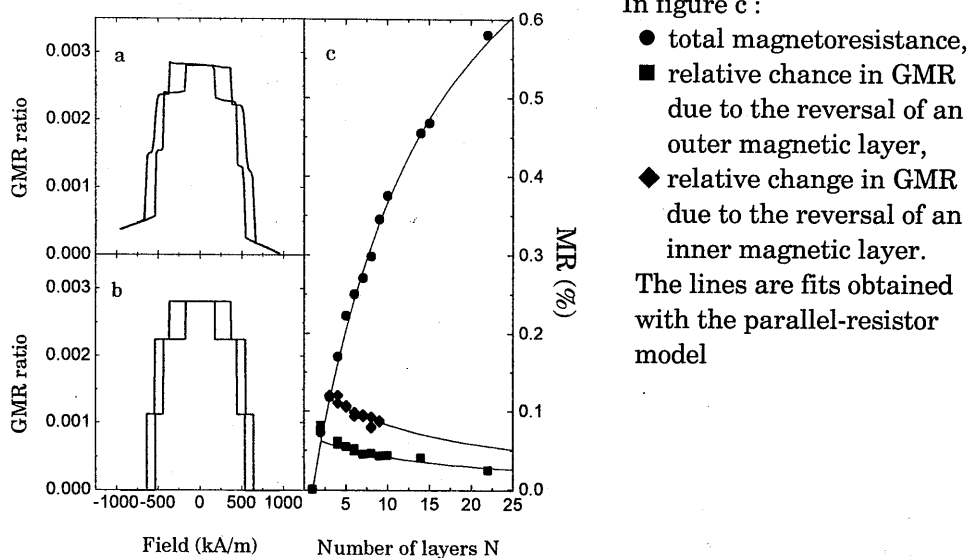


Figure 4.6: a) and b) data and model calculations resp. of the relative change in MR obtained for perpendicular fields at $T = 300$ K for the sample with 6 magnetic layers; c) total magnetoresistance and relative change in MR due to the magnetization reversal of an inner or outer magnetic layer. The lines are fits obtained with the resistor model, equation 4.4, with $\alpha = 15.128$ and $\beta = 1.0099$.

When λ_M is much smaller than the thickness of the magnetic layers, the layers can be considered as resistors in parallel and there is no N -dependence. In this case the difference between the conductance of the parallel state and of the antiparallel state (ΔG) divided by N' is constant as is shown in figure 4.7 for $\lambda_M = 0.5$ Å. When λ_M is of the order of the layer thickness or larger ($\lambda_M = 25$ or 500 Å in figure 4.7) $\Delta G/N'$ increases with N' merely because the diffusive scattering at the outer boundaries, that limits for these large values of λ_M the

area contributing to ΔG , is gradually removed when N' increases. Here we would like to remark again that the presence of a base and caplayer will lead to an additional N -dependence for *all* values of λ_M . The magnitude of this additional N -dependence is determined by the conductance of the base and caplayer compared to the conductance of the total multilayer stack.

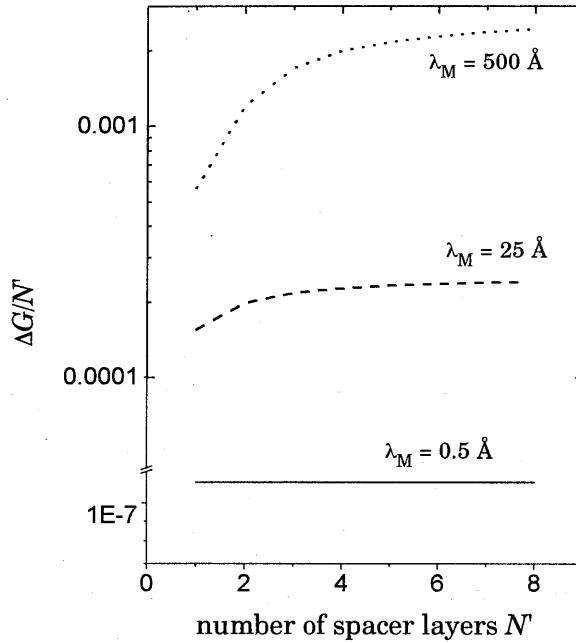


Figure 4.7: Difference in conductance between parallel and anti-parallel alignment (ΔG) per period ($22 \text{ \AA} \text{ M} + 8 \text{ \AA} \text{ NM} + 22 \text{ \AA} \text{ M}$). In these calculations it was assumed that at the N/NM interfaces up-electrons are transmitted and down-electrons are diffusely scattered, at the outer boundaries all electrons are diffusely scattered, $\lambda_{\text{NM}} = 8 \text{ \AA}$, and λ_M is indicated in the figure and is the same for both up- and down-electrons.

Let us now investigate the relative contributions to the GMR ratio from the reversal of an outer or inner magnetic layer within the CB-model. Our calculations have confirmed that indeed the contribution to the GMR ratio from an inner layer is twice that of an outer layer, provided that the electron mean free path in the magnetic layer (λ_M) is much smaller than the thickness of the magnetic layer for both spin-up and spin-down electrons. This is the same limit as described above where the layers can be considered as parallel resistors

similar to our resistor model. Recalling that the MR-effect originates from electrons that travel from one magnetic layer to another magnetic layer which has its magnetization direction parallel or antiparallel, it is easy to understand that the factor two stems from the fact that electrons coming from an outer layer can cross only one spacer layer before being scattered, and electrons from an inner layer can cross a spacer layer on either side. Naturally the GMR ratio is very small for these small mean free paths since only small regions in the magnetic layer near the interfaces with the spacer can contribute to the MR, which is in agreement with our measurements.

When the mean free path increases electrons are able to cross more than one spacer layer before being scattered which means that the parallel resistor model is no longer valid. In this case the outer boundaries and, when present, base and caplayer, will be of influence on the GMR ratio. When a layer is closer to the outer boundaries this influence will be larger which results in deviations in the factor of two between inner and outer layers.

From our calculations with the CB-model we can therefore conclude that the mean free path of (spin-up as well as spin-down) conduction electrons within the magnetic Co/Pd layers should be smaller than the thickness of the Co/Pd layers to be consistent with our measurements.

It should be emphasized that the decisive role of the position of a magnetic layer within the multilayered structure for the size of the relative MR, might be a general phenomenon in layered systems, although it has only been clearly observed in some cases (Nog94, Mul95). Finally, we remark that the applied Boltzmann transport equation assumes no spin-flip processes, which is a $T = 0$ approximation. In view of this, we have performed additional MR measurements at temperatures down to $T = 4$ K. Except for the increasing magnitude of the MR at lower temperatures, there is no visible effect on the relative MR changes for inner and outer layers.

4.5 Conclusions

We have measured the magnetization, anisotropy (K), and magneto-resistance of $[(\text{Co/Pd})_4\text{-Ru}]_N$ multilayers. All magnetization and magneto-resistance curves show sharp transitions corresponding to the magnetization reversal of individual magnetic layers. This enables us to determine the coupling strength J between each pair of layers. J and K increase when the number of layers increases, which may be due to an improvement in texture or a decreasing interface roughness. In the MR-curves, in combination with the MOKE loops, we can clearly distinguish between the reversal of an outer layer or an inner layer. This fact as well as the N -dependence of the GMR ratio can be described with a simple resistor model. Calculations in which we have solved the Boltzmann transport equation have revealed all the features of our resistor model, provided

that the mean free paths of conduction electrons within the magnetic layer are small compared to the thickness of the magnetic layer.

5. Spin valves for the investigation of spin-dependent scattering: interface versus bulk

5.1 Introduction

It is generally accepted that the GMR effect in magnetic layered structures is induced by spin-dependent scattering (SDS), i.e. an asymmetry in the scattering rates between spin-up and spin-down electrons. However, whether this spin-dependent scattering occurs predominantly in the bulk of the ferromagnetic layers or at the interfaces between the magnetic and nonmagnetic layers is one of the most prominent fundamental issues in studies on the GMR effect.

For a number of materials experiments have been performed to elucidate this issue (see e.g. Hei94 and references therein). The relative importance of the bulk and interface contributions are usually evaluated by comparing magnetoresistance measurements with model calculations based on a resistor network, the semiclassical Boltzmann transport equation, or the quantum model of Zhang, Levy and Fert. Due to the large number of input parameters, the conclusions obtained in this way are often questionable.

In recent years especially the Co/Cu system has drawn much attention. One reason for this is that Co/Cu is a suitable candidate for verifying theoretical predictions on the period(s) of oscillation in the exchange coupling strength as a function of Cu layer thickness. Another reason is that in Co/Cu one of the largest GMR effects so far has been observed (65% at room temperature (Par91)).

A number of experiments both with the Current In the Plane of the layers (CIP geometry), which is experimentally the most accessible geometry, and with the Current Perpendicular to the Plane of the layers (CPP geometry) has been performed on the Co/Cu system. As already explained at the end of chapter 3, CPP geometry provides a relatively simple way of separating contributions from bulk and interface spin-dependent scattering, yielding two parameters, β and γ respectively. The general conclusion from these CPP measurements is that spin-dependent interface scattering for the Co/Cu system is larger than spin-dependent bulk scattering ($\gamma > \beta$), as is shown in table 5.1. Nevertheless, the actual reported values for β and γ can be quite different. Without going into details, we note that this difference might not be so strange since not all these CPP measurements are alike. In some cases β and γ were obtained from measurements on molecular beam epitaxy (MBE) grown Co/Cu multilayers deposited on grooved substrates (Oep96), and in other cases from measurements on sputtered samples with superconducting current and voltage leads (sch93, Oep96) or on electrodeposited Co/Cu nanowires in the pores of a nanoporous membrane (Voe95, Blo97, Dub97). Since, in addition, the geometry is different

from CIP magnetoresistance, it is interesting to investigate the contributions from bulk and interface spin-dependent scattering also for the CIP geometry.

Table 5.1: Parameters β and γ (as defined in chapter 3) determined from various CPP-magnetoresistance measurements on Co/Cu. Also included are $\alpha_b \equiv \rho^\downarrow / \rho^\uparrow = (1+\beta)/(1-\beta)$, and $\alpha_i \equiv R_{m/nm}^\downarrow / R_{m/nm}^\uparrow = (1+\gamma)/(1-\gamma)$, to facilitate comparison with CIP-magnetoresistance.

ref	T (K)	β	α_b	γ	α_i
Oep96	4.2	0.17±0.03	1.41	0.45±0.09	2.64
Oep96	300	0.12	1.27	0.32	1.94
Sch93	4.2	0.47±0.14	2.8±0.8	0.72±0.06	6.1±1.5
Voe95	4.2	0.50±0.10	3	0.76±0.05	7.3
Voe95	300	0.44±0.06	2.57	0.40±0.10	2.33
Dub97	77	0.36	2.13	0.85	12.3
Blo97	20	0.25-0.30	1.7-1.9	0.55	3.4
Blo97	300	0.25-0.30	1.7-1.9	0.4	2.3
Oep96	4.2	0.38±0.06	2.23	0.71±0.05	5.90

To investigate contributions from bulk and interface spin-dependent scattering in the CIP geometry, which is more complicated than in the CPP geometry, various experiments have been performed. In some experiments thin layers at the Co/Cu interfaces have been substituted to modify the interface scattering, leaving the bulk scattering unaltered (Wel94, Wel95), or to investigate how the magnetoresistance depends on the thickness of this interface layer (Par93). Other experiments are based on changing the relative amounts of bulk to interface. Sometimes this is done by varying the thickness of the (non)magnetic layers (Die92a, Die93, Len94, Shu94, Rij96). In other cases the thickness of the mixed zone at the interface was enlarged by interdiffusion of Co and Cu due to annealing (Hal93) or by co-deposition at the interfaces (Suz93). However, all of these experiments do not give consistent conclusions. Some authors emphasize the importance of bulk spin-dependent scattering (Hal93, Wel95), whereas others ascribe the magnetoresistance of Co/Cu completely to interface spin-dependent scattering (Par93, Shu94). In table 5.2 we reproduce some of the parameters that are measured or used to fit the CIP magnetoresistance of the Co/Cu system. We may conclude that the observation of a dominant interface contribution, as in the CPP experiments, does not automatically follow from all the CIP experiments as well.

In this respect it is extremely relevant to realize that experiments based on a modification of the interface structure of antiferromagnetic (AF) coupled Co/Cu layers will probably alter the strength of the AF coupling as well. For example, Bruno and Chappert have argued that the interlayer exchange coupling strength

Table 5.2: Parameters α_b and α_i , denoting the asymmetry in the scattering rates between spin-up and spin-down electrons in the bulk and at the interfaces respectively. Values are determined from CIP-magnetoresistance measurements on the Co/Cu system. λ^\uparrow and λ^\downarrow represent the electron mean free path of spin-up and spin-down electrons. T is the transmission coefficient characterizing the interface scattering, as defined in chapter 3. The symbol (-) in the table means that the parameter is not determined.

ref	T (K)	$\alpha_{b(ulk)}$	$\alpha_{i(interface)}$
Hal93	5	8	1
Fre93	300	$\lambda^\uparrow/\lambda^\downarrow = 60/10 = 6$	$T^\uparrow/T^\downarrow = 0.85/0.25 = 3.4$
Die93	1.5	$\lambda^\uparrow/\lambda^\downarrow = 140/10 = 14$	$T^\uparrow/T^\downarrow = 1/0.2 = 5$
Len94	4	2.6 ± 0.3	21 ± 3
Gur93	300	$\lambda^\uparrow = 55 \pm 4, \lambda^\downarrow \leq 10$	-
Rij96	5	-	$T^\uparrow/T^\downarrow = 1/0 = \infty$
Duv94	4.2	7	19.5
Duv94	300	7	11.4

depends on the flatness of the interfaces (Bru91, Bru92). Geometrical roughness (deviations from flatness of the interface between two homogeneous materials) will reduce the interlayer exchange coupling strength. Alteration of the coupling strength can lead to deviations of the perfect antiparallel alignment and can therefore affect the GMR effect. Honda and Nawate (Hon94) have shown that after annealing of Co/Cu multilayers the GMR effect and the coupling strength have decreased in the same way. Therefore, in order to obtain a clear interpretation of the results, these experiments should be performed on *decoupled* magnetic layers (Die93, Spe93). This can be realized in spin valve structures in which the magnetization direction of one of the layers is pinned in a certain direction, for instance by AF coupling to a third magnetic layer, or by exchange biasing using an exchange-coupled antiferromagnetic layer.

In the following of this chapter we will describe two of such sample structures in which two magnetic layers can switch between antiparallel and parallel upon the application of a magnetic field, although these two layers are *not* magnetically coupled. Then, in chapters 6, 7, 8, and 9 we will use these structures to investigate effects of intermixing at the interfaces, analyzing bulk scattering lengths or demonstrate the presence of interface spin-dependent scattering.

5.2 Co/Ru/Co/Cu/Co spin valves

As explained in the previous section the search for the spatial origin (bulk versus interface) of the GMR effect should preferably be performed in spin valves with uncoupled magnetic layers. For this purpose we designed a new spin-engineered structure consisting of three magnetic layers: $M_1/6 \text{ \AA Ru}/M_2/d \text{ \AA Cu}/M_3$, as shown in the inset of figure 5.1. The idea was based on a system introduced by Parkin and Mauri to determine the ferromagnetic coupling between two layers from magnetization measurements (Par91a). The 6 \AA Ru layer provides a strong antiferromagnetic coupling between the magnetic layers M_1 and M_2 , which acts as a biasing for the magnetization direction of layer M_2 . Therefore, in the following, we will refer to this kind of spin valves as AF-biased spin valves. The thickness d of the Cu layer is chosen such that there is essentially no magnetic coupling between layers M_2 and M_3 . Nevertheless, the magnetization directions of these layers can switch between parallel and antiparallel upon the application of a magnetic field, mediated by the AF coupling between layers M_1 and M_2 , as we will explain below. The three magnetic layers of the example in figure 5.1 are composed of $M_1 = 75 \text{ \AA Co}$, $M_2 = 25 \text{ \AA Co}$, and $M_3 = 100 \text{ \AA Co}$.

The spin valves are high vacuum (HV)-magnetron sputter deposited on SiO_2 substrates at room temperature at an Ar pressure of 7 mTorr (0.9 Pa). Before sputtering the vacuum chamber was evacuated to a background pressure of approximately 5×10^{-7} Torr (7×10^{-5} Pa). All samples have a base layer of 200 \AA Ru and on top a protection layer of 30 \AA Ru. Ru, Co, and Cu were deposited at sputter rates of 1, 2, and 2 \AA/s , respectively. From X-ray diffraction measurements it follows that the samples have a (111) texture; however, broad rocking curves (full width at half maximum $\approx 13^\circ$) indicate that the texture is rather poor.

5.2.1 Magnetization of AF-biased spin valves

Since the Cu thickness d in our spin valves is chosen such that layer M_3 is not coupled to the other magnetic layers, the magnetization direction of this layer will always be along the field direction. On the other hand, layers M_1 and M_2 are coupled antiferromagnetically. Therefore, at small applied fields the magnetization directions of these layers will be antiparallel, with the magnetization direction of the thinner layer (M_2) pointing opposite to the field direction. When the applied field is enlarged, the Zeeman energy of layer M_2 will increase and eventually, when the Zeeman energy equals the coupling energy, the magnetization direction of layer M_2 will reverse towards the field direction.

A typical $M(H)$ curve is shown in figure 5.1. Between $H = 0$ and $H = H_1$ there is a clear plateau in the magnetization. At this plateau, layer M_2 is aligned

antiparallel with layers M_1 and M_3 . The magnetic moment corresponding to this plateau ($M = (0.765 \pm 0.02) \times M_{sat}$) agrees well with what one would expect for a complete antiparallel configuration ($M = 0.75 \times M_{sat}$). Between $H = H_1$ and $H = H_2$ the magnetization direction of layer M_2 reverses along the field direction. Since the layers are grown in the (111) direction and the field is applied in the plane of the layers no magnetic anisotropy is involved here and the magnetization reversal will be a gradual rotation process as can be seen in figure 5.1. For fields larger than $H = H_2$, the magnetization directions of all layers point in the field direction.

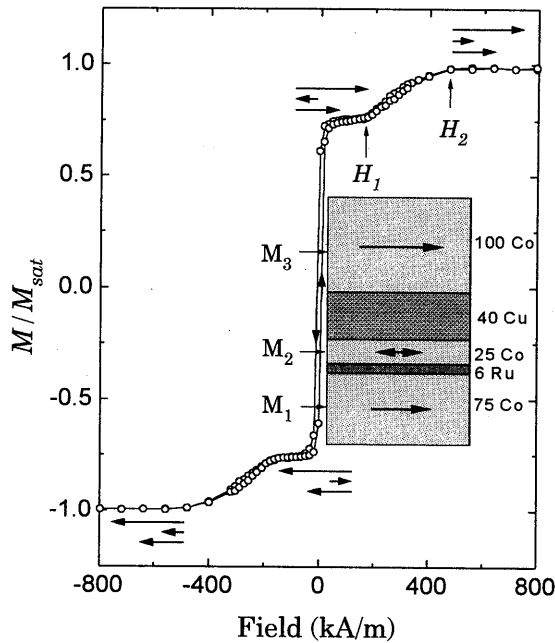


Figure 5.1: $M(H)$ loop at $T = 300$ K for the system $\text{SiO}_2/200 \text{ \AA Ru}/75 \text{ \AA Co}/6 \text{ \AA Ru}/25 \text{ \AA Co}/40 \text{ \AA Cu}/100 \text{ \AA Co}$. The arrows indicate the magnetization directions of the Co layers. The magnetization direction of layer M_2 can be either parallel or antiparallel to the magnetization directions of layers M_1 and M_3 , depending on the strength of the applied field H . Also the direction in which the loop was measured is indicated with arrows.

From the values of H_1 and H_2 , where the magnetization starts to deviate from the value of the antiparallel or parallel configuration, the strength of the antiferromagnetic coupling, J_{Ru} (in J/m^2), between layers M_1 and M_2 across the Ru layer can be calculated. The starting point for this calculation forms the energy expression for the layers $M_1/6 \text{ \AA} \text{ Ru}/M_2$, which is given by:

$$E = -\mu_0 M_S H d_1 \cos \theta_1 - \mu_0 M_S H d_2 \cos \theta_2 - J_{Ru} \cos(\theta_1 - \theta_2) \quad (5.1)$$

where $\mu_0 M_S$ denotes the saturation magnetization of Co, $d_{1,2}$ the thickness of layer 1 and 2 respectively and $\theta_{1,2}$ the angles of the magnetization directions of layers 1,2 with the field direction. The only variables in this equations are $\theta_{1,2}$. Starting from the antiparallel or parallel configuration the fields H_1 and H_2 , respectively, can be calculated (Die90) from the stability condition:

$$\frac{\partial^2 E}{\partial \theta_1^2} \times \frac{\partial^2 E}{\partial \theta_2^2} - \left(\frac{\partial^2 E}{\partial \theta_1 \partial \theta_2} \right)^2 > 0, \text{ yielding:}$$

$$H_1 = -J_{Ru} \left(\frac{1}{\mu_0 M_S d_2} - \frac{1}{\mu_0 M_S d_1} \right) \text{ and} \quad (5.2a)$$

$$H_2 = -J_{Ru} \left(\frac{1}{\mu_0 M_S d_1} + \frac{1}{\mu_0 M_S d_2} \right). \quad (5.2b)$$

Inserting values for H_1 and H_2 determined from magnetization curves like figure 5.1, it follows that the exchange coupling strength calculated according to equation 5.2b is always larger by a factor of approximately 1.4 than the coupling strength according to equation 5.2a. Presumably, this difference is due to local variations around some average coupling strength induced for instance by small variations in layer thickness. The areas with smaller coupling strength cause the magnetic moments to rotate at magnetic fields smaller than $H = H_1$, and areas with larger coupling strength cause an increase in the saturation field H_2 . When the coupling strength calculated from equations 5.2a and b are averaged and determined for more than one sample we find a coupling strength of $J_{Ru} = -1.18 \pm 0.06 \text{ mJ/m}^2$, which agrees well with the maximum coupling value of the Co/Ru system reported by Bloemen (Blo94).

The most essential feature of the magnetization of the AF-biased spin valve is the possibility to create a parallel and an antiparallel alignment of the magnetization directions of layers M_2 and M_3 through the application of a magnetic field although they are not coupled to each other. Therefore, in this type of spin valve structure it is possible to investigate e.g. the influence of

intermixing at the Co/Cu interfaces without complicating effects due to AF coupling between the constituents of the valve.

5.2.2 Magnetoresistance of AF-biased spin valves

In figure 5.2 we show the magnetoresistance curve corresponding to the $M(H)$ curve in figure 5.1. Clearly the resistance is low when the field is large enough to saturate the magnetization and high for small magnetic fields where the magnetization directions of M_2 and M_3 are aligned antiparallel, resulting in a maximum GMR ratio ($=\Delta R/R_p$) of $\approx 3.8\%$.

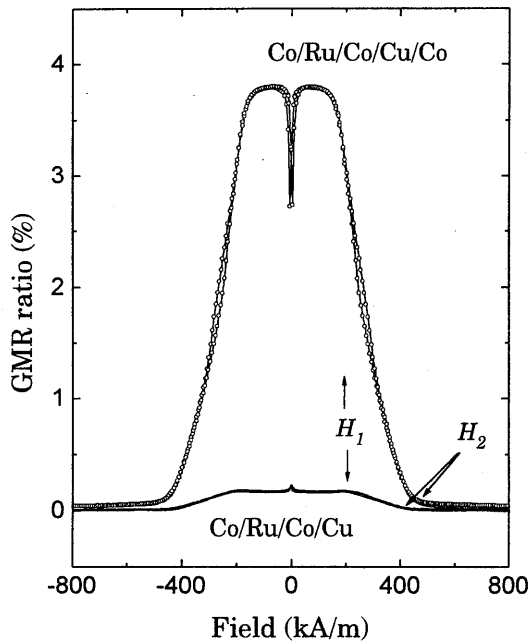


Figure 5.2: GMR ratio ($=\Delta R/R_p$) of the underlying 75 \AA Co/ 6 \AA Ru/ 25 \AA Co spin valve compared to the magnetoresistance of the total 75 \AA Co/ 6 \AA Ru/ 25 \AA Co/ 40 \AA Cu/ 100 \AA Co system. The MR values are measured in the transverse configuration ($H \perp I$) at $T = 300 \text{ K}$.

At this point we would like to emphasize that this spin valve consists of three magnetic layers and the bottom layer M_1 in principle may contribute to the MR effect as well. However, the MR effect of a Co/Ru/Co spin valve is typically an order of magnitude smaller than that of the Co/Cu/Co system. Dieny (Die93)

reports even no measurable MR in Co/Ru/NiFe/FeMn exchange-biased spin valves. Although it is difficult to compare $\Delta R/R$ values with literature because this quantity is influenced also by the choice of, for example, base and cap layers, a small GMR ratio ($\approx 0.03\%$) is reported by Bloemen for Co/Ru multilayers (Blo94). A MR effect of the same order of magnitude has been reported by Arbaoui, Dinia, and Panissod for Co/Ru epitaxial superlattices (Arb93). The highest value for the GMR ratio is obtained by Parkin in dc magnetron-sputtered Co/Ru superlattices. At a Ru thickness of 6 \AA Ru a value of $\approx 4\%$ is reached (Par90).

To elucidate the effect of the underlying Co/Ru/Co system we have measured the MR effect of the system 200 \AA Ru/ 75 \AA Co/ 6 \AA Ru/ 25 \AA Co/ 150 \AA Cu/ 30 \AA Ru where the free Co layer is substituted by Cu. The GMR ratio of this system is also shown in figure 5.2 and is clearly much smaller than the GMR ratio of the original sample. This result is in agreement with our measurements described in chapter 7, where we have observed that the GMR ratio of the system 25 \AA Co/ $d \text{ \AA}$ Ru/ 30 \AA Cu/ $d \text{ \AA}$ Ru/ 100 \AA Co decreases by more than a factor of 20 when d is increased from 0 to 2 \AA . We will therefore neglect the contribution of the Co/Ru/Co part.

For both curves all magnetization directions are aligned parallel for fields larger than H_2 where the resistance is relatively low. Between $H = H_2$ and $H = H_1$, the magnetization direction of the 25 \AA Co layer reverses, and the magnetoresistance increases. Between $H = H_1$ and $H = 0$ the magnetizations are aligned antiparallel and the resistance is high. The small peak in the GMR ratio of the system 200 \AA Ru/ 75 \AA Co/ 6 \AA Ru/ 25 \AA Co/ 150 \AA Cu/ 30 \AA Ru around $H = 0$, where both Co layers reverse their magnetization direction, might be due to the changing angles between the magnetization directions and the current (anisotropic magnetoresistance effect). The GMR ratio of the original sample shows a dip around $H = 0$. This is caused by the reversal of the magnetization direction of all layers, resulting in a nonperfect antiparallel alignment which is here apparently a much larger effect than the effect due to the anisotropic magnetoresistance.

The magnitude of $\approx 4\%$ at room temperature of the GMR ratio of Co/Cu/Co, and $\approx 6.5\%$ at $T = 4.2 \text{ K}$ which is not shown here, is comparable with the results of Speriosu for exchanged-biased spin valves on a base layer of $8 \cdot (20 \text{ \AA}$ Ru + 12 \AA Cu) (Spe91). It is, however, smaller than the MR effect reported by Dieny *et al.* (Die 93) and Parkin (Par93) ($\approx 9.5\%$ at 1.5 K and $\approx 7\%$, respectively) probably because of the 200 \AA Ru base layer and the 75 \AA Co layer, used here to obtain the antiparallel alignment, which act as a shunt. We are here however not concerned with maximizing the MR effect. The only thing important for us is that there is a plateau in the magnetoresistance where there is an antiparallel alignment between the magnetization directions of two uncoupled layers. In the next chapters we will utilize this feature of our AF-biased spin valves.

Finally we remark that all the measurements presented in the rest of this thesis were performed with the applied magnetic field in the plane of the layers, perpendicular to the current direction. The GMR ratio is determined from states where the magnetization direction of each layer is either parallel or antiparallel to the applied field, and therefore always perpendicular to the current direction. This means that the quantity ΔG is not affected by the anisotropic magneto-resistance (AMR) effect. The conductance G , however, does depend on the angle between the magnetization direction (and thus applied field) and current via the AMR effect, and is largest when the magnetization points parallel to the current direction. Therefore, the maximum measured GMR ratio ($\Delta G/G_{ap}$) will in general be smaller when the magnetic field is applied parallel to the current direction. For our AF-biased spin valves this is only a small effect and the differences between the two field directions are typically smaller than 0.1 %.

5.3 Exchange-biased spin valves

Another type of spin valve in which it is possible to switch between a parallel and an antiparallel state of the magnetization directions of two uncoupled magnetic layers through the application of an external magnetic field, is the exchange-biased spin valve. This type of spin valve requires only two ferromagnetic layers. The magnetization direction of one of these layers is pinned in a certain direction via an anisotropic exchange interaction with an antiferromagnet. This exchange anisotropy was first observed already in 1956 by Meiklejohn and Bean for fine, oxidized, Co particles (Mei56). In general the effect occurs at the interface between a ferromagnetic and an antiferromagnetic material, which also applies to layered materials. The interfacial exchange coupling causes a unidirectional anisotropy in the ferromagnetic layer when the sample is grown in a magnetic field or when the sample is cooled in a magnetic field after heating above the Néel temperature of the antiferromagnetic layer.

The general composition of an exchange-biased spin valve is $M_1/NM/M_2/AF$, where M_1 and M_2 are ferromagnetic layers, NM is a nonmagnetic spacer and AF represents an antiferromagnet. In this chapter we will describe the system 100 Å Co/40 Å Cu/50 Å Co/100 Å Fe₅₀Mn₅₀ in more detail. We note that, instead of Co, Ni₈₀Fe₂₀ is a material that is very often used in this type of spin valve when it is to be applied as a magnetic field sensor (Rij96) and that besides Fe₅₀Mn₅₀ also other antiferromagnetic materials, such as NiO or CoO, can be used (see for instance Koo96).

The Co/Cu/Co/FeMn spin valves described in this chapter are grown at room temperature by dc magnetron sputtering on Si(100) substrates. Before sputtering, these substrates were chemically etched using a 2% HF solution to remove the oxidic skin. The spin valves were grown on a 30 Å Ta buffer layer and on top of the spin valve a 30 Å Ta cap layer was grown to protect the spin valve

from oxidation. It has been observed that a thin Ta buffer layer can induce a strong (111) texture in the magnetic layers regardless of what substrate is used. X-ray diffraction measurements confirmed that indeed our spin valves are polycrystalline with a (111) texture. The sputter rates for Co and Cu were about 1 Å/s; Ta and FeMn were sputtered at about 2.1 Å/s and 2.5 Å/s respectively. The base pressure before sputtering was 10^{-8} Torr (1.33×10^{-6} Pa) while the Ar pressure during sputtering was usually 5 mTorr (0.67 Pa). During deposition a magnetic field of 10 kA/m was applied to define the direction of the exchange anisotropy.

5.3.1 Magnetization of exchange-biased spin valves

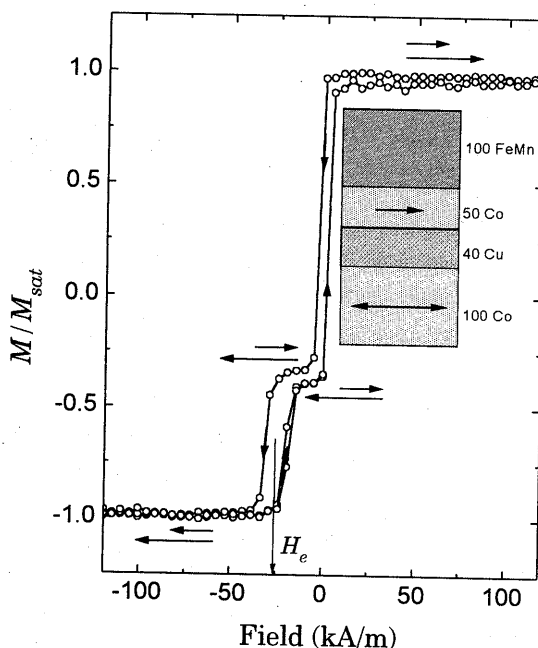


Figure 5.3: $M(H)$ loop at $T = 300$ K, measured with SQUID magnetometer, for the system Si(100)/30 Å Ta/100 Å Co/40 Å Cu/50 Å Co/100 Å Fe₅₀Mn₅₀/30 Å Ta. The arrows indicate the magnetization directions of the Co-layer. H_e denotes the exchange-biasing field.

In figure 5.3 a typical magnetization curve is shown for an exchange-biased spin valve. The specific spin valve in the figure has the composition Si(100)/30 Å Ta/100 Å Co/40 Å Cu/50 Å Co/100 Å Fe₅₀Mn₅₀/30 Å Ta. Since the Cu thickness, 40 Å, is chosen such that the two Co layers are not coupled to each other, the $M(H)$ curve is in fact a superposition of two separate simple square $M(H)$ curves characteristic for ferromagnetic layers. One $M(H)$ curve is centered around $H = 0$ and belongs to the 100 Å Co layer. This layer is often called the free layer since it is not magnetically coupled to any other layer. The second $M(H)$ curve belongs to the 50 Å Co layer that is often referred to as the pinned layer. Due to the unidirectional anisotropy induced by the neighboring antiferromagnet this $M(H)$ curve is shifted away from $H = 0$ over a distance H_e , the exchange-biasing field. Note that apart from the field shift, the biasing has also increased the coercivity of the pinned layer. This is a common phenomenon for exchange-biased layers, depending on both the thickness of the ferromagnetic and the antiferromagnetic layer, and is believed to be related to inhomogeneities in the AF layer (Jun94). The exact nature of these inhomogeneities however is still unclear.

Most important for our purpose in the next chapter where we will investigate the influence of intermixing at the Co/Cu interfaces, is that again there is a state where the magnetization directions of the layers are antiparallel although the layers are not coupled to each other.

5.3.2 Magnetoresistance of exchange biased spin valves

In figure 5.4 the magnetoresistance curve corresponding to the magnetization curve of figure 5.3 is shown. Analogous to the magnetoresistance curve of the AF-biased spin valves the magnetoresistance is low when the magnetizations are aligned parallel and there is a clear plateau where the (magneto)resistance is high when the magnetization directions point antiparallel. The maximum GMR ratio obtained in our exchange-biased spin valves ($\approx 5.5\%$ at room temperature) is a bit higher than in the AF-biased spin valves, probably because the 100 Å FeMn layer is a poor conductor, representing only a small shunt resistor compared to the 200 Å Ru/75 Å Co combination used in the AF-biased spin valves.

Again we note that the GMR curve of figure 5.4 was measured with the direction of the applied magnetic field perpendicular to the current direction. When the field is applied along the current direction, the maximum GMR ratio is a bit ($\approx 0.1\%$) lower.

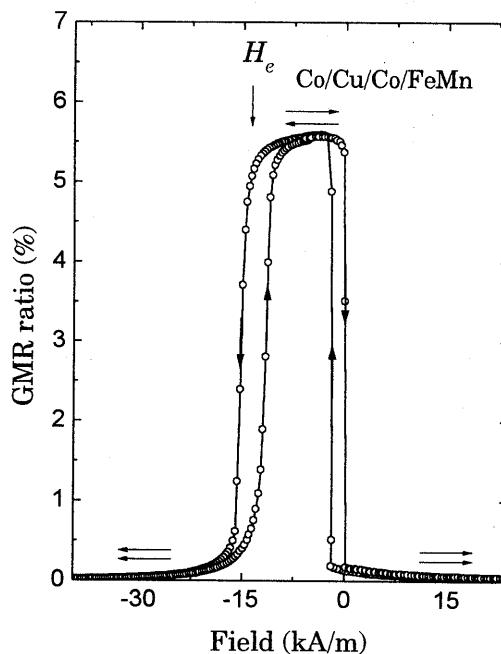


Figure 5.4: Magnetoresistance at room temperature of the sample Si(100)/30 Å Ta/100 Å Co/40 Å Cu/50 Å Co/100 Å Fe₅₀Mn₅₀/30 Å Ta. The horizontal arrows indicate the magnetization directions, and the vertical arrows denote the field course.

5.4 Conclusion

In this chapter we explained the magnetization and magnetoresistance curves of two types of spin valves: AF-biased spin valves and exchange-biased spin valves. All the samples used in our investigations described in chapters 6, 7, 8, and 9 are based on one of these two types of spin valves. The most important feature of these samples is that two magnetic layers can switch between a state of completely parallel magnetization directions and a state of completely antiparallel magnetization directions upon the application of a magnetic field, although they are not magnetically coupled. This is possible because the magnetization direction of one of these layers is pinned in a certain direction. Since the magnetic layers are not coupled to each other, the degree of antiparallel alignment can not depend on coupling effects. This is the main reason why spin valves are preferred above AF-coupled multilayers for investigating the contributions of spin-dependent bulk and interface scattering to the GMR effect.

6. Interface intermixing and magnetoresistance in Co/Cu/Co spin valves

The contents of this chapter has been published in a slightly modified form in J. Appl. Phys. 78, 7202 (1995) and in Mat. Res. Soc. Symp. Proc. Vol. 384, 391 (1995).

6.1 Introduction

In the search for the spatial origin of the GMR effect one approach is to investigate the effect of intermixing at the interfaces between the magnetic and nonmagnetic layers. Apart from layer thicknesses and intrinsic material quantities, such as (spin-dependent) conductivities of the layers, interface roughness (e.g. intermixing) is one of the parameters that determines the magnitude of the giant magnetoresistance. On the one hand it is known that dilute impurities in ferromagnetic materials such as Fe, Co, and Ni can lead to spin-dependent electron scattering and thus some intermixing at the interfaces could enhance the GMR. On the other hand, when the interfaces are too rough, the large amount of interface scattering will reduce the probability of electrons to cross the nonmagnetic spacer layer and therefore reduce the GMR. One could imagine that some optimum in the interface roughness exists. Evidence for this is reported for the Fe/Cr system (Pet91).

As explained in the previous chapter this type of investigation should be performed in spin valves with uncoupled magnetic layers in which the degree of antiparallel alignment is not affected by the intermixing. In this chapter we will report on the effect of interface intermixing on the magnetoresistance in Co/Cu/Co spin valves with uncoupled Co layers. Two different types of spin valves were used although not both were investigated to the same extent. One type consists of exchange-biased spin valves and the other of spin valves in which one of the Co layers of the Co/Cu/Co spin valve is antiferromagnetically coupled to a third magnetic layer, the AF-biased spin valves. Details on both kind of structures can be found in the previous chapter. The Co/Cu interfaces in our samples are intentionally intermixed by co-deposition of Co and Cu in the exchange-biased spin valves and by alternately depositing very thin layers (< 1 ML) of Co and Cu in the AF-biased spin valves.

Since the samples that are described here are grown by sputtering, they will always possess some intermixing originating from the sputtering process. For the samples employed in the present study this intrinsic diffuse intermixing was found to be of the order of a few Å. This intermixed region is intentionally increased to a nominal thickness of 36 Å. Therefore, the results of these samples rather will provide mainly information on the "bulk properties" of the intermixed

regions. Finally we will compare our experimental results with results of calculations on a model system.

6.2 Samples with intermixed interface(s)

According to the bulk phase diagram of $\text{Co}_x\text{Cu}_{1-x}$ (Han58) no thermodynamically stable solid solutions exist at any temperature in the composition range $0.05 \leq x \leq 0.88$ due to the immisibility of the two components. However, it has been established that it is possible to produce a metastable $\text{Co}_x\text{Cu}_{1-x}$ alloy over the whole concentration range by co-evaporation (Kne62) and co-sputtering (Chi91).

In our AF-biased spin valves $\text{Co}_1/\text{Ru}/\text{Co}_2/\text{Cu}/\text{Co}_3$ (where the subscript is just to discern between the different Co layers), the Co/Cu interfaces are intermixed by alternately sputtering 1 Å Co and 1 Å Cu. In some samples an intermixed region of thickness d was grown at the Cu/ Co_3 interface and in other samples intermixed regions of thickness $d/2$ were grown at both the Co_2/Cu and the Cu/ Co_3 interface. The total thickness d of the mixed region(s) has been varied between 0 and 36 Å. When there is an intermixed region, the thickness of the Co and Cu layers are decreased such that the total amount of Co and Cu is kept constant. Since the amount of 1 Å Co and 1 Å Cu that is alternately sputtered in the samples of the present study is smaller than the distance between the (111) planes of fcc Co and Cu (2.0467 and 2.088 Å, respectively) we may expect that due to this intentional intermixing an alloy-like region at the interface will form.

In the exchange-biased type spin valves the Co-Cu mixed regions were formed by co-sputtering of Co and Cu. This results in spin valves with composition: $\text{Si}(100)/30 \text{ Å Ta}/(100-d/4) \text{ Å Co}/(d/2) \text{ Å Co-Cu}/(40-d/2) \text{ Å Cu}/(d/2) \text{ Å Co-Cu}/(50-d/4) \text{ Å Co}/100 \text{ Å Fe}_{50}\text{Mn}_{50}/30 \text{ Å Ta}$. In these samples the nominal thickness of the total intermixed Co-Cu region, d , varies from 0 to 30 Å. To vary the intrinsic initial intermixing two series were grown in which the Co/Co-Cu/Cu/Co-Cu/Co-stack was deposited at Ar-pressures of 5 and 10 mTorr while all other layers are always grown at an Ar-pressure of 5 mTorr. Kools (Koo95) has shown that in $\text{Ni}_{80}\text{Fe}_{20}/\text{Cu}$ exchange-biased spin valves almost similar to the exchange-biased spin valves that were used in the present study, the initial intermixing decreases when the Ar-pressure increases. This is caused by a decrease in flux of energetic metal atoms reaching the substrate due to a higher rate of inelastic collisions with Ar atoms.

Childress and Chien (Chi91) and Kneller (Kne62) both have reported a reduction of magnetic moment of Co atoms when intermixed with Cu. For a metastable alloy of 50% Co and 50% Cu co-sputtered at 77 K on glass or mica, Childress reports a saturation magnetization of $\approx 125 \text{ emu/g}_{\text{Co}}$ compared to $175 \text{ emu/g}_{\text{Co}}$ for bulk fcc Co. In our samples, however, we did not measure any reduction of magnetic moment (at $T = 210 \text{ K}$) as a function of intermixed region

thickness, neither in the AF-biased spin valves nor in the exchange-biased spin valves. Even in an additional series of samples (not spin valves) with the composition: $200 \text{ \AA Ru}/6 \cdot [(40-x) \text{ \AA Cu}/x \cdot (1 \text{ \AA Co} + 1 \text{ \AA Cu}) / (25-x) \text{ \AA Co}] / 10 \text{ \AA Cu} / 30 \text{ \AA Ru}$ with x up to 23 such that 92% of the Co is intermixed with Cu, we did not observe any loss of magnetic moment. This indicates that the intermixing of Co and Cu in our samples is not extending down to an atomic scale and that there are probably Co clusters in the intermixed regions. This might be due to the fact that our samples are sputtered at room temperature, and not at $T = 77 \text{ K}$ like the samples of Childress (Chi91), which causes a higher mobility of the atoms reaching the substrate.

To investigate the intermixing in our samples, glancing incidence X-ray measurements have been performed. In these measurements a highly collimated X-ray beam (Cu $K\alpha$ radiation) impinges on a flat sample at a small angle θ . In most cases the specular reflectivity at an angle 2θ is recorded as is described in chapter 2. Often these measurements are combined with X-ray fluorescence measurements. While the fluorescence yields information on the chemical composition of the material, the $\theta - 2\theta$ scans contain information on the density and the thickness of each layer as well as on the lateral average interface widths of the layers (Boe91, Boe95).

To extract the desired parameters such as layer thicknesses, densities, and interface width from the experiment, the measurements are to be compared with calculations. In these calculations the shape of both reflectivity and fluorescence can be described using a Fresnel-based formalism. To describe the intentionally introduced interface intermixing in our samples in an appropriate way, we assumed in our calculations an extra layer between Co and Cu. Furthermore, at each interface an error-function-shaped profile with a certain interface width was assumed.

As an illustration, in figure 6.1 the experimental X-ray reflectivity curves including calculations are shown for some of the AF-biased samples with a nominal thickness of the intermixed region (from top to bottom) of 0, 8, 20, and 32 \AA . In table 6.1 the experimentally determined thickness d_{expt} of the intermixed region, as resulting from our calculations, is given for the same samples shown in figure 6.1. The thickness denoted by d_{nom} is the nominal thickness of the intermixed regions. The thickness d_{expt} in table 6.1 is the total thickness of the intermixed region including its interface width. It is important to realize that in general the interface width contains a contribution from geometrical roughness (deviations from the flatness of the interface between two homogeneous materials on a lateral length scale of a few tens of nanometers) which is not important for the GMR effect, and compositional roughness (=interdiffusion with a lateral length scale of atomic size, $\approx 2 \text{ \AA}$). With X-ray measurements we cannot discern between both kinds of roughness because the X-ray information is obtained from an average over the correlation length of the

X-rays projected on the film-plane, which is several μm . For this same reason we cannot distinguish between perfect intermixing between Co and Cu or the existence of Co-clusters in the mixed regions with X-ray measurements.

Table 6.1: Nominal and experimental (determined by glancing incidence X-ray reflectivity measurements) layer thicknesses.

Sample	d_{nom} (\AA)	d_{expt} (\AA)
1	0	9
2	8	17
3	20	20
4	32	34

It clearly follows from the X-ray analysis that the thickness of the mixed Co-Cu interface layer we have to assume in our calculations to fit the measurements increases with the thickness of the alternately sputtered region. As mentioned before, there will be some intermixing between all layers even without alternately sputtering. The thickness of 9 \AA Co-Cu for the sample

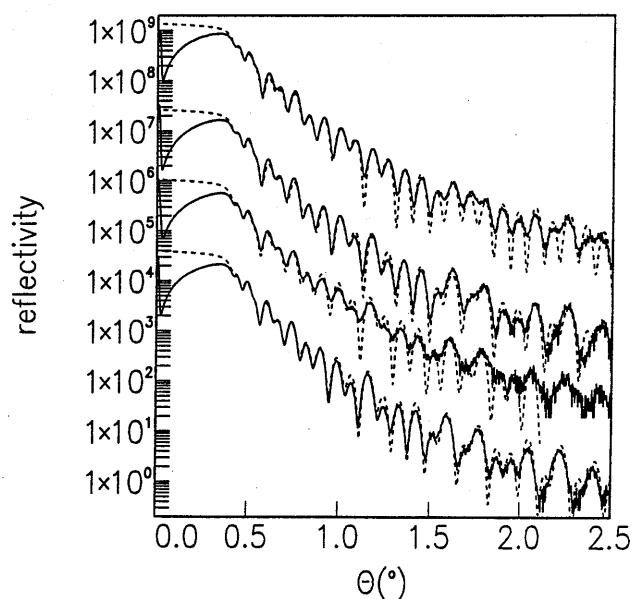


Figure 6.1: X-ray reflectivity curves (solid lines) and fits (dashed lines) for the samples of table 6.1. From top to bottom: sample 1, sample 2, sample 3, and sample 4. For clarity the reflectivity of samples 1, 2 and 4 have been multiplied by 1000, 10, and 0.01 respectively.

without deliberately intermixing (sample 1) denotes an upper limit for the sum of this "initial intermixing" and the geometrical roughness. In exchange-biased spin valves almost similar to the exchange-biased spin valves that are investigated here, Kools has observed a geometrical roughness of about 5 Å by atomic force microscopy measurements (Koo95), which is smaller than the 9 Å found for sample 1. This could indicate that the initial diffuse intermixing in our samples is of the order of 4-5 Å.

As stated in the previous chapter the AF-biased spin valves have a rather poor texture where the full width at half maximum (FWHM) of the [111] rocking curves is about 13°. In figure 6.2 we show the FWHM of the rocking curves of the exchange-biased spin valves as a function of the total intermixed thickness d . In the next section we will relate this behavior to the measured conductance and magnetoresistance for these samples.

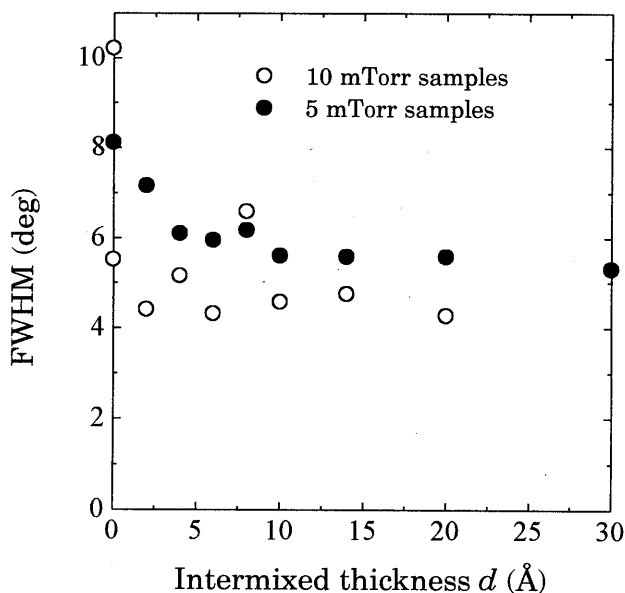


Figure 6.2: Full width at half maximum (FWHM) of the [111] XRD rocking curves versus total intermixed thickness d , for the exchange-biased spin valves.

6.3 Results

In figure 6.3 the measured variation of G_p , ΔG and GMR ratio ($=\Delta G/G_{ap}$) with the nominal thickness of the total intermixed region(s) is shown for both AF-biased and exchange-biased spin valves at room temperature. The inter-

mixing at the interfaces results in a decrease in the electrical conductivity of the samples. When compared to data at $T = 10$ K (for the AF-biased samples these results are shown in figure 6.4) the conductance G is naturally smaller at room temperature due to additional scattering processes (phonons, magnons, etc). Also ΔG and the GMR ratio are lower at $T = 300$ K. The reduction with a factor of ≈ 1.85 for the GMR ratio of the samples without intentionally intermixing when the temperature is increased from 10 to 300 K is comparable to the factor of 1.7 measured by Mosca *et al.* (Mos91) for Co/Cu multilayers. Such a reduction can be explained within the Camley-Barnas (CB) model when including (Duv94):

1. temperature-dependent phonon and magnon resistivity terms for the Co and Cu layers that are determined from bulk materials and
2. a temperature-dependent resistance term resulting from the interfaces.

At small thickness the exchange-biased samples, grown at 5 mTorr, show a remarkable increase in ΔG and GMR ratio. It would be tempting to relate this behavior to a change in the spin-dependent interface scattering. However, for these samples the FWHM of the rocking curves (figure 6.2) show an initial decrease and a saturation at about 10 Å. This could point at an increasing grain size or a smaller degree of misalignment at the grain boundaries which seems to be in agreement with the initial increase in conductivity observed in these samples. It is known from other experiments (Rij95) that, for samples grown on a Ta buffer layer, a non-negligible part of the resistance is due to grain boundary scattering. In polycrystalline $\text{Ni}_{80}\text{Fe}_{20}$ -films it is found (Rij95) that the effective value of $\alpha = \lambda^\uparrow / \lambda^\downarrow$ is smaller than the bulk value due to grain boundary scattering of mainly the spin-up electrons. Because of their larger (bulk) mean free path, spin-up electrons are more sensitive to grain boundary scattering than spin-down electrons. Therefore, an increase in the grain size or a reduction of the degree of misalignment near the grain boundaries can 1) decrease the scattering probability, leading to an increase in conductivity and 2) increase the spin dependence of the scattering, leading to a larger value of ΔG . This is just what is shown in figure 6.3 for the samples grown at 5 mTorr for small intermixing. Possible effects of the artificial intermixing on the (spin-dependent) interface scattering, if there are any with the present degree of initial intermixing, are not distinguishable from these structural effects.

The exchange-biased samples grown at 10 mTorr and the AF-biased spin valves do not show large changes in structural quality. In these samples clearly no dramatic changes in G_p , ΔG , and GMR ratio are observed when the thickness of the intermixed region is increased. They rather show a gradual decrease even when the intermixed thickness grows larger than the Cu spacer. Of course in this case it is difficult to speak of interface intermixing since the "interface" between Co and Cu has now become a layer of its own.

These results are in marked contrast with Suzuki and Taga (Suz93) who have reported a sharp decrease in GMR ratio from 27 to 4% when only co-sputtering 1.5 Å Co and Cu at the interfaces of AF-coupled Co/Cu multilayers. This difference could be explained either by a coupling effect in the samples of Suzuki and Taga, or to a different amount of initial intermixing (see foregoing paragraphs).

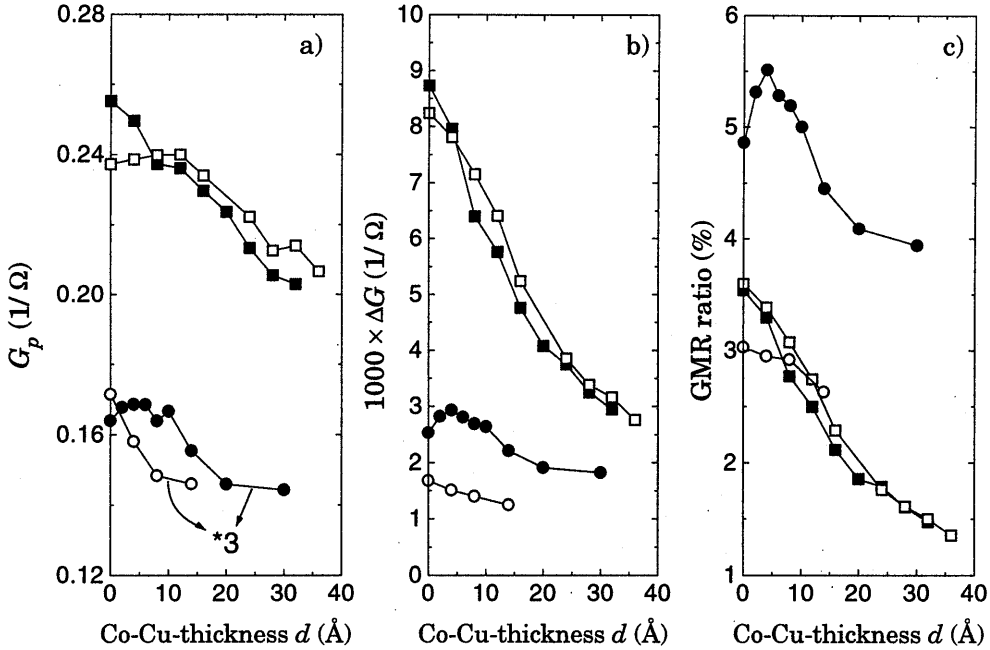


Figure 6.3: (a) G_p , (b) ΔG , and (c) GMR ratio ($\Delta G/G_{ap}$) as a function of total intermixed region thickness d measured at room temperature for both AF-biased and exchange-biased spin valves. The conductance G_p of the exchange-biased samples is multiplied by a factor of 3. ■ AF-biased spin valves with one interface intermixed, □ AF-biased spin valves with two interfaces intermixed, ● exchange-biased spin valves deposited at 5 mTorr, and ○ exchange-biased spin valves deposited at 10 mTorr.

From figure 6.3 we can see that there seems to be no significant difference between an intermixed region of thickness d at the interface between the Cu layer and the free Co layer or intermixed regions of thickness $d/2$ at both Co/Cu interfaces. Both cases result, at least for the AF-biased samples for which we investigated this, in the same slope of G_p , ΔG , and GMR ratio as a function of intermixed thickness. A small difference in magnitude is already present in samples of the same composition (e.g., the samples without intermixing 75 Å Co/6 Å Ru/25 Å Co/40 Å Cu/100 Å Co) and is therefore ascribed to nonperfect reproducibility. A similar experimental observation has been reported for the Fe/Cr system by Baumgart *et al.* (Bau91), when ultrathin layers (0–4 Å) of V, Mn, Al, Ir and Ge are inserted at the Fe/Cr interfaces. It makes no difference whether a thickness d of these layers is inserted at alternate interfaces or a thickness $d/2$ at every Fe/Cr interface. What seems to be more important than the number of interfaces, is the overall number of additional scatterers per multilayer period. This result, combined with the fact that the GMR ratio decreases with increasing intermixing, indicates that in the intermixed regions, at least for the thicknesses we have investigated here, the increase in the scattering rates compared to Co and Cu is of more importance than a possible spin-dependence in the scattering.

6.4 Discussion

At this point we would like to substantiate our provisional conclusions with model calculations and find some quantitative parameters that confirm that the most essential feature of our samples is an increase in the scattering rates (i.e. a reduction in the mean free paths) in the Co-Cu-mixed regions. Moreover we might obtain information on the scattering asymmetry in the Co layers and at each interface.

The GMR ratio as a function of interface roughness is calculated by various authors (Hoo94, Bar95, Lit97), describing the interface roughness in terms of two parameters: the root mean square of the height deviations of the ideal flat interface and the in-plane lateral correlation length (see also chapter 3). It is, however, not explicitly explained if and how these parameters could be related to interface intermixing, which is one particular form of roughness distinct from, e.g., geometrical roughness. Moreover, both an increase and a decrease with increasing roughness is reported. Theoretically this difference has not been clarified yet. Also experimentally the results of these models are not verified since it is not yet possible to control the interface roughness with atomical resolution. Furthermore, the results of the Hood-Falicov-Penn (HFP) model (Hoo94), that the most important changes in the GMR ratio due to increasing roughness occur within a rough interface of thickness ≤ 2 Å, cannot be checked in our samples. This is because the present study uses sputtered layers that have

as grown already an intermixed region $\geq 2 \text{ \AA}$. Therefore we will try to interpret our results with the common CB-model (Cam89, Bar90) as treated in chapter 3).

With the help of the CB-model it is possible to simulate bulk spin-dependent scattering by choosing different λ^\uparrow and λ^\downarrow in the magnetic layers. Interface spin-dependent scattering will be the result of the asymmetry in the transmission and reflection coefficients, T^σ and R^σ , for different σ . In the model each layer is considered to have a perfectly flat interface. Therefore, to simulate some geometrical or chemical (intermixing) roughness at the interface one can either vary the parameters T^σ and R^σ or, following the approach of Johnson and Camley (Joh91) to describe intermixing in the Fe/Cr system, assume an additional layer at the interface with a "bulk mean free path" of its own. Since in our samples the intermixed regions become quite large, we have chosen for the latter approach which of course will also provide an additional interface.

An example of a fit with the CB-model to the low-temperature data of the AF-biased spin valves is shown in figure 6.4, which shows that it is possible to fit the data when assuming small or no scattering asymmetry in the intermixed regions; however, because of the large number of fit parameters it was possible to describe the data also with a different set of parameters. For example, when no interface scattering was assumed ($T^\uparrow = T^\downarrow = 1$) it is possible to fit the data as well, when assuming $\lambda_{\text{Cu}} = 500 \text{ \AA}$, $\lambda_{\text{Ru}} = 2.6 \text{ \AA}$, $\lambda_{\text{Co}}^\uparrow / \lambda_{\text{Co}}^\downarrow = 240 \text{ \AA} / 0.45 \text{ \AA}$, and $\lambda_{\text{Co-Cu}}^\uparrow / \lambda_{\text{Co-Cu}}^\downarrow = 88 \text{ \AA} / 48 \text{ \AA}$. We conclude that this model description does not provide us with unique parameters, and we further refrain from a quantitative analysis. We will restrict ourselves to more transparent qualitative calculations on a model system to gain insight in the role of the scattering processes as a function of intermixed region thickness.

As a model system we take a simple trilayer: $50 \text{ \AA} \text{ Co} / 40 \text{ \AA} \text{ Cu} / 50 \text{ \AA} \text{ Co}$. We represent the intermixed regions as extra layers with "bulk" parameters $\lambda_{\text{Co-Cu}}^\uparrow$ and $\lambda_{\text{Co-Cu}}^\downarrow$ and interfaces of their own. In fact this is the same system that we have investigated experimentally both in the AF-biased as in the exchange-biased spin valves, however, we have omitted here the Co/Ru part of our samples since this part does not contribute to the magnitude of the magnetoresistance. The total thickness of the structure is always kept constant at 140 \AA . Electron transmission through the interfaces is described by the parameter T^σ . We assume that electrons that are not transmitted are diffusely scattered such that there is no reflection ($R^\sigma = 0$). At the outer boundaries we assume completely diffusive scattering ($p^\sigma = 0$). Further input parameters that we use are: $\lambda_{\text{Co}}^\uparrow + \lambda_{\text{Co}}^\downarrow = 100 \text{ \AA}$ and $\lambda_{\text{Cu}}^\uparrow = \lambda_{\text{Cu}}^\downarrow = 200 \text{ \AA}$, which are known from literature to be reasonable values (Die93, Fre93). As the conductivity decreases when the intermixed thickness increases, we take a smaller conductivity of the mixed layer: $\lambda_{\text{Co-Cu}}^\uparrow + \lambda_{\text{Co-Cu}}^\downarrow = 50 \text{ \AA}$. In the following we consider the effect of interface intermixing on the GMR effect in two different cases: 1) no interface spin-dependent scattering (SDS), or 2) no bulk SDS.

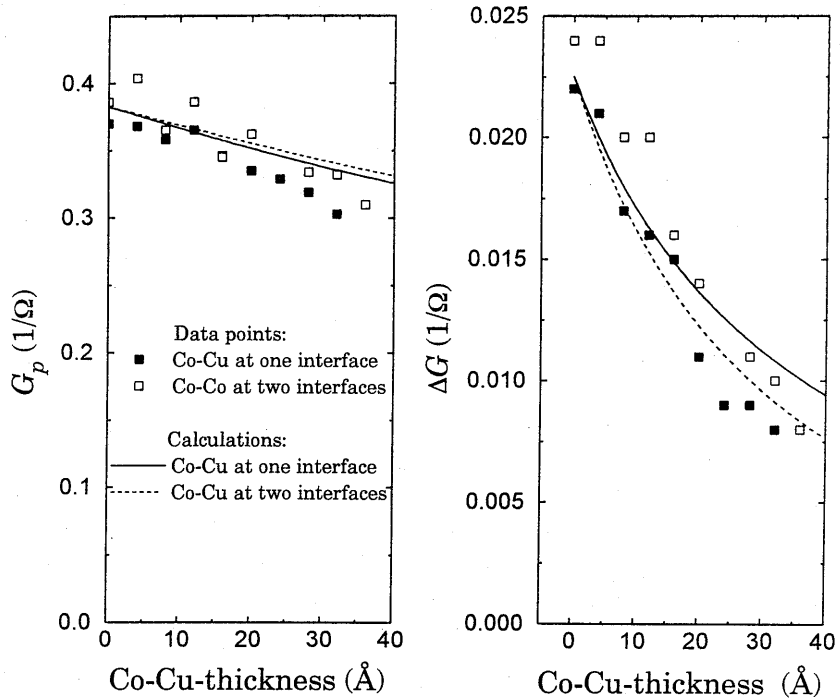


Figure 6.4: Example of a fit of the low temperature data ($T=10$ K) for the AF-biased spin valves according to the CB-model. The fit parameters are: $\lambda_{\text{Co}}^{\uparrow} = 140$ Å; $\lambda_{\text{Co}}^{\downarrow} = 10$ Å; $\lambda_{\text{Cu}}^{\uparrow} = \lambda_{\text{Cu}}^{\downarrow} = 795$ Å; $\lambda_{\text{Co-Cu}}^{\uparrow} = \lambda_{\text{Co-Cu}}^{\downarrow} = 78.9$ Å; $\lambda_{\text{Ru}}^{\uparrow} = \lambda_{\text{Ru}}^{\downarrow} = 10$ Å, $T_{\text{Co/Ru}}^{\uparrow} = T_{\text{Co/Ru}}^{\downarrow} = 0.75$; $T_{\text{Co/Cu}}^{\uparrow} / T_{\text{Co/Cu}}^{\downarrow} = 1/0.2$; $T_{\text{Co-Cu/Cu}}^{\uparrow} / T_{\text{Co-Cu/Cu}}^{\downarrow} = 1/1$; and $T_{\text{Co-Cu/Co}}^{\uparrow} / T_{\text{Co-Cu/Co}}^{\downarrow} = 1/0.2$.

6.4.1 No interface spin-dependent scattering

In the case of no interface spin-dependent scattering the interface parameter T^{σ} is set at $T^{\sigma} = 1$ at all interfaces. It is assumed that there is an asymmetry in the mean free paths of Co: $\lambda_{\text{Co}}^{\uparrow} / \lambda_{\text{Co}}^{\downarrow} = 90$ Å/10 Å. Two different alternatives are compared. In the first case we take the scattering in the intermixed regions to be spin-independent ($\lambda_{\text{Co-Cu}}^{\uparrow} = \lambda_{\text{Co-Cu}}^{\downarrow} = 25$ Å), in the other case we will assume in the intermixed layers the same asymmetry in the scattering as in the Co layers ($\lambda_{\text{Co-Cu}}^{\uparrow} / \lambda_{\text{Co-Cu}}^{\downarrow} = 45$ Å/5 Å).

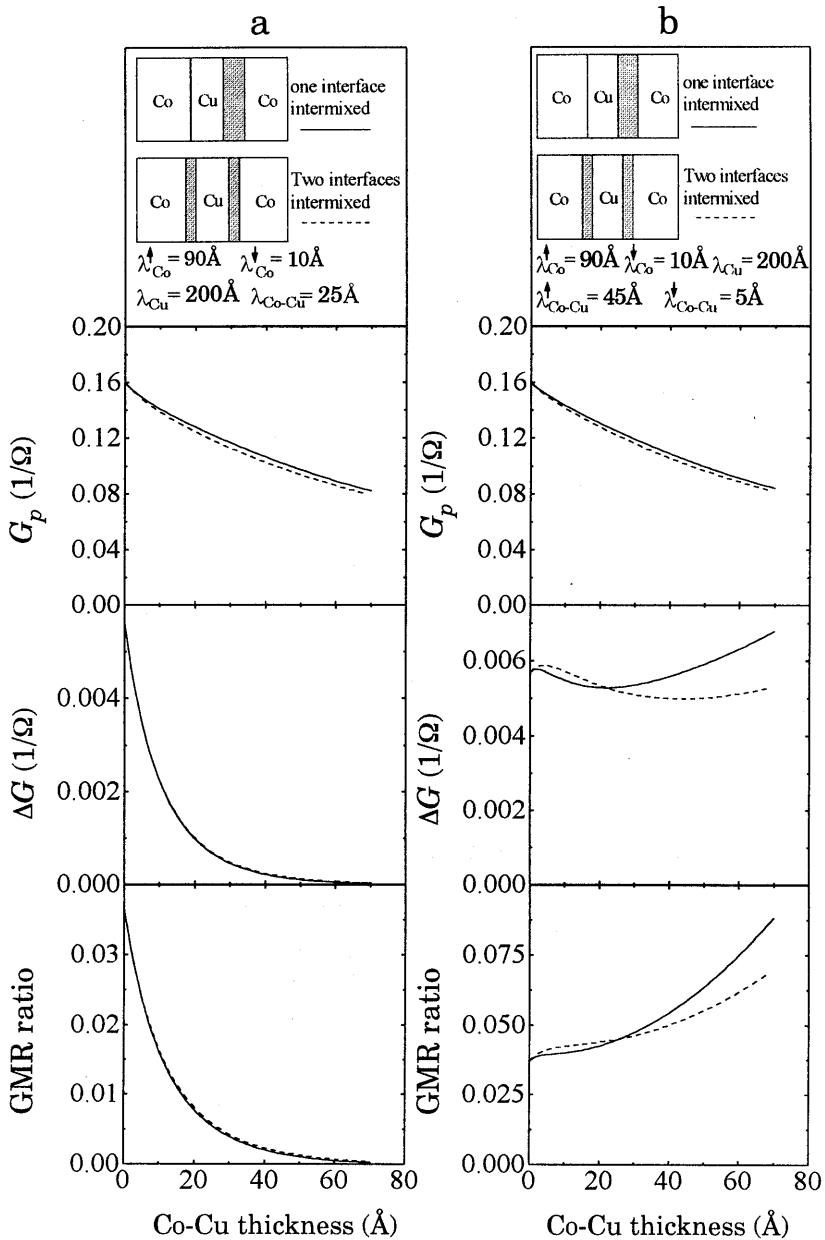


Figure 6.5: Calculation of G , ΔG , and GMR ratio ($\Delta G/G_{ap}$) with the CB-model for a model system Co/Cu/Co with intermixing at one interface (solid line) and intermixing at two interfaces (dashed line) in the case where no interface SDS is assumed ($T^{\uparrow} = T^{\downarrow} = 1$ at each interface). The input parameters are drawn in the top panels of the figure.

The results for G_p , ΔG and the GMR ratio ($=\Delta G/G_{ap}$) are shown in figure 6.5. In both cases the conductivity decreases because the resistivity of the intermixed layers is larger than that of Co and Cu. In the case of spin-independent scattering in the intermixed layers (figure 6.5a) ΔG and the GMR ratio decrease monotonously. This can be understood because the intermixed layers in this case can be viewed as part of the nonmagnetic spacer layer. Thus intermixing in this case leads effectively to an increase in spacer layer thickness and a decrease in Co layer thickness. Both effects will result in a decrease of ΔG and GMR ratio.

In the case of spin-dependent scattering in the intermixed layers (figure 6.5b) the behavior of ΔG is more complicated. First, when the intermixed layers are very thin, a small part of the Cu spacer has been substituted by Co-Cu that displays spin-dependent scattering. This results in an increase of ΔG . Then, when the intermixed layers grow thicker, another effect becomes dominant. Since the conductivity of the intermixed layers is smaller than the conductivity of Co, these layers will prevent part of the electrons from the Co layers from crossing the Cu spacer and contribute to ΔG . This effect will lead to a decrease of ΔG until the intermixed layers have reached a thickness such that they will completely mask the Co layers and we have effectively a Co-Cu/Cu/Co-Cu spin valve system. In this regime a further increase of thickness of the intermixed layers will decrease the Cu spacer thickness which yields an increase in ΔG again. The behavior of the GMR ratio simply follows from the ratio of ΔG and G_{ap} .

6.4.2 No bulk spin-dependent scattering

We have made simulations for the case of no bulk spin-dependent scattering using $\lambda^\uparrow = \lambda^\downarrow$ in each layer. We use $\lambda_{\text{Co}}^\uparrow = \lambda_{\text{Co}}^\downarrow = 50 \text{ \AA}$, $\lambda_{\text{Co-Cu}}^\uparrow = \lambda_{\text{Co-Cu}}^\downarrow = 25 \text{ \AA}$ and $\lambda_{\text{Cu}}^\uparrow = \lambda_{\text{Cu}}^\downarrow = 200 \text{ \AA}$. At the interfaces between Co and Cu we will assume spin-dependent interface scattering: $T^\uparrow/T^\downarrow = 1/0.2$. When there is an intermixed region we will again consider two cases. In the first case we will assume spin-dependent scattering at the interfaces between the Co layers and the intermixed layers ($T^\uparrow/T^\downarrow = 1/0.2$) but no spin-dependent scattering at the interfaces between the Cu layers and the intermixed layers ($T^\uparrow/T^\downarrow = 1/1$). In the other case we will assume spin-dependent scattering at the interfaces between the Cu layer and the intermixed layers ($T^\uparrow/T^\downarrow = 1/0.2$), but no spin-dependent scattering at the interfaces between the Co layers and the intermixed layers ($T^\uparrow/T^\downarrow = 1/1$). The interfaces where we assume spin-dependent scattering are shown in the top-panels of figure 6.6.

The results for G_p , ΔG and GMR ratio are shown in figure 6.6. In the case of spin-dependent scattering at the Co interfaces as well as in the case of spin-dependent scattering at the Cu interfaces the conductivity of the system

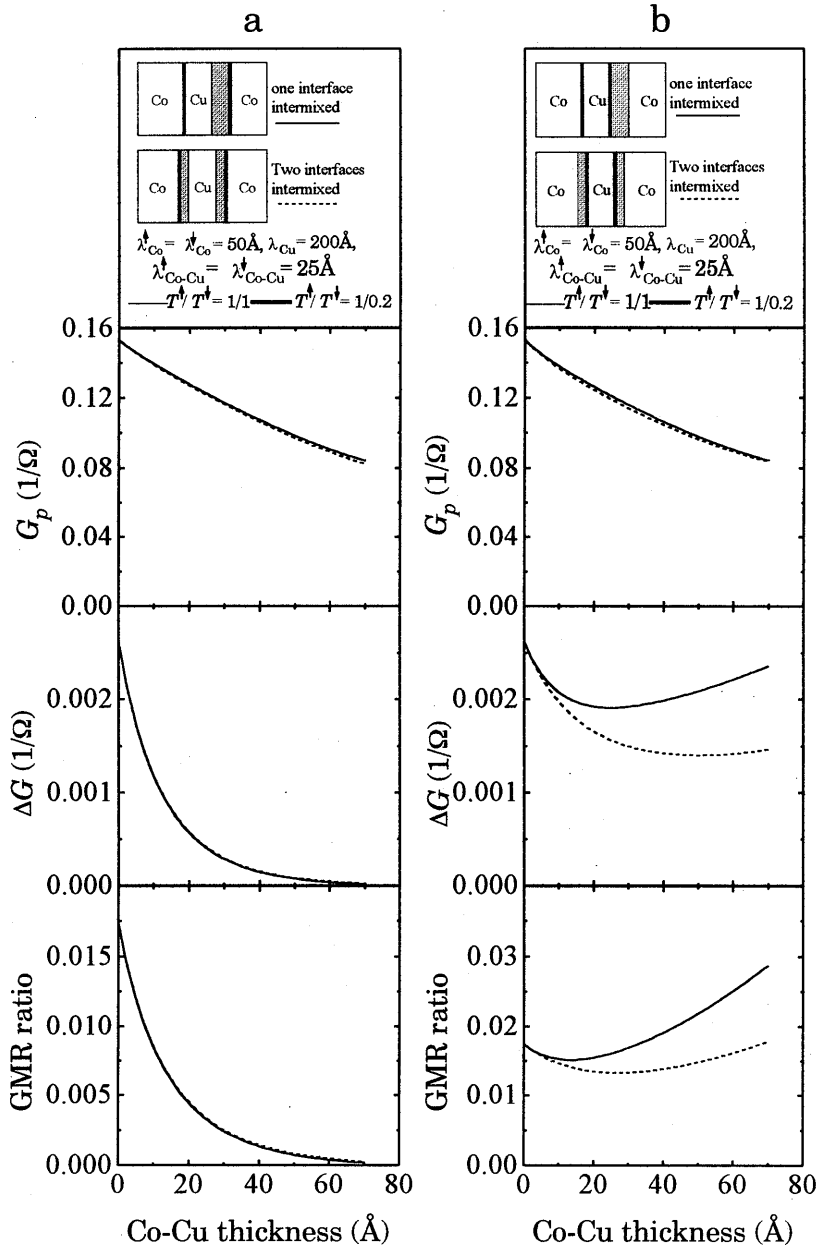


Figure 6.6: Calculation of G , ΔG , and GMR ratio ($\Delta G/G_{ap}$) with the CB-model for a model system Co/Cu/Co with intermixing at one interface (solid line) and intermixing at two interfaces (dashed line) in the case where no bulk SDS is assumed ($\lambda^{\uparrow} = \lambda^{\downarrow}$ in each layer). The input parameters are drawn in the top panels of the figure.

decreases as the intermixing increases due to the high resistivity of the intermixed Co-Cu layer(s).

In case of spin-dependent scattering at the Co interfaces (figure 6.6a) ΔG decreases monotonously as one would expect as intermixing in this case leads effectively to an increase of spacer layer thickness and an increase of spacer resistivity.

Assuming spin-dependent scattering at the Cu interfaces (figure 6.6b) leads to a minimum in ΔG . This minimum occurs when the thickness of the intermixed layer(s) equals 25 Å which is the mean free path in the intermixed layers. We can understand this result in the following way. For small thickness of the intermixed layers ΔG decreases because the mean free paths in the intermixed layers are smaller than those in the Co layers, see chapter 3. This decrease will stop when the thickness of the intermixed layers is such that they shield the Co layers completely, i.e., when the thickness of the intermixed layers equals the mean free path in the intermixed layers. Effectively we have now a Co-Cu/Cu/Co-Cu spin valve in which the Co layers merely act as shunt layers. Increasing the intermixing even further will result in a smaller distance between the Cu interfaces and therefore to an increase of ΔG .

From comparison of the experimental data and the model calculations one may conclude that the best description is obtained when no spin-dependent scattering in the Co-Cu-mixed region is assumed in the case of no interface spin-dependent scattering (figure 6.5a) or when assuming spin-dependent scattering at the Co/Co-Cu interfaces in the case of no bulk spin-dependent scattering (figure 6.6a). In both cases a monotonous decrease of G , ΔG and GMR ratio is observed and there is almost no difference between intermixing at one interface or divided over two interfaces, as can be seen by the solid and dashed curves in figures 6.5a and 6.6a. Note that these model calculations for bulk as well as for interface spin-dependent scattering are in agreement with our provisional conclusion, based on the measurements, that a reduction of the mean free paths in the intermixed Co-Cu regions for both spin directions, is of more importance than a possible spin-dependence in the scattering in these regions.

It should be noted, however, that the intermixed regions are not uniform in composition, but will show a compositional gradient. This was not taken into account in our calculations, where the intermixed regions were modelled as additional homogeneous layers with well-defined interfaces. Tentatively we can distinguish between three zones, each with a different Co concentration, as is schematically indicated in figure 6.7a. In the middle of the Co-Cu region there will be an equal amount of Co and Cu. According to the magnetic moment measurements there might be Co clusters in this region. At the interfaces with the Co and Cu layers there will be compositional gradients. As these gradients are from Co to Co-Cu at one side and from Cu to Co-Cu at the other side of the

Co-Cu region, there will be a larger thickness that has a surplus Co and a larger thickness that has a surplus Cu than when there is a compositional gradient directly between Co and Cu, as in figure 6.7b. All three areas can have a different spin dependence, which we cannot discern from our experiment. When the scattering in one of the areas is spin-independent, this can already decrease the magnetoresistance. It might therefore be worthwhile to investigate other compositions of artificial intermixing (e.g., $\text{Co}_{0.75}\text{Cu}_{0.25}$ instead of $\text{Co}_{0.5}\text{Cu}_{0.5}$) also.

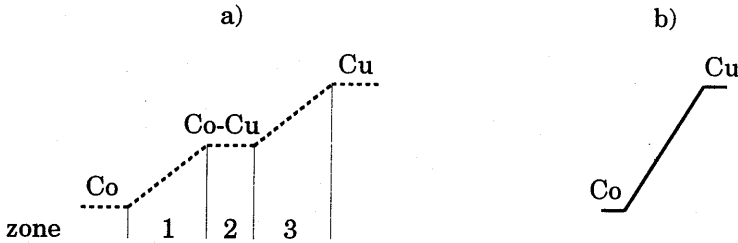


Figure 6.7: Schematic representation of the Co (Cu) concentration. a) The intermixed region is large. In zone 1 the Co concentration is > 0.5 , in zone 2 the Co concentration is 0.5 , in zone 3 the Co concentration is < 0.5 . b) There is no deliberate intermixing. Due to initial intermixing there will be a compositional gradient directly from Co to Cu.

6.5 Conclusions

We have measured the effect of interface intermixing in two different types of Co/Cu/Co spin valves with uncoupled Co layers. The intermixing is induced by alternately sputtering of 1 \AA Co and 1 \AA Cu in the AF-biased spin valves or by co-sputtering in the exchange-biased spin valves. The intermixing does not affect the magnetic moment of the Co atoms. A gradual, monotonic decrease of G , ΔG and GMR ratio at low temperature as well as at room temperature is observed when the nominal thickness of the intermixed regions, d , is increased from 0 \AA to maximal 36 \AA in the AF-biased spin valves. There is no significant difference between an intermixed region of thickness $d \text{ \AA}$ at one Co/Cu interface or intermixed regions of thickness $d/2 \text{ \AA}$ at both Co/Cu interfaces. These results indicate that the increase in the overall scattering rates for both spin-down and spin-up, due to the intermixed Co-Cu regions, is of more importance than a possible (small) increase in the spin-dependence in the scattering. Calculations on a model system according to the CB-model yield the same qualitative behavior as our measurements, when assuming no interface spin-dependent scattering

and spin-independent scattering in the intermixed regions or assuming no bulk spin-dependent scattering and spin-independent scattering at the Cu/Co-Cu interfaces.

7. Analysis of scattering lengths in Co/Cu/Co and Co/Cu/Co/Cu spin valves

The contents of this chapter has been published in a slightly modified form in Phys. Rev. B54, 9365 (1996).

7.1 Introduction

From the previous chapter we have learned that, at least for the sputtered samples that we investigated, increasing the initial intermixing of Co and Cu at the interfaces of Co/Cu/Co spin valves leads to a significant decrease of the magnetoresistance, although the effect is less dramatic than the steep decrease reported by Suzuki and Taga (Suz93). In this chapter we will try to determine the electron mean free paths as well as the asymmetry in the scattering lengths, if there is any, between spin-up and spin-down electrons inside the Co and Cu layers.

As stated before, experimental verification of the scattering asymmetry between spin-up and spin-down electrons is usually indirect via fitting experimental data with models such as a resistor network (Edw91), models based on the semiclassical Boltzmann transport equation (Cam89) or the quantum model of Zhang, Levy and Fert (Zha92). Due to the large number of input parameters these fits often do not give unambiguous results.

Recently Parkin (Par) proposed a more straightforward method to determine whether bulk spin-dependent scattering, represented by an asymmetry in the mean free paths λ^\uparrow and λ^\downarrow for spin-up and spin-down electrons respectively, plays an important role in ferromagnetic materials such as Co. It was suggested that in a spin valve, in which the spatial position of a thin, highly resistive, Ru barrier layer was shifted through one of the magnetic constituents, the GMR ratio is proportional to $1 - \exp(-t/\xi)$, with t the position of the Ru layer and ξ a characteristic length. Since the position of the Ru layer determines how far electrons may propagate into the ferromagnetic layer, ξ was suggested to represent the longest of the mean free paths, λ^\uparrow . Subsequently, a comparison was made in various magnetic and nonmagnetic systems such as Co, $\text{Ni}_x\text{Fe}_{1-x}$, and $\text{Cu}_x\text{Au}_{1-x}$ between λ^\uparrow and their bulk conductivity σ , that is proportional to $\lambda^\uparrow + \lambda^\downarrow$ according to equation (3.30). For a magnetic material with $\lambda^\uparrow \neq \lambda^\downarrow$, this would result in a slope of σ versus λ^\uparrow that is different from the case for a nonmagnetic material where $\lambda^\uparrow = \lambda^\downarrow$. In the limit that $\lambda^\downarrow = 0$, this difference in slope would amount to a factor of two. In figure 7.1 we have reproduced these results of Parkin. From the fact that all the data, from magnetic as well as nonmagnetic materials, lie on a single straight line, Parkin concluded that there was no evidence for a substantial bulk spin-dependent scattering at room temperature.

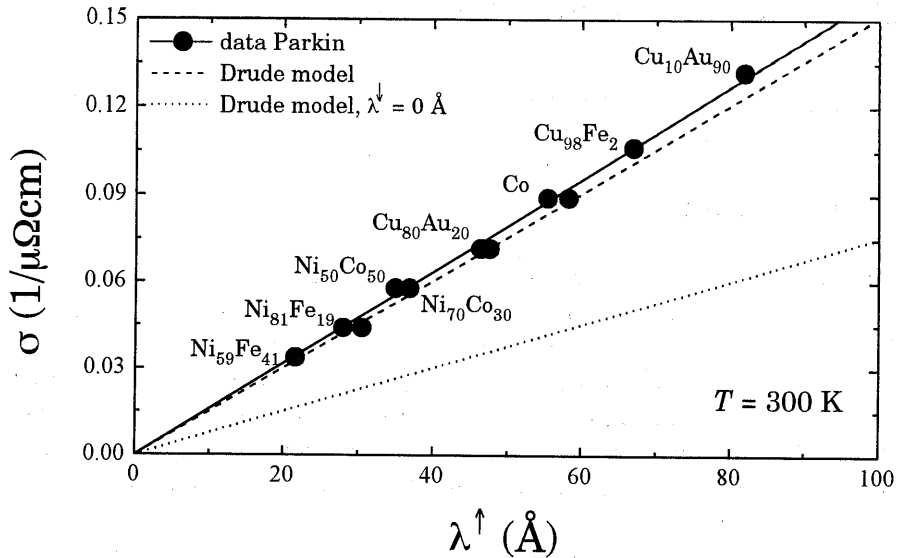


Figure 7.1: Conductivity σ as a function of the longest mean free path, λ^\uparrow , for various magnetic and nonmagnetic materials at room temperature. Data are taken from Parkin (Par). For comparison also the conductivity calculated with the Drude model with $\lambda^\uparrow = \lambda^\downarrow$ (dashed line) and $\lambda^\downarrow = 0$ (dotted line) are shown. These lines are calculated using the Fermi velocity of bulk Cu ($v_F = 1.57 \times 10^6$ m/s).

In this chapter we will investigate to what extent a theoretical basis for this method exists. For this purpose we analyze the transport properties of AF-biased spin valves like those described in chapter 5, with a shifting Ru barrier through the uncoupled ferromagnetic layer, using the Boltzmann transport equation. In particular we will investigate with model calculations what parameters determine the characteristic length scale ξ observed in the experimental data. It will be concluded that ξ is indeed related to λ^\uparrow provided that there is a large amount of bulk and/or interface spin-dependent scattering, however not by a simple equality relation as suggested by Parkin. Experimentally, Parkin applied the method to a number of alloys and Co only at room temperature, whereas we have concentrated on spin valves consisting of Cu and Co only, in which we first verified the efficiency of the diffusive scattering at an embedded thin Ru layer. Thereafter, the temperature dependence of the evaluated Co and Cu scattering

lengths and conductivity are used to address the role of bulk spin-dependent scattering.

7.2 Experimental

For our investigations we have grown three series of spin valves, all of which are based on the AF-biased spin valve discussed in chapter 5. The first series of spin valves was grown to test the effectiveness of the Ru barrier layer. This series has the composition: 200 Å Ru/75 Å Co/6 Å Ru/25 Å Co/ d_{Ru} Å Ru/30 Å Cu/ d_{Ru} Å Ru/100 Å Co/10 Å Cu/30 Å Ru, with d_{Ru} in the range 0-6 Å. The second series was designed to probe the longest of the mean free paths in Co, $\lambda_{\text{Co}}^{\uparrow}$, and has the following composition: 200 Å Ru/75 Å Co/6 Å Ru/25 Å Co/30 Å Cu/250 Å Co/30 Å Ru. A Ru barrier layer with a thickness of 2 Å was incorporated at various positions in the 250 Å Co layer. The thickness of this layer was chosen 2 Å because a thicker Ru layer, which might be a more effective barrier, resulted in antiferromagnetic coupling between the two parts of the 250 Å Co layer separated by Ru. Finally, the third series was designed to probe the scattering lengths in Cu and has for that purpose the composition: 200 Å Ru/75 Å Co/6 Å Ru/25 Å Co/30 Å Cu/25 Å Co/300 Å Cu/30 Å Ru, with a Ru barrier layer of 5 Å moving through the 300 Å Cu layer. Furthermore single Co and Cu layers were grown with the compositions: 200 Å Ru/ d_{Co} Å Co/30 Å Ru and 200 Å Ru/ d_{Cu} Å Cu/30 Å Ru, with $d_{\text{Co}} = 250, 500, 1000, \text{ and } 2000$ Å, and $d_{\text{Cu}} = 2000, 4000, 8000, \text{ and } 10000$ Å. All samples were grown on SiO₂ substrates, the 200 Å Ru base layer provides equal texture for all samples, and the 30 Å Ru cap layer prevents oxidation of the Co and Cu layers.

7.3 Results

The magnetic behavior of the spin valves without barrier layer is already described extensively in chapter 5. The presence of the Ru barrier layers only affects the magnitude of the GMR ratio while the qualitative behavior does not change. The barrier layer makes these spin valves suitable for the determination of λ^{\uparrow} . We define a barrier as a layer that diffusely scatters all incoming electrons. To be sure that we have fulfilled this condition we have checked the properties of the barrier layer by adding thin layers of Ru at the interfaces of the Co/Cu/Co spin valves. Figure 7.2 shows the GMR ratio for the first series of spin valves with the basic composition 25 Å Co/ d Å Ru/30 Å Cu/ d Å Ru/100 Å Co as a function of the thickness of the Ru layers d_{Ru} . By adding only a 2 Å Ru layer at the Co/Cu interfaces of the spin valve, the GMR ratio decreases by more than a factor 20 from about 6% to 0.25%, and then saturates at about 0.15% for thicker Ru layers. This clearly demonstrates that Ru is very effective in blocking electrons and that Ru is an excellent candidate for a barrier layer. At this point

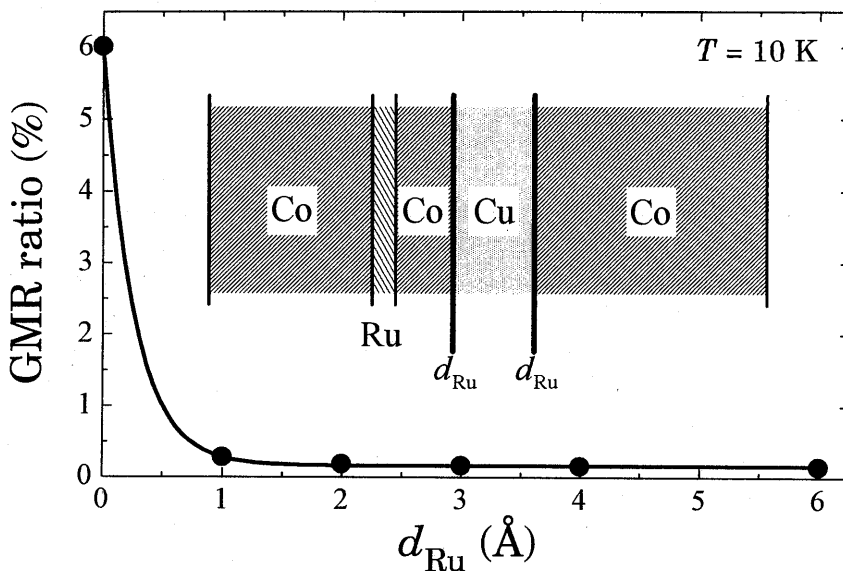


Figure 7.2: GMR ratio at $T = 10$ K of the spin valves with the composition $200 \text{ \AA Ru}/75 \text{ \AA Co}/6 \text{ \AA Ru}/25 \text{ \AA Co}/d_{\text{Ru}} \text{ \AA Ru}/30 \text{ \AA Cu}/d_{\text{Ru}} \text{ \AA Ru}/100 \text{ \AA Co}/10 \text{ \AA Cu}/30 \text{ \AA Ru}$ as a function of Ru thickness d_{Ru} .

we would like to note that the bottom part of our stack of layers, $75 \text{ \AA Co}/6 \text{ \AA Ru}/25 \text{ \AA Co}$, also forms a spin valve, and this produces the saturation GMR ratio of 0.15%. This small background contribution will be neglected in the following (see also chapter 5).

Subsequently, we have measured the transport properties of the Co/Cu/Co/(Cu) structures as a function of the position of the Ru barrier layer (second and third series of spin valves). In the left panel of figure 7.3 a typical result of the sheet conductance G , the differential conductance ΔG and the GMR ratio are plotted for the second series of spin valves, composed of Co/Cu/Co with a 2 \AA Ru barrier shifted through the Co layer. The sheet conductance G in antiparallel alignment of the magnetic moments in the spin valve (G_{ap}) and parallel alignment (G_p) first decreases and then increases as a function of t , which might seem somewhat confusing as the total thickness of the stack of layers is constant. However, for the layer thickness regime discussed here, mean free paths are not only restricted by the boundaries of the layers but also by diffusive scattering introduced by the Ru barrier layer, which leads to the observed minimum in G when the barrier is roughly in the middle of the spin valve.

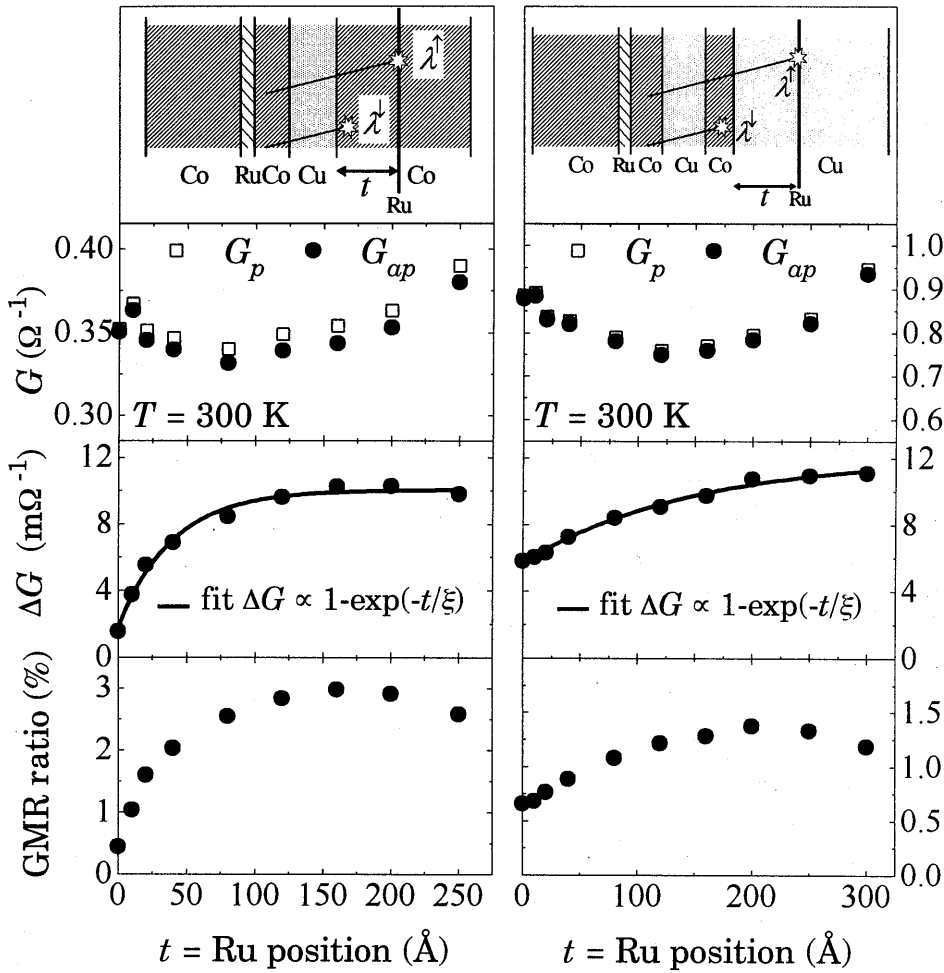


Figure 7.3: Experimental results at $T = 300$ K of the conductance G , the differential conductance ΔG , and the GMR ratio as a function of the Ru barrier layer position t for the spin valves 200 \AA Ru/ 75 \AA Co/ 6 \AA Ru/ 25 \AA Co/ 30 \AA Cu/ $t \text{ \AA}$ Co/ 2 \AA Ru/ $(250-t) \text{ \AA}$ Co/ 30 \AA Ru (left panel) and the spin valves 200 \AA Ru/ 75 \AA Co/ 6 \AA Ru/ 25 \AA Co/ 30 \AA Cu/ 25 \AA Co/ $t \text{ \AA}$ Cu/ 5 \AA Ru/ $(300-t) \text{ \AA}$ Cu/ 30 \AA Ru (right panel). The solid line indicates an exponential fit proportional to $1 - \exp(-t/\xi)$.

More important for the determination of the mean free paths in Co and Cu is the behavior of ΔG . Upon an increase of t the differential conductance ΔG increases and finally saturates. We have illustrated this in figure 7.3 by

schematically drawing the imaginary trajectories of a spin-up and a spin-down electron. Due to spin-dependent scattering (represented by a star) the mean free path is smaller for spin-down than for spin-up electrons. However, the spin-up electrons will be scattered by the Ru barrier which is most effective when the Ru barrier is located near the Co/Cu interface. On the contrary, at higher t spin-up electrons may experience their full bulk mean free path and then the difference in spin-up and spin-down conductance and hence ΔG is maximal. The increase of ΔG shows exponential behavior as is demonstrated by the solid line in figure 7.3. Finally, because G_p and G_{ap} are roughly constant, the GMR ratio shows similar behavior as ΔG , although the GMR ratio decreases at higher t because of the small but noticeable increase of G_{ap} . In the following we therefore fit ΔG and not the GMR ratio with an exponential expression. We note that this is different from Parkin, who used the GMR ratio to determine λ^\uparrow .

In figure 7.4a ΔG is presented as a function of the position of the Ru barrier layer at several temperatures between $T = 10$ K and $T = 300$ K. For each temperature the figure is supplemented with a solid line which is a fit $\propto 1 - \exp(-t/\xi)$, yielding the characteristic length ξ as a function of temperature. We will analyze ξ later on.

In the right panel of figure 7.3 we present room temperature measurements of G , ΔG and GMR ratio for the third series of spin valves, composed of Co/Cu/Co/Cu, as a function of the position t of the shifting 5 Å Ru barrier through the Cu layer. We will refer to the top Co layer as the *filter* layer and to the Cu layer as the *back* layer, a concept originally introduced by Gurney *et al.* (Gur93). First, the sheet conductance shows similar behavior as for the Co/Cu/Co spin valves, with a minimum in the conductance for intermediate values of t . Next, ΔG increases as a function of t , and although ΔG does not saturate completely we can identify an exponential behavior demonstrated by the exponential fit of ΔG (solid line). For $t = 0$ Å it is observed that the differential conductance ΔG has an offset, which we attribute to the Co/Cu/Co part of the sample. The GMR ratio clearly decreases at larger t due to the increase in G_{ap} .

In figure 7.4b we have plotted ΔG as a function of the position of the Ru barrier layer for $T = 100$ -300 K. Unfortunately, the exponential fits, denoted with the solid lines in figure 7.4b resulted in characteristic lengths ξ with a large error (larger than 13% to almost 30% for $T = 100$ K, in comparison to an error of approximately 10% for the Co/Cu/Co spin valves). Therefore, we restrict ourselves in the following to the experimental data for $T = 250$ K and $T = 300$ K, for which the error is acceptable. We think that part of the error is caused by the fact that ΔG is not completely saturated at maximal t , which explains why the error decreases with increasing temperature, as the high-temperature ΔG seems almost saturated in contrast to the low-temperature ΔG .

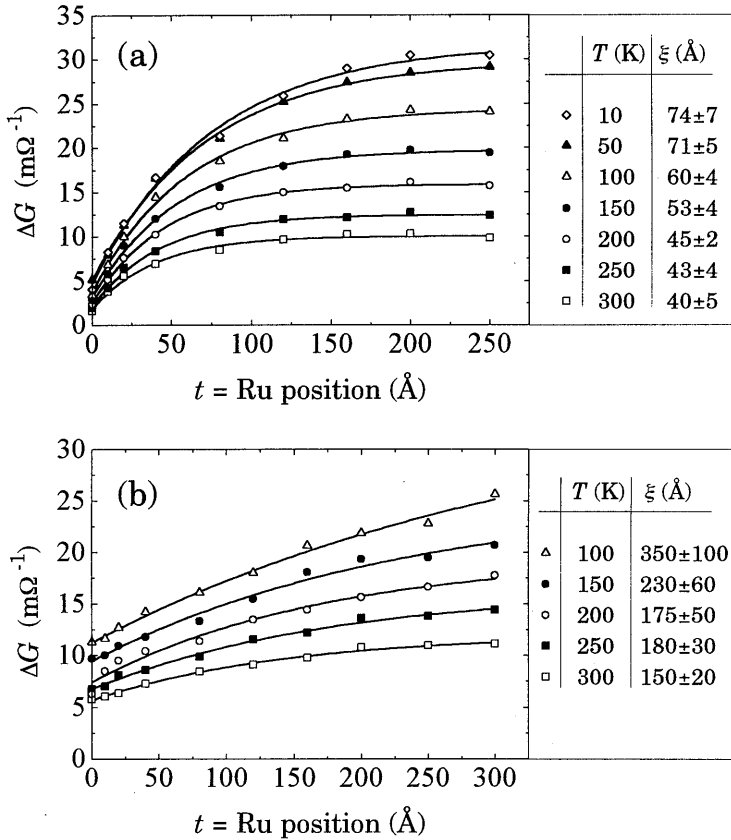


Figure 7.4: ΔG as a function of the Ru barrier layer position in (a) Co/Cu/Co and (b) Co/Cu/Co/Cu spin valves for different temperatures. In each figure the characteristic lengths ξ as derived from experimental fits (solid lines) are shown.

The last part of the experimental results deals with the conductance of the single Co layers for temperatures between $T = 10$ K and 300 K and the single Cu layers for the temperatures $T = 250$ K and 300 K. In figure 7.5 the sheet conductance of the single Co and Cu layers is plotted as a function of thickness. The macroscopic conductivity is determined from the slope of the sheet conductance as a function of thickness. For the Cu single layers, which varied in thickness between 2000 Å and 10 000 Å, a fit of the sheet conductance with a linear equation, indicated by the solid lines in figure 7.5, resulted in conductivities $\sigma_{\text{Cu}} = 0.71$ ($\mu\Omega \text{ cm}$)⁻¹ for $T = 250$ K and $\sigma_{\text{Cu}} = 0.58$ ($\mu\Omega \text{ cm}$)⁻¹ for

$T = 300$ K. For the single Co layers however, which varied in thickness between 250 \AA and 2000 \AA , the slope of the sheet conductance as a function of thickness is not constant. This is probably caused by boundary effects for smaller thickness as the mean free path for Co is in the range of the thickness of the layers. We have therefore fitted only the larger thicknesses, indicated by the solid lines, where the slope of the sheet conductance as a function of the Co thickness becomes nearly constant. As a typical result we have found $\sigma_{\text{Co}} = 0.096 (\mu\Omega \text{ cm})^{-1}$ for $T = 300$ K.

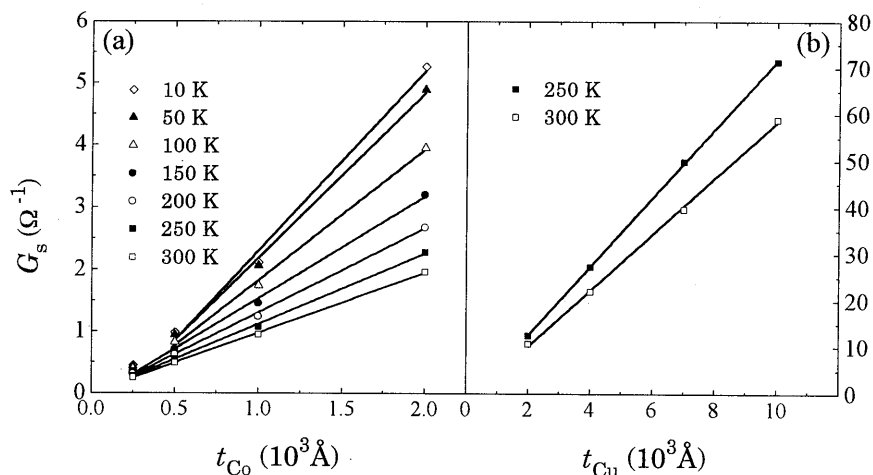


Figure 7.5: Sheet conductance G ($=\sigma d$) as a function of layer thickness of (a) single Co layers and (b) single Cu layers. The slope of the conductance as a function of layer thickness, as indicated with the solid lines, is the macroscopic conductivity σ .

7.4 Model calculations

In this chapter we use again the Camley-Barnas (CB) model to calculate the conduction and the GMR ratio in our spin valves. In subsequent studies (Hei94, Bar91, Die93) it was shown that, although the CB-model is not designed to predict *ab initio* the magnitude of the GMR ratio, the experimental behavior of ΔG and GMR ratio on ferromagnetic and nonmagnetic layer thickness can be described qualitatively very well. In view of this, we will apply the CB-model to investigate under what conditions the behavior of the differential conductance ΔG can be used to extract the longest of the mean free paths in Co and Cu.

The input parameters in the model are: (a) the mean free paths of the different metals in the spin valves λ_{Co} , λ_{Cu} , and λ_{Ru} , (b) probabilities of coherent transmission, specular reflection and diffusive scattering T^σ , R^σ and D^σ at the each interface, and (c) the Fuchs specularity factor p at the outer surfaces. Bulk spin-dependent scattering in the Co layers is modelled via spin-dependent mean free paths $\lambda_{\text{Co}}^\uparrow$ and $\lambda_{\text{Co}}^\downarrow$. Interface spin-dependent scattering at the Co/Cu interfaces is modelled by spin-dependent transmission coefficients $T_{\text{Co/Cu}}^\uparrow$ and $T_{\text{Co/Cu}}^\downarrow$. At the barrier and at the outer boundaries we will assume that there is no reflection ($R = 0$, $p = 0$), which are both reasonable assumptions as we have shown that Ru is a good diffusive barrier. Remember that at the outer boundaries of our spin valves also a Ru base and cap layer was grown.

To make interpretations with the CB-model more transparent we have performed model calculations on two spin valves in which we ignore the Ru base and cap layers and the Co/Ru bias layers. The first has the composition $25 \text{ \AA} \text{ Co}/30 \text{ \AA} \text{ Cu}/t \text{ \AA} \text{ Co}/2 \text{ \AA} \text{ Ru}/(250-t) \text{ \AA} \text{ Co}$ with $0 \leq t \leq 250 \text{ \AA}$, and the second is composed of $25 \text{ \AA} \text{ Co}/30 \text{ \AA} \text{ Cu}/25 \text{ \AA} \text{ Co}/t \text{ \AA} \text{ Cu}/5 \text{ \AA} \text{ Ru}/(300-t) \text{ \AA} \text{ Cu}$, with $0 \leq t \leq 300 \text{ \AA}$, based on the actual spin valve designs. In the following we will refer to the first model spin valves as Co/Cu/Co and to the second as Co/Cu/Co/Cu spin valves. As a starting point we will adopt parameters which are known from literature to be reasonable values (Par93). For the Cu mean free path $\lambda_{\text{Cu}} = 200 \text{ \AA}$ is taken and for the spin-dependent Co mean free paths a ratio $\lambda_{\text{Co}}^\uparrow / \lambda_{\text{Co}}^\downarrow = 10$. Spin-dependent scattering at the Co/Cu interfaces will be modelled with spin-dependent transmission coefficients $T_{\text{Co/Cu}}^\uparrow = 1$, $T_{\text{Co/Cu}}^\downarrow = 0.2$ and $D_{\text{Co/Cu}}^{\uparrow(\downarrow)} = 1 - T_{\text{Co/Cu}}^{\uparrow(\downarrow)}$. For Ru we adopt a mean free path $\lambda_{\text{Ru}} = 0$ (for both spins), representing the fact that Ru is a very efficient barrier layer for electrons, although in reality $\lambda_{\text{Ru}} \neq 0$.

A. Co/Cu/Co

The left panel of figure 7.6 shows the calculations of the parallel sheet conductance G_p , the differential conductance $\Delta G = G_p - G_{ap}$ and the GMR ratio $\Delta G/G_{ap}$ as a function of the position of the Ru barrier layer t for the first model spin valve. As this spin valve was designed to probe the longest of the Co mean free paths, $\lambda_{\text{Co}}^\uparrow$ was varied from 50 \AA to 150 \AA , which is in the typical range of mean free paths for Co as reported in literature (Len94). The Cu mean free path was kept at a constant value $\lambda_{\text{Cu}} = 200 \text{ \AA}$. The calculated conductance G_p , the differential conductance ΔG and the GMR ratio are in perfect *qualitative* agreement with the experimental results of the Co/Cu/Co spin valves presented in the left panel of figure 7.3. As anticipated, ΔG increases exponentially with a characteristic length ξ , determined from an exponential fit to the calculated ΔG . The plot is supplemented with the relation between $\lambda_{\text{Co}}^\uparrow$ and ξ . We find that $\lambda_{\text{Co}}^\uparrow$ is typically about a factor of 2 higher than ξ .

We can understand the exponential behavior of ΔG in a more direct way from the CB-expression for the differential conductance (see also equations 3.21-3.24)

$$\Delta G = G_p - G_{ap} = \frac{1}{E_x} \frac{e}{4\pi^3} \left(\frac{m}{\hbar}\right)^3 \sum_i \int_{z_{i-1}}^{z_i} \sum_{\sigma=\uparrow, \downarrow} \sum_{+, -} \left(g_{i\sigma, p}^{\pm} - g_{i\sigma, ap}^{\pm} \right) v_x d^3v dz \quad (7.1)$$

where g is an exponential function, *viz.* equation (3.24). When we substitute $\gamma\lambda$ for $\tau|v_z|$ in this g , with γ a constant, one can easily derive that ΔG is proportional to $1 - \exp(-t/\gamma\lambda_{Co}^{\uparrow})$ for the case that $\lambda_{Co}^{\downarrow}$ is much smaller than λ_{Co}^{\uparrow} . In fact, this is our analytical approach to the CB-model described in chapter 3, and yields equations similar to (3.32) and (3.33), where we used $\gamma = 1/2$. When we do not approximate $\tau|v_z|$ with a constant, $\gamma\lambda$, ΔG behaves roughly as $1 - \exp(-t/\xi)$ with $\xi \approx 2\lambda_{Co}^{\uparrow}$ as seen in figure 7.6, which can be understood from geometrical arguments; the average thickness traversed by the conduction electrons before scattering is about a factor of 2 smaller than their mean free path because of the various angles of incidences. In fact, it is because of this result that we have taken $\cos\beta = 1/2$ in our analytical approach of chapter 3.

One of the main goals of this chapter is to test to what extent bulk spin-dependent scattering in Co plays an important role in the GMR effect, and therefore our interpretation of ξ being a measure for λ_{Co}^{\uparrow} must be independent of the degree of bulk or interface spin-dependent scattering present in our samples. Therefore we will calculate the influence of nonperfect filtering of spin-down electrons at the Co/Cu interfaces and the influence of the degree of bulk scattering on the ratio $\alpha = \lambda_{Co}^{\uparrow}/\xi$. We also consider the influence of a variation of the magnitude of λ_{Cu} , as a variation with temperature of the mean free path of the Cu spacer layer might affect the penetration depth of electrons in Co and consequently ξ .

In figure 7.7 (a), first the dependence of α on the variation of the Cu mean free path λ_{Cu} is shown. Upon an increase of λ_{Cu} from 200 Å to 600 Å, the ratio α only slightly increases. Intuitively, we suggest that when electrons are not much disturbed in crossing the relative thin spacer layer, because of the long scattering lengths of electrons in Cu, a variation of λ_{Cu} does not influence our interpretation of ξ . We are confident that this is the case for our spin valves as our Cu spacer layer is only 30 Å thick.

Figure 7.7(b) shows the variation of α as a function of the ratio $\lambda_{Co}^{\downarrow}/\lambda_{Co}^{\uparrow}$, which in fact represents the amount of bulk spin-dependent scattering present in Co. The ratio $\lambda_{Co}^{\downarrow}/\lambda_{Co}^{\uparrow}$ also represents to what extent spin-down electrons are filtered in Co. First we consider the case (solid circles) of a significant amount of spin-dependent scattering at the Co/Cu interfaces described by the transmission

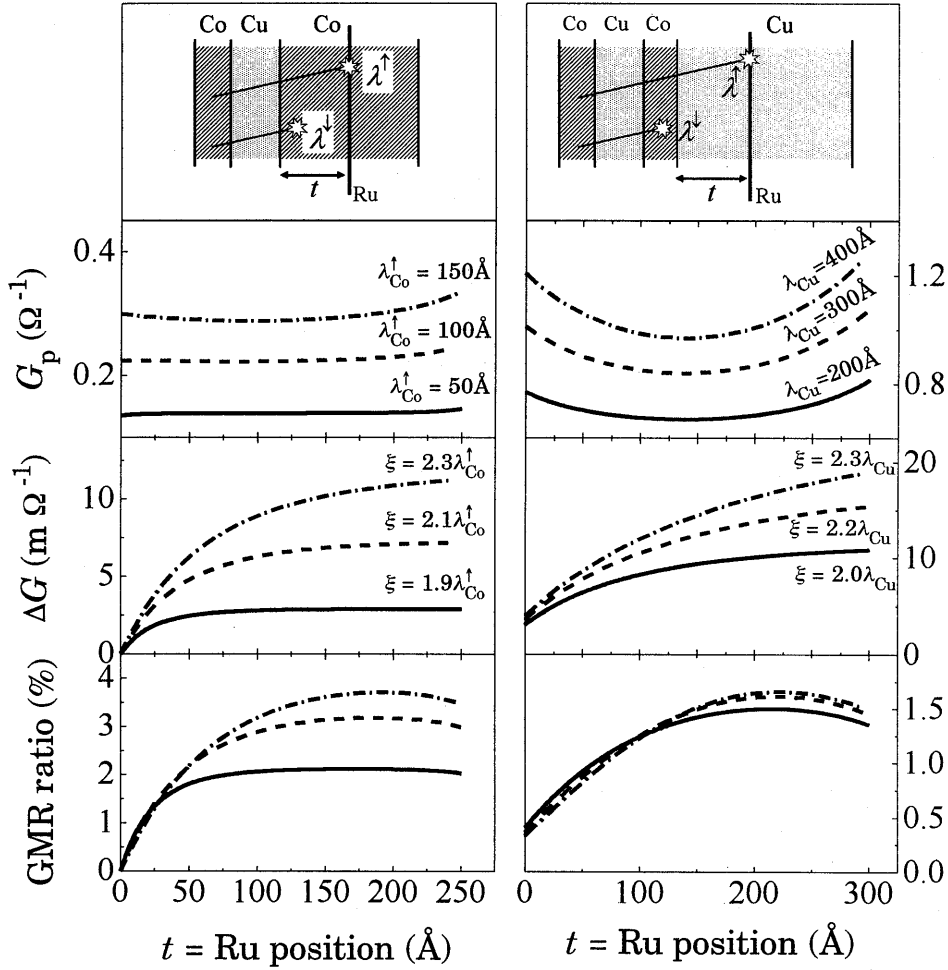


Figure 7.6: The left panel shows Camley-Barnas calculations of G_p , ΔG , and GMR ratio for the model spin valve $25 \text{ \AA} \text{ Co} / 30 \text{ \AA} \text{ Cu} / t \text{ \AA} \text{ Co} / 2 \text{ \AA} \text{ Ru} / (250-t) \text{ \AA} \text{ Co}$ with $0 \leq t \leq 250 \text{ \AA}$ for $\lambda_{\text{Co}}^\uparrow = 50, 100, \text{ and } 150 \text{ \AA}$. The input parameters in the model are: $\lambda_{\text{Cu}} = 200 \text{ \AA}$, $\lambda_{\text{Co}}^\uparrow / \lambda_{\text{Co}}^\downarrow = 10$, $T_{\text{Co}/\text{Cu}}^\uparrow = 1$ and $T_{\text{Co}/\text{Cu}}^\downarrow = 0.2$. The right panel represents the calculations for $25 \text{ \AA} \text{ Co} / 30 \text{ \AA} \text{ Cu} / 25 \text{ \AA} \text{ Co} / t \text{ \AA} \text{ Cu} / 5 \text{ \AA} \text{ Ru} / (300-t) \text{ \AA} \text{ Cu}$, with $0 \leq t \leq 300 \text{ \AA}$ for $\lambda_{\text{Cu}} = 200, 300, \text{ and } 400 \text{ \AA}$. The input parameters in the model are: $\lambda_{\text{Co}}^\uparrow = 100 \text{ \AA}$, $\lambda_{\text{Co}}^\downarrow = 10 \text{ \AA}$, $T_{\text{Co}/\text{Cu}}^\uparrow = 1$ and $T_{\text{Co}/\text{Cu}}^\downarrow = 0.2$.

coefficients $T_{\text{Co/Cu}}^{\uparrow}=1$ and $T_{\text{Co/Cu}}^{\downarrow}=0$. Starting from our initial value of $\lambda_{\text{Co}}^{\downarrow}/\lambda_{\text{Co}}^{\uparrow}=0$, we see that an increase of $\lambda_{\text{Co}}^{\downarrow}/\lambda_{\text{Co}}^{\uparrow}$ from 0 to 1 has almost no influence on the ratio α . At an intermediate scattering asymmetry, $T_{\text{Co/Cu}}^{\uparrow}=1$ and $T_{\text{Co/Cu}}^{\downarrow}=0.5$ (open triangles), ξ still appears to be a good measure for $\lambda_{\text{Co}}^{\uparrow}$. Only in the situation of no spin-dependent scattering at the Co/Cu interfaces (solid squares), α significantly decreases from about 2 to approximately 1.2 upon an increase of $\lambda_{\text{Co}}^{\downarrow}$ towards $\lambda_{\text{Co}}^{\uparrow}$, and in this regime ξ is no longer a valid measure for the longest mean free path.

From figure 7.7 we conclude that, when there is a significant amount of spin-dependent scattering either at the Co/Cu interfaces or in the Co bulk, ξ is to a good approximation about half the longest of the mean free paths in Co (the mean free path for spin-up electrons), independent of the Cu mean free path and the Co mean free path for spin-down electrons. Note that this is essentially the same result reported by Rijks (Rij96), who found the following phenomenological expression for ξ :

$$\xi = \frac{1}{2} \left(\lambda^{\uparrow} + \frac{T^{\downarrow}}{T^{\uparrow}} \lambda^{\downarrow} \right), \quad (7.2)$$

which was obtained also from exponential fits to calculations of ΔG according to the CB-model.

B. Co/Cu/Co/Cu

For the Co/Cu/Co/Cu model spin valve we also have calculated G_p , ΔG and the GMR ratio as a function of the position of the Ru barrier layer t (right panel of figure 7.6). As this spin valve was designed to probe the mean free path of Cu, we have varied λ_{Cu} between 200 Å and 400 Å. In general we conclude that the calculated conductance G_p , the differential conductance ΔG and the GMR ratio are again in perfect *qualitative* agreement with the experimental results of the Co/Cu/Co/Cu spin valves presented in the right panel of figure 7.3. We find that λ_{Cu} is typically about a factor of 2 higher than ξ for similar reasons as discussed in the foregoing paragraphs. Again we have calculated the influence of various parameters in the CB-model on the ratio $\delta = \lambda_{\text{Cu}}/\xi$.

In figure 7.7(c) the dependence of $\delta = \lambda_{\text{Cu}}/\xi$ is shown as a function of the longest of the mean free paths in Co. When the longest of the mean free paths in Co becomes larger compared to the thickness of the back layer, δ increases only slightly. Figure 7.7(d) shows the dependence of δ on the ratio $\lambda_{\text{Co}}^{\downarrow}/\lambda_{\text{Co}}^{\uparrow}$, which represents as mentioned before the amount of bulk spin-dependent scattering. We have discriminated three cases; the first (solid circles) with significant amount of Co/Cu interface spin-dependent scattering, represented by $T_{\text{Co/Cu}}^{\uparrow}=1$ and $T_{\text{Co/Cu}}^{\downarrow}=0$, the second (open triangles) with intermediate $T_{\text{Co/Cu}}^{\uparrow}=1$ and

$T_{\text{Co/Cu}}^{\downarrow} = 0.5$, and the third with no Co/Cu interface spin-dependent scattering. From figure 7.7 (b) it is clear that in case of large interface spin-dependent scattering or bulk spin-dependent scattering ξ is a perfect measure for λ_{Cu} .

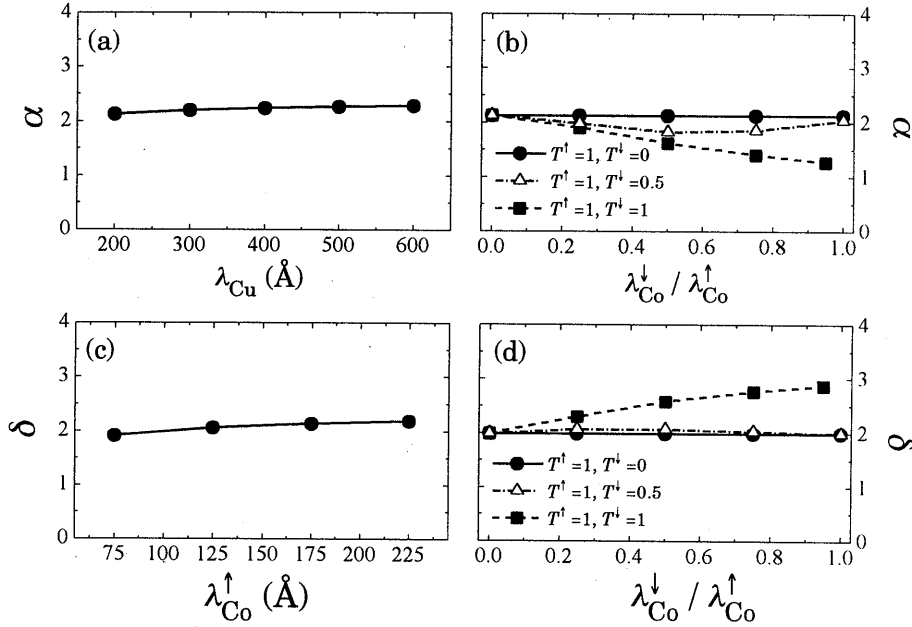


Figure 7.7: Influence of the variation of several parameters in the CB-model on the ratio $\alpha = \lambda_{\text{Co}}^{\uparrow} / \xi$ and $\delta = \lambda_{\text{Cu}} / \xi$. As a starting point we have adopted the following mean free paths and transmission coefficients: $\lambda_{\text{Cu}} = 200$ Å, $\lambda_{\text{Co}}^{\uparrow} = 100$ Å, $\lambda_{\text{Co}}^{\downarrow} = 0$ Å, $T_{\text{Co/Cu}}^{\uparrow} = 1$, and $T_{\text{Co/Cu}}^{\downarrow} = 0$. (a) Impact of a variation of λ_{Cu} on α for the Co/Cu/Co spin valves. (b) Relationship between α and the bulk scattering ratio $\lambda_{\text{Co}}^{\downarrow} / \lambda_{\text{Co}}^{\uparrow}$ for the Co/Cu/Co spin valves in case of significant interface spin-dependent scattering (solid circles / solid line) and no interface spin-dependent scattering at Co/Cu interfaces (solid squares / dashed line). (c) Impact of a variation of $\lambda_{\text{Co}}^{\uparrow}$ on δ for the Co/Cu/Co/Cu spin valves. (d) Relationship between δ and the bulk scattering ratio $\lambda_{\text{Co}}^{\downarrow} / \lambda_{\text{Co}}^{\uparrow}$ for the Co/Cu/Co/Cu spin valves in case of significant interface spin-dependent scattering (solid circles / solid line) and no interface spin-dependent scattering at Co/Cu interfaces (solid squares / dashed line).

7.5 Discussion

From the calculations with the CB-model it followed that there exists a proportionality of approximately a factor of 2 between ξ and $\lambda_{\text{Co}}^{\uparrow}$ or λ_{Cu} , provided that one of the current channels is sufficiently filtered due to a considerable spin-dependent scattering in the bulk of the ferromagnetic layer or at the interface. If this condition is not satisfied, the characteristic length ξ also contains, at least partially, the shortest of the mean free paths, as can be seen also, e.g., from equations (3.32) and (3.33). However, from several studies (Par93, Die93, Gij94, Sch93) it has become clear that there exists a large bulk and/or interface scattering asymmetry, especially in Co/Cu based systems. Therefore we feel confident that we may interpret ξ as being uniquely related to

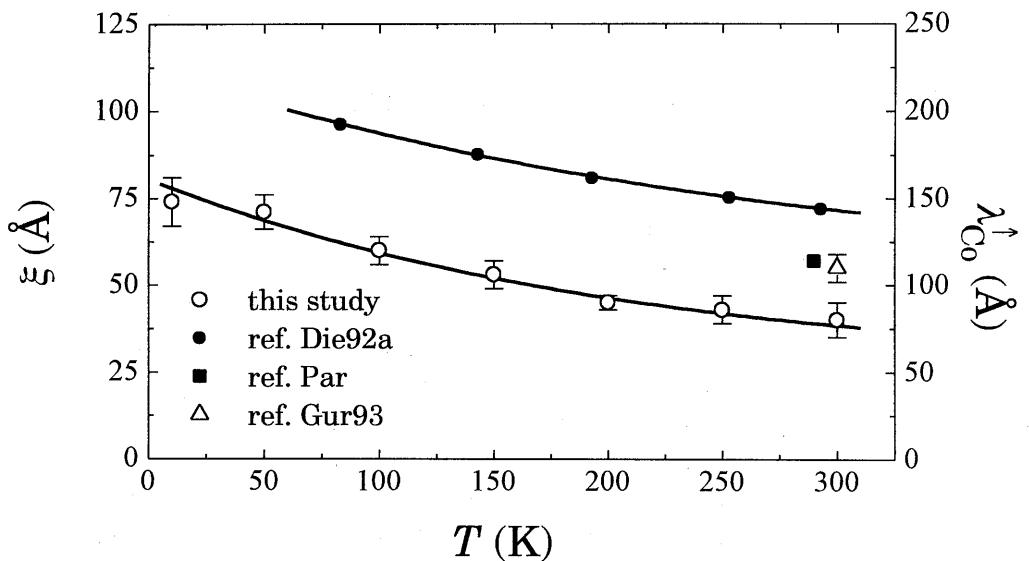


Figure 7.8: characteristic length ξ as measured in our structures as a function of temperature (open circles) and comparison with literature from Dieny (Die92a) (solid circles), Parkin (Par) (solid square) and Gurney (Gur93) (open triangle). The scale at the right represents $\lambda_{\text{Co}}^{\uparrow}$ which is taken equal to 2ξ for all measurements to take into account the angle dependence of the electron trajectories as discussed in the text.

the longest of the mean free paths as suggested by Parkin. We note, however, that our data on Co and Cu by themselves do not contain straightforward quantitative evidence for sufficient spin-dependent filtering of the electrons. In

figure 7.8 the longest of the Co mean free paths is estimated from the results presented in figure 7.3a, via $\lambda_{\text{Co}}^{\uparrow} = 2\xi$ (open circles) and is shown to decrease with increasing temperature. This is in agreement with a lower conductivity due to increasing phonon scattering at higher temperatures. The figure is supplemented with data obtained by Parkin (Par), Dieny and co-workers (Die92a, Die94), and Gurney *et al.* (Gur93) who have determined in a similar way a characteristic length from magnetoresistance measurements on related structures. Note that we have taken $\lambda_{\text{Co}}^{\uparrow} = 2\xi$ for all the data in figure 7.8, although this fact was not recognized by Parkin (see also figure 7.1) and Gurney. We think that the observed discrepancies in figure 7.8 are a consequence of the growth conditions of the samples, which obviously may have a considerable impact on scattering lengths.

We will now concentrate on the role of bulk spin-dependent scattering which does not depend on the magnitude of the derived mean free paths, $\lambda_{\text{Co}}^{\uparrow}$, but rather on the proportionality between λ^{\uparrow} and the macroscopic conductivity, as argued by Parkin. The conductivity in the relaxation time approximation is proportional to the sum of λ^{\downarrow} and λ^{\uparrow} , when we assume a free-electron-like conduction band for Co and Cu. This is well known for Cu, and although Co possesses a more complicated band structure, transport in Co is dominated by free-electron-like behavior as well (Mot64, Pap86). We may expect that a large asymmetry in the bulk scattering lengths of Co ($\lambda^{\downarrow} \ll \lambda^{\uparrow}$) would be manifested in a different proportionality or slope when Co is compared to Cu ($\lambda^{\downarrow} = \lambda^{\uparrow}$).

Figure 7.9 presents the macroscopic conductivity, as determined from the separate single layers (see figure 7.5), versus the measured $\lambda_{\text{Co}}^{\uparrow}$ and $\lambda_{\text{Cu}}^{\uparrow}$ ($\lambda_{\text{Co,Cu}}^{\uparrow}$). It is clear that the data for Co and those for Cu almost coincide on one single line (solid line in figure 7.9), although the data for Co are a little to the right of this line and the data for Cu a little to the left. The fact that the data for Co are on the other side of the solid line could indicate a small difference in the mean free paths λ^{\uparrow} and λ^{\downarrow} but, as we will explain in the following, there are some complicating factors in this interpretation. First of all we note that the slope of the line through our data is rather close to Drude's formula $\sigma = (e^2 m^2 v_F^2 / 3\pi^2 \hbar^3) \lambda$ (dashed line in figure 7.9), where $\lambda^{\downarrow} = \lambda^{\uparrow} = \lambda$. For comparison, we have also plotted in figure 7.9 Drude's equation in the limiting case of large bulk spin-dependent scattering $\lambda^{\downarrow} = 0 \text{ \AA}$ (dashed-dotted line in figure 7.9). We ascribe the deviations from the theoretical Drude line to the use of a model based on a single free-electron-like conduction band with Fermi velocity $v_F = 1.57 \times 10^6 \text{ m/s}$, the value of bulk Cu, which may be different for our thin films. Therefore we attach more importance to the fact that the data of Co and Cu almost coincide on one single line. From this we conclude that within our experimental accuracy, which is rather limited for Cu, we find no clear evidence for *significant* bulk spin-dependent scattering in Co for the covered temperature regime.

At this point we remark that also the solid line through our data assumes a single free-electron-like conduction band with the same (effective) electron mass m and Fermi velocity v_F for spin-up and spin-down electrons. Several authors (Hoo92, Ogu93, Zah95, But96) have pointed out that GMR can also result from differences in the Fermi velocities between spin-up and spin-down electrons and between different materials. When there would be a large difference in Fermi velocity between different materials, we would not expect measured conductivities versus λ^\uparrow for different materials to lie on a single line in the first place. Nevertheless, all materials measured by Parkin and shown in figure 7.1 appear to possess the same relation between σ and λ^\uparrow . Note, however, that when we assume that the Fermi velocity of Co is smaller than the Fermi velocity of Cu as is reported by Butler *et al.* (But96), this would, at least partly, account for the small shift of the Co-data to the right compared to the Cu-data in figure 7.9.

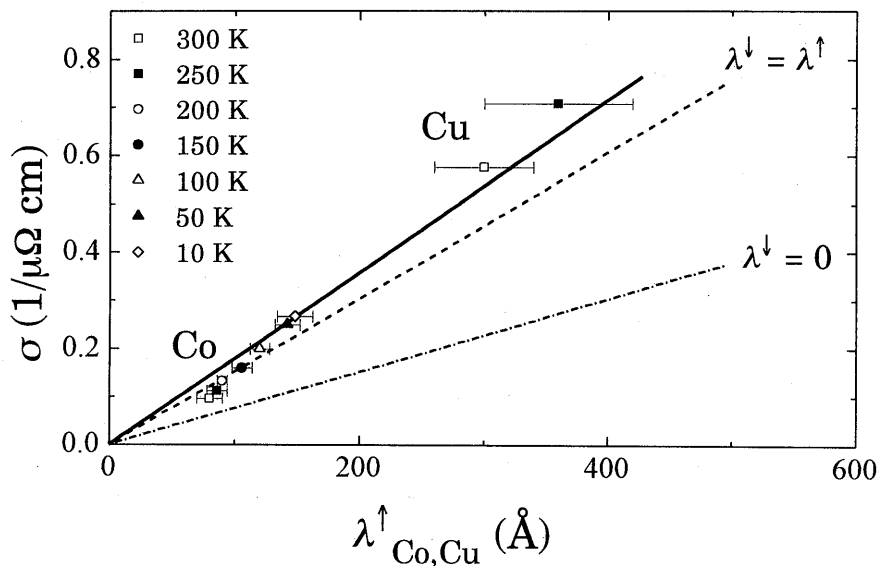


Figure 7.9: Conductivity σ as a function of the longest of the mean free paths for Co and Cu, with the solid line representing a linear fit of the data points of both Co and Cu. The dashed and dashed-dotted lines are based on the Drude model; the dashed line represents maximal spin asymmetry ($\lambda^\downarrow = 0$), whereas the dashed-dotted line represents the absence of bulk spin-dependent scattering ($\lambda^\uparrow = \lambda^\downarrow$).

Also the determination of $\lambda^\uparrow + \lambda^\downarrow$ via the bulk conductivity may be subject to errors in the interpretation. In order to exclude boundary effects, we have determined the bulk conductivity of Co and Cu from single *thick* layers of Co and Cu. An extrapolation of this bulk conductivity to thin layer conductivity is not correct if layer quality or grain sizes (Rij95) change drastically with layer thicknesses. However, in figure 7.5 we see that the conductivity scales linearly with thickness, at least for large thicknesses where boundary effects play no role, which demonstrates a constant layer quality, although we did not check this separately, for instance by visualization of the grains.

An additional complication in the interpretation is that the CB-model is only applicable to low temperatures. The proposed analysis of our data at higher temperatures and the room temperature data from Parkin may still be valid, however, provided that the additional scattering processes do not mix the spin-up and spin-down current channels. In that case the Boltzmann equation should be supplemented with a term containing a spin-mixing relaxation time $\tau_{\uparrow\downarrow}$, which complicates a straightforward interpretation of ξ as a measure for λ^\uparrow . However, in Co/Cu no evidence was found for substantial spin-flip scattering (Gij94, Oep96), and therefore the determination of $\lambda_{\text{Co}}^\uparrow$ and λ_{Cu} via the analysis presented in the foregoing paragraphs can be safely extended to higher temperatures. For other ferromagnetic materials the role of spin-flip scattering should be separately considered in view of the analysis of the mean free paths.

Finally we focus again on the proportionality factor 2 between ξ and $\lambda_{\text{Co,Cu}}^\uparrow$. As argued before, the *magnitude* of λ^\uparrow is not crucial in the comparison of the longest of the mean free paths in Co and Cu with bulk conductivities, provided that the proportionality factor is the same for both the Co/Cu/Co and the Co/Cu/Co/Cu structures. We have seen in figure 7.7 that deviations from $\lambda^\uparrow = 2\xi$ occur when electrons are not completely filtered at the interface of the Co layers. However, this would result in an overestimation of the longest of the Co mean free paths and an underestimation of the Cu mean free paths, and consequently our result of $\lambda^\downarrow \approx \lambda^\uparrow$ (within experimental accuracy) represents an upper limit for the bulk scattering asymmetry.

We have shown now that there are some complications in a straightforward interpretation of our measurements. Nevertheless we still conclude from the fact that our data for Co and Cu coincide almost on the same solid line in figure 7.9, that our data do not contain evidence for a significant difference between λ^\uparrow and λ^\downarrow , although we can not exclude it with the present accuracy of our data. The absence of a considerable bulk spin-dependent scattering is in striking contrast with Gurney *et al.* (Gur93) who reported a $\lambda_{\text{Co}}^\downarrow \leq 10 \text{ \AA}$ from an analysis of ΔG as a function of d_{Co} in backed spin valves of the basic composition $d \text{ \AA}$ Co/20 \AA NiFe/23 \AA Cu/50 \AA NiFe/80 \AA FeMn. However, meaningful and quantitative comparison with these results is difficult, because in their analysis the impact of averaging over all electron angles was not recognized and their

calculation of $\lambda_{\text{Co}}^{\downarrow}$ was not explained in full detail. In addition, the resistivities reported for Co and Cu reported by Gurney are almost 1.5 times as large as the resistivities measured by Parkin and us.

Furthermore, our results are in agreement with the general conclusion from CPP-measurements, where bulk and interface contributions are easier to separate, that for the Co/Cu system the spin-dependence in the interface scattering is larger than the spin-dependence in the bulk scattering, i.e., $\gamma > \beta$ (see also table 5.1). As already shown in figure 7.1, Parkin (Par) has found results similar to our data from the study of Ru barriers in exchange-biased spin valves at room temperature.

7.6 Conclusions

In conclusion, we have investigated the giant magnetoresistance behavior of uncoupled Co/Cu/Co and Co/Cu/Co/Cu spin valves with shifting Ru barriers through Co and Cu. With the help of the semiclassical model of Camley and Barnas we showed that the exponential behavior of the differential conductance ΔG as a function of the Ru barrier layer is uniquely related to the longest of the mean free paths in Co and Cu, provided there exists significant filtering of spin-down electrons in the bulk or at the interface of Co.

Under this assumption we have determined the longest of the mean free paths in Co and Cu at various temperatures. Comparison of λ^{\uparrow} with bulk conductivities obtained from separately grown films of Co and Cu, yields no evidence for significant bulk spin-dependent scattering in the ferromagnetic Co layer.

8. Interface-selective determination of spin-dependent scattering

8.1 Introduction

In chapter 6 we have investigated intermixing at the interfaces between Co and Cu, and it was demonstrated that intermixing decreases the GMR effect. In chapter 7 we concentrated on the scattering lengths inside the Co and Cu layers. From our measurements we found no clear evidence for a large asymmetry between the bulk mean free paths, λ_{Co}^{\uparrow} and $\lambda_{Co}^{\downarrow}$. In this chapter we will with the help of a specifically designed spin valve structure, establish unambiguously the relevance of interface spin-dependent scattering (SDS) both in Co/Cu/Co and in NiFe/Cu/NiFe spin valves.

To be able to investigate interface SDS we should fulfil two conditions. First of all we must eliminate the influence of the diffuse scattering at the outer boundaries and second we should know precisely the bulk contribution to the SDS, or reduce it to a minimum. This may be understood from figure 8.1, where we have calculated with the help of the CB-model the GMR effect of a trilayer 25 Å Co/30 Å Cu/ d 2 Å Co, with diffuse scattering at the outer boundaries, in case of interface SDS ($\lambda_{Co}^{\uparrow} = \lambda_{Co}^{\downarrow} = 100$ Å and $T_{Co/Cu}^{\uparrow} = 1$, $T_{Co/Cu}^{\downarrow} = 0$) and in case of bulk SDS ($\lambda_{Co}^{\uparrow} = 100$ Å, $\lambda_{Co}^{\downarrow} = 10$ Å, and $T_{Co/Cu}^{\uparrow} = T_{Co/Cu}^{\downarrow} = 1$). From figures 8.1a and b it follows that for very thin layer thickness d 2, despite the maximum interface asymmetry, there is almost no GMR effect due to the diffuse scattering at the outer boundaries. Moreover, from figures 8.1c and d it follows that bulk SDS results in qualitatively the same behavior as interface SDS, which makes it impossible to discriminate experimentally between these two contributions in such a trilayer. In order to minimize the effects of diffuse outer boundary scattering as well as the bulk SDS we have carried out experiments using the following basic structure: F/S/PR/B, where F is a ferromagnetic layer, S a nonmagnetic spacer layer, PR a ferromagnetic layer that we refer to as probe layer and B is a nonmagnetic but well-conducting back layer. Although this is the same structure as used by Gurney *et al.* (Gur93), who varied the back layer thickness in order to determine the longest of the mean free paths in their possibly magnetic back layer, we have employed this structure in a different manner.

In our case, the role of the back layer is to remove the effect on the magnetoresistance of the diffuse scattering at the outer boundary. As the contribution to the current density of the up-electrons in this layer may still be different from that of the down-electrons, as we have already seen in chapter 3 (figure 3.12), the back layer itself, although nonmagnetic, actually contributes to the GMR effect. This enables us to selectively investigate interface SDS at the

S/PR/B interface by choosing a very thin probe layer PR in which case we can safely neglect bulk SDS. The back layer thereby acts as a medium where the spin-polarized electrons are allowed to experience their full (bulk) mean free path after leaving the ferromagnetic probe layer where the asymmetry in the scattering rates is actually induced; see figure 8.2. Consequently, when the scattering at the S/PR and PR/B interfaces is spin-dependent, the GMR effect should persist down to the limit of a very small PR layer thickness.

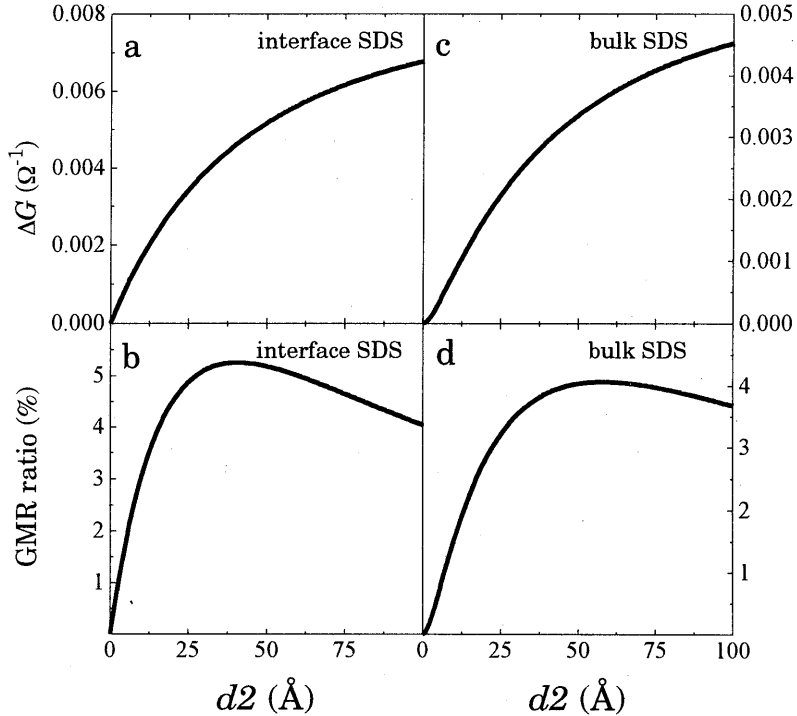


Figure 8.1: Calculation of the GMR ratio according to the Camley-Barnas model for the trilayer system $25 \text{ \AA} \text{ Co}/30 \text{ \AA} \text{ Cu}/d2 \text{ \AA} \text{ Co}$. In case of interface SDS we assumed $T_{\text{Co/Cu}}^{\uparrow} = 1$, $T_{\text{Co/Cu}}^{\downarrow} = 0$, and $\lambda_{\text{Co}}^{\uparrow} = \lambda_{\text{Co}}^{\downarrow} = 100 \text{ \AA}$, in case of bulk SDS we assumed $\lambda_{\text{Co}}^{\uparrow} = 100 \text{ \AA}$, $\lambda_{\text{Co}}^{\downarrow} = 10 \text{ \AA}$, and $T_{\text{Co/Cu}}^{\uparrow} = T_{\text{Co/Cu}}^{\downarrow} = 1$. In both cases the mean free path in the Cu was chosen $\lambda_{\text{Cu}} = 200 \text{ \AA}$.

8.2 Model calculations

To clarify the features of our structures we have applied our analytical approach to the CB-model (discussed in section 3.3) to the system F/S/PR/B and calculated ΔG for the cases of *only* interface SDS ($\lambda_m^{\uparrow} = \lambda_m^{\downarrow}$) and *only* bulk SDS

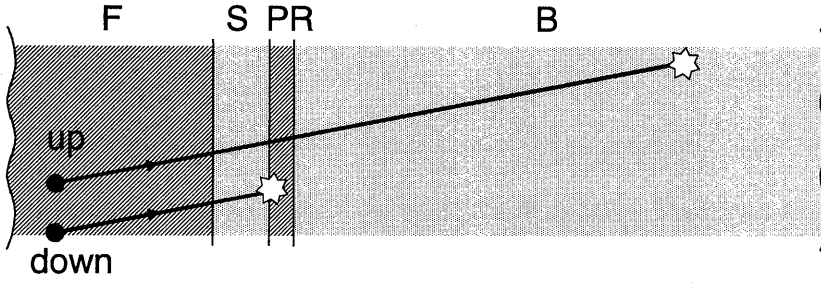


Figure 8.2: Schematic representation of our structure F/S/PR/B where the down electrons are scattered at the interfaces and the up electrons can experience their full mean free path due to the presence of the back layer.

($T^\uparrow = T^\downarrow$). In the case of only interface SDS we assumed that the transmission of the electrons at the interfaces between magnetic and nonmagnetic layers is given by T^\uparrow and T^\downarrow ($T^\uparrow \neq T^\downarrow$) for spin-up and spin-down electrons, respectively, and that the mean free path in the magnetic layers, λ_m , is spin-independent. The mean free path in the spacer and back layer, which in our case are both Cu layers, is denoted by λ^* . This yields for ΔG :

$$\Delta G_{\text{int}} = C_0 \times (T^\uparrow - T^\downarrow)^2 \times \lambda_m^2 \times e^{-2d_S/\lambda^*} \times (1 - e^{-2d_F/\lambda_m}) \times \left[1 + \left\{ (T^\uparrow + T^\downarrow) \times \lambda^* / \lambda_m \times (1 - e^{-2d_B/\lambda^*}) \right\} \times e^{-2d_{PR}/\lambda_m} \right] \quad (8.1)$$

In the case of bulk spin-dependent scattering we assumed that at each interface $T^\uparrow = T^\downarrow = 1$. In the magnetic layers we assumed for this case a spin-dependent mean free path denoted by λ_m^\uparrow and λ_m^\downarrow , yielding:

$$\Delta G_{\text{bulk}} = C_0 \times e^{-2d_S/\lambda^*} \times \left[\lambda_m^\uparrow (1 - e^{-2d_F/\lambda_m^\uparrow}) - \lambda_m^\downarrow (1 - e^{-2d_F/\lambda_m^\downarrow}) \right] \times \left\{ \lambda^* (1 - e^{-2d_B/\lambda^*}) (e^{-2d_{PR}/\lambda_m^\uparrow} - e^{-2d_{PR}/\lambda_m^\downarrow}) + \left[\lambda_m^\uparrow (1 - e^{-2d_{PR}/\lambda_m^\uparrow}) - \lambda_m^\downarrow (1 - e^{-2d_{PR}/\lambda_m^\downarrow}) \right] \right\} \quad (8.2)$$

$$\text{with } C_0 = \frac{e^2 m^2 v_F^2}{12\pi^2 \hbar^3}.$$

Since we did not vary d_S or d_F , equation 8.1 can in our case be reduced to:

$$\Delta G_{\text{int}} \propto (T^\uparrow - T^\downarrow)^2 \lambda_m^2 \left[1 + \left\{ (T^\uparrow + T^\downarrow) \times (\lambda^* / \lambda_m) \times (1 - e^{-2d_B / \lambda^*}) - 1 \right\} e^{-2d_{PR} / \lambda_m} \right] \quad (8.3)$$

In figure 8.3 we have calculated ΔG_{int} and ΔG_{bulk} as a function of probe layer thickness d_{PR} for three different back layer thicknesses for the system 25 Å F/25 Å S/ d_{PR} Å PR/ d_B Å B. In figure 8.3a we show ΔG_{int} as a function of probe layer thickness d_{PR} for $d_B = 0$ Å, 100 Å and ∞ . From equation (8.3) we can see that when there is no back layer ($d_B = 0$), ΔG_{int} varies as $\Delta G_{\text{int}} \propto (1 - e^{-2d_{PR} / \lambda_m})$ with d_{PR} such that $\Delta G \rightarrow 0$ when $d_{PR} \rightarrow 0$. This is the situation that is shown in figure 8.1a. When there is a back layer present, however, there is an offset in ΔG_{int} for $d_{PR} = 0$ (infinitely thin interface), which is in accordance with the aforementioned intuitive explanation. This offset reaches its maximum $\propto (T^\uparrow - T^\downarrow)^2 [(T^\uparrow + T^\downarrow) \lambda^* \times \lambda_m]$ when $d_B \rightarrow \infty$, see equation (8.3) again. As a contrast we show in figure 8.3b ΔG_{bulk} as a function of d_{PR} also for $d_B = 0$ Å, 100 Å, and ∞ according to equation 8.2. Clearly the presence of a back layer in this case does not result in an offset in ΔG_{bulk} . Rather ΔG_{bulk} is in this case

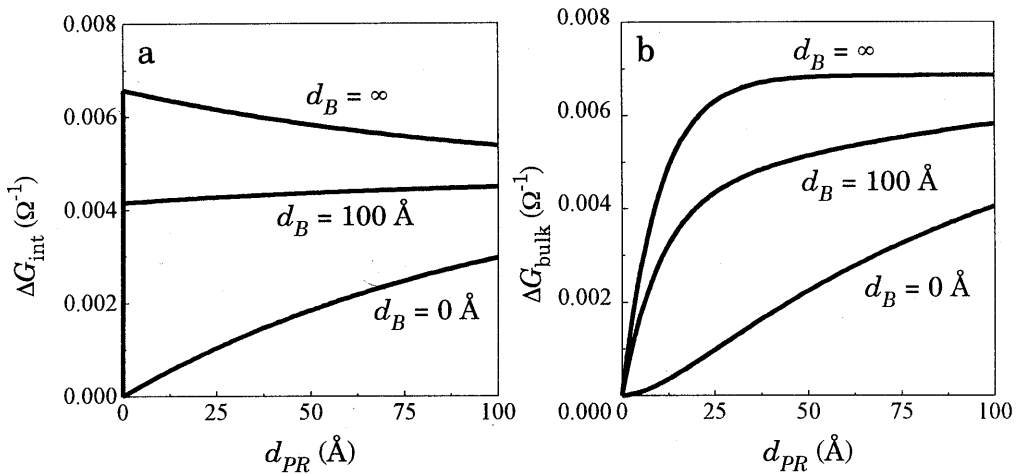


Figure 8.3: Calculations of ΔG_{int} and ΔG_{bulk} according to equations (8.1) and (8.2), respectively, as a function of probe layer thickness for the system 25 Å F/25 Å S/ d_{PR} Å PR/ d_B Å B. In the case of interface SDS we assumed as input parameters $T^\uparrow = 1$, $T^\downarrow = 0.4$, and $\lambda_m^\uparrow = \lambda_m^\downarrow = \lambda^* = 200$ Å. In the case of bulk SDS we assumed $T^\uparrow = T^\downarrow = 1$ at each interface and spin-dependent mean free paths: $\lambda_m^\uparrow = \lambda^* = 200$ Å and $\lambda_m^\downarrow = 20$ Å.

characterized by an exponential growth, starting from zero. For small probe layer thickness this roughly means that ΔG_{bulk} is proportional to d_{PR} . When there is a large asymmetry between λ_m^\uparrow and λ_m^\downarrow , ΔG_{bulk} saturates at a probe layer thickness that is mainly determined by λ_m^\downarrow (see Eq. 8.2). Note, however, that figure 8.3 is based on calculations only. In a real physical system we cannot make d_{PR} infinitely thin without changing the (magnetic) properties of the probe layer. This means that in a real system ΔG always decreases to 0 when $d_{PR} \rightarrow 0$. Nevertheless, we still expect an exponential increase of ΔG as a function of d_{PR} when bulk SDS is dominant, whereas ΔG is expected to persist down to the limit of an interfacial PR layer thickness where it displays an abrupt decrease to 0, when interface SDS is active.

In this chapter we will show that indeed this 'discontinuous' behavior is observed in the GMR effect both for Co/Cu/Co and NiFe/Cu/NiFe spin valves with a Cu back layer. We will analyze our experimental data in detail and come to the conclusion that indeed interface spin-dependent scattering is active in both kinds of spin valves.

8.3 Experimental

Three different types of spin valves were grown to investigate SDS at the interfaces, although not all of them are analyzed to the same extent. To investigate SDS at the Co/Cu interfaces AF-biased spin valves (see chapter 5) were sputtered of the form: SiO₂/200 Å Ru/75 Å Co/6 Å Ru/25 Å Co/30 Å Cu/PR/B/20 Å Ru, where PR is a Co probe layer with a thickness $3 \text{ \AA} \leq d_{PR} \leq 100 \text{ \AA}$ and B is the Cu back layer with a thickness d_B of 0, 100, 200, or 400 Å. Details about the growth of these samples were identical to those already described in chapter 5.

Also exchange-biased spin valves of the form: glass/500 Å NiO/20 Å F/25 Å Cu/PR/200 Å Cu/100 Å NiO were grown. Here F and PR are either both Ni₈₀Fe₂₀ layers or both Co layers with a thickness varying between 4 and 150 Å. In total four series of exchange-biased samples were grown, two series with Co and two series with NiFe as the magnetic material. In the first series of a particular material d_{PR} varied between 4 Å and 25 Å, while in the second series $25 \text{ \AA} \leq d_{PR} \leq 150 \text{ \AA}$. The F layer is exchange-biased to the 500 Å NiO layer which is an antiferromagnet, the top 100 Å NiO layer protects the spin valve against oxidation. The 500 Å NiO layer is sputtered at an elevated temperature of $T = 200 \text{ }^\circ\text{C}$ since this proved to yield a better (111) texture as shown by X-ray diffraction measurements. The top NiO layer was however sputtered at room temperature to prevent interdiffusion at the magnetic/nonmagnetic interfaces. The Ar-pressure during the sputtering process was 1 mTorr for NiO and 7 mTorr for the other layers. Typical sputtering rates were 0.6 Å/s for NiO and 2 Å/s for Ni₈₀Fe₂₀, Co, and Cu.

8.4 Results and discussion

We start here with the AF-biased spin valves. In figure 8.4 we show the difference between conduction of the parallel and antiparallel configuration of the magnetic layers (ΔG) and the GMR ratio ($100 \times \Delta G / G_{ap}$) as a function of Co probe layer thickness for all four back layer thicknesses 0, 100, 200 and 400 Å Cu. These measurements were performed at $T = 300$ K. Measurements performed at $T = 10$ K show qualitatively the same behavior, but the absolute values are larger, as is shown in figure 8.5 for $d_B = 200$ Å. The experimental data for the series without back layer indeed display the exponential-like behavior shown in figure 8.1. When a back layer is grown on top however, the presence of scattering at or immediately after the interface follows clearly from the observation that both ΔG and the GMR ratio persist down to nominally very thin, almost mono-atomical ferromagnetic layers. Only when the thickness of the probe layer decreases to values below 6 Å, the effect is progressively suppressed. It is not surprising that the GMR effect eventually collapses when d_{PR} approaches the monolayer regime since the stability of the ferromagnetic state (and therefore the SDS induced, e.g., at the interfaces with the probe layer) of the sputtered probe layer will be affected. Ferromagnetism will finally disappear when $d_{PR} \rightarrow 0$.

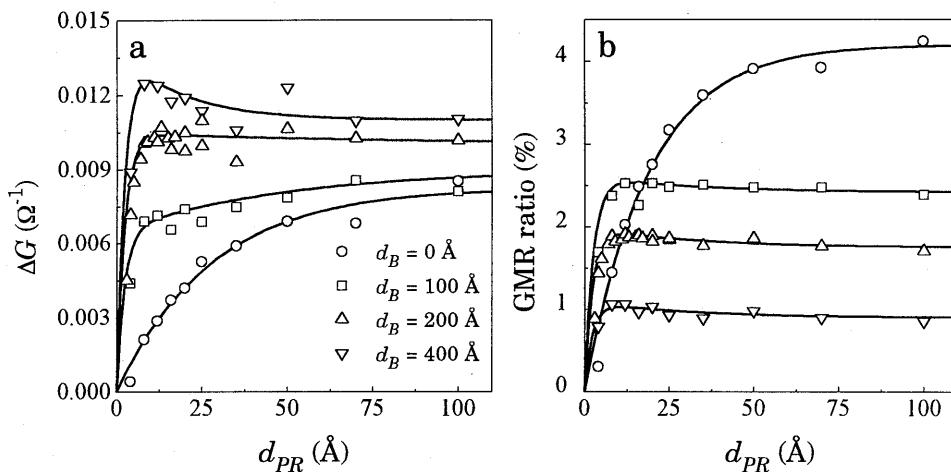


Figure 8.4: ΔG and GMR ratio for the AF-biased spin valves $\text{SiO}_2/200 \text{ Å Ru}/75 \text{ Å Co}/6 \text{ Å Ru}/25 \text{ Å Co}/30 \text{ Å Cu}/\text{PR}/\text{B}/20 \text{ Å Ru}$ as a function of d_{PR} for different back layer thickness ($B = \text{Cu}$). The measurements were performed at room temperature and the lines are guides to the eye.

The fact that ΔG and the GMR ratio in figure 8.4 saturate extremely fast, within a few \AA , clearly demonstrates that all spin-dependent scattering responsible for the GMR occurs within a probe layer thickness of approximately 6 \AA . This fact by itself, however, does not prove the existence of interface spin-dependent scattering. Theoretically, also in the case of bulk spin-dependent scattering with an extremely short mean free path λ_m^\downarrow for the spin-down electrons, these electrons will scatter immediately after the interface which will result in an extremely fast saturation of the GMR effect. However, additional temperature dependent measurements unambiguously demonstrate that this extremely fast saturation indeed comes from interface spin-dependent scattering, since the GMR effect at low temperatures saturates within even a smaller probe layer thickness d_{PR} , as can be seen in figure 8.5. We will discuss these measurements later.

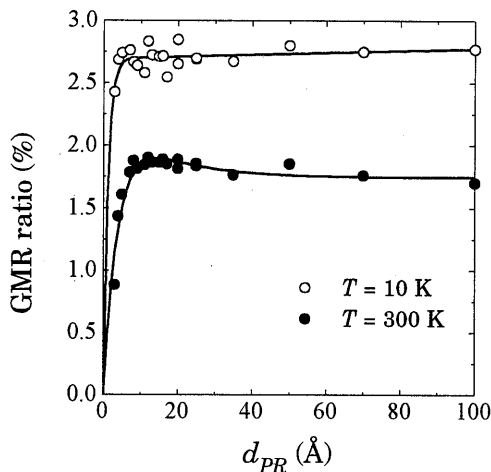


Figure 8.5: GMR ratio of the AF-biased spin valves with a back layer thickness $d_B = 200 \text{ \AA}$ at $T = 300 \text{ K}$ compared to the GMR ratio at $T = 10 \text{ K}$.

Of course the degree to which the propagation length of the spin-polarized electrons can be enhanced by a back layer is determined by the thickness of this back layer. This means that the largest thickness also results in the largest ΔG . The GMR ratio on the contrary, reduces when the back layer thickness increases, due to current shunting in the back layer. Note that it is possible that ΔG shows a maximum before it saturates for large d_{PR} (data with $d_B = 400 \text{ \AA}$), which is similar to figure 8.3a where we calculated ΔG assuming only interface spin-dependent scattering.

For each back layer thickness shown, however, an almost constant ΔG and GMR ratio are sustained, even for the samples with a probe layer thickness of

only 4 Å, demonstrating that a Cu back layer of at least 100 Å is sufficiently thick to obtain a structure that is selective for the spin dependence of the interface scattering. We will now examine the structures with a back layer of 200 Å Cu in more detail.

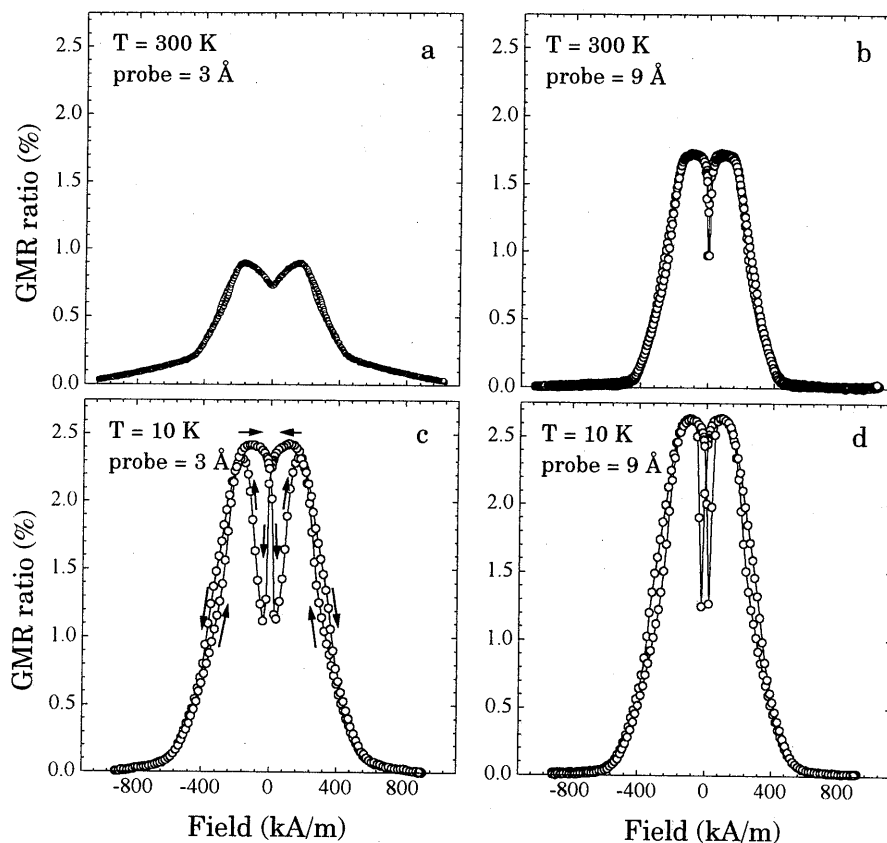


Figure 8.6: GMR ratio at room temperature and at $T = 10\text{ K}$ of AF-biased spin valves $\text{SiO}_2/200\text{ Å Ru}/75\text{ Å Co}/6\text{ Å Ru}/25\text{ Å Co}/30\text{ Å Cu}/d_{PR}/200\text{ Å Cu}/20\text{ Å Ru}$ with $d_{PR} = 3\text{ Å}$ (a and c) and $d_{PR} = 9\text{ Å}$ (b and d) respectively. The arrows in (c) represent the field direction.

Since we are interested especially in spin-dependent *interface* scattering, let us zoom in at the magnetoresistance measurements with the smallest probe layer thickness. In figure 8.6 results of MR-measurements with a probe layer thickness of 3 and 9 Å Co are shown. We first concentrate on the measurements at room temperature (figure 8.6a and b). It is clear that the form of the MR-curve

of the 9 Å Co sample is the form expected for this kind of spin valves as was described earlier in chapter 5. The magnetoresistance curve of the sample with only a 3 Å Co probe layer however, shows a different behavior in three ways. 1) The absence of clear plateaus in the curve, 2) No saturation is reached at large magnetic field, and 3) The dip at $H = 0$ is strongly reduced. All these differences could be indications that the probe layer is no longer a uniform ferromagnetic layer, but consists of Co clusters with a paramagnetic response. This paramagnetic behavior would explain the slow saturation of the GMR. In addition it would explain the absence of clear plateaus, since there is no complete anti-parallel configuration, resulting in a reduction of the GMR. At $H = 0$ the paramagnetic cluster moments are almost random in direction. Thus, when at $H = 0$ the 75 Å Co and 25 Å Co layers reverse their magnetization direction, this has almost no effect on the relative orientation of the magnetization directions of the 25 Å Co layer and the Co probe layer which explains the reduction of the dip at $H = 0$.

When the results of the room-temperature measurements are compared with the measurements at $T = 10$ K (figures 8.6c and d), the most remarkable difference is that the characteristic form of the MR-curve for AF-biased spin valves is more or less recovered for the 3 Å Co probe layer sample although there is a large hysteresis. This result could be explained by assuming that the 3 Å Co layer at these low temperatures no longer acts as a paramagnet, but is ferromagnetic with a large remanent magnetization and a large coercive field. This is supported by the results shown in figure 8.5, where at room temperature the GMR ratio of the sample with the 3 Å probe layer is strongly reduced, whereas at $T = 10$ K the GMR ratio of this sample still almost reaches the saturation value.

A similar result, where a 4 Å thick Co layer is broken into small clusters and behaves superparamagnetic at room temperature, but shows a broad ferromagnetic loop at low temperatures, was observed by P. Holody *et al.* (Hol94) in hybrid magnetic nanostructures of the form $15 \times [4 \text{ Å Co}/d_{Ag} \text{ Å Ag}/(20 \text{ or } 40) \text{ Å Ni}_{80}\text{Fe}_{20}/d_{Ag} \text{ Å Ag}]$. (Hybrid means here that the structure contains both clusters and layers.)

In the foregoing paragraphs some provisional conclusions were drawn on the magnetic state of the Co probe layer. To substantiate these we did perform magnetization measurements with a SQUID magnetometer. The results of these measurements are shown in figure 8.7, again for the sample with the 3 Å Co probe layer.

First of all we should note that the GMR effect is almost completely determined by the magnetization direction of the Co probe layer with respect to the 25 Å Co layer and is enhanced by the presence of the back layer. The magnetization measurements on the other hand are almost completely determined by the 75 Å Co and 25 Å Co layer whereas the probe layer contributes only a very small part to the total magnetic moment. Thus the

differences between the various magnetization curves resulting from a different magnetic behavior of the probe layer are quite small.

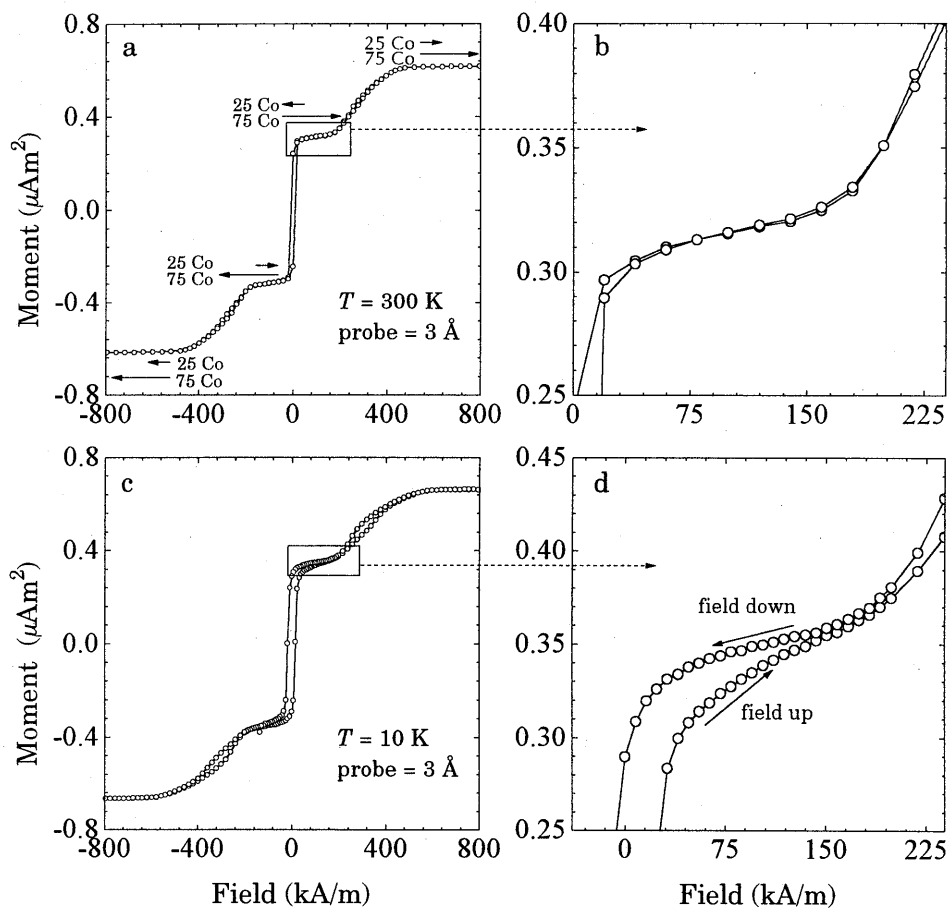


Figure 8.7: Magnetization measurements performed with a SQUID of the sample $\text{SiO}_2/200 \text{ \AA} \text{ Ru}/75 \text{ \AA} \text{ Co}/6 \text{ \AA} \text{ Ru}/25 \text{ \AA} \text{ Co}/30 \text{ \AA} \text{ Cu}/3 \text{ \AA} \text{ Co}/200 \text{ \AA} \text{ Cu}/20 \text{ \AA} \text{ Ru}$ at (a and b) room temperature and (c and d) $T = 10$ K.

Nevertheless, when the magnetization curves are examined in detail as shown in figure 8.7b and d, there is a clear difference between the measurement at $T = 300$ K and $T = 10$ K. We interpret these results as being consistent with our conclusions on the magnetic state of the probe layer. At $T = 300$ K the $3 \text{ \AA} \text{ Co}$ probe layer behaves as a paramagnet. The Co clusters are probably not saturated even at a magnetic field $H = 800$ kA/m. It is however difficult to identify the slow increase in magnetic moment, due to the saturation process of the probe layer, in the total magnetic moment. This means that the shape of the

magnetization curve at $T = 300$ K is virtually completely determined by the 75 Å Co and 25 Å Co layer as indicated with arrows in figure 8.7a. At $T = 10$ K the plateau, that is shown in detail in figure 8.7d, behaves differently when the field is decreased or increased as is indicated by the arrows that here denote the field direction. We ascribe this difference to the behavior of the probe layer, which is consistent with the assumption that at sufficiently low temperatures the probe layer displays a broad ferromagnetic loop with a high remanent magnetization and a large coercive field.

Returning to figure 8.4 we once more conclude that when a back layer is present, an almost constant ΔG or GMR ratio is sustained when the thickness of the probe layer decreases, until the probe layer makes a transition from a ferromagnetic state to a paramagnetic state due to the formation of Co clusters. At low temperatures, the ferromagnetic state persists to a smaller probe layer thickness, which means that the GMR ratio as a function of d_{PR} saturates faster at low temperatures as can be observed in figure 8.5. This behavior clearly proves the presence of an interfacial scattering mechanism.

To demonstrate that this method for measuring the distance from the S/PR interface, within which all spin-dependent scattering contributing to the GMR effect has taken place, can be applied more generally, we also investigated spin valves containing ferromagnetic permalloy ($\text{Ni}_{80}\text{Fe}_{20}$). We chose the combination NiFe/Cu since for this system the mechanism behind SDS is still under dispute. In particular it was suggested (Spe93) that the presence of a compositionally intermixed (magnetically "dead") zone at the NiFe/Cu interfaces leads to spin-independent scattering, reducing the interface contribution to the spin-dependent scattering and thus favoring the hypothesis that for NiFe/Cu/NiFe systems spin-dependent bulk scattering is the dominant mechanism that leads to GMR.

For this purpose we have investigated Co/Cu/Co and NiFe/Cu/NiFe exchange-biased spin valves. In figure 8.8 we show ΔG and the GMR ratio at $T = 10$ K and $T = 300$ K for these spin valves. From these data it becomes immediately evident that the exchange-biased samples qualitatively show the same behavior as the AF-biased spin valves of figure 8.4, although both ΔG and the GMR ratio saturate at a larger thickness d_{PR} . We ascribe this difference in saturation thickness to structural differences between our AF-biased and exchange-biased spin valves. This is based on the observation of a NiO(111) and a NiO(200)-diffraction peak in X-ray measurements on exchange-biased spin valves similar to the ones used in the present investigation (Str95), indicating that the structure of the NiO-layers is not well defined. Obviously, this may affect the structure of the other layers in the stack as well.

The difference in ΔG between Co and NiFe is larger than the difference in the conductance G , which is approximately $0.65 \Omega^{-1}$ for both Co and NiFe exchange-biased spin valves at $T = 10$ K. This might indicate that the asymmetry between

T_{Co}^{\uparrow} and T_{Co}^{\downarrow} is larger than the asymmetry between T_{NiFe}^{\uparrow} and T_{NiFe}^{\downarrow} , which is consistent with the observation of Parkin (Par93) that thin Co layers of only 2.5 Å inserted at the interfaces of NiFe/Cu/NiFe spin valves almost double the GMR ratio.

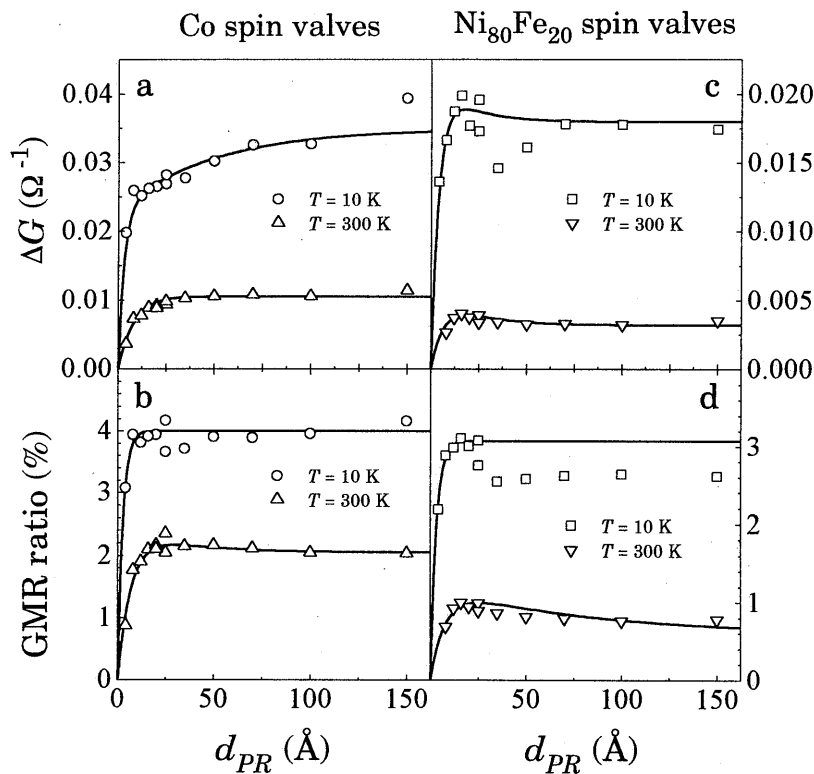


Figure 8.8: ΔG and GMR ratio for exchange-biased spin valves of the type glass/500 Å NiO/20 Å F/25 Å Cu/PR/200 Å Cu/100 Å NiO as a function of d_{PR} . In figure (a) and (b) the F and PR layers are Co layers and in (c) and (d) F and PR consist of permalloy.

A linear extrapolation of the ΔG versus d_{PR} data from thick probe layers to $d_{PR} = 0$ Å yields an offset for ΔG . This offset denotes the value for ΔG that would be obtained for $d_{PR} \rightarrow 0$ when the probe layer would remain ferromagnetic for an infinitely small thickness. The value of this offset depends of course on the spin-dependent interface parameters T^{\uparrow} and T^{\downarrow} , as we can see from equation 8.1. Therefore, the offset in principle provides us with a unique possibility of a direct

comparison of the interface spin-dependent scattering of (in this case) Co/Cu and NiFe/Cu. Nevertheless, a quantitative determination of T^\uparrow and T^\downarrow separately was not possible from our data. This is because, when we assume that there is no additional bulk SDS that could contribute to the offset as well, the value of the offset still also depends on the mean free paths in the magnetic and nonmagnetic layers, yielding too many fit parameters.

Again magnetoresistance as well as magnetization measurements on the exchange-biased spin valves indicate that the thickness needed to saturate ΔG or the GMR ratio is strongly correlated with the formation of a continuous, ferromagnetic probe layer. To support this point we show in figure 8.9 magnetoresistance and magnetization measurements for exchange-biased NiFe spin valves with a probe layer of 4 Å NiFe and 12 Å NiFe respectively.

When we first concentrate on the low-temperature measurements of the sample with the 12 Å NiFe probe layer (figure 8.9c and d), we clearly recognize the basic characteristics of exchange-biased spin valves as explained in chapter 5. At room temperature these characteristics are still present although the hysteresis of both NiFe layers has decreased. Also the exchange biasing field of the biased layer is smaller at room temperature than at low temperature. From the magnetization curve (figure 8.9b) it appears that coming from a negative magnetic field, the transition field of the biased layer coincides with the transition field of the probe layer. In the MR curve (figure 8.9a) this reveals itself as a lower peak value than the peak value coming from a positive magnetic field that corresponds to the plateau in the magnetization curve.

The results of the sample with the 4 Å NiFe probe layer are interpreted in the same way as for the AF-biased spin valves with extremely thin probe layer. At room temperature the probe layer responds paramagnetically to a magnetic field, thus not yielding a plateau with antiparallel magnetization directions in the magnetization curve. The MR curve is consistent with this behavior, showing a very small GMR ratio that reaches its maximum at $H = 0$ kA/m when the NiFe cluster moments point in a random direction. At $T = 10$ K, the hysteresis of both layers has increased considerably and two plateaus begin to emerge in the magnetization and magnetoresistance curves, indicating that the probe layer at this temperature is ferromagnetic.

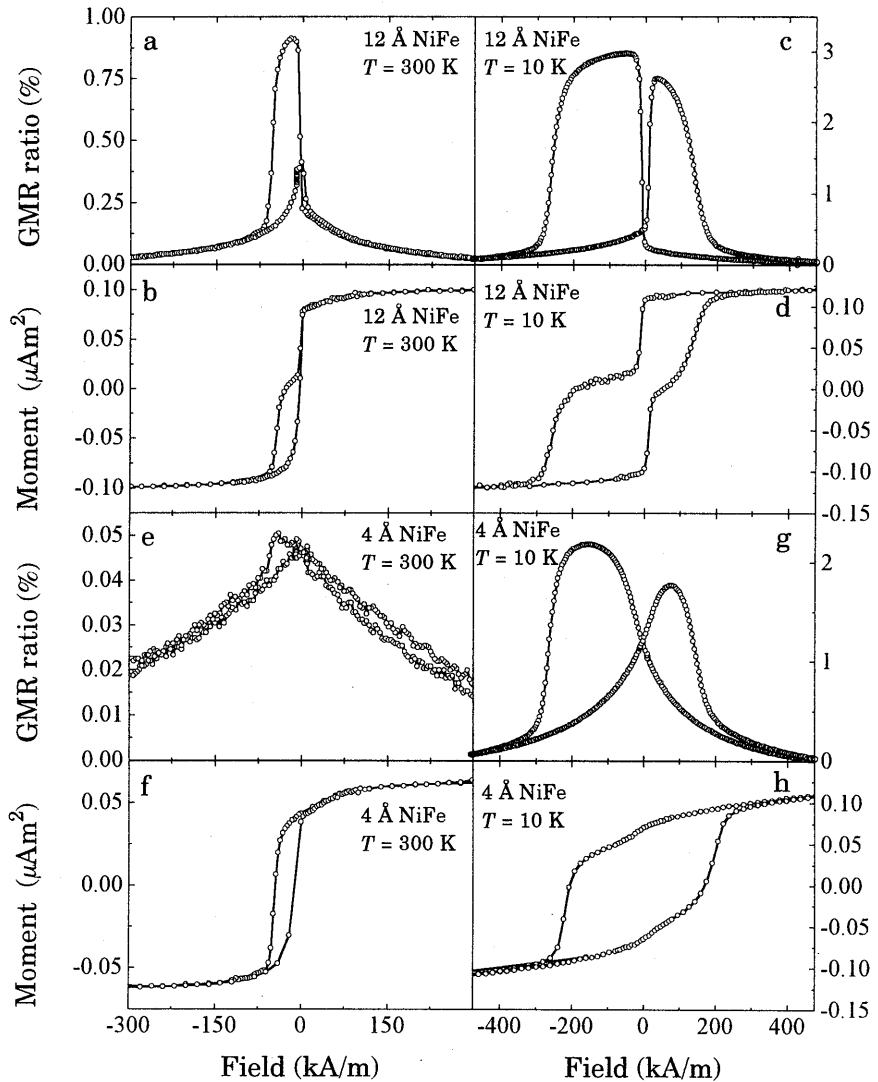


Figure 8.9: magnetoresistance and magnetization measurements of exchange-biased spin valves of composition: glass/500 Å NiO/20 Å Ni₈₀Fe₂₀/25 Å Cu/PR/200 Å Cu/100 Å NiO with PR = 4 and 12 Å Ni₈₀Fe₂₀ both at room temperature and at $T = 10$ K.

We did try to quantify the deviating behavior of the extremely thin probe layers and their different magnetic response at different temperatures by an experimental determination of the magnetic moments of each of the various

layers in a spin valve structure. For instance, in the exchange-biased spin valves the saturation moment is equal to the sum of the magnetic moment of the biased layer, m_F in our notation, and the moment of the probe layer m_{PR} ($m_{SAT} = m_F + m_{PR}$) while the magnetic moment of the plateau denotes the difference: $m_F - m_{PR}$. Unfortunately, since the plateaus are not exactly flat and even tend to disappear for the smallest probe layer thickness, an accurate determination was not possible for the exchange-biased spin valves nor for the AF-biased spin valves.

As additional proof of the existence of clusters we measured the coercivity of our samples as a function of temperature as is shown in figure 8.10a for AF-biased spin valves with a probe layer thickness of 3 Å and 9 Å Co. As a measure for the coercivity we have taken the characteristic field H_{ch} , determined as indicated in figure 8.10b, that is roughly the coercive field H_C of the probe layer. The fact that H_{ch} for the 3 Å sample becomes considerably larger below $T \approx 55$ K may indicate a blocking temperature of $T \approx 55$ K. Above this temperature the clusters show superparamagnetic behavior and below the blocking temperature a ferromagnetic hysteresis loop is measured.

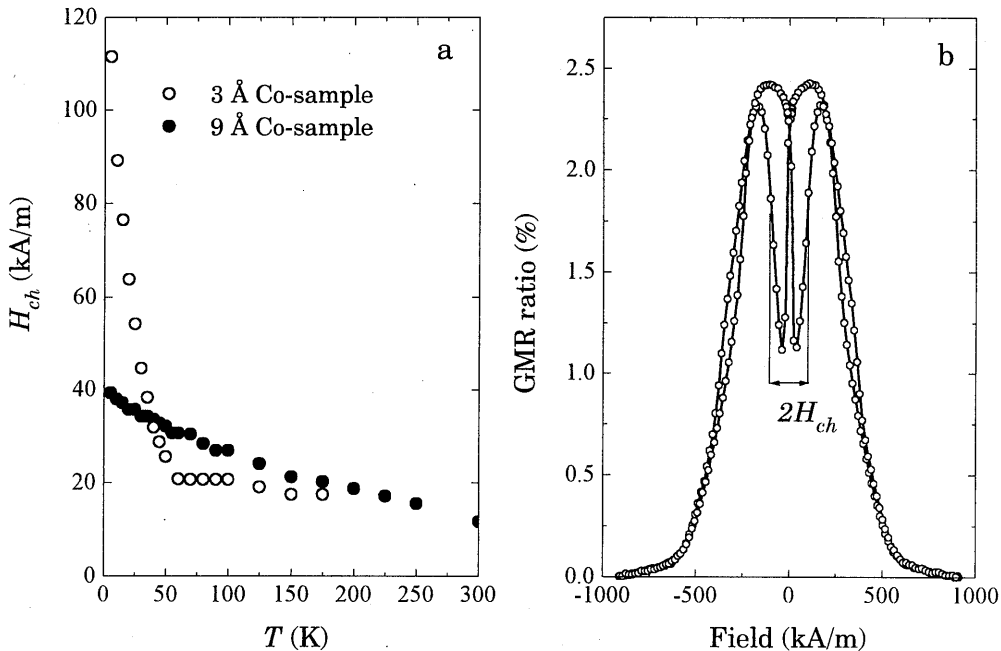


Figure 8.10: (a) Characteristic field H_{ch} determined as indicated in (b) as a function of temperature for the AF-biased spin valves with $d_{PR} = 3$ Å and $d_{PR} = 9$ Å.

We should remark here that for very thin fcc Co layers evaporated epitaxially on atomically flat Cu(100) surfaces a reduction of Curie temperature has been reported down to $T_c = 130$ K for a Co layer thickness of 1.5 monolayer as well as an increase of the coercivity when the temperature is decreased (Sch90). In principle this behavior could also account for our experimental observations. The coercivity of these thin Co layers is however typically an order of magnitude smaller than the field H_{ch} defined above. Therefore, although we cannot exclude that a lowering of Curie temperature also occurs in our samples when the probe layer is extremely thin, we still feel confident that our sputtered layers break up into clusters at very low thickness. This is confirmed also by preliminary NMR measurements (Str97) on sputtered Co/Cu multilayers. The NMR spectra indicate that for a nominal Co thickness below ≈ 5 Å the Co layers gradually break up into clusters.

As we mentioned before, we cannot conclude that interface SDS is dominant from the sole fact that ΔG in our samples remains at an almost constant value until d_{PR} reaches the monolayer regime. Note that also ΔG_{bulk} in the case of an ultrasmall mean free path for the down electrons, λ^\downarrow , in combination with a thick back layer, although starting at zero for $d_{PR} = 0$, saturates extremely fast. It is therefore experimentally not discernible from interface SDS that experimentally also always starts at zero for $d_{PR} = 0$ due to the breakdown of the ferromagnetism for small probe layer thickness. This is not surprising since an ultrasmall λ^\downarrow means that all the down electrons are scattered at or immediately after the interface which is thus effectively also an interface effect. Therefore we have investigated the temperature dependence of the length scale needed to saturate the magnetoresistance as we will discuss in the next paragraphs.

To have a quantitative measure for the variation of the GMR ratio at small d_{PR} , we have used a phenomenological exponential expression of the form $\text{GMR} = \text{GMR}_0 \times (1 - e^{-d_{PR}/\xi})$ to fit the data. We have chosen the GMR ratio instead of ΔG since the spread in the GMR ratio is smaller, yielding a more accurate value for ξ . Only the data with $d_{PR} \leq 25$ Å are taken into account in the fit since for larger d_{PR} the value of the GMR ratio depends on several aspects such as for instance a possible bulk contribution to the SDS, which we want to exclude here. The result, as a function of temperature, is shown in figure 8.11. Again we observe that for the exchange-biased samples ξ for $\text{Ni}_{80}\text{Fe}_{20}$ is comparable to that of Co. The fact that ξ displays a slow *increase* with temperature for all three types of spin valves can be regarded as additional evidence that ξ is related to the probe layer thickness above which a stable ferromagnetic state is established, leading to interface SDS. A (bulk) scattering length would certainly reveal just the opposite temperature dependence. When ξ is interpreted as a length scale at which a continuous interface is being formed however, the magnitude of for instance $\xi \approx 1$ Å at $T = 10$ K for the AF-biased Co/Cu spin valves seems surprisingly low since the interface roughness of these

spin valves was estimated in the range 4-9 Å (see chapter 6). In this respect we should recall that although a PR layer of only 3 or 4 Å appears to display ferromagnetic behavior at low temperatures, magnetoresistance and magnetization measurements at room temperature indicate that the PR layers in this thickness regime are stabilized in clusters.

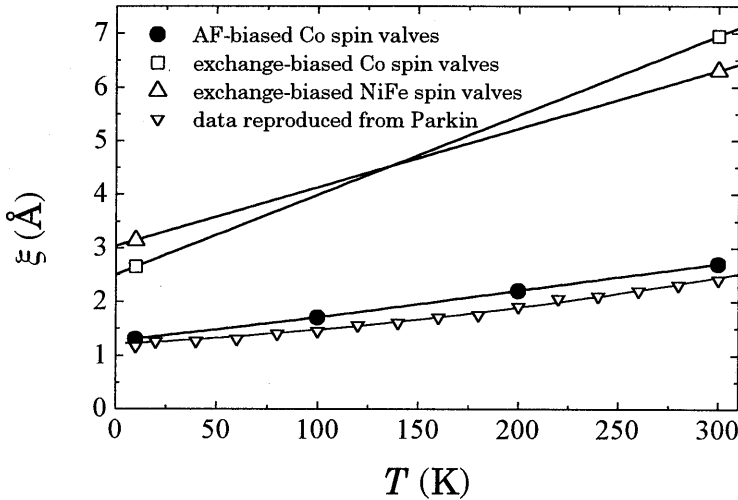


Figure 8.11: ξ as determined from a fit to the GMR ratio for the samples with probe layer thickness $d_{PR} \leq 25$ Å as a function of temperature. For comparison we have also reproduced the values for ξ reported by Parkin (Par93).

A similar length scale ξ and a similar temperature dependence was found by Parkin (Par93) who inserted thin layers of a second ferromagnetic material at the interfaces of sputtered exchange-biased spin valves. For example, the length scale on which the GMR ratio saturates as a function of Co thickness inserted at the interfaces of NiFe/Cu/NiFe spin valves was found to increase from $\xi \approx 1.3$ Å at $T = 4.2$ K to $\xi \approx 2.5$ Å at room-temperature. For comparison we have shown these data in figure 8.11. Based on his results, also Parkin concluded that the magnitude of ξ was too small to represent a bulk scattering length (λ_m^{\downarrow}), and moreover that the increase of ξ with temperature definitely rules out any relation with λ . Therefore Parkin concluded that ξ is related to the electronic or structural nature of the interfaces.

In this chapter we have demonstrated that the formation of the ferromagnetic probe layer via clusters should be incorporated in the interpretation of ξ . On the other hand it was shown (Bad96) from a photoemission study on UHV-evaporated Co/Cu wedges that a minimum thickness of only (0.6-2.2 Å) Co is sufficient to form spin-polarized Quantum-Well (QW) states in a Cu layer confined by vacuum on the one side and Co on the other side, which shows that

the observed length scale ξ may also be intricately related to the evolution of QW states. Our interface-selective device may therefore become extremely suitable to study how spin-dependent interface scattering is related to structural and electronic details of the interfacial regions in artificial magnetic structures, which, also from a theoretical point of view, is one of the most prominent remaining challenges in GMR studies.

Finally we want to remark that, although we have established the presence of interface SDS, we cannot exclude from the measurements presented in this chapter that bulk SDS is also present in our spin valves. In this chapter, we have focused on interface SDS and our structures are not suitable to determine whether a bulk SDS mechanism is active. One can understand this for instance from figure 8.3a, where ΔG_{int} increases as a function of probe layer thickness d_{PR} for a back layer thickness $d_B = 100 \text{ \AA}$, although there is no bulk SDS. To distinguish this increase from an increase caused by bulk SDS, quantitative values for the mean free paths and transmission parameters T should be known.

8.5 Conclusions

We have investigated interface spin-dependent scattering in F/S/PR/B spin valves with a nonmagnetic back layer (B) grown on top. The nonmagnetic back layer allows one to investigate magnetoresistance at very small probe (PR) layer thickness, without disturbing effects of diffuse boundary scattering. With these structures we have unambiguously demonstrated the presence of an interfacial scattering mechanism for both Co/Cu/Co and NiFe/Cu/NiFe spin valves. Firstly, the interfacial character reveals itself in an almost constant value of the GMR ratio and ΔG down to very small probe layer thickness. For even lower probe layer thicknesses, both ΔG and the GMR ratio decrease because the ferromagnetic response of the probe layer decreases, probably due to formation of clusters in the probe layer, yielding superparamagnetic behavior. Secondly, the characteristic length scale needed for the GMR ratio to reach its maximum value increases with temperature. This increase eliminates the possibility that this length scale is determined by a bulk scattering length, which would certainly result in just the opposite temperature dependence.

9. Enhanced giant magnetoresistance in spin valves sandwiched between insulating NiO

The contents of this chapter has been published in a slightly modified form in *Phys. Rev.* **B53**, 9108 (1996).

9.1 Introduction

Since the discovery of the giant magnetoresistance (GMR) effect in layered magnetic structures the majority of investigations (Hei94, Die94) has been focused on the elucidation of the spatial origin of spin-dependent scattering (SDS), in the bulk of the ferromagnetic layers or at the interface with the spacer material, which is still a matter of debate. Also chapters 6, 7, and 8 of this thesis were devoted to this subject.

The discovery of GMR intensified the search for theoretical models for transport in thin films and multilayers, and in recent years several semiclassical (Cam89, Bar91, Dim85, Joh91) and quantum-statistical theories (Lev90, Zha92, Ved92, Bar94) have been proposed. These theories were already discussed in chapter 3. Most of these approximations have in common that they deal with a (nearly) free electron gas with a constant potential throughout the chemical constituents of the layered structure. Hood and Falicov (Hoo92) in 1992 however, speculated that electron channelling or reflectivity is expected to show up in magnetoresistance experiments when, generally speaking, one goes beyond the assumption of a flat potential throughout the layers. Recently Butler *et al.* (But96) showed from calculations of the Fermi surfaces of Co and Cu that indeed part of the majority (spin-up) electrons in the Cu layers of Co/Cu multilayers may undergo total internal reflection, such that they are confined to the Cu layers.

Electron reflectivity should have a significant positive effect on the GMR ratio of a spin valve when all the electrons would be specularly reflected at the *outer surfaces*. In a normal spin valve of the form $d_1 \text{ \AA} \text{ F1} / d_2 \text{ \AA} \text{ NM} / d_3 \text{ \AA} \text{ F2}$, where F1 and F2 represent ferromagnetic layers and NM the nonmagnetic spacer, the GMR effect is relatively small due to diffuse, spin-independent scattering at the outer boundaries. We recall that this is why we had to implement the back layer in the previous chapter where we used very thin magnetic probe layers to investigate interface spin-dependent scattering. When all electrons were specularly reflected at the outer boundaries however, the trilayer would effectively transform to a superlattice with an infinite number of repetitions of the basic unit ($2d_1 \text{ \AA} \text{ F1} / d_2 \text{ \AA} \text{ NM} / 2d_3 \text{ \AA} \text{ F2} / d_2 \text{ \AA} \text{ NM}$). This should necessarily enhance the GMR, since the conduction in the case of parallel alignment is then not reduced by the outer boundary scattering.

Reflectivity, which may also be called specular scattering, can be achieved in a trilayer when the trilayer is sandwiched between high potential barriers with perfectly flat interfaces. It may be envisaged that this can be realized, e.g., by making use of an insulating top and bottom layer. All the electrons are then internally reflected or channelled within the barriers and the trilayer mimics an infinite multilayered system.

In this chapter we will present the results of an experimental investigation of the possibility of increased (specular) reflectivity in a metallic spin valve incorporated in a metallic/oxidic structure, consisting basically of Co/Cu/Co or Ni₈₀Fe₂₀/Cu/Ni₈₀Fe₂₀ metal trilayers sandwiched between the antiferromagnetic insulator NiO. More precisely, the large potential step at the insulator/metal interface is expected to induce an increased reflectivity of the electron wave functions, which in turn would lead to enhanced magnetoresistivity compared to all-metal spin valves. Indeed, as we will show, we have found in e.g. Co/Cu/Co unusually high GMR ratios, *viz.* 15% at room temperature and almost 25% at low temperatures. Recently Anthony *et al.* (Ant94), Kitakami *et al.* (Kit96), and Egelhoff *et al.* (Ege95) also reported large magnetoresistances in structures including NiO layers, and the latter authors suggest that a simple intuitive model analysis of their results provides some evidence that a certain degree of specular scattering of electrons at the Co/NiO interfaces is present (Ege95). In this chapter the considerably enhanced GMR ratio in our new spin-engineered structures will be analyzed more systematically by the introduction of specular reflection of the electrons at the potential barrier of the impenetrable NiO in the Camley-Barnas model (Cam89, Bar90), discussed in chapter 3. We will however also discuss alternative possibilities that may lead to the observed enhanced giant magnetoresistance.

9.2 Experimental

The samples were grown on glass substrates by magnetron sputtering in Ar atmosphere at $p = 7$ mTorr for Co and Cu and $p = 1$ mTorr for NiO, in the presence of a magnetic field. The NiO layer directly on top of the substrate was deposited at 200 °C to ensure a (111) texture of the layer, whereas the remainder of the stack was grown at ambient temperature to avoid diffusion between the separate chemical constituents. We have used SQUID and MOKE for magnetic characterization. Resistance measurements were made in the four point contact geometry described in chapter 2, with the current in the plane of the sample (CIP).

We have basically studied the following spin valve structures: 500 Å NiO/F1/NM1/F2/NM2/100 Å NiO, with NM1 = 20 Å Cu, and NM2 = 12 Å non-magnetic Cu; see the schematic representation in the top of figure 9.1. As NiO is an anti-ferromagnet, exchange-biasing a magnetic layer in contact with it, these spin

valves are expected to qualitatively show the same behavior as the exchange-biased spin valves of chapter 5 where FeMn was used as the antiferromagnet. A typical example of magnetoresistance and magnetization for $F1 = 20 \text{ \AA}$ Co and $F2 = 40 \text{ \AA}$ Co is shown in figure 9.1b/c and 9.1d/e, respectively, and reflects an antiparallel (AP) state of F1 and F2 most clearly visible at negative magnetic fields. This is the key element to our Co/Cu/Co and $\text{Ni}_{80}\text{Fe}_{20}/\text{Cu}/\text{Ni}_{80}\text{Fe}_{20}$ spin valve structures and, qualitatively, the observed behavior can be understood as follows. The bottom NiO layer imposes an exchange biasing H_{ex} on layer F1, accompanied by a strong increase in coercive field H_c with $|H_c| > |H_{ex}|$. This is in accordance with separately investigated NiO with a single magnetic layer on top. On the other hand, the top ferromagnetic layer F2 switches its magnetization direction almost at zero field since it is intentionally magnetically isolated from NiO on top by a thin nonmagnetic layer NM2 to circumvent exchange-biasing and enhancement of H_c of F2 as well. As we have learned from the previous chapter such a nonmagnetic Cu back layer does not destroy the GMR effect but may even enhance it.

The reversal of F2 at zero field also reflects the essentially decoupled behavior of this layer in the case of a 20 \AA spacer NM1. We found that for a smaller Cu interlayer thickness ($d_{\text{Cu}} < 20 \text{ \AA}$) the magnetoresistance as well as the exchange-biasing is suppressed which may be explained from deterioration of the antiparallel alignment of the magnetization directions of layers F1 and F2 when interlayer coupling becomes effective. Without coupling, the magnetizations of the ferromagnetic layers F1 and F2 are simply additive and this results in the characteristic magnetic and magnetoresistive behavior of the entire spin valves, as exemplified for Co/Cu/Co in panel d/e and b/c of figure 9.1, respectively.

Now we will focus on the *magnitude* of the observed GMR which is expected to embody the impact of increased specular reflectivity at the insulating barriers, as we will show later on. To allow for comparison with conventional all-metal spin valves, mostly exchange-biased with metallic FeMn, we applied a common practice in studies on GMR (Hei94, Die94), *viz.* a variation of the thickness of the uncoupled ferromagnetic layer d_{F2} , whereas the thickness of the exchange-biased layer is kept unchanged since otherwise the switching fields of this layer and therefore the AP alignment of the spin valve may be affected. Upon variation of d_{F2} , the GMR ratio, defined as $100 \times (G_P - G_{AP}) / G_{AP}$ with G the sheet conductivity, in general displays a maximum at $d_{F2, \text{max}} = 50\text{-}100 \text{ \AA}$ in all-metal spin valves (Hei94, Die92a, Die94, Rij96). This is brought about by saturation of the

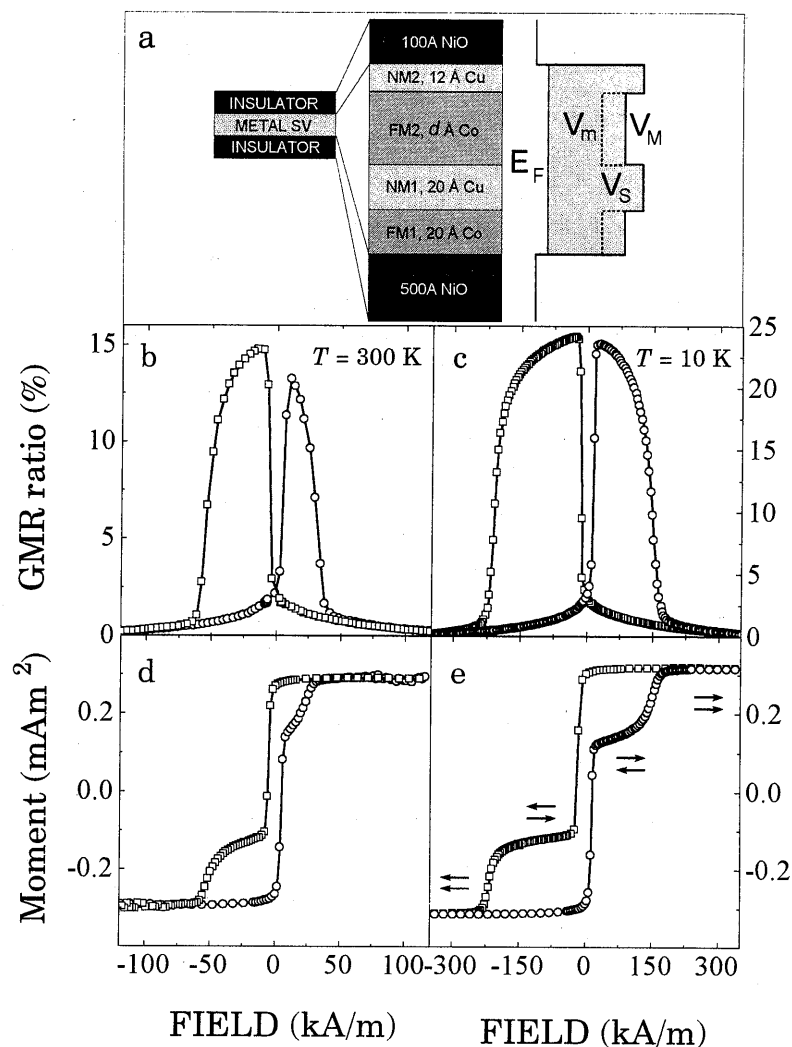


Figure 9.1: (a) Illustration of an insulating/metal artificial layered structure consisting basically of 500 Å NiO/F1/NM1/F2/NM2/100 Å NiO, with F1 = 20 Å Co, NM1 = 20 Å Cu, F2 = d Å Co, and NM2 = 12 Å Cu. At the far right of this panel the potential landscape is schematically depicted, with E_F the Fermi-level, and V_S , V_m^\uparrow , and V_m^\downarrow , the potentials for spacer electrons, spin-up electrons and spin-down electrons of the ferromagnet, respectively. The room-temperature GMR ratio ($= [G_P - G_{AP}]/G_{AP}$) and magnetization of a system with F2 = 40 Å Co is shown in panel (b) and (d) respectively; panel (c) and (e) are data obtained at 10 K. The magnetic field was applied along the bias direction. Arrows in the low-temperature magnetization data (e) visualizes the direction of the magnetization F1 and F2.

differential sheet conductivity $G_P - G_{AP}$ when d_F is roughly speaking¹ larger than half the bulk mean free path in which case the movement of the (spin-polarized) electron is not limited by boundary scattering. On the other hand, G_{AP} (and G_P) is almost linearly increasing with d_{F2} , since in the lowest order of approximation the current is carried in parallel in the various layers (Die92a).

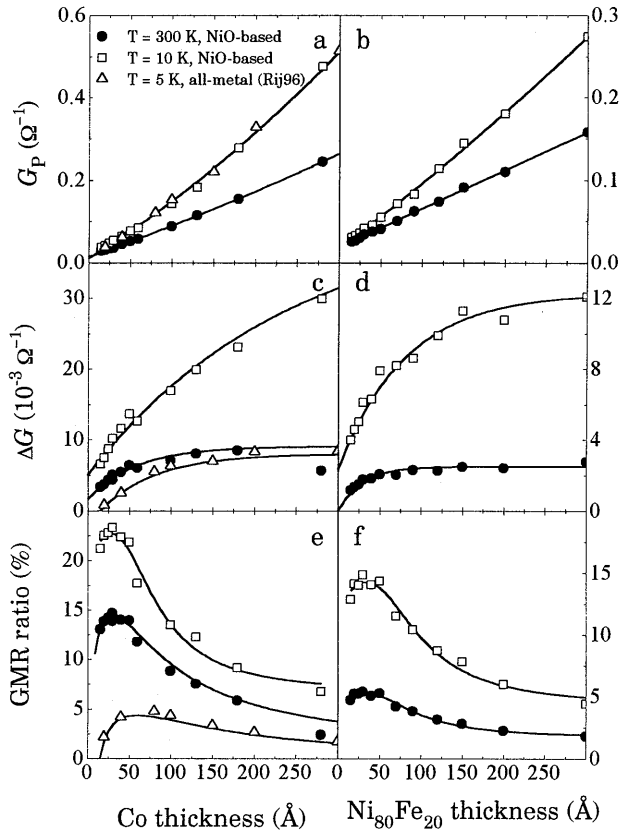


Figure 9.2: Parallel sheet conductivity G_P (panel a,b), differential sheet conductivity $G_P - G_{AP}$ (panel c,d) and GMR ratio $[G_P - G_{AP}]/G_{AP}$ (panel e,f) of Co- and Ni₈₀Fe₂₀-based structures consisting of 500 Å NiO/F1/NM1/F2/NM2/100 Å NiO, with NM1 = 20 Å Cu, NM2 = 12 Å Cu, the ferromagnetic layer F1 fixed at 20 Å, and a variable thickness of the ferromagnetic layer F2. In the left panels F1 and F2 refer to Co, the right panels refer to Ni₈₀Fe₂₀. The data are obtained at $T = 300$ K (●) and $T = 10$ K (□). Low-temperature data (Δ) of FeMn exchange-biased all-metal spin valves (Rij96) of the type 30 Å Ta/d Co/30 Å Cu/20 Å Co/100 Å FeMn/20 Å Ta are included for comparison. All the curves in the figure are guides to the eye only!

¹ More precisely, in chapter 7 we showed that the behavior of $G_P - G_{AP}$ is exponential, with a characteristic length scale that is roughly half the mean free path of the spin-up electrons due to spatial averaging over all the electron angles, a result also found by Diény (Die94).

This characteristic behavior is also observed in our material, see figure 9.2, although the maximal GMR ratio is located at smaller ferromagnetic layer thickness, roughly between 20 Å and 40 Å. A comment should be made at this point about the possibility that the maximum might appear due to structural degradation of the uncoupled ferromagnetic layer when its thickness becomes very small. In this respect, we could not detect indications for nonuniform or clusterlike behavior of Co from both magnetoresistance and magnetization, down to the smallest thickness covered in the experiments ($d_{\text{Co}} = 15 \text{ Å}$), which is in favor of the true spin valve nature of the observed maximum. Note that this is consistent with our measurements described in chapter 8, where probe layers thicker than 15 Å are always ferromagnetic. In the discussion we will return to this maximum in more detail.

The most prominent feature of the data is the magnitude of both $\Delta G = G_{\text{P}} - G_{\text{AP}}$ and the GMR ratio. In the Co/Cu/Co system an unusually high GMR ratio of 15% at room temperature, increasing at low temperatures to almost 25%, has been measured, whereas the systems containing $\text{Ni}_{80}\text{Fe}_{20}/\text{Cu}/\text{Ni}_{80}\text{Fe}_{20}$ yield more than 5% at room temperature and 15% at low temperatures, which is illustrated in figure 9.2. The permalloy data cannot be easily compared with reports in literature due to differences in the individual layer thicknesses, although the GMR ratio in FeMn-based $\text{Ni}_{80}\text{Fe}_{20}/\text{Cu}/\text{Ni}_{80}\text{Fe}_{20}$ spin valves does never exceed 10% at low temperatures (Die92a, Rij96), whereas in our case the low temperature maximum amounts to 15%. To allow for comparison with the Co/Cu/Co materials, figure 9.2 is supplemented with low-temperature data obtained in UHV-sputtered 30 Å Ta/ d Å Co/30 Å Cu/20 Å Co/100 Å FeMn/20 Å Ta all-metal spin valves (Rij96) in which the thickness of the pinned Co layer is also 20 Å, and this clearly demonstrates enhanced magnetoresistivity in the NiO structures by a factor of 5. To be complete we mention here that also in all-metal spin valves GMR ratios larger than 12% can be reached at low temperatures, but only for thicker values of the pinned magnetic layer (see for instance Rij96). In the all-metal FeMn structure for which data are given in figure 9.2, the Cu thickness is 10 Å more than for the NiO material. However, the resulting negative effect on the GMR ratio will not exceed a factor of two (Hei94, Die94). Furthermore, our data are consistent with the observation by Anthony *et al.* (Ant94) of large GMR ratios in $\text{Ni}_{80}\text{Fe}_{20}/\text{Co}/\text{Cu}/\text{Co}/\text{Ni}_{80}\text{Fe}_{20}$ spin valves grown on NiO. Egelhoff *et al.* (Ege95) reported a GMR ratio exceeding 21% at room temperature in symmetric Co/Cu/Co/Cu/Co spin valves sandwiched between NiO, but in both two cases the spin-engineered structures are very much different from our spin valve design, which complicates a straightforward and meaningful comparison with the present data. In the following we will specifically evaluate the Co/Cu/Co data and focus on the physical mechanism behind the unusually large GMR ratios observed in this novel type of spin valve.

9.3 Interpretation

The description of electronic conduction within the metallic part of the spin valves, confined between insulating NiO layers (see figure 9.1a at far right), requires a treatment in which the potential steps at the insulating barriers are included. Since we are outside the regime of quantum-size effects ($k_F^{-1} \ll L$, with L the potential width) and quantum-interference effects ($k_F^{-1} \ll \lambda$, with λ the mean free path), we may in this case safely adopt (Cam92) semiclassical theories such as the Camley-Barnas model (Cam89) or the Hood and Falicov model (Hoo92), as was already discussed in chapter 3. According to the Hood-Falicov model, the spin-dependence of the inner potentials within the magnetic layers ($V^\uparrow \neq V^\downarrow$) and the difference with the spacer layer inner potential, V_S , as shown in the top panel of figure 9.1 at far right, may be an important source for giant magnetoresistance in Co/Cu/Co trilayers (Hoo92, chapter 3) due to the channelling effect within the Cu spacer that is effectuated when V_S is larger than both V^\uparrow and V^\downarrow . However, our main goal here is to consider the effect of the *dominant* potential step that is located at the interfaces between insulating NiO and the adjacent metallic spin valve, and thus we assumed a constant potential within the metal part of the structure, $V^\uparrow = V^\downarrow = V_S$. Scattering at the insulating NiO layer, where $V > E_F$, is expected to be reflective, provided that the interface is perfectly flat. The description of our structures is then identical to the description used originally by Camley and Barnas (Cam89), in which R is the reflectivity at NiO and the remainder of the electrons is diffusely scattered at the barrier ($D = 1 - R$), since the transmission T is zero.

With this model we have calculated the magnetoresistance of NiO/F1/NM1/F2/NiO with F1 = 20 Å Co and NM1 = 20 Å Cu, as a function of the layer thickness of F2 for three cases of the barrier reflectivity R at NiO/F1 and F2/NiO insulator/metal interfaces: (1) $R = 0$, representing perfectly diffuse scattering in which case electrons that strike the barriers lose all memory of their previous velocity, (2) $R = 1$, representing full specular reflectivity ($D = 0$), and (3) an intermediate situation $R = \frac{1}{2}$, where half of the electrons reflect and the remaining part is diffusely scattered ($D = \frac{1}{2}$). With increasing specular reflectivity R the shape of the magnetoresistance curve as a function of free magnetic layer thickness (d_{F2}) is significantly changed. Generally speaking, the maximum in the GMR ratio is pushed to a lower ferromagnetic thickness. Most importantly, the reflectivity induces a dramatic enhancement of the GMR ratio, which is a common feature in semiclassical calculations when a trilayer system is compared with an infinite multilayer (Hei94, Die94) that in fact represents a trilayer buried within infinite potentials.

When we focus on the enhancement of the GMR ratio this may be understood easily from the right panel of figure 9.3 in which the trajectory of a spin-up electron is schematically drawn. In sandwiches the differential conductivity $G_P -$

G_{AP} is considerably reduced by spin-independent boundary scattering, corresponding to $R = 0$ (see the top of the sketch). When the reflectivity of the electron is unity ($R = 1$) a spin-up electron in the parallel configuration may experience its full bulk mean free path before being scattered and is thereby able to induce a significant increase of G_P . In contrast, no substantial increase of conductivity is expected in the antiparallel case (G_{AP}) since the 'lifetime' of an electron that is spin-up in one magnetic layer is still to a great extent limited by spin-dependent scattering in the other magnetic layer where the same electron is a spin-down electron. This explains the enhanced difference between the conductivity in the parallel and antiparallel state when a spin valve is confined within reflective barriers.

Quantitatively, the actual enhancement of the GMR ratio induced by electron reflectivity at the outer boundaries of the trilayer depends very much on the (spin-dependent) parameters chosen in the calculations. As an example, when the mean free path of the carriers is small compared to the ferromagnetic layer thicknesses the enhancement is only very modest, whereas with increasing scattering lengths it may become arbitrarily large. In the calculations presented in figure 9.3 the maximal attainable GMR ratio is enhanced by at least a factor of 4 when choosing a set of parameters in the range of what has been reported previously in sputtered Co/Cu/Co spin valves (Die92a,b).

Subsequently, the calculations are compared with the experimental data for Co/Cu/Co spin valves (see again figure 9.3) obtained at low temperatures, that is the limit to which the semiclassical calculation applies when no spin-mixing terms are taken into account (Cam89). It is clearly seen that the data for FeMn are fairly close to the situation with no reflectivity at the surfaces, $R = 0$, whereas in the present NiO-based material a non-zero reflectivity seems indispensable to predict a considerable higher GMR ratio observed at a smaller ferromagnetic layer thickness. We would like to emphasize that although it is not our aim in this paper to pursue *quantitative* description of the observed magneto-resistive enhancement, the data can be simply understood by the introduction of reflectivity at the insulating barrier. Moreover, it is gratifying that a fair agreement with the data (*with* and *without* the insulating barrier) has been established by using a set of parameters close to reports in literature (Die92a,b), see the caption of figure 9.3. We like to mention however that the apparent agreement may be somewhat fortuitous as we will see in the discussion of the specular reflectivity later on.

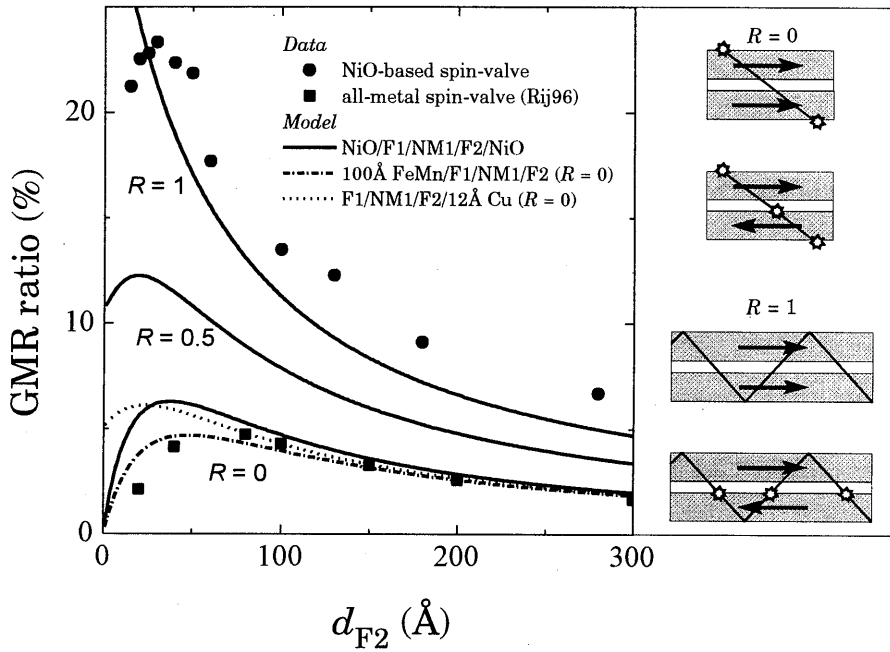


Figure 9.3: In the left panel the solid curves represent the calculated GMR ratio of a model system NiO/F1/NM1/F2/NiO with F1 = 20 Å Co, NM1 = 20 Å Cu, as a function of the ferromagnetic layer thickness of F2, for $R = 0, 0.5$, and 1, i.e. the reflectivity at the insulator/metal interfaces NiO/F1 and F2/NiO. The dashed-dotted curve represents a model system 100Å FeMn/F1/NM1/F2 with F1 = 20 Å Co, NM1 = 20 Å Cu, $\lambda = 12$ Å estimated for the mean free path in FeMn (Rij96), and with diffusive scattering at the outer boundaries ($R = 0$). The dotted curve represents a system F1/NM1/F2/NM2, again with F1 = 20 Å Co, NM1 = 20 Å Cu, and diffusive boundary scattering ($R = 0$), and with NM2 = 12 Å Cu. For comparison the low-temperature data of all-metal Co/Cu/Co spin valves are included (■, Rij96) together with the data obtained in our stacks (●), see also figure 9.2. The parameters used for these semiclassical calculations are $R^\uparrow = 0$, $T^\uparrow = 1$, $R^\downarrow = 0$, $T^\downarrow = 0.2$ for the Co/Cu interfaces, $\lambda^\uparrow = 80$ Å, $\lambda^\downarrow = 20$ Å for the spin-dependent mean free paths in Co, and $\lambda_{Cu} = 200$ Å. Note that these parameters are close to those used by Dieny *et al.*, (Die92a,b). In the panel at right the solid lines represent the trajectory of a spin-up electron, stars (★) indicate scattering events. It is shown that the conductivity in parallel configuration is dramatically enhanced when diffusive boundary scattering ($R = 0$) is replaced by specular reflectivity ($R = 1$). For a more detailed explanation see the text.

It should be noted at this point that one may argue that even without reflectivity of electrons ($R = 0$) the impenetrable NiO prevents any shunting of current through subsidiary layers (such as FeMn in the metallic case) and may

result in an effective enhancement of the GMR ratio. To calculate the role of current shunting we have applied the semiclassical approach to a model system representative for the aforementioned exchange-biased all-metal spin valves, *viz.* 100 Å FeMn/F1/NM1/F2, with F1 = 20 Å, and NM1 = 20 Å, assuming diffuse scattering at the outer boundaries (which in fact corresponds to $R = 0$). The low-temperature mean free path of FeMn is estimated as $\lambda = 12$ Å (Rij96). The calculated dashed-dotted curve in figure 9.3 represents the GMR ratio of this structure and shows that shunting in the FeMn layer reduces the GMR ratio. The reduction is however relatively small compared to the effect of electron reflectivity. Parenthetically we note that a reduced GMR ratio in FeMn-based spin valves can also (partially) be understood if spin-flip (magnon) scattering is present in the antiferromagnetic part of the stack, which is obviously absent in the case of the impenetrable NiO.

Additionally, one should realize that the nonmagnetic layer at the outer surface of the spin valve trilayer, NM2 (see figure 9.1a), also contributes to $G_P - G_{AP}$, and hence the GMR ratio as we have seen in the previous chapter. However, we estimated from a calculation of the model system F1/NM1/F2/NM2, again with F1 = 20 Å, NM1 = 20 Å, $R = 0$, and with NM2 = 12 Å Cu according to our actual spin valve design, that this does not really affect the maximal attainable GMR ratio, see the dotted line in figure 9.3. Although we have shown in chapter 8 (see figure 8.4) that the GMR ratio depends on the thickness of the back layer, a thickness of 12 Å is too small to cause a significant change in maximum magnitude of the GMR ratio of our present spin valves. This maximum however, occurs at a smaller magnetic layer thickness of F2 due to the fact that the outside nonmagnetic layer effectively enlarges the regime that contributes to the differential sheet conductivity $G_P - G_{AP}$.

Summarizing the semiclassical calculations presented here, we find strong indication for the presence of increased reflectivity at an insulating NiO barrier since without specular reflections a proper description of the data obtained for these spin valves seems impossible.

9.4 Discussion

In order to obtain more straightforward evidence for the occurrence of enhanced reflective scattering at interfaces with NiO, we have measured the sheet resistivity of single Co layers (with thicknesses in between 10 Å and 100 Å) on top of a 500 Å NiO layer and capped with Cu to avoid oxidation of the Co. The results are shown by the open squares in the top panel of figure 9.4. A magnetic field was applied during the measurement to obtain a reproducible saturated magnetic state of the ferromagnetic Co. We expect that the outside Cu layer, interfaced to air, scatters all conduction electrons in a random direction (diffuse scattering) due to contamination and irregular oxidation after growth. When this

system is compared with a Co layer capped with a second top NiO layer, we found an *increase* of the sheet resistance (see again the figure), opposite of what one would expect when specular reflections at this top NiO interface were increased compared to the Cu/air interface. Although it would be possible to unravel the origin of the apparent lack of reflectivity in these specific structures, it was more obvious to test the role of the top NiO layer also in the actual spin valve structures, which for this purpose were designed with and without a capping NiO layer in one series of sputter-deposited samples. Again we did not find evidence for increased specular scattering of electrons at the *top* NiO layer from the observation that the GMR ratio is not significantly affected, see the data in figure 9.4b². However, in this respect it is important to note that very recently Egelhoff *et al.* (Ege97) have reported also an increased specular reflection for Au, Ag, or Cu deposited on a Si(100)/50 Å NiO/25 Å Co/20 Å Cu/30 Å Co spin valve. Therefore, it is still possible that there is specular scattering at the top NiO interface, but that the degree of specular scattering at the top Cu layer is comparable to the degree of specular scattering at the top NiO layer. This would be consistent with the results of Swagten *et al.* (Swa97) who report an increase in the specular reflection at the top NiO layer in Si(100)/35 Å Ta/80 Å Ni₈₀Fe₂₀/25 Å Cu/*d* Å Ni₈₀Fe₂₀/400 Å NiO spin valves compared to a top FeMn layer in Si(100)/35 Å Ta/80 Å Ni₈₀Fe₂₀/25 Å Cu/*d* Å Ni₈₀Fe₂₀/100 Å FeMn/35 Å Ta spin valves.

One would be tempted to test the role of the bottom NiO layer also, just by removing the bottom NiO and monitor the impact on the GMR. This layer is however the key element to our spin valves and, when removed, the antiparallel (AP) magnetic state will be absent and no magnetoresistance will be left. Nevertheless, it should be emphasized that the bottom NiO layer is not identical to the top NiO layer. To start with, from XRD we have observed that NiO grown at room temperature, which in fact is the growth condition of NiO on top, does not yield a well-defined texture [(111) and (200) Bragg reflections were observed] and this may actually lead to a loss of interface quality. Hence, the interface reflectivity may be rather poor and e.g. semiclassical calculations (Hoo94) have predicted that progressive roughening of the interface (beyond a few Å) reduces the GMR ratio irrespective of the details of the potential landscape of the spin valve or multilayer. In contrast to the top NiO, the bottom NiO layer was grown at 200 °C temperature to obtain a (111) texture, which might have a positive impact on the interface quality.

² We have checked that the switching fields of the exchange-biased ferromagnetic layer are not affected by the specific design of the spin valves in these additional experiments, which justifies a meaningful comparison of the measured GMR ratios.

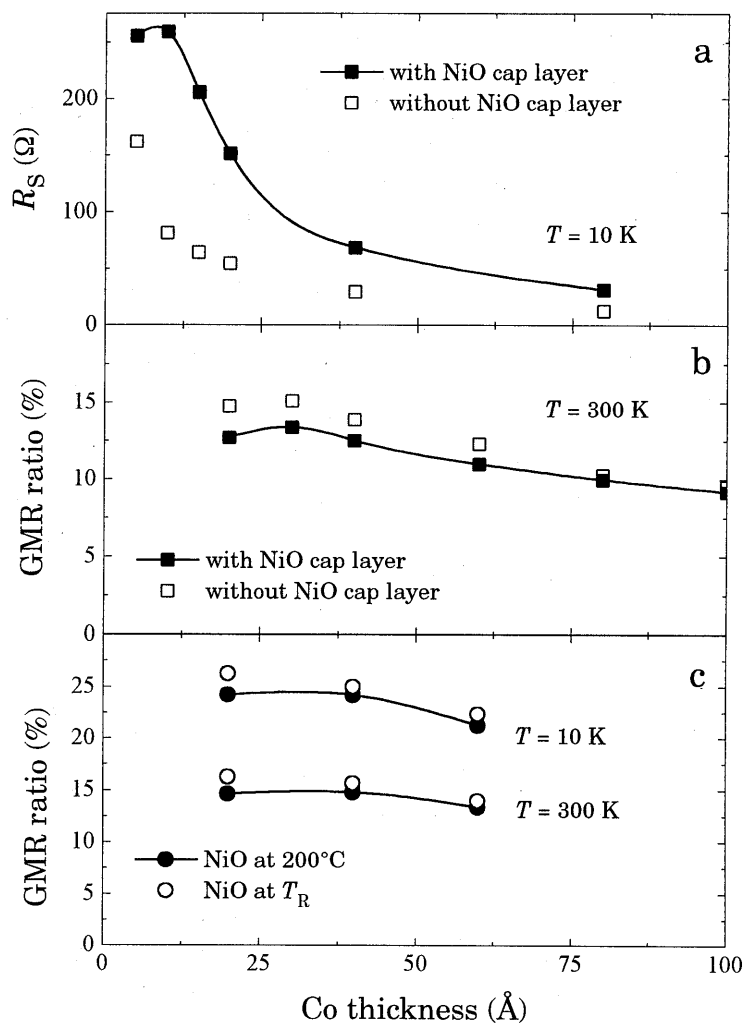


Figure 9.4: (a) Low-temperature sheet resistance R_s of 500 Å NiO/d Co/100 Å NiO/30 Å Cu (■) and 500 Å NiO/d Co/30 Å Cu (□). The data do not support increased reflectivity at the Co/NiO interface. (b) GMR ratio of 500 Å NiO/20 Å Co/20 Å Cu/d Co/12 Å Cu/100 Å NiO, (■) and 500 Å NiO/20 Å Co/20 Å Cu/d Co/12 Å Cu taken at $T = 300$ K (□). Reflectivity at the top Cu/NiO interface is also in this case not evidenced. (c) GMR ratio at $T = 10$ K and $T = 300$ K of 500 Å NiO/20 Å Co/20 Å Cu/d Co/12 Å Cu/100 Å NiO, in which the bottom 500 Å NiO layer is grown at 200°C (●) and ambient temperature (○), yielding no substantial difference in magnetoresistance.

We tried to affect the structural properties of the interfacial NiO/Co region by growing one series of samples at both 200 °C and room temperature. Although we observed that the (111) texture is present only when the bottom NiO is grown

at elevated temperatures this does not change the GMR properties², which is exemplified by the data presented in figure 9.4c. For the room-temperature grown samples even a slight enhancement of the GMR ratio is observed, which means that the presence of reflectivity may not be concluded from this type of experiment and it is conceivable that diffusion between e.g. NiO and Co may be a relevant factor for the observed behavior in figure 9.4c.

To investigate the role of the bottom NiO layer in more detail we performed several experiments that directly influence this particular layer. Successively we varied the Ar sputter pressure at which this bottom layer is grown, we used a different substrate, *viz.* single crystalline SrTiO₃, we varied the thickness of the bottom NiO layer, and we deliberately enlarged the intermixing at the bottom NiO/Co interface by alternately sputtering 0.5 Å NiO and 0.5 Å Co up to a total thickness of 5 Å mixed NiO and Co. Although, for instance, the use of the single crystalline SrTiO₃ or a thicker NiO bottom layer and even intermixing lead to a small increase in the GMR ratio and could thus in principle indicate the presence of an enhanced reflectivity, none of these experiments yielded direct or convincing evidence for an enhancement. This is caused mainly by the interaction of the bottom NiO layer with the adjacent Co layer. In each experiment where the GMR ratio increased, also an increase in the coercive field of this Co layer was observed, resulting in a somewhat better antiparallel configuration between the two magnetic layers at small magnetic fields, which explains an increase of GMR ratio just as well.

Another difference between the top NiO layer and the bottom NiO layer is the fact that the top NiO layer is grown on nonmagnetic Cu whereas the bottom NiO is directly interfaced with a ferromagnetic layer. Hypothetically, it might be the magnetic character of the interface between the oxidic antiferromagnetic NiO and the ferromagnetic Co that is most favorable for reflectivity of the electron wave function. In fact, the scattering of electrons impinging on an antiferromagnetic oxide may be profoundly affected by the spin-dependence of the electron lifetime in ferromagnetic materials. No experimental data or theoretical models are yet available, and this certainly requires further investigation. We intend to address this experimentally by replacing NiO by CoO, since the Néel temperature of the latter is around room temperature, whereas NiO orders at a much higher temperature ($T_N \approx 250^\circ\text{C}$). This means that with CoO it would be possible to monitor the (spin-dependent) scattering at barriers in the antiferromagnetic state of CoO below room temperature, but also when CoO is paramagnetic at higher temperatures, which might yield some clues about the underlying fundamental mechanism.

In the discussion about possible reflections at insulating NiO we should not forget to mention one final point of interest which also focuses on structural aspects. In all-metal spin valves (Hei94, Die94) the trilayer is grown often on a thin metallic buffer layer [e.g. 20Å Ta (Rij96)] to improve the texture, and

thicker buffer layers are avoided to prevent considerable shunting of the current that effectively suppresses the GMR ratio. In contrast, the NiO we use as a base layer is in all cases relatively thick (500 Å), which is not disadvantageous in view of shunting due to its insulating behavior, but on the other hand it might improve the structural integrity of the subsequently grown stack. It is rather difficult to address this experimentally since a thick NiO layer is indispensable for the required exchange-biasing of the first ferromagnetic layer. ^{59}Co -NMR experiments on the samples glass/500 Å NiO/20 Å Co/20 Å Cu/ d Å Co/12 Å Cu/100 Å NiO have shown however that the magnetic layers do not seem to possess a well-defined structure. Rather the Co layers consist of a mixture of fcc Co, hcp Co and stacking faults. Also the measurements indicate rather rough interfaces that do not seem to support the presence specular reflections.

A final comment concerns the ferromagnetic layer thickness at which a maximal GMR ratio is observed ($d_{\text{F,max}}$) in both our structures (see figure 9.2) and the symmetric structures of the type 500 Å NiO/ d_2 Co/18 Å Cu/ d_1 Co/18 Å Cu/ d_2 Co/NiO studied by Egelhoff *et al.* (Ege95). The latter authors argued intuitively that a study of the GMR ratio as a function of d_1 and d_2 might provide evidence for the relevance of specular reflectivity. More precisely, it was suggested that in the case of perfectly specular scattering the optimum thickness of the center Co layer ($d_{1,\text{max}}$) is expected to be twice the optimum thickness of the outer two Co layers ($d_{2,\text{max}}$). From the observation that in their case $d_{1,\text{max}}$ was somewhat less than $2 \times d_{2,\text{max}}$, it was subsequently concluded that only a fraction of the electrons scatters specularly. However, our semiclassical transport calculations applied to these symmetric spin valves do only partially corroborate this intuitive model. It appears that with reflectivity the location of the maxima is determined by a delicate balance between interface and bulk spin-dependent scattering (SDS) and is certainly not simply a factor of 2, although in general it follows from the calculations that $d_{2,\text{max}}$ is *always smaller* than $d_{1,\text{max}}$. But most interestingly, we found that without reflectivity, i.e. with diffuse scattering at the outer boundaries of d_2 , the situation is completely reversed, *viz.* $d_{2,\text{max}}$ is *larger* than $d_{1,\text{max}}$, since the thickness of the outside layers d_2 should be at least of the order of the bulk mean free path to avoid the negative effect of boundary scattering on the GMR ratio (see chapter 3). The experimental observation by Egelhoff *et al.* ($d_{2,\text{max}} < d_{1,\text{max}}$) may thus be regarded as a straightforward additional proof for the presence of specular reflectivity in NiO-based spin valves.

For our structures with only two ferromagnetic layers such a thickness analysis is not possible and consequently it appears that the low value of $d_{\text{F,max}}$ is not simply indicative for the presence of specular reflectivity. That would require a detailed fitting procedure of solutions given by the semiclassical transport equation to the experimental data, which is far outside the scope of this chapter and would certainly not yield unambiguous conclusions on the role of reflections. Nevertheless, we like to mention that calculations for our system

with two ferromagnetic layers do predict that when diffusive boundary scattering is replaced by reflective barrier scattering, $d_{F,max}$ will be located at a *smaller* layer thickness. This is consistent with our observation that $d_{F,max}$ in the NiO structures is considerably less (20-40 Å) than commonly seen in conventional FeMn-based spin valves (Die92a,b, Rij96) where $d_{F,max}$ is always more than 50 Å, although we should not forget that also the 12 Å Cu layer on top of the Co/Cu/Co trilayer lowers the optimum thickness.

9.5 Conclusions

To summarize, we have presented experimental evidence for enhanced magnetoresistivity in spin valve trilayers contained within insulating barriers of antiferromagnetic NiO. From semiclassical transport calculations we have found indications that this enhancement is induced by reflectivity of electron waves at the insulator/metal interface. In particular, the bottom NiO/Co interfaces are expected to play a key role in the observed increased giant magnetoresistance in the NiO-based spin valves.

References

- Ant94: T.C. Anthony, J.A. Brug, and S. Zhang, *IEEE Trans. Magn.* **30**, 3819 (1994).
- Arb93: A. Arbaoui, A. Dinia, and P. Panissod, *Solid State Commun.* **85**, 475 (1993).
- Ash76: N. W. Ashcroft and N.D. Mermin in *Solid State Physics*, Saunders College, Philadelphia (1976).
- Bad96: S.D. Bader and Dongqi Li, *J. Magn. Magn. Mater.* **156**, 153 (1996).
- Bai88: M.N. Baibich, J.M. Broto, A. Fert, F. Nguyen Van Dau, and F. Petroff, *Phys. Rev. Lett.* **61**, 2472 (1988).
- Bar82: *Physics and Applications of the Josephson Effect*, Antonio Barone and Gianfranco Paternò, John Wiley & Sons, Inc. (1982).
- Bar90: J. Barnas, A. Fuss, R.E. Camley, P. Grünberg and W. Zinn, *Phys. Rev.* **B42**, 8110 (1990).
- Bar90a: A. Barthélémy, A. Fert, M.N. Baibich, S. Hadjoudj, F. Petroff, P. Etienne, R. Cabanel, S. Lequien, F. Nguyen Van Dau, and G. Creuzet, *J. Appl. Phys.* **67**, 5908 (1990).
- Bar91: A. Barthélémy and A. Fert, *Phys. Rev.* **B43**, 13124 (1991).
- Bar94: J. Barnas, *J. Magn. Magn. Mater.* **131**, L14 (1994).
- Bar95: J. Barnas and Y. Bruynseraede, *Europhys. Lett.* **32**, 167 (1995).
- Bar96: J. Barnas and Y. Bruynseraede, *Phys. Rev.* **B53**, 5449 (1996).
- Bau91: P. Baumgart, B.A. Gurney, D.R. Wilhoit, Thao Nguyen, B. Dieny, and V.S. Speriosu, *J. Appl. Phys.* **69**, 4792 (1991).
- Ben90: W.R. Bennet, W. Schwarzacher, and W.F. Egelhoff, Jr., *Phys. Rev. Lett.* **65**, 3169 (1990).
- Bin89: G. Binasch, P. Grünberg, F. Saurenbach, and W. Zinn, *Phys. Rev.* **B39**, 4828 (1989).
- Blo92: P.J.H. Bloemen, M.T. Johnson, J. aan de Stegge, and W.J.M. de Jonge, *J. Magn. Magn. Mater.* **116**, L315 (1992).

- Blo94: P.J.H. Bloemen, H.W. van Kesteren, H.J.M. Swagten, and W.J.M. de Jonge, *Phys. Rev.* **B50**, 13505 (1994).
- Blo97: A. Blondel, B. Doudin, and J.-Ph Ansermet, *J. Magn. Magn. Mater.* **165**, 34 (1997).
- Boe91: D.K.G. de Boer, *Phys. Rev.* **B44**, 498 (1991).
- Boe95: D.K.G. de Boer, A.J.G. Leenaers, and W.W. van den Hoogenhof, *X-Ray Spectrometry* **24**, 91 (1995).
- Bon95: M.A. Bongers, Master's thesis, internal report, Eindhoven University of Technology (1995).
- Boz57: R.M. Bozorth, *Ferromagnetism*, Van Nostrand Reinhold, New York (1957).
- Bra91: R.E.A. Braun, Master's thesis, internal report, Eindhoven University of Technology (1991).
- Bro87: F.J.A. den Broeder, H.C. Donkersloot, H.J.G. Draaisma, and W.J.M. de Jonge, *J. Appl. Phys.* **61**, 4317 (1987).
- Bro89: F.J.A. den Broeder, D. Kuiper, H.C. Donkersloot, and W. Hoving, *Appl. Phys. A* **49**, 507 (1989).
- Bru88: P. Bruno, *J. Phys. F: Met. Phys.* **18**, 1291 (1988).
- Bru91: P. Bruno and C. Chappert, *Phys. Rev. Lett.* **67**, 1602 (1991).
- Bru92: P. Bruno and C. Chappert, *Phys. Rev.* **B46**, 261 (1992).
- But96: W.H. Butler, X.-G. Zhang, D.M.C. Nicholson, T.C. Schulthess and J.M. MacLaren, *Phys. Rev. Lett.* **76**, 3216 (1996).
- Cam82: I.A. Campbell and A. Fert, in *Ferromagnetic Materials*, edited by E.P. Wohlfarth, North-Holland, Amsterdam, Vol. **3**, 747 (1982).
- Cam89: R.E. Camley and J. Barnas, *Phys. Rev. Lett.* **63**, 664 (1989).
- Cam92: H.E. Camblong and P.M. Levy, *Phys. Rev. Lett.* **69**, 2835 (1992).
- Cam95: H.E. Camblong, *Phys. Rev.* **B51**, 1855 (1995).
- Car85: P.F. Carcia, A.D. Meinhaldt, and A. Suna, *Appl. Phys. Lett.* **47**, 178 (1985).

- Chi91: J.R. Childress and C.L. Chien, *Phys. Rev.* **B43**, 8089 (1991).
- Coe97: R. Coehoorn in *Magnetic thin films and multilayer systems: Physics, analysis and industrial applications*, Springer Series in Materials Science, U. Hartmann, ed. (to be published in 1997).
- Cou74: T.J. Coutts, *Electrical conduction in thin metal films*, Elsevier Scientific Publishing Company (1974).
- Cul72: B.D. Cullity, *Introduction to Magnetic Materials*, Addison-Wesley, New York (1972).
- Dah88: E. Dan Dahlberg, K. Riggs, and G.A. Prinz, *J. Appl. Phys.* **63**, 4270 (1988).
- Die90: B. Dieny, J.P. Gavigan, and J.P. Rebouillat, *J. Phys.: Condens. Matter* **2**, 159 (1990); B. Dieny and J.P. Gavigan, *J. Phys.: Condens. Matter* **2**, 187 (1990).
- Die91: B. Dieny, *Europhys. Lett.* **17**, 261 (1991).
- Die91a: B. Dieny, V.S. Speriosu, S.S.P. Parkin, B.A. Gurney, D.R. Wilhoit, and D. Mauri, *Phys. Rev.* **B43**, 1297 (1991).
- Die92: B. Dieny, J.P. Nozieres, V.S. Speriosu, B.A. Gurney, and D.R. Wilhoit, *Appl. Phys. Lett.* **61**, 2111 (1992).
- Die92a: B. Dieny, P. Humbert, V.S. Speriosu, S. Metin, B.A. Gurney, P. Baumgart, and H. Lefakis, *Phys. Rev.* **B45**, 806 (1992).
- Die92b: B. Dieny, *Europhys. Lett.* **17**, 261 (1992).
- Die93: B. Dieny, V.S. Speriosu, J.P. Nozières, B.A. Gurney, A. Vedyayev, and N. Ryzhanova, in *Magnetism and Structure in Systems of Reduced Dimension*, edited by R.F.C. Farrow, B. Dieny, M. Donath, A. Fert, and B.D. Hermsmeier (Plenum, New York), 279 (1993).
- Die93a: B. Dieny, A. Vedyayev, and N. Ryzhanova, *J. Magn. Magn. Mater.* **121**, 366 (1993).
- Die94: B. Dieny, *J. Magn. Magn. Mater.* **136**, 335 (1994).
- Dim85: R. Dimmich, *J. Phys. F: Met. Phys.* **15**, 2477 (1985).
- Dub97: S. Dubois, J.M. Beuken, L. Piraux, J.L. Duvail, A. Fert, J.M. George, and J.L. Maurice, *J. Magn. Magn. Mater.* **165**, 30 (1997).

- Dug77: J.S. Dugdale, *The Electrical Properties of Metals and Alloys*, Edward Arnold, London (1977).
- Duv94: J.L. Duvail, A. Fert, L.G. Pereira, and D.K. Lottis, *J. Appl. Phys.* **75**, 7070 (1994).
- Edw91: D.M. Edwards, J. Mathon, and R. Bechara Muniz, *IEEE transac. on magn.* **27**, 3548 (1991); D.M. Edwards and J. Mathon, *J. Magn. Magn. Mater.* **93**, 85 (1991).
- Ege95: W.F. Egelhoff, Jr., T. Ha, R.D.K. Misra, Y. Kadmon, J. Nir, C.J. Powell, M.D. Stiles, R.D. McMichael, C.-L. Lin, J.M. Sivertsen, J.H. Judy, K. Takano, A.E. Berkowitz, T.C. Anthony, and J.A. Brug, *J. Appl. Phys.* **78**, 273 (1995).
- Ege97: W.F. Egelhoff, Jr., P.J. Chen, C.J. Powell, M.D. Stiles, R.D. McMichael, J.H. Judy, K. Takano, A.E. Berkowitz, and J.M. Daughton, to be published in *IEEE Trans. Magn.* (1997).
- Fol91: W. Folkerts, *J. Magn. Magn. Mater.* **94**, 302 (1991).
- Fre93: P.P. Freitas, I.G. Trindade, L.V. Melo, N. Barradas, and J.C. Soares, in *Magnetism and Structure in Systems of Reduced Dimension*, edited by R.F.C. Farrow, B. Dieny, M. Donath, A. Fert, and B.D. Hermsmeier (Plenum, New York), 343 (1993).
- Fuc38: K. Fuchs, *Proc. Camb. Phil. Soc.* **34**, 100 (1938).
- Ful92: E.E. Fullerton, J.E. Mattson, S.R. Lee, C.H. Sowers, Y.Y. Huang, G. Felcher, S.D. Bader, and F.T. Parker, *J. Magn. Magn. Mater.* **117**, L301 (1992).
- Ful92a: E.E. Fullerton, D.M. Kelly, J. Guimpel, I.K. Schuller, and Y. Bruynseraede, *Phys. Rev. Lett.* **68**, 859 (1992).
- Gal76: J.C. Gallop and B.W. Petley, *J. Phys. E: Sci. Instrum.*, Vol. **9**, 417 (1976).
- Gas74: Stephen Gasiorowicz, *Quantum Physics*, John Wiley & Sons, Inc., New York (1974).
- Geo94: J.M. George, L.G. Pereira, A. Barthélémy, F. Petroff, L. Steren, J.L. Duvail, A. Fert, R. Loloee, and P.A. Schroeder, *Phys. Rev. Lett.* **72**, 408 (1994).
- Gij93: M.A.M. Gijs, S.K.J. Lenczowski, and J.B. Giesbers, *Phys. Rev. Lett.* **70**, 3343 (1993).
- Gij94: M.A.M. Gijs, S.K.J. Lenczowski, R.J.M. van de Veerdonk, J.B. Giesbers, M.T. Johnson, and J.B.F. aan de Stegge, *Phys. Rev.* **B50**, 16733 (1994).

- Gij97: M.A.M. Gijs and G.E.W. Bauer, Perpendicular Giant Magnetoresistance of Magnetic Multilayers, to be published in *Advances in Physics* (1997).
- Grü86: P. Grünberg, R. Schreiber, Y. Pang, M.B. Brodsky, and H. Sowers, *Phys. Rev. Lett.* **57**, 2442 (1986).
- Gur93: B.A. Gurney, V.S. Speriosu, J.P. Nozieres, H. Lefakis, D.R. Wilhoit, and O.U. Need, *Phys. Rev. Lett.* **71**, 4023 (1993).
- Hal93: M.J. Hall, B.J. Hickey, M.A. Howson, M.J. Walker, J. Xu, D. Greig, and N. Wisser, *Phys. Rev.* **B47**, 12785 (1993).
- Han58: M. Hansen and K. Anderko, *Constitution of Binary Alloys*, McGraw-Hill, New York (1958).
- Hec80: Eugene Hecht, *Physics in perspective*, Addison-Wesley Publishing Company, Inc. (1980).
- Hei94: *Ultrathin Magnetic Structures II, Measurement Techniques and Magnetic Properties*, edited by B. Heinrich and J.A.C. Bland (Springer-Verlag, Berlin 1994), A. Fert and P. Bruno, *ibid.* pp. 82-116; S.S.P. Parkin, *ibid.* pp. 148-185.
- Hol94: P. Holody, L.B. Steren, R. Morel, A. Fert, R. Loloee, and P.A. Schroeder, *Phys. Rev.* **B50**, 12999 (1994).
- Hon94: S. Honda and M. Nawate, in *Proceedings of the 3rd International Symposium on Magnetic Materials, Processes, and Devices*, Vol. **94**, 189 (1994).
- Hoo92: Randolph Q. Hood and L.M. Falicov, *Phys. Rev.* **B46**, 8287 (1992).
- Hoo94: Randolph Q. Hood, L.M. Falicov and D.R. Penn, *Phys. Rev.* **B49**, 368 (1994).
- Jan57: J.P. Jan in *solid state physics*, edited by F. Seitz and D. Turnbull, New York, academic Press, Vol. **5**, 1 (1957).
- Joh91: B.L. Johnson and R.E. Camley, *Phys. Rev.* **B44**, 9997 (1991).
- Jun94: R. Jungblut, R. Coehoorn, M.T. Johnson, J. aan de Stegge, and A. Reinders, *J. Appl. Phys.* **75**, 6659 (1994).
- Kes91: H.W. van Kesteren, F.J.A. den Broeder, P.J.H. Bloemen, E.A.M. van Alphen, and W.J.M. de Jonge, *J. Magn. Magn. Mater.* **102**, L9 (1991).

- Kit96: O. Kitakami, H. Takashima, and Y. Shimada, *J. Magn. Magn. Mater.* **164**, 43-48 (1996).
- Kne62: E. Kneller, *J. Appl. Phys.* **3**, 1355 (1962).
- Koh97: J. Kohlhepp, M. Valkier, A. van der Graaf, and F.J.A. den Broeder, *Phys. Rev.* **B55**, R696 (1997).
- Koo95: J.C.S. Kools, *J. Appl. Phys.* **77**, 2993 (1995).
- Koo96: J.C.S. Kools, *IEEE transactions on magnetics*, vol **32**, 3165 (1996).
- Lau59: J. de Lanau, R.L. Dolecek, and R.T. Webber, *J. Phys. Chem. Solids* **11**, 37 (1959).
- Lee92: S.F. Lee, W.P. Pratt, Jr., R. Loloee, P.A. Schroeder, and J. Bass, *Phys. Rev.* **B46**, 548 (1992).
- Len94: S.K.J. Lenczowski, M.A.M. Gijs, J.B. Giesbers, R.J.M. van de Veerdonk, and W.J.M. de Jonge, *Phys. Rev.* **B50**, 9982 (1994).
- Lev90: P.M. Levy, S. Zhang, and A. Fert, *Phys. Rev. Lett.* **65**, 1643 (1990).
- Lin91: C.J. Lin, G.L. Gorman, C.H. Lee, R.F.C. Farrow, E.E. Marinero, H.V. Do, H. Notarys, and C.J. Chien, *J. Magn. Magn. Mater.* **93**, 194 (1991).
- Lit97: V.I. Litvinov, V.K. Dugaev, M.M.H. Willekens, and H.J.M. Swagten, *Phys. Rev.* **B55**, 8374 (1997).
- Liv96: James D. Livingston in "DRIVING FORCE, the natural magic of magnets, Harvard University Press (1996).
- Lui93: S.B. Luitjens, *Nederlands tijdschrift voor natuurkunde*, nr **15** (1993).
- Mat91: J. Mathon, *Contemporary physics* **32**, 143 (1991).
- McG75: T.R. McGuire and R.I. Potter, *IEEE Trans. Mag.*, **MAG-11**, 1018 (1975).
- Mei56: W.H. Meiklejohn and C.P. Bean, *Phys. Rev.* **102**, 1413 (1956).
- Mos91: D.H. Mosca, F. Petroff, A. Fert, P. Schroeder, W.P. Pratt, Jr., R. Loloee, and S. Lequien, *J. Magn. Magn. Mater.* **94**, L1 (1991).
- Mot36: N. Mott, *Proc. Roy. Soc.* **156**, 368 (1936).
- Mot64: N. Mott, *Adv. Phys.* **13**, 325 (1964).

- Mul95: M. Mulloy, E. Velu, C. Dupas, M. Galtier, E. Kolb, D. Renard, and J.P. Renard, *J. Magn. Magn. Mater.* **147**, 177 (1995).
- Nog94: S. Noguchi, R. Nakatani, K. Hoshino, and Y. Sugita, *Jpn. J. Appl. Phys.* part 1, Vol. **33**, 5734 (1994).
- Oep96: W. Oepts, M.A.M. Gijs, A. Reinders, R.M. Jungblut, R.J.M. van Gansewinkel, and W.J.M. de Jonge, *Phys. Rev.* **B53**, 14024 (1996).
- Ogu92: A. Oguri, Y. Asano, and S. Maekawa, *J. Phys. Soc. Jpn.* **61**, 2652 (1992).
- Ogu93: T. Oguchi, *J. Magn. Magn. Mater.* **126**, 519 (1993).
- Oun92: K. Ounadjela, D. Muller, A. Dinia, A. Arbaoui, P. Panissod, and G. Suran, *Phys. Rev.* **B45**, 7768 (1992).
- Pap86: D. Papaconstantopoulos, *Handbook of the Band Structures of Elemental Solids*, Plenum, New York (1986).
- Par: S.S.P. Parkin (unpublished).
- Par90: S.S.P. Parkin, N. More, and K.P. Roche, *Phys. Rev. Lett.* **64**, 2304 (1990).
- Par91: S.S.P. Parkin, Z.G. Li, and David J. Smith, *Appl. Phys. Lett.* **58**, 2710 (1991).
- Par91a: S.S.P. Parkin and D. Mauri, *Phys. Rev.* **B44**, 7131 (1991).
- Par93: S.S.P. Parkin, *Phys. Rev. Lett.* **71**, 1641 (1993).
- Pet91: F. Petroff, A. Barthélémy, A. Hamzic, A. Fert, P. Etienne, S. Lequien, and G. Creuzet, *J. Magn. Magn. Mater.* **93**, 95 (1991).
- Pip89: A.B. Pippard, *Magnetoresistance in metals*, Cambridge University Press (1989).
- Pir96: L. Piraux, S. Dubois, and A. Fert, *J. Magn. Magn. Mater.* **159**, L287 (1996).
- Pou1899: V. Poulsen, Danish patent No. **2653**; V. Poulsen, P.O. Pedersen, and C. Schou, US patent No. **789,336** (1905).
- Pra91: W.P. Pratt, Jr., S.-F. Lee, J.M. Slaughter, R. Loloee, P.A. Schroeder, and J. Bass, *Phys. Rev. Lett.* **66**, 3060 (1991).
- Pri79: F. Primdahl, *J. Phys. E: Sci. Instrum.*, Vol. **12**, 241 (1979).

- Rij95: Th.G.S.M. Rijks, R.L.H. Sour, J.C.S. Kools, D.G. Neerinck, M.F. Gillies, A.E.M. De Veirman, R. Coehoorn, and W.J.M. de Jonge, *IEEE Trans. Magn.* **31**, 3865 (1995).
- Rij96: Th.G.S.M. Rijks, Ph.D. Thesis, Eindhoven University of Technology (1996).
- Rop93: F.A. Rops, Master's thesis, internal report, Eindhoven University of Technology (1993).
- Sch77: Superconductor Applications: SQUIDS and Machines, Brian B. Schwartz and Simon Foner, Plenum Press, New York (1977).
- Sch90: C.M. Schneider, P. Bressler, P. Schuster, J. Kirschner, J.J. de Miguel, and R. Miranda, *Phys. Rev. Lett.* **64**, 1059 (1990).
- Sch93: P.A. Schroeder, J. Bass, P. Holody, S.-F. Lee, R. Loloee, W.P. Pratt, Jr., and Q. Yang, *Mat. Res. Soc. Symp. Proc.* Vol **313**, 47 (1993).
- Sch94: R. Schad, C.D. Potter, G. Verbanck, V.V. Moshchalkov, and Y. Bruynseraede, *Appl. Phys. Lett.* **64**, 3500 (1994).
- Seg73: A. Segmüller and A.E. Blakeslee, *J. Appl. Cryst.* **6**, 19 (1973).
- Shu94: A.M. Shukh, D.H. Shin, and H. Hoffmann, *J. Appl. Phys.* **76**, 6507 (1994).
- Slo89: J.C. Slonczewski, *Phys. Rev.* **B39**, 6995 (1989).
- Smi51: J. Smit, *Physica* **16**, 612 (1951).
- Smi92: J. Smits, *Physics World* nr. **5**, 48 (1992).
- Son52: E.H. Sondheimer, *Adv. Phys.* **1**, 1 (1952).
- Spe91: V.S. Speriosu, B. Dieny, P. Humbert, B.A. Gurney, and H. Lefakis, *Phys. Rev.* **B44**, 5358 (1991).
- Spe93: V.S. Speriosu, J.P. Nozières, B.A. Gurney, B. Dieny, T.C. Huang, and H. Lefakis, *Phys. Rev.* **B47**, 11579 (1993).
- Ste92: Mary Beth Stearns, *J. Appl. Phys.* **72**, 5354 (1992).
- Str95: G.J. Strijkers, Master's thesis, internal report, Eindhoven University of Technology (1995).

- Str97: G.J. Strijkers, H.J.M. Swagten, A.H.M. Mettler, M.M.H. Willekens, and W.J.M. de Jonge, to be published in *Mat. Res. Soc. Symp. Proc.* (1997).
- Swa97: H.J.M. Swagten, J.C.S. Kools, G.J. Strijkers, R.H.J.N. Bitter, and W.J.M. de Jonge, *Digest of the 15th International Colloquium on Magnetic Films and Surfaces, Queensland, Australia, August 4-8 (1997).*
- Suz93: M. Suzuki, and Y. Taga, *J. Appl. Phys.* **74**, 4660 (1993).
- Tes86: Z. Tesanovic, M.V. Jaric, and S. Maekawa, *Phys. Rev. Lett.* **57**, 2760 (1986).
- Val93: T. Valet and A. Fert, *Phys. Rev.* **B48**, 7099 (1993).
- Ved92: A. Vedyayev, B. Dieny, and R. Ryzhanova, *Europhys. Lett.* **19**, 329 (1992).
- Ved93: A. Vedyayev, C. Cowache, N. Ryzhanova, and B. Dieny, *J. Phys.: Condens. Matter* **5**, 8289 (1993).
- Voe95: B. Voegeli, A. Blondel, B. Doudin, and J.-Ph. Ansermet, *J. Magn. Magn. Mater.* **151**, 388 (1995).
- Vor93: M. van de Vorst, Master's thesis, internal report, Eindhoven University of Technology (1993).
- Wel94: K.P. Wellock, B.J. Hickey, D. Greig, M.J. Walker, and J. Xu, *J. Appl. Phys.* **75**, 7055 (1994).
- Wel95: K.P. Wellock, B.J. Hickey, J. Xu, M.J. Walker, and N. Wiser, *J. Magn. Magn. Mater.* **140-144**, 585 (1995).
- Woh82: I.A. Campbell and A. Fert in *Ferromagnetic Materials, Vol. 3*, Edited by E.P. Wohlfarth, North-Holland Publishing Company (1982).
- Zah95: P. Zahn, I. Mertig, M. Richter, and H. Eschrig, *Phys. Rev. Lett.* **75**, 2996 (1995).
- Zep91: W.B. Zeper, Ph.D. thesis, University of Twente (1991).
- Zha92: S. Zhang, P.M. Levy, and A. Fert, *Phys. Rev.* **B45**, 8689 (1992).
- Zha95: X.G. Zhang and W.H. Butler, *Phys. Rev.* **B51**, 10085 (1995).
- Zim67: J.M. Ziman, *Electrons and phonons: the theory of transport phenomena in solids*, Oxford, Clarendon press (1967).

Samenvatting

Het grootste gedeelte van het onderzoek dat in dit proefschrift wordt beschreven, is gericht op het verschijnsel "reuze-magnetoweerstand". Dit verschijnsel, dat voor het eerst werd waargenomen in 1988, kan bijvoorbeeld voorkomen in systemen die zijn opgebouwd uit een stapeling van lagen die afwisselend magnetisch en niet-magnetisch zijn. Reuze-magnetoweerstand wil zeggen dat de elektrische weerstand sterk afhangt van de hoek tussen de magnetisatie-richtingen van de verschillende magnetische lagen. Toepassingen van het reuze-magnetoweerstandseffect kunnen bijvoorbeeld gevonden worden in magneetveld sensoren (leeskoppen), maar ook in plaats- en snelheidssensoren of in magnetische geheuelementen (MRAMs).

De precieze samenstelling van het systeem moet zodanig gekozen worden dat de magnetisatie-richtingen van de magnetische lagen in de afwezigheid van een magnetisch veld antiparallel gericht zijn, zodat, als een voldoende groot magnetisch veld wordt aangelegd, een overgang van antiparallel naar parallel optreedt. Hierbij is de weerstand minimaal als alle magnetisatie-richtingen dezelfde kant op wijzen. Dit wordt veroorzaakt doordat één soort elektronen, we onderscheiden elektronen met hun spin parallel aan de lokale magnetisatie-richting (spin-op elektronen) en elektronen met hun spin antiparallel aan de lokale magnetisatie (spin-neer elektronen), minder weerstand ondervinden dan elektronen met een tegengestelde spinrichting, hetgeen wordt aangeduid met de term spin-afhankelijke verstrooiing. Een van de doelstellingen waarop het onderzoek zich heeft gericht, is of deze spinafhankelijke verstrooiing vooral optreedt binnen de magnetische lagen, of vooral aan de grensvlakken met de niet-magnetische lagen. In ons specifieke geval hebben we ons vooral geconcentreerd op twee ferromagnetische Co (of $\text{Ni}_{80}\text{Fe}_{20}$) lagen, met een typische dikte van 2-100 Å, die van elkaar gescheiden worden door een Cu-laag met een typische dikte van 30-40 Å.

Metingen die in dit proefschrift beschreven worden, bestaan vooral uit metingen van de weerstand en de magnetisatie van de samples. De opstellingen die hiervoor zijn gebruikt staan beschreven in hoofdstuk 2. In hoofdstuk 3 is uitgebreid ingegaan op de modellering van het reuze-magnetoweerstandseffect, hoofdzakelijk via een semi-klassieke benadering.

In hoofdstuk 4 is een onderzoek beschreven naar de antiferromagnetische koppeling tussen magnetische lagen die zijn samengesteld uit $M = 2 \text{ \AA Co} + 4 \times (3 \text{ \AA Co} + 6 \text{ \AA Pd}) + 5 \text{ \AA Co}$, gescheiden door lagen Ru met een dikte van 8 Å. Door deze specifieke samenstelling, waarbij de magnetisatie bij voorkeur loodrecht op het samplevlak staat, draaien de magnetisatie-richtingen van de magnetische lagen om bij goed gedefinieerde velden. Het blijkt dat iedere laag bij een ander veld draait. Uit de waarden van deze overgangsvelden hebben we kunnen afleiden dat de koppeling toeneemt met het aantal lagen. Als een laag

binnenin de stapeling omdraait van magnetisatierichting levert dit een bijdrage aan het reuze-magnetowerstandseffect die tweemaal zo groot is als wanneer één van de twee buitenste lagen omdraait. Dit is in overeenstemming met modelberekeningen wanneer de gemiddelde vrije weglengte van de geleidings-elektronen klein is in vergelijking tot de dikte van de magnetische lagen.

Het onderzoek dat beschreven is in de hoofdstukken 5 tot en met 9 is gericht op het reuze-magnetowerstandseffect dat veroorzaakt wordt door twee magnetische lagen die niet (antiferromagnetisch) met elkaar gekoppeld zijn. Het is dan toch mogelijk zowel een parallelle als een antiparallelle configuratie tussen de magnetisatierichtingen te verkrijgen door de magnetisatierichting van één van de twee lagen enigszins vast te houden in een bepaalde richting. Dit kan door deze laag direct te koppelen aan een antiferromagneet (we spreken dan over een exchange-biased spin valve) of antiferromagnetisch te koppelen aan een derde magnetische laag (AF-biased spin valve). De term spin valve (spin klep) duidt hier op het feit dat de weerstand van een magnetische laag voor een elektron met een bepaalde spinrichting hoog of laag kan zijn, afhankelijk van de magnetisatierichting van de laag ten opzichte van de spin van het elektron. Details over de specifiek gebruikte structuren zijn gegeven in hoofdstuk 5.

In hoofdstuk 6 is het effect onderzocht van menging van Co en Cu aan het grensvlak tussen deze lagen. Door de manier waarop de lagen zijn gegroeid, is er intrinsiek al een gemengde laag met een dikte in de orde van 4 Å aanwezig. Als deze laag dikker wordt gemaakt (tot 36 Å), dan blijkt het reuze-magnetowerstandseffect monotoon af te nemen. Hieruit en uit de vergelijking met modelberekeningen is geconcludeerd dat deze afname veroorzaakt wordt door een toenemende verstrooiing voor zowel spin-neer als spin-op elektronen. Een eventuele kleine toename in de asymmetrie in de verstrooiingskans van spin-op en spin-neer elektronen is daardoor niet meer te onderscheiden.

In hoofdstuk 7 hebben we ons gericht op de vraag of er binnen een Co-laag een asymmetrie bestaat tussen de gemiddelde vrije weglengte van de geleidings-elektronen met spin-op en spin-neer, λ_{Co}^{\uparrow} en $\lambda_{Co}^{\downarrow}$, wat overeenkomt met spin-afhankelijke verstrooiing binnen de magnetische lagen. In dit hoofdstuk is de langste gemiddelde vrije weglengte, voor Co is dit λ_{Co}^{\uparrow} , bepaald alsmede de bulkgeleiding ($\propto \lambda_{Co}^{\uparrow} + \lambda_{Co}^{\downarrow}$). Uit de vergelijking met gelijksoortige metingen aan niet-magnetisch Cu, zijn geen duidelijke aanwijzingen gevonden voor een grote asymmetrie in de vrije weglengte, alhoewel we deze op grond van onze metingen ook niet kunnen uitsluiten.

In hoofdstuk 8 is aangetoond dat zowel voor de combinatie Co/Cu/Co als Ni₈₀Fe₂₀/Cu/Ni₈₀Fe₂₀ spin-afhankelijke verstrooiing in ieder geval optreedt aan het grensvlak tussen de twee magnetische lagen en de Cu-laag. Om dit aan te tonen is gebruik gemaakt van een tweede, relatief dikke, Cu-laag (de achterlaag) die gegroeid wordt op de bovenste magnetische laag. Deze laag maakt het mogelijk om onderzoek te doen aan zeer dunne magnetische lagen zonder dat

storende effecten afkomstig van de buitenoppervlakken van het sample optreden. Zonder deze achterlaag zou de diffuse verstrooiing van de geleidings-elektronen aan het buitenoppervlak, de asymmetrie in de stroomdichtheid van de spin-op en spin-neer elektronen, die ontstaat aan het grensvlak tussen de magnetische lagen en de Cu-lagen en zich kan uitstrekken over een laagdikte van de orde van λ^{\uparrow} , voor een groot gedeelte opheffen.

Tenslotte is in hoofdstuk 9 onderzoek verricht naar de mate waarin de geleidings-elektronen spiegelend worden verstrooid aan de buitenste oppervlakken van de spin valve. Dit is van belang omdat als de elektronen aan de buitenwanden perfect spiegelend worden gereflecteerd, een systeem met twee magnetische lagen zich effectief gedraagt als een oneindige multilaag, hetgeen leidt tot een groter reuze-magnetoweerstandseffect. De metingen die beschreven staan in hoofdstuk 9 leveren aanwijzingen dat elektronen aan een grensvlak met NiO gedeeltelijk spiegelend worden gereflecteerd.

List of publications

On the magnetic phase diagram of PbSnMnTe; carrier-induced magnetism,
(abstract),

H.J.M. Swagten, T. Story, R.J.T. van Kempen, M.M.H. Willekens, and W.J.M. de Jonge,
J. Appl. Phys. **69**, 6118 (1991).

Magnetic and transport behavior of AF-coupled layers with a limited number of repetitions,

M.M.H. Willekens, H.J.M. Swagten, A.M. Duif, P.J.H. Bloemen, R.J.T. van Kempen, S.K.J. Lenczowski, and W.J.M. de Jonge,
MRS symposium on Magnetic Ultrathin Films, Multilayers and Surfaces, Interfaces and Characterization, San Francisco, April 12-16, 1993,
Mat. Res. Soc. Symp. Proc. **313**, 129 (1993).

Effects of interface intermixing on the magnetoresistance of spin valves with uncoupled Co-layers,

M.M.H. Willekens, Th.G.S.M. Rijks, H.J.M. Swagten, R.A. van de Roer, and W.J.M. de Jonge,
MRS symposium on Magnetic Ultrathin Films, Multilayers and Surfaces, San Francisco, April 17-21, 1995,
Mat. Res. Soc. Symp. Proc. **384**, 391 (1995).

Interface intermixing and magnetoresistance in Co/Cu spin valves with uncoupled Co layers,

M.M.H. Willekens, Th.G.S.M. Rijks, H.J.M. Swagten, and W.J.M. de Jonge,
J. Appl. Phys. **78**, 7202 (1995).

Analysis of scattering lengths in Co/Cu spin valves using a Ru barrier,

H.J.M. Swagten, G.J. Strijkers, M.M.H. Willekens, and W.J.M. de Jonge,
Second International Symposium on Metallic Multilayers, Cambridge, UK, September 11-14, 1995,
J. Magn. Magn. Mater. **156**, 329 (1996).

Enhanced giant magnetoresistance in spin valves sandwiched between insulating NiO,

H.J.M. Swagten, G.J. Strijkers, P.J.H. Bloemen, M.M.H. Willekens, and W.J.M. de Jonge,
Phys. Rev. **B53**, 9108 (1996).

Analysis of scattering lengths in Co/Cu/Co and Co/Cu/Co/Cu spin valves using a Ru barrier,

G.J. Strijkers, M.M.H. Willekens, H.J.M. Swagten, and W.J.M. de Jonge,
Phys. Rev. **B54**, 9365 (1996).

The resonant state of $4f^{14}13$ Yb ion in $Pb_{1-x}Ge_xTe$,
E. Grodzicka, W. Dobrowolski, T. Story, E.I. Slynko, Yu.K. Vygranenko, M.M.H. Willekens, H.J.M. Swagten, and W.J.M. de Jonge,
Proceedings of the XXV International School of Semiconducting Compounds,
Jaszowiec 1996,
Acta Physica Polonica **A90**, 801 (1996).

Current-in-plane magnetoresistance: An approach to boundary conditions,
V.I. Litvinov, V.K. Dugaev, M.M.H. Willekens, and H.J.M. Swagten,
Phys. Rev. **B55**, 8374 (1997).

Interface-selective determination of spin-dependent scattering,
H.J.M. Swagten, G.J. Strijkers, G.L.J. Verschueren, M.M.H. Willekens, and
W.J.M. de Jonge,
J. Magn. Magn. Mater. (to be published in 1997).

Giant magnetoresistance induced by ultrathin magnetic layers,
G.J. Strijkers, H.J.M. Swagten, A.H.M. Mettler, M.M.H. Willekens, and W.J.M.
de Jonge,
MRS symposium on Magnetic Ultrathin Films, Multilayers and Surfaces,
San Francisco, March 31-April 4, 1997,
Mat. Res. Soc. Symp. Proc. (to be published in 1997).

*The giant magnetoresistance effect, experimental aspects and an analytical
approach to the Boltzmann equation,*
H.J.M. Swagten, M.M.H. Willekens, and W.J.M. de Jonge,
"Frontiers in Magnetism of reduced Dimension Systems", NATO ASI Series, eds.
P. Wigen and V. Baryachtar, Kluwer Acad. Publ. (to be published).

Dankwoord

Hoewel op de kaft van dit proefschrift slechts één auteur staat vermeld, hebben velen aan het beschreven onderzoek bijgedragen. Binnenin het boekje is daarom ook veelvuldig het woord "wij" gebruikt. Op deze plaats wil ik graag iedereen die op één of andere wijze een bijdrage heeft geleverd bedanken. Dit zijn met name:

- Wim de Jonge en Henk Swagten voor de dynamische en inspirerende wijze waarop zij mij steeds hebben begeleid en gestimuleerd,
- Reinder Coehoorn voor het kritisch doorlezen van het proefschrift en zijn waardevolle suggesties,
- Pascal Bloemen, André Duif, Rob van Kempen, Klaas Kopinga, Staszek Lenczowski, Theo Rijks, Kees Schep, Gustav Strijkers en Coen Swüste voor hun metingen, berekeningen, kritische opmerkingen en waardevolle discussies,
- Jef Noijen, Gerrie Baselmans, Cees van der Steen en Hans Dalderop voor hun onmisbare technische ondersteuning,
- Dick de Boer en An Leenaers van Philips Research voor het verrichten van röntgenverstrooiings metingen,
- Rini Bongers, Maurice Janssen, Rob van Kempen, Siebe Landheer, Robert van de Roer, Frans Rops, Gustav Strijkers en Geert Verschuieren die als afstudeerders hun bijdrage hebben geleverd en dus een groot deel van de metingen voor hun rekening hebben genomen evenals
- Stefan Belfroid, Paul Böcker, Marco Bosch, Seth Brussaard, Thijs Elenbaas, Michel Hamers, John van der Heijden, Joost van den Heuvel, Onno Hovers, Cees Lazaroms, Roel Moors, Katrijn Rombouts, Ad Rovers, Hassan Tijani, Francis Witwicki, Johnny Vogels en Hans van de Wassenberg die dat als stagair(e)s hebben gedaan,
- alle (ex)leden van de groep Coöperatieve Verschijnselen voor de gezelligheid,
- Henk Munsters van Philips Research en Gustav Strijkers voor het vervaardigen van de samples,
- Wil Delissen en Jos van Amelsvoort voor het leveren van heel veel vloeibaar helium,
- Vladimir Litvinov voor de samenwerking dichtbij en ver weg,
- Noucha Duncker en Rianne van Vinken voor de administratieve ondersteuning,
- de onderzoeksschool Cobra, de faculteitswerkplaats Natuurkunde en de glastechnische groep CTD,
- en niet in de laatste plaats, alhoewel wel hier als laatste genoemd, het thuisfront.

Curriculum vitae

M.M.H. Willekens

- 18 april 1968 geboren te Tilburg.
- 1980-1986 VWO, Gymnasium β ,
Sint Odulphuslyceum te Tilburg.
- 1986-1992 Studie Technische Natuurkunde,
Technische Universiteit Eindhoven.
Afstudeeronderzoek binnen de Vakgroep Vaste Stof,
groep Coöperatieve Verschijnselen.
Titel: Magnetische eigenschappen van de IV-VI-groep
verdunde magnetische halfgeleider $Pb_{1-x-y}Sn_yMn_xTe$.
- 1992-1994 Korte Onderzoekersopleiding Technische
Natuurkunde, Instituut Vervolgopleidingen,
Technische Universiteit Eindhoven,
Titel: Exchange coupling in perpendicular magnetic
multilayers.
- 1994-1997 Promovendus (als Assistent in Opleiding) aan de
Technische Universiteit Eindhoven, Faculteit der
Technische Natuurkunde, in de Vakgroep Vaste Stof,
groep Coöperatieve Verschijnselen.
Promotie: 15 oktober 1997.
Titel: Giant Magnetoresistance in Spin Valves.

Stellingen

behorende bij het proefschrift

Giant Magnetoresistance in Spin Valves

M.M.H. Willekens

15 oktober 1997

1. De depositie van Au-onzuiverheden aan de grensvlakken van Co/Cu multilagen geeft geen informatie over de relatieve bijdragen van bulk en grensvlak spin-afhankelijke verstrooiing in het Co/Cu systeem.

K.P. Wellock, B.J. Hickey, D. Greig, M.J. Walker, en J. Xu, J. Appl. Phys. 75, 7055 (1994).

2. Een toename in het reuze-magnetoweerstands effect bij de depositie van ~ 2 monolagen Au boven op een "geïnverteerde" spin valve kan ook zonder spiegellende elektron reflectie.

W.F. Egelhoff, Jr., P.J. Chen, C.J. Powell, M.D. Stiles, R.D. McMichael, J.H. Judy, K. Takano, A.E. Berkowitz, and J.M. Daughton, wordt gepubliceerd in IEEE Trans. Magn. (1997).

3. Hoewel met de Röntgen-straling staande golf techniek in theorie adsorbaten op verschillende posities kunnen worden onderscheiden en de relatieve bezetting kan worden bepaald, blijkt in de praktijk dat een systeem met verschillende posities niet eenduidig oplosbaar is indien niet bekend is hoeveel adsorptieposities een adsorbaat op een oppervlak inneemt.

Zegenhagen, Surf. Sci. Rep. 18, 199 (1993); G. Scragg, B.C.C. Cowie, M. Kerker, D.P. Woodruff, A. Daimellah, S. Turton, en R.G. Jones, J. Phys.: Condens. Mat. 6, 1869 (1994); D. Heskett, P. Xu, L. Berman, C.-C. Kao, en M.J. Bedzyk, Surf. Sci. 344, 267 (1995).

4. De structuur die door Gurney *et al.* is gebruikt om de langste elektron gemiddelde vrije weglengte binnen een magnetische laag van een spin valve te bepalen is juist uitermate geschikt om (spin-afhankelijke) verstrooiing aan de grensvlakken te bestuderen.

B.A. Gurney, V.S. Speriosu, J. Nozieres, H. Lefakis, D.R. Wilhoit, en O.U. Need, Phys. Rev. Lett. 71, 4023 (1993),
Dit proefschrift, hoofdstuk 8.

5. In de interpretatie van Mössbauer resonantie spectra van een dunne Fe_3O_4 film, dienen niet alleen de kristallijne en magneto-elastische anisotropie in beschouwing te worden genomen, maar ook de vorm-anisotropie.

T. Fujii, M Takano, R. Katano, Y. Bando, en Y. Isozumi, J. of Crystal Growth 99, 606 (1990).

6. De absolute gevoeligheid (minimaal detecteerbare moment), opgegeven door de fabricant van een SQUID magnetometer, is vooral van belang in relatie tot de verkoopprijs van een dergelijke magnetometer.
7. Binnen één type nano-kristallijn materiaal kan een groot reuze-magnetoweerstands effect en een hoge magnetische permeabiliteit niet tegelijkertijd gerealiseerd worden.
8. De stelling van karate grootmeesters dat karate-do veel meer een levensstijl is dan een sport, komt onvoldoende tot uitdrukking in de overvloed aan boeken over karate die hoofdzakelijk uit foto's zijn samengesteld.
9. Zwembaden zijn te klein voor een eerlijke beoordeling van zwemwedstrijden waarbij een bepaalde afstand zo snel mogelijk gezwommen dient te worden; lange zwemmers zijn hier in het voordeel.
10. Wetenschap en politiek zouden zich op mondiaal niveau moeten inzetten om de gemiddelde lichaamslengte van de mens te reduceren.